

**NORTHWESTERN UNIVERSITY**

**A Search for Dark Matter Produced in Association with a Top Quark Pair at  
 $\sqrt{s} = 13$  TeV in the Dilepton Final State with the CMS Detector**

**A DISSERTATION**

**SUBMITTED TO THE GRADUATE SCHOOL  
IN PARTIAL FULFILLMENT OF THE REQUIREMENTS**

**for the degree**

**DOCTOR OF PHILOSOPHY**

**Field of Physics and Astronomy**

**By**

**Stanislava Lubomirova Sevova**

**EVANSTON, ILLINOIS**

**June 2018**



## Abstract

A vast portion of the Universe is predicted to consist of an as-of-yet undetected, non-luminous form of matter, known as dark matter. Evidence of its existence has been corroborated by various astrophysical observations at many cosmological scales, and its relative abundance has been determined. However, knowledge of its nature and non-gravitational interactions is entirely lacking. Nonetheless, the predicted particle nature of dark matter allows for multiple complementary methods of its detection.

This work presents a search for dark matter produced in association with a top quark pair performed using the data recorded by the CMS detector at the LHC in Geneva, Switzerland during 2016. The collision center-of-mass energy of the dataset in question is 13 TeV, and the integrated luminosity of the dataset corresponds to  $35.9 \text{ fb}^{-1}$ . The analysis performed considers only the dilepton decay of top quark pairs. The results are interpreted using simplified models of dark matter and are compared to corresponding results from direct detection experiments. While the work does not provide evidence of the production of dark matter in association with a top quark pair in the dilepton final state from proton-proton collisions, it sets important constraints on the properties of dark matter.



## Declaration

The following dissertation is the result of my own work conducted while based at Northwestern University and CERN. Explicit references are made to acknowledge the work of others. This dissertation has not been submitted for another qualification to Northwestern University or any other university.

Stanislava Sevova



## Acknowledgements

A great number of people deserve recognition for directly or indirectly providing me with the support required to complete this work. Of particular prominence are my advisor at Northwestern, Kristian Hahn, and the post-doctoral researcher who has provided invaluable mentorship since day one, Kevin Sung. I would like to thank Kristian for his strong leadership and constant support of my research as a graduate student. His guidance and creativity have only amplified my own passion for particle physics throughout the years, and it has truly been a rewarding experience to work with him. To Kevin, I owe an immense amount of gratitude for his patience, understanding, and attention to detail. I have been extremely fortunate to learn from someone as knowledgeable and precise as Kevin, and I am beyond grateful for all the help he has provided over the years! I will especially and genuinely miss the office camaraderie. In addition, I would like to thank other excellent CMS colleagues, Phil Harris, Nhan Tran, and Marco Trovato who provided additional support and interesting research opportunities for me to pursue.

Throughout my graduate career, I was lucky to be surrounded by a wonderful group of friends both in Chicago and Geneva, a few of whom I feel should be mentioned by name. I would like to thank my dear friend Mary Crofton for her constant ability to take my mind off research with fun activities, and also for giving me a place to stay and feeding me while in Chicago! I would like to thank my friends Rickard Strom, Sophie Baker, and Andrew Carnes for imparting a bit of their undying sense of

adventure onto me, and for the laughs they always provide. Finally, I would like to thank Leonora Vesterbacka for always being there, always knowing what to say, and always having my back! I will cherish our friendship for life.

I would be remiss if I did not acknowledge how much Doug Schaefer has rejuvenated my quality of life in recent months, and would like to thank him not only for his immense support in recent weeks, but also for the joy he has provided me in all of our adventures together, big or small.

To conclude, above all I am deeply thankful to my family. To my younger sister, Ralitza, I am thankful for all the ways you are able to make me smile, and I truly cherish your youthful wisdom! I look forward to giving you the same love and support you've provided me with, as you reach new heights. I dedicate this work to my parents, Penka and Lubomir, to whom I cannot express in enough words how grateful I am. You have taught me to follow my passions, persevere through the obstacles, and never be afraid of the unknown. Your support is eternal, as is my love for you. Thank you.

# Contents

<b>1. Dark matter: beyond the Standard Model</b>	<b>1</b>
1.1. Introduction to dark matter . . . . .	2
1.2. The Standard Model . . . . .	7
1.2.1. Electroweak theory and the Higgs mechanism . . . . .	12
1.2.2. Yukawa interactions . . . . .	18
1.3. Dark matter candidates . . . . .	23
1.4. Dark matter detection . . . . .	26
1.4.1. Indirect detection . . . . .	27
1.4.2. Direct detection . . . . .	29
1.4.3. Collider searches . . . . .	34
1.5. Simplified models of DM: beyond the Standard Model . . . . .	35
<b>2. The experimental apparatus</b>	<b>41</b>
2.1. The LHC . . . . .	41
2.2. The CMS experiment . . . . .	45
2.2.1. The magnet . . . . .	47
2.2.2. The inner tracker . . . . .	50
2.2.3. The calorimeters . . . . .	54
2.2.4. The muon detectors . . . . .	59
2.2.5. The readout system . . . . .	61

2.2.6. Computing and data storage . . . . .	68
<b>3. Object and event reconstruction</b>	<b>71</b>
3.1. The Particle Flow algorithm . . . . .	72
3.2. Leptons . . . . .	73
3.2.1. Muons . . . . .	74
3.2.2. Electrons . . . . .	77
3.3. Jets . . . . .	80
3.3.1. b-jet tagging . . . . .	85
3.4. Missing transverse energy . . . . .	87
<b>4. Signal simulation and event selection</b>	<b>89</b>
4.1. $t\bar{t} + \chi\bar{\chi}$ simplified models . . . . .	89
4.2. Signal region event selection . . . . .	93
4.2.1. The $M_{T2}^{\ell\ell}$ variable . . . . .	94
<b>5. Background processes</b>	<b>99</b>
5.1. $t\bar{t}(2\ell)$ . . . . .	101
5.1.1. Top $p_T$ re-weighting . . . . .	102
5.2. $t\bar{t} + V$ , diboson, and single top processes . . . . .	103
5.3. Drell-Yan . . . . .	104
5.3.1. The $R_{in/out}$ method . . . . .	109
5.4. Fake lepton background . . . . .	117
5.4.1. Fake rate measurement . . . . .	118
5.4.2. Fake rate application . . . . .	120
5.4.3. Fake rate method validation . . . . .	122
<b>6. Analysis</b>	<b>125</b>
6.1. Search strategy . . . . .	125

<b>6.2. Data to simulation corrections</b>	<b>126</b>
6.2.1. Trigger efficiency	127
6.2.2. PU reweighting	129
6.2.3. b-tagging efficiency	131
<b>6.3. Discriminating observables</b>	<b>134</b>
<b>6.4. Systematic uncertainties</b>	<b>140</b>
6.4.1. Sources of systematic uncertainty	142
<b>6.5. Statistical analysis</b>	<b>148</b>
6.5.1. Maximum likelihood	148
6.5.2. Hypothesis testing	149
6.5.3. Signal extraction	152
6.5.4. Post-fit diagnostics	153
<b>7. Dark matter interpretation</b>	<b>161</b>
7.1. Upper limits on $t\bar{t}(2\ell) + \chi\bar{\chi}$ production at the LHC	162
7.2. Comparison with direct detection	167
7.2.1. Spin-indepedent comparison	168
<b>8. Conclusions</b>	<b>171</b>
<b>A. Shape systematics</b>	<b>173</b>
A.1. $t\bar{t}(2\ell)$ shape systematics	174
A.2. Signal shape systematics: scalar mediated, $m_\phi = 10 \text{ GeV}$ , $m_\chi = 1 \text{ GeV}$	179
<b>Bibliography</b>	<b>183</b>
<b>List of figures</b>	<b>191</b>
<b>List of tables</b>	<b>193</b>



# Chapter 1.

## Dark matter: beyond the Standard Model

The Standard Model (SM) of particle physics, albeit a successful theory encoding the properties of elementary particles and their interactions, nonetheless has some shortcomings. For one, cosmological and astrophysical observations supply compelling evidence [1–3] for the existence of dark matter (DM), a piece of the astro-particle physics puzzle that is not covered by the SM. In Section 1.1, evidence of the existence of DM and motivations for its search are briefly detailed. Subsequently, an outline of the SM is presented in Section 1.2, in order to provide context for the prevalent DM candidates described in Section 1.3, while in Section 1.4 the three main modes of DM detection are outlined, with a particular emphasis on particle colliders. The chapter concludes with a focus on beyond the Standard Model (BSM) simplified models of DM currently being probed at general-purpose detectors at the Large Hadron Collider (LHC) in Geneva, Switzerland.

## 1.1. Introduction to dark matter

Observations at all scales, from smaller dwarf galaxies to large galactic superclusters point to the existence of more matter than can be reconciled with the amount of visible matter in our universe. The existence of additional non-luminous matter and its dominance in amount compared to luminous matter, was first postulated by Swiss physicist Fritz Zwicky in 1933 during his studies of the Coma cluster. Zwicky's observations pointed to the necessity for approximately 400 times [4] the mass density as observed from the luminous matter from the cluster to ensure the gravitational bounding of nebulae within Coma. It is worth noting that Zwicky's calculations made extensive use of Hubble's constant at the time,  $H_0 = 558 \text{ km/s/Mpc}$ , and if rescaled by the modern value of  $H_0 = 67.27 \pm 0.66 \text{ km/s/Mpc}$  [5] Zwicky's results point to approximately a mass density 10 times larger than observed [6]. The period around the 1950's and 1960's marks a time when various astronomical explanations for the missing mass in galaxy clusters began to be ruled out, such as the hypothesis that dark matter consists of hot intracluster gas. [7] presents evidence that the amount of gas required for gravitational binding is 98% larger than that observed from X-ray emission spectra. During the 1970's the first explicit statements began to emerge regarding the need for the missing mass to be concentrated in the outer parts of galaxies based on spectroscopic and radio astronomy observations of the galactic rotation velocity curves. Namely, Kent Ford and Vera Rubin published results from observations of the Andromeda galaxy which extended the observational reach out to 110 minutes of arc away from the center of M31, revealing a flat dependence of  $v$ , the galactic rotation velocity, as a function of the radius  $r$  beyond the visible galactic disk as shown in Figure 1.1. The visible matter in M31 would suggest a steady decrease in  $v$  as a function of  $r$ , but the findings reported by Rubin and Kent point to a flat linear dependence, meaning there is a non-luminous contribution of matter accounting for

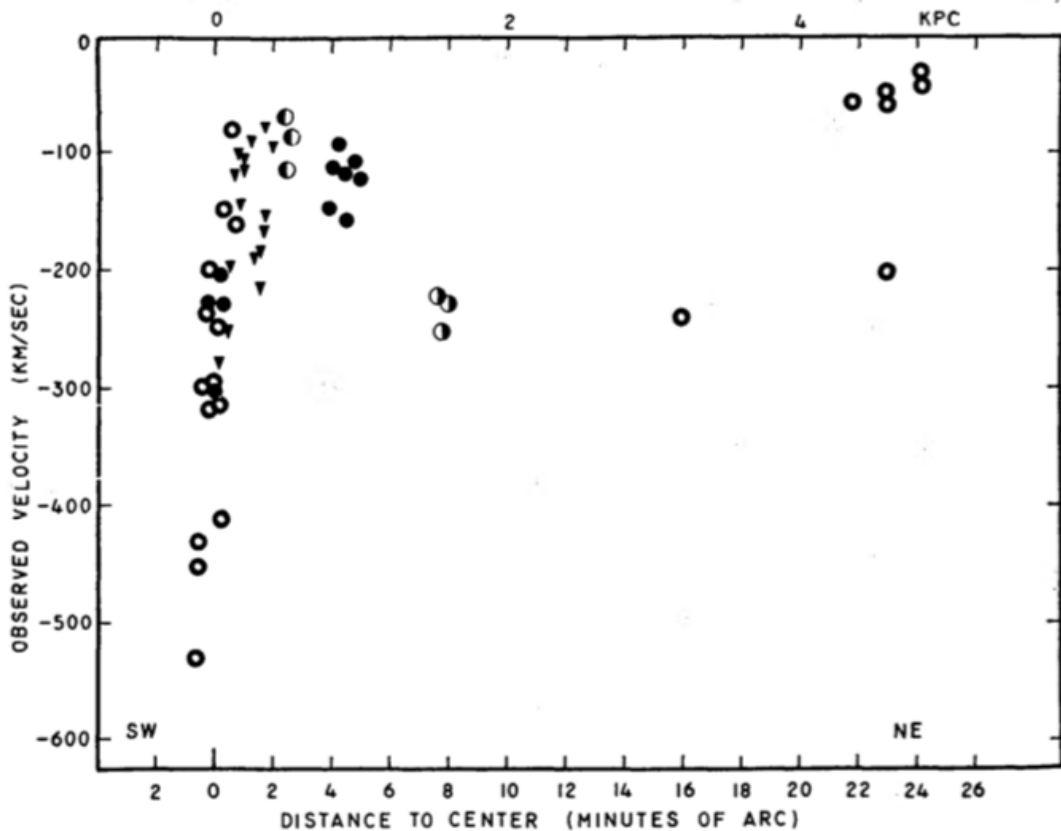


**Figure 1.1.:** The velocities of emission regions from M31 as a function of distance to the center of the galaxy measured in minutes of arc along the NE major axis as reported by Rubin and Ford in [8].

the additional  $v$  beyond the visible disk. By the onset of the 1980's the majority of the astrophysical community was convinced that a substantial amount of DM exists in the universe based on the observational evidence of mass-to-light ratios of galaxies and galactic rotation curves.

Studies of the large scale structure of the universe have provided clues on the nature of dark matter. Just as on the small scale, ordinary visible matter consists of protons, electrons, neutrons, or groups of atoms held together by the electromagnetic force, analogously groups of massive stars and planets were bound together by the gravitational force in order to form stellar clusters. These groups were in turn merged with gas and the postulated DM to form galaxies, and the galaxies were bound together

to form clusters, and subsequently superclusters. This standard theory of cosmic structure formation is often referred to as the “bottom-up” approach, and essentially posits that the current structure of the Universe is a result of the gravitational amplification of tiny matter fluctuations that were generated during the very early epochs of the Universe [9]. The evidence from the 20th century for the existence of non-luminous matter has been further supplemented with data from weak [10] and strong [11] gravitational lensing by large scale structures. The distortion of the appearances of distant objects or the duplication of the apparent image is caused by the bending of the light these objects emit by the gravitational force of the large scale structures in between the observer and the object. The data from a survey of the Bullet cluster as observed by the Chandra [12] experiment best illustrates how the distribution of the hot gas and stars originating from the collision of two galaxies and comprising the baryonic matter are bound together by a much greater contribution of non-luminous matter as seen in Figure 1.2. The calculation of the approximate contribution of visible matter was performed using data from gravitational lensing.

The aforementioned experiments and measurements buttress the necessity for the existence of DM, however the first attempts to precisely quantify the amount of DM in the Universe began with the discovery and subsequent analyses of the cosmic microwave background (CMB) by Peebles, Wilkinson, Dicke, and Roll [13]. In brief, the CMB is the relic radiation energy content from beyond our galaxy, emitted shortly before the period of recombination [14] which occurred approximately 380 000 years after the Big Bang. At this stage, photons began to decouple from the baryonic matter and over time have been redshifted to the microwave frequency range as a result of the expansion of the Universe over the past 13.81 billion years. Although the dominant contributions of the CMB are homogeneous and isotropic wherein the CMB temperature is almost uniformly  $T \simeq 2.72$  K, slight temperature fluctuations of  $\mathcal{O}(10^{-5})$  have been observed which are indicative of the state of the early Universe and



**Figure 1.2.:** A composite image from the Hubble, Chandra, and Magellan telescopes of the 1E 0657-558 cluster of galaxies (Bullet cluster) depicting the X-rays emitted by the baryonic matter as a diffuse red gas, while the approximate location of the DM surrounding the visible matter is represented in a blue hue.

the relative abundance of visible and dark matter during this period. As gravity acted on the photon-baryon plasma, the fluid pressure increased giving way to its expansion. This cycle was repeated once the pressure decreased as a result of the expansion, and gravity once more won over causing a fluid compression, hence the photons emitted during different compression stages were of varying energies. More specifically, the period of photon decoupling leading to these relic temperature variations, known as the CMB anisotropy, can be interpreted as a power spectrum in terms of multipole orders,  $\ell$ . The effects produced by the acoustic oscillations of the photon-baryon plasma just prior to the emission of the CMB are captured in this spectrum. Since both types of matter contribute to the temperature oscillations via gravitational effects, the power spectrum shown in Figure 1.3 contains information about the relative content of both visible and dark matter. The parametrization of the temperature anisotropies is in terms of spherical harmonics ( $Y_{\ell m}$ ) contained in the two-dimensional function,  $T(\theta, \phi)$  projected over the entire visible sky defined as,

$$T(\theta, \phi) = \sum_{\ell=0}^{\infty} \sum_{m=-\ell}^{\ell} a_{\ell m} Y_{\ell m}(\theta, \phi), \quad (1.1)$$

where  $\theta$  and  $\phi$  are angular coordinates,  $\ell$  is the multipole order, and  $a_{\ell m}$  are the multipole moments. Following the theory of temperature fluctuations, the distributions of the coefficients  $a_{\ell m}$  are approximately Gaussian centered about zero with a variance defined as  $C_{\ell} \equiv < |a_{\ell m}|^2 >$ , where there are only  $2\ell + 1$  values of  $m$  for each  $\ell$ , hence

$$C_{\ell} \equiv < |a_{\ell m}|^2 > \equiv \frac{1}{2\ell + 1} \sum_{m=-\ell}^{+\ell} |a_{\ell m}|^2. \quad (1.2)$$

The power spectrum,  $C_\ell$  is expressed as  $\ell(\ell + 1)C_\ell/2\pi$  in Figure 1.3, and the fit to the Planck data provides the abundances of baryonic and dark matter. The location of the first peak is related to the flat geometry of the Universe and requires that the total energy-matter density ratio,  $\Omega_{\text{total}} = 1$ . The resolution of this peak is connected to the expansion of the Universe which is driven by the repulsive force of dark energy [15]. The angular resolution of the second peak, at  $\ell_2 \simeq 500$ , provides the amount of ordinary matter that exists in the Universe, and correspondingly, the difference between the third peak, at  $\ell_3 \simeq 700$ , and the second peak provides the density of the dark matter in the early Universe. The extracted total densities of baryonic and dark matter are respectively,

$$\Omega_b h^2 = 0.02222 \pm 0.00023, \quad \Omega_\chi h^2 = 0.1186 \pm 0.0020, \quad (1.3)$$

where  $h = H_0/100$  is the reduced Hubble's constant. The relic abundances translate to 24% and 4.8% of the total matter in the Universe as being dark and baryonic, respectively, while the rest consists of dark energy [16].

## 1.2. The Standard Model

In the pursuit of a suitable candidate for what comprises close to 24% of the total matter in the Universe, a segue to the fundamental underpinnings of the SM of particle physics is required. In this section, an overview of the SM is presented along with its most successful predictions of experimentally observed particle physics phenomena and its greatest deficiencies in the quest to explain the nature of DM.

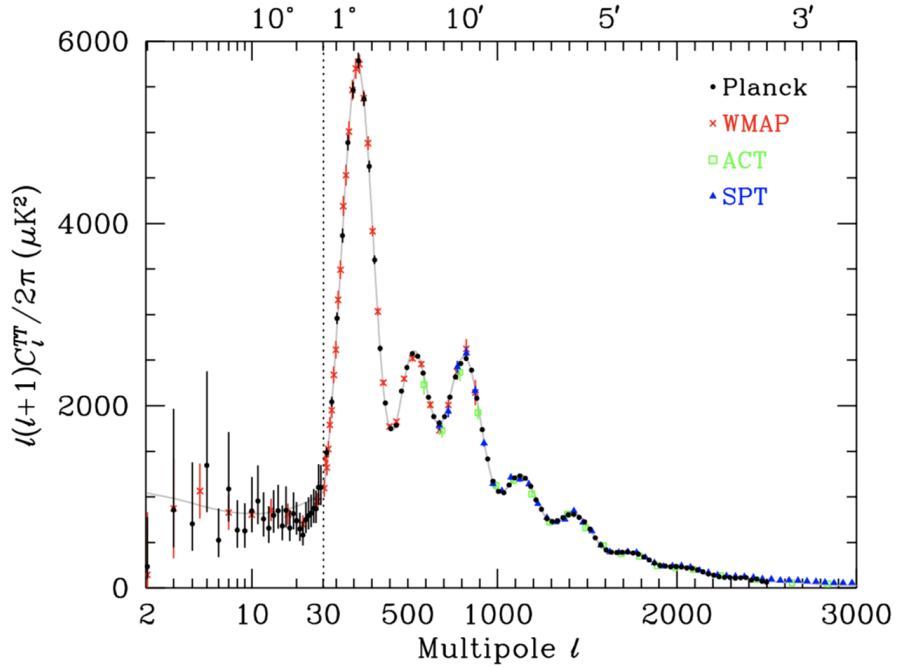


**Figure 1.3.:** The CMB radiation temperature anisotropy power spectrum as a function of the multipole order,  $\ell$ , as measured by various experiments [16]. The angular scales that correspond to the multipole orders are listed across the top of the graph. The data points correspond to the experimental measurements and the error bars account for measurement uncertainties. The black curve represents the best global fit of the standard model of cosmology to the Planck data.

As a framework that describes the fundamental constituents of observed matter and their corresponding interactions, in this respect the SM is deemed exceedingly successful. Not only are such observations predicted accurately by the SM, but its organization of the fundamental building blocks of our Universe within a framework can be thought of as analogous to the organization of elements within Mendeleev's periodic table [17]. In the theory of the SM, three of the four fundamental forces are responsible for particle matter interactions: the electromagnetic, weak, and strong forces. A few of the matter particles which these forces act upon include protons, neutrons, electrons, and quarks, whose properties are described in detail later in this section. An example of particle interactions described by the SM is the binding of neutrons and protons via the strong force in the atomic nucleus. By contrast, the weak force is responsible for the process of a neutron decaying to a proton, during which one type of quark is transmuted to another (nuclear  $\beta$  decay). The electromagnetic (EM) force is responsible for such phenomena as Bremsstrahlung, the process of EM radiation as a result of the deceleration of a charged particle deflected off another charged particle.

The foundations of the SM began with the unification of the weak and electromagnetic forces in the Glashow-Weinberg-Salam (GWS) theory of electroweak (EW) interactions [18–20] leading to the theory of quantum electrodynamics (QED), and making the first firm prediction of mass possible [21]. The strong force is described by what constitutes as the remainder of the SM, the theory of quantum chromodynamics (QCD) [22,23]. The remaining of the four fundamental forces, gravity, does not have a place within the SM as of yet, as it is a quantum theory used to describe the “micro” world and is difficult to fit into the same framework as Einstein’s general theory of relativity describing the “macro” world, where gravity plays a significant role. Acting with vastly larger strengths over significantly shorter ranges, the EW and strong forces render the effects of gravity negligible in the context of particle physics phenomena.

The elementary matter components of the SM are particles obeying Fermi-Dirac statistics called *fermions* and have half-integer spins, while the force carriers or so-called “messenger” particles obey Bose-Einstein statistics, known as *bosons* have integer spin. Individual fermion particle states can interact via the strong force to form *baryons* such as the proton and the neutron, which consist of three *quarks* (the elementary fermion particles comprising the substructure of the nucleon). Similarly, a *meson* is a bosonic two-fermion bound state consisting of a quark and anti-quark pair. Any particles, whether composite like baryons or mesons, or elementary like the quark, which interact via the strong force are classed as *hadrons*. Of course, there are also fermions like the electron and the neutrino which do not interact via the strong force, but rather via the electromagentic (EM), which are called *leptons*. The elementary quarks, leptons, and bosons carry quantum numbers that dictate their interactions such as charge (Q), lepton number (L), baryon number (B), and spin. It should be noted that color charge (C), weak isospin ( $T_3$ ), and hypercharge (Y) are also additional elementary particle quantum numbers that characterize the symmetry groups comprising the SM to be introduced later. The leptons and quarks listed in the first six rows of Table 1.1 are divided into three generations where a mass hierarchy is established with increase in generation. Despite the increase in mass with generation, the lifetime in general decreases, although *c* and *b* quarks are an exception to this trend, providing an experimental handle for their discrimination in high energy experiments. In addition, quarks and leptons of higher generations can decay to quarks and leptons of the corresponding first generation. The bottom five rows in Table 1.1 list the weak force carrying bosons,  $W$  and  $Z$ , the strong force carrying boson,  $g$ , the EM force carrying boson,  $\gamma$ , and the Higgs boson,  $H$ , which gives the other particles mass.

The SM is defined in terms of a quantum field theory (QFT) Lagrangian density that adheres to certain symmetries. Just as the classical field theory of electricity and mag-

Generation	Particle Symbol	Particle Name	Spin	Electric Charge	Mass [GeV]	Force Interaction/Carrier
1st	$e^-$	Electron	1/2	-1	$5.11 \times 10^{-4}$	EM, Weak
	$\nu_e$	Electron Neutrino	1/2	0	-	Weak
2nd	$\mu^-$	Muon	1/2	-1	0.106	EM, Weak
	$\nu_\mu$	Muon Neutrino	1/2	0	-	Weak
3rd	$\tau^-$	Tau	1/2	-1	1.78	EM, Weak
	$\nu_\tau$	Tau Neutrino	1/2	0	-	Weak
1st	$u$	Up Quark	1/2	2/3	$\approx 2.3 \times 10^{-3}$	EM, Weak, Strong
	$d$	Down Quark	1/2	-1/3	$\approx 4.8 \times 10^{-3}$	EM, Weak, Strong
2nd	$s$	Strange Quark	1/2	-1/3	$\approx 9.5 \times 10^{-2}$	EM, Weak, Strong
	$c$	Charm Quark	1/2	2/3	1.28	EM, Weak, Strong
3rd	$b$	Bottom Quark	1/2	-1/3	4.2	EM, Weak, Strong
	$t$	Top Quark	1/2	2/3	172.5	EM, Weak, Strong
-	$W^\pm$	W Boson	1	$\pm 1$	80.4	Weak
-	$Z$	Z Boson	1	0	91.2	Weak
-	$\gamma$	Photon	1	0	0	EM
-	$g$	Gluon	1	0	0	Strong
-	H	Higgs Boson	0	0	125	-

**Table 1.1.:** The particles of the SM including the leptons ( $e^-$ ,  $\mu^-$ ,  $\tau^-$ ,  $\nu_e$ ,  $\nu_\mu$ ,  $\nu_\tau$ ), the quarks ( $u$ ,  $d$ ,  $c$ ,  $s$ ,  $t$ ,  $b$ ), the gauge bosons ( $W^\pm$ ,  $Z$ ,  $g$ ,  $\gamma$ ), and the scalar Higgs boson (H). The spin, charge, and mass are specified where the neutrinos are taken to be massless, and indirect measurements posit the mass eigenstates are less than 0.23 eV [17]. The forces via which the particles interact are listed for each lepton and quark and the force mediated is listed for the gauge bosons.

netism, as fully described by Maxwell's equations, remains unchanged under position, rotation, reflection, and Lorentz transformations, so the SM remains invariant under certain transformations, better known as symmetries. In the case of Maxwell's equations, when invariance under the standard translational, rotational, and reflectional symmetries are combined with invariance under Lorentz symmetry, the combined group of symmetries is termed the Poincaré Lie group. The Poincaré symmetry is a global (spacetime) symmetry, whereas the Lie groups of the symmetries associated with the SM are local transformations associated with fields rather than particles defined by space and time coordinates. The local or internal symmetries which are the starting point for the various parts of the SM Lagrangian, are also known as gauge symmetries. The interactions within the SM are described by specific interaction terms which modify the Lagrangian leaving it invariant under the gauge transformations. Hence, the SM is defined as a gauge QFT based on the  $SU(3)_C \otimes SU(2)_L \otimes U(1)_Y$  symmetry groups, where the elementary particle interactions dictated by the strong force are described by the  $SU(3)_C$  Lie group, and interactions dictated by the electroweak forces are described by  $SU(2)_L \otimes U(1)_Y$ .

### 1.2.1. Electroweak theory and the Higgs mechanism

The point of departure for the description of interactions in the SM is the Dirac Lagrangian density,

$$\mathcal{L}_D = \bar{\psi}(i\gamma^\mu \partial_\mu - m)\psi, \quad (1.4)$$

where  $\gamma^\mu$  are the Dirac  $\gamma$ -matrices,  $\bar{\psi} = \gamma^0 \psi$  is the conjugate fermion field, and  $m$  is the fermion mass. Defining the interactions between a two spin- $\frac{1}{2}$  fields, which can be re-written as the doublet,

$$\Psi := \begin{pmatrix} \psi_1 \\ \psi_2 \end{pmatrix}, \quad (1.5)$$

requires a locally  $SU(2)$  invariant Lagrangian achieved through the addition of the extra term  $i\bar{\Psi}\gamma_\mu \frac{\sigma_i}{2} W_i^\mu \Psi$  which describes the interactions between two spin- $\frac{1}{2}$  and three massive spin-1 fields  $W_i^\mu$ . This process exploits a local internal symmetry of  $W_i^\mu$  where  $W_i^\mu \rightarrow W_i'^\mu = W_i^\mu + \partial^\mu a_i(x)$ . Neglecting the mass terms, the Lagrangian then reads,

$$\mathcal{L}_{D1+D2+int} = i\bar{\Psi}\gamma_\mu \partial^\mu \Psi + \bar{\Psi}\gamma_\mu \frac{\sigma_i}{2} W_i^\mu \Psi, \quad (1.6)$$

but equation (1.6) is missing the term for the three free spin-1 fields which includes the internal symmetry as described above. When this term is added, equation (1.6) turns into,

$$\mathcal{L}_{SU(2)} = i\bar{\Psi}\gamma_\mu \partial^\mu \Psi + \bar{\Psi}\gamma_\mu \frac{\sigma_i}{2} W_i^\mu \Psi - \frac{1}{4}(W_{\mu\nu})_j (W^{\mu\nu})_j, \quad (1.7)$$

with  $(W_{\mu\nu})_i = \partial_\mu (W_\nu)_i - \partial_\nu (W_\mu)_i$ , and leading to an  $SU(2)$  invariant Lagrangian. equation (1.7) is nonetheless lacking mass terms because the introduction of terms such as  $m_1 \bar{\Psi}\Psi$  or  $m_2 (W^\mu)_i (W_\mu)_i$  would destroy the  $SU(2)$  symmetry. Acquiring the

mass terms will be done through the breaking of this symmetry by the addition of a spin-0 field. Before this however, it is possible to unify the locally  $SU(2)$  invariant Lagrangian in equation (1.7) with a locally  $U(1)$  invariant Lagrangian in order to additionally describe fermion EM interactions. Hence, the spin-1 field  $B^\mu$ , also known as the  $U(1)$  gauge field, is introduced where its locally  $U(1)$  invariant Lagrangian goes as,

$$\mathcal{L}_{U(1)} = -m\bar{\psi}\psi + \bar{\psi}\gamma_\mu(i\partial^\mu + gB^\mu)\psi - \frac{1}{4}B_{\mu\nu}B^{\mu\nu} \quad (1.8)$$

where  $B^{\mu\nu} := \partial^\mu B^\nu - \partial^\nu B^\mu$ . Combining equation (1.7) and equation (1.8) then yields the  $SU(2)$  and  $U(1)$  locally invariant Lagrangian,

$$\mathcal{L}_{SU(2) \otimes U(1)} = \bar{\Psi}\gamma_\mu(i\partial^\mu + gB^\mu + g'\sigma_i W_i^\mu)\Psi - \frac{1}{4}(W_{\mu\nu})_j(W^{\mu\nu})_j - \frac{1}{4}B_{\mu\nu}B^{\mu\nu}, \quad (1.9)$$

where the coupling constant for the three  $W_i^\mu$  fields is ignored and simply denoted by  $g'$ . As mentioned earlier, the mass terms cannot be added “by hand” to the Lagrangian since they effectively spoil the symmetry, but by writing a locally  $SU(2)$  invariant Lagrangian for doublets of spin-0 fields, just as done in equation (1.6) earlier for spin- $\frac{1}{2}$  fields, it will be shown how the mass terms for the  $W_i^\mu$  and  $B_i^\mu$  fields are

attained. Thus for the spin-0 doublet  $\Phi := \begin{pmatrix} \phi_1 \\ \phi_2 \end{pmatrix}$ , equation (1.9) turns into,

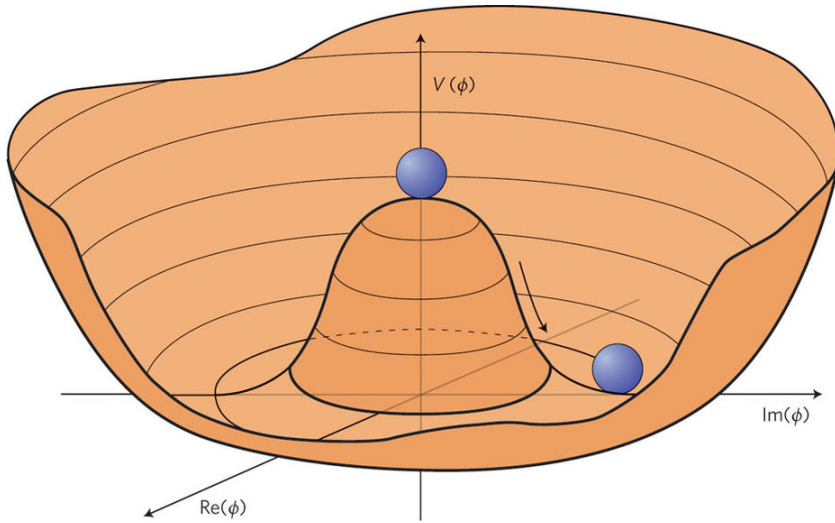


**Figure 1.4.:** The vacuum value, or the lowest-energy state, of the Higgs potential as shown in the 3-dimensional plot is described by a randomly chosen point at the bottom of the “sombrero” [24].

$$\begin{aligned} \mathcal{L}_{SU(2) \otimes U(1)} = & ((\partial_\mu - ig' \sigma_i (W_\mu)_i - i \frac{1}{2} g B_\mu) \Phi^\dagger) ((\partial^\mu - ig' \sigma_i (W^\mu)_i + i \frac{1}{2} g B^\mu) \Phi) \\ & + \rho^2 \Phi^\dagger \Phi - \lambda (\Phi^\dagger \Phi)^2, \end{aligned} \quad (1.10)$$

where the last two terms on the right-hand side are defined collectively as  $-V(\Phi)$ , or are better known as the Higgs potential.  $V(\Phi)$  can in fact be written as a function of one of the spin-0 doublet fields,  $V(\phi)$ , so that the minimum of  $V(\phi) = -\rho^2 |\phi|^2 + \lambda |\phi|^4$  can be computed in the traditional way by  $\frac{\partial V(\phi)}{\partial \phi} = 0$ . This leads to a minimum  $\phi_{\min} = \sqrt{\frac{\rho^2}{2\lambda}} e^{i\phi}$  meaning that for every  $\phi$  value there exists a minimum and thus there are an infinite number of minima, all of which lie on a circle with radius  $\sqrt{\frac{\rho^2}{2\lambda}}$ . Best visualized by the 3-dimensional  $V(\phi)$  function in the complex plane in Figure 1.4, a minimum is chosen out of the infinite possibilities (i.e. symmetry breaking), in the same sense that a marble would roll down from the top of the “sombrero” potential and spontaneously or randomly choose a vacuum value to settle in, out of infinite possibilities.

The spin-0 doublet can then be re-written as,

$$\Phi_{\min} = \begin{pmatrix} 0 \\ \sqrt{\frac{\rho^2}{2\lambda}} \end{pmatrix} \equiv \begin{pmatrix} 0 \\ \frac{v}{\sqrt{2}} \end{pmatrix}, \quad (1.11)$$

where the redefinition of the minimum in terms of  $v$  is chosen for brevity. Substituting the field  $\Phi$  with the minimum shifted field in what is known as the unitary gauge,  $\Phi_{\min}$ , and subsequently performing the matrix algebra of the first term in equation (1.10), the following expression is attained,

$$\frac{v^2}{8}(g')^2((W_1^\mu)^2 + (W_2^\mu)^2) + (g' W_3^\mu - g B^\mu)^2, \quad (1.12)$$

where two new spin-1 fields can be defined from the old ones,

$$W_+^\mu \equiv \frac{1}{\sqrt{2}}(W_1^\mu - iW_2^\mu) \quad (1.13)$$

$$W_-^\mu \equiv \frac{1}{\sqrt{2}}(W_1^\mu + iW_2^\mu), \quad (1.14)$$

where  $W_+^\mu$  and  $W_-^\mu$  are complex conjugates of one another, and the first term in equation (1.12) becomes  $\frac{1}{8}v^2g'^2(W^+)_\mu(W^-)^\mu$ . At last, the W boson mass term ( $\frac{1}{2}M_W^2 = \frac{1}{8}v^2g'^2$ ) is given! Similarly, the second term in equation (1.12) can be expanded with matrix diagonalization, and the remaining spin-1 fields,  $W_3^\mu$  and  $B^\mu$ , can be interpreted in terms of the new spin-1 fields,

$$Z_\mu = W_3^\mu \cos \theta_W - B^\mu \sin \theta_W, \quad (1.15)$$

$$A^\mu = W_3^\mu \sin \theta_W + B^\mu \cos \theta_W, \quad (1.16)$$

where  $\theta_W$  is the weak mixing angle (or Weinberg angle), and is given by  $\tan^{-1}(\frac{g'}{g})$  and the terms in equation (1.12) become,

$$\frac{1}{8}v^2 g'^2 (W^+)_\mu (W^-)^\mu + \frac{1}{8}v^2 \frac{g'^2}{\cos \theta_W^2} Z_\mu^2 + \frac{1}{8}v^2 \cdot 0 \cdot A_\mu^2. \quad (1.17)$$

The fields can then be identified with the bosons in Table 1.1 where  $A_\mu$  is the photon. The masses of the fields can be read off as,

$$\begin{aligned} M_W &= \frac{g' v}{2} \\ M_Z &= \frac{g' v}{2 \cos \theta_W} = \frac{M_W}{\cos \theta_W} \\ M_A &= 0 \end{aligned} \quad (1.18)$$

Hence, the Higgs mechanism is the means by which the gauge theory of massless bosons, after symmetry breaking, becomes a theory of massive bosons. In addition, the Higgs field vacuum expectation value,  $v$  is 246 GeV. From the steps above which lead to the field responsible for the  $Z$  boson  $Z_\mu$  and the field responsible for the photon  $A_\mu$ , it can be seen that both have a common point of departure, since they are orthogonal linear combinations of the fields  $B_\mu$  and  $W_\mu^3$ .

### 1.2.2. Yukawa interactions

In addition to allowing bosons to have mass, the Higgs mechanism gives fermions their masses without destroying gauge invariance after symmetry breaking. This is a particularly attractive feature of the SM, since the same Higgs doublet that generates the  $W^\pm$  and Z masses suffices to allow for lepton and quark masses. In order to ensure that gauge invariance is retained, the new interaction terms in the Lagrangian between

the spin- $\frac{1}{2}$  fields and the spin-0 Higgs field with the doublet as  $\Phi := \frac{1}{\sqrt{2}} \begin{pmatrix} 0 \\ v + h \end{pmatrix}$ ,

where  $h$  describes a physical Higgs boson, is

$$\mathcal{L}_{Hf\bar{f}} = -(h_d)_{ij} \bar{q}_{L_i} \Phi d_{R_j} - (h_u)_{ij} \bar{q}_{L_i} (-i\sigma_2 \Phi^*) u_{R_j} - (h_\ell)_{ij} \bar{\ell}_{L_i} \Phi \ell_{R_j}. \quad (1.19)$$

From this, it can be seen that the Higgs couples to quark doublets, which are left chiral states (L) under  $SU(2)$  transformations, and to either up or down-type right chiral (R) quark singlets (i.e.  $u_R$  and  $d_R$ ). The Higgs doublet also has couplings to left-handed lepton doublets and charged right-handed lepton singlets. Once the  $SU(2) \otimes U(1)$  symmetry is spontaneously broken then equation (1.19) becomes,

$$\mathcal{L}_{m_f} = (m_d)_{ij} \bar{d}_{L_i} d_{R_j} + (m_u)_{ij} \bar{u}_{L_i} u_{R_j} + (m_e)_{ij} \bar{e}_{L_i} e_{R_j}, \quad (1.20)$$

where  $m_f = \frac{y_f v}{\sqrt{2}}$ , with  $y_f$  being the Yukawa coupling for a fermion  $f$ .  $u_L$ ,  $d_L$ , and  $e_L$  are the up-type quark, down-type quark and lepton doublet components defined as,

$$\begin{pmatrix} u \\ d' \end{pmatrix}_L \begin{pmatrix} c \\ s' \end{pmatrix}_L \begin{pmatrix} t \\ b' \end{pmatrix}_L \quad (1.21)$$

$$\begin{pmatrix} \nu_e \\ e \end{pmatrix}_L \begin{pmatrix} \nu_\mu \\ \mu \end{pmatrix}_L \begin{pmatrix} \nu_\tau \\ \tau \end{pmatrix}_L$$

Thus, the relation between the fermion mass and the Yukawa coupling demonstrates that heavier fermions correspond to fields that are more strongly coupled to the Higgs boson. In order to go from the quark weak eigenstates  $(d', s', b')$  to the corresponding mass eigenstates, the Cabibbo-Kobayashi-Maskawa (CKM) matrix below is used,

$$\begin{pmatrix} d' \\ s' \\ b' \end{pmatrix} = \begin{pmatrix} V_{ud} & V_{us} & V_{ub} \\ V_{cd} & V_{cs} & V_{cb} \\ V_{td} & V_{ts} & V_{tb} \end{pmatrix} \begin{pmatrix} d \\ s \\ b \end{pmatrix} \quad (1.22)$$

where the CKM matrix values are,

$$\begin{pmatrix} V_{ud} & V_{us} & V_{ub} \\ V_{cd} & V_{cs} & V_{cb} \\ V_{td} & V_{ts} & V_{tb} \end{pmatrix} = \begin{pmatrix} 0.974 & 0.225 & 0.004 \\ 0.225 & 0.973 & 0.041 \\ 0.009 & 0.040 & 0.999 \end{pmatrix} \quad (1.23)$$

It can be noted that the CKM matrix is nearly the identity, thus transitions between fermion generations are heavily suppressed, but by contrast a top quark decays to a W boson and b quark at a rate of 99.9%. Quark couplings to the W boson are in part characterized by the CKM matrix in what follows as the Lagrangian for charged currents,

$$\mathcal{L}_{\text{CC}} = \frac{g}{\sqrt{2}} W_\mu^+ (\nu_L \gamma^\mu e_L + V_{\text{CKM}} \bar{u}_L \gamma^\mu d_L) + \frac{g}{\sqrt{2}} W_\mu^- (\bar{e}_L \gamma^\mu \nu_L + V_{\text{CKM}} \bar{d}_L \gamma^\mu u_L), \quad (1.24)$$

where  $u$  denotes up-type quarks,  $d$  denotes down-type quarks,  $\nu$  denotes neutrinos, and  $e$  denotes charged leptons. From the subscript, it can be noted that only left-handed fermions (and right-handed antifermions) couple to the  $W^\pm$ , hence there is a 100% breaking of parity ( $\mathcal{P}$ ) and charge conjugation ( $\mathcal{C}$ ), however gauge invariance is still preserved under the combined  $\mathcal{CP}$  symmetry. Similarly, quarks and leptons couple to the neutral carriers of electroweak interactions, the Z boson and the photon, via the neutral current Lagrangian given by,

$$\mathcal{L}_{\text{NC}} = \sum_j \bar{\psi}_j \gamma^\mu \left\{ A_\mu \left[ g \frac{\sigma_3}{2} \sin \theta_W + g' y_j \cos \theta_W \right] + Z_\mu \left[ g \frac{\sigma_3}{2} \cos \theta_W - g' y_j \sin \theta_W \right] \right\} \psi_j, \quad (1.25)$$

where for simplicity we take,

$$\psi_1 = \begin{pmatrix} u \\ d \end{pmatrix}_L, \quad \psi_2 = u_R, \quad \psi_3 = d_R, \text{ or} \quad (1.26)$$

$$\psi_1 = \begin{pmatrix} \nu_e \\ e^- \end{pmatrix}_L, \quad \psi_2 = \nu_{eR}, \quad \psi_3 = e^-_R. \quad (1.27)$$

The EM coupling is defined as  $e = g \sin \theta_W = g' \cos \theta_W$  and a relation between the fermion hypercharge ( $Y$ ), electric charge ( $Q$ ) and weak isospin ( $T_3$ ) quantum numbers can be established with  $T_3 \equiv \sigma_3/2$  and  $Y = Q - T_3$ . Hence, for quarks and leptons,

$$\text{Quarks : } y_1 = Q_u - \frac{1}{2} = Q_d + \frac{1}{2} = \frac{1}{6}, \quad y_2 = Q_u = \frac{2}{3}, \quad y_3 = Q_d = -\frac{1}{3}, \quad (1.28)$$

$$\text{Leptons : } y_1 = Q_\nu - \frac{1}{2} = Q_e + \frac{1}{2} = -\frac{1}{2}, \quad y_2 = Q_\nu = 0, \quad y_3 = Q_e = -1. \quad (1.29)$$

Thus, it is shown that fermions with the same electric charge have the same universal couplings, and neutrinos do not have EM interactions ( $Q_\nu = 0$ ) although their coupling to the W and Z boson is non-zero. Examining the properties of the neutrino more closely, one might be tempted to propose it as a viable DM particle candidate since it satisfies *some* of the key requirements for a suitable candidate, those being:

- Stability on the order of the cosmic timescale, as required to remain in existence currently
- No strong or EM interactions
- Non-baryonic, since the potential baryon fraction of DM is known to be small

- Combined with any other DM particles/constituents, the total DM must have the correct relic density

It will however, become clear in the following section, why the neutrino, as predicted by the SM, is an insufficient contender for 24% of the matter fraction in the Universe. Analogously, the SM, as briefly described in this section, successfully predicts observed particle physics phenomena to a high degree of accuracy, with the most recent experimental confirmation being the discovery of a 125 GeV particle compatible with the predicted Higgs boson, by the ATLAS and CMS experiments at the LHC in 2012 [25, 26]. Nonetheless, there exist a number of theoretical and phenomenological problems, which cannot be accommodated by the SM. Among those are the hierarchy problem, wherein the Planck scale ( $M_{Pl} \sim 10^{18}$  GeV), the point at which gravity is as strong as the gauge interactions, is nearly  $\mathcal{O}(10^{15})$  larger than the electroweak scale, both of which are widely considered fundamental energy scales in nature. In addition, the matter-antimatter asymmetry that exists in the Universe today does not jive with the SM prediction that approximately equal amounts of matter and antimatter should have been created during the earliest phases of the Universe, had a proportionate amount of matter compared to antimatter existed during the initial conditions. Other open issues such as the addition of small, but nonetheless experimentally observed neutrino mass [27] to the SM is not possible unless other key free parameters are modified which leads to further theoretical complications of the SM framework. Alongside these open questions is the lack of a fundamental particle candidate supplied by the SM to explain the vast amount of DM in as observed in the Universe. Possible extensions to the SM can help to alleviate the tension presented between the above physical phenomena and the to-date widely accepted model, where the hints of BSM physics would manifest as experimental observations of deviations from SM processes.

### 1.3. Dark matter candidates

Returning to the example of a neutrino as a possible particle DM candidate can help to elucidate the properties which have lead to the most dominant model, currently. During the early stages of the Universe, when the rate of cosmic expansion overtook the rate at which weak interactions in equilibrium proceeded, such as neutron-proton conversion given by  $n \leftrightarrow p + e^- + \bar{\nu}_e$ , the process of SM neutrino decoupling from the background radiation occurred. At this so-called “freeze out” stage, the neutrino is relativistic and remains as such during the later stages of galaxy and larger structure formation, owing also to its near massless nature. Relativistic particles moving throughout the Universe, however, are generators of high pressure, which cause a smoothening and subsequent destruction of any small matter density fluctuations and would ultimately not lead to the large scale structure formation as observed today. Evidence from N-body simulations made as early as 1983 by White, Frenk, and Davis [28] present a vastly inconsistent picture of galaxy clustering than what is observed, and consequently definitively rule out a neutrino-dominated Universe.

The SM neutrino is part of a larger classification of particle DM, known as hot dark matter (HDM). HDM candidates are very light particles with  $m_{\text{HDM}} < 1 \text{ eV}$ , and are typically disfavored as leading candidates since they hinder large scale structure formation as a result of their relativistic energies. Although HDM certainly exists in our Universe today, such as SM neutrinos, current observational data place an upper limit of 0.25% of the fraction of mass in the Universe as contributed by HDM. On the other hand, at the other end of the energy spectrum are DM candidates which are non-relativistic at the time of decoupling from the thermal bath, and are classed as cold dark matter (CDM). With a mass ranging between  $\mathcal{O}(\text{GeV}) < m_{\text{CDM}} < \mathcal{O}(\text{TeV})$ , the lower velocities of CDM in contrast to those of HDM would result in a short range dispersion with respect to the size of the Universe, and generate very little pressure,

allowing for the clustering of stars and galaxies to form the filaments and structures observed today. Numerous N-body simulations commencing from random density fields of non-interacting CDM demonstrate these observations [29]. Situated between HDM and CDM, warm dark matter (WDM), is postulated to have  $m_{\text{WDM}} \simeq \mathcal{O}(\text{keV})$ . Although relativistic at the time of decoupling, WDM then cools during the radiation-to-matter transition phase and becomes non-relativistic causing some smoothening of dense knots of matter, but still allowing for structure formation. Sterile neutrinos, gravitinos, and photinos fall under this category, but WDM is disfavored in large part because N-body simulations are less consistent with observations than those for CDM candidates.

The leading DM candidate, which is classified as a type of CDM, is the weakly interacting massive particle (WIMP) and to-date it is the most theoretically desirable candidate for a number of reasons. One of the strongest arguments for a WIMP as a DM candidate, should it exist and be stable, is that the relic density it would produce is consistent with that required by DM. The mechanism via which this occurs is referred to as the “WIMP miracle”, alluding to the notion that WIMPs, although originally proposed as a solution to the gauge hierarchy problem, are extremely suitable DM candidates as well. As mentioned earlier, the thermal freeze-out period of the Universe occurred when interactions with the thermal bath which reach an equilibrium can no longer keep up with the rate of expansion of the Universe, hence after freeze-out, interactions which affect the total number of WIMPs are negligible. The exchange of energy between SM particles and WIMPs may still proceed efficiently, however. Quantitatively, the number density of the DM particle,  $n$ , can be described by the Boltzmann equation,

$$\frac{dn}{dt} = -3Hn - \langle\sigma_A v\rangle(n^2 - n_{\text{eq}}^2), \quad (1.30)$$

where  $H$  is the Hubble constant,  $\langle\sigma_A v\rangle$  is the thermally averaged annihilation cross section and  $n_{\text{eq}}$  is the DM number density in thermal equilibrium. In order to obtain the thermal relic density, equation (1.30) is solved numerically, where the freeze-out time is defined as  $n\langle\sigma_A v\rangle = H$  and leads to [30],

$$\Omega_\chi \simeq \frac{m_\chi T_0^3}{\rho_c M_{Pl} T_f} (\langle\sigma_A v\rangle)^{-1}, \quad (1.31)$$

where  $\rho_c$  denotes the critical density,  $m_\chi$  denotes the DM mass, and  $T_0$  and  $T_f$  denote the present and freeze-out time temperatures. It can be noted that  $\Omega_\chi$  has an inversely proportional relationship to the velocity-averaged annihilation cross section and does not strongly depend on the mass of the DM. Thus, for WIMPs postulated to be in the  $\mathcal{O}(\text{GeV}) < m_\chi < \mathcal{O}(\text{TeV})$  mass range, assuming that the annihilation cross section into SM particles is on the order of the electroweak scale, the observed  $\Omega_\chi$  is correctly predicted by the WIMP miracle, as visualized in Figure 1.5.

Thus, yielding a naturally correct  $\Omega_\chi$  via the freeze-out production mechanism, and characterized by the kinematic qualities of CDM which predict the structure formation observed in the Universe today, the WIMP is the most theoretically preferred DM candidate. WIMPs are predicted by many BSM theories, whether as neutralinos in supersymmetric (SUSY) theories, super-heavy and super-weakly-interacting particles coupling to SM fields via the Higgs portal called WIMPzillas, or through effective field theory operators (EFT) which describe the weak contact interaction between SM particles and DM. In short, the WIMP provides model-independent grounds for

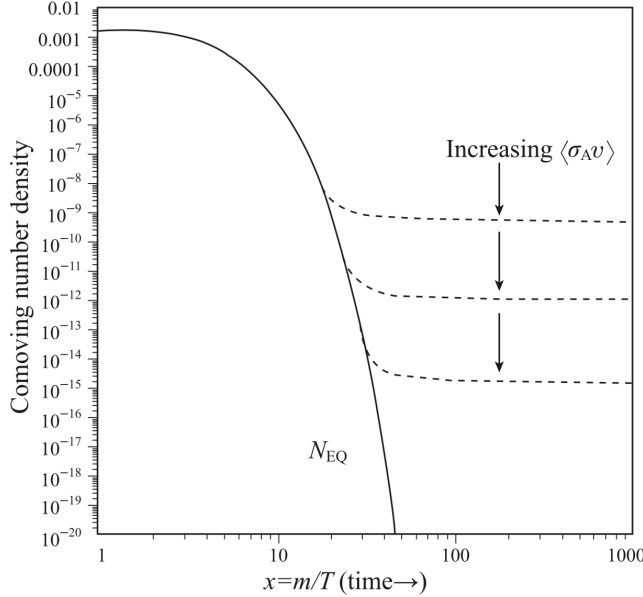


**Figure 1.5.:** The WIMP comoving number density as a function of time, also parametrized as  $x_f = \frac{m_\chi}{T_f}$ , where an increase in the annihilation cross section ultimately results in a later freeze-out time, and a correspondingly lower thermal relic density [31].

weak scale DM production, which furthermore allows the experimental community to search for its existence via multiple independent and complementary methods.

## 1.4. Dark matter detection

Favorable implications for DM detection arise as a result of the WIMP miracle. In order to reach the correct relic density, the WIMP DM particles must also annihilate to other particles, which are assumed to be SM particles. The process of  $\chi\bar{\chi} \rightarrow \text{SM SM}$  means it is possible to write down the elastic scattering and annihilation cross sections of DM and ordinary particles within a framework of a particle physics theory. It has been established that DM is responsible in part for the dynamics of galaxies and clusters, which in turn lead to the large scale structures observed today. The galactic halo of our own Milky Way galaxy is predicted to be abundantly filled with DM particles, and the

WIMP model would allow for the detection of signals emitted by DM annihilation to SM particles. Conversely, the stability and proliferation of WIMPs would allow DM particles to reach terrestrial laboratories, where a potential DM signal would reveal itself as elastic scattering of DM off ordinary particles depositing energy in sensitive detectors. By construction, the WIMP paradigm would also allow for the reversal of the annihilation process, such that the production of pairs of DM particles from extremely highly energetic SM particles is possible. The annihilation, elastic scattering, and production of DM are the underlying strategies respectively used by indirect, direct, and collider methods of DM detection detailed in this section.

### 1.4.1. Indirect detection

Although DM makes up a substantial part of the Universe, it nonetheless, does not constitute the entirety of the energy-mass density ratio, thus the observed  $\Omega_\chi$  was reached through its annihilation. The WIMP miracle implies that DM-SM interactions must be efficient, thus if DM annihilation occurred during the early Universe, it must also proceed in the same way today albeit at a lower frequency, making it possible to detect the SM products from the reaction. Indirect searches for DM target a large region of the cosmos, such as the sun, the galactic halo of the Milky Way and that of other galaxies. An indirect detection (ID) signal would typically manifest itself as an anomalous event of cosmic rays, where DM annihilation results in an abnormally high rate of SM particle-anti-particle pair production. Fluxes of cosmic rays can encompass a large number of particles though most ID experiments focus on signatures of charged particles ( $e^- e^+$ ,  $p\bar{p}$ , deuterium and antideuterium), photons (in the form of gamma rays, X-rays, or synchrotron radiation), and lastly, neutrinos. Experiments dedicated to searches of charged anti-particle fluxes make good use of the under-abundance of anti-particles with respect to their corresponding particles in the Universe, whereas

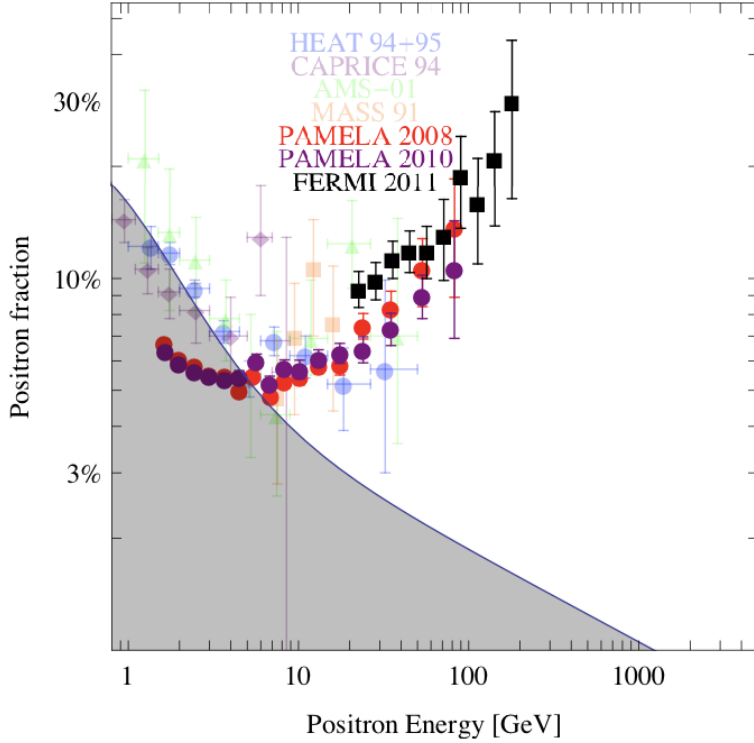


**Figure 1.6.:** The positron energy spectra measured by a compilation of recent (PAMELA and FERMI) and less recent ID experiments dedicated to measurements of secondary charged particles emitted in cosmic ray fluxes. The data is superimposed on a compilation of uncertain astrophysical backgrounds from secondary production. [32]

dedicated photon and neutrino flux experiments target areas of the cosmos that can maximize the potential DM signal to noise from astrophysical sources. The cosmic fluxes of the aforementioned elementary particles are a result of the showering and hadronization of the pair-produced primary particles from the DM annihilation, such as  $b\bar{b}$ ,  $\mu^+\mu^-$ ,  $\tau^+\tau^-$ , and  $W^+W^-$ . The spectra of the cosmic rays depends in large part on the mass of the primary particles that emitted the flux, but in general the distribution features a 'bump'-like structure which is characterized by a high-energy cutoff at the  $m_\chi$ .

Myriad ID experiments are currently under operation or are projected for future searches. An example of one such experiment is the PAMELA satellite [33] which

presented an excess over a potential but uncertain background from secondary astrophysical sources in the positron energy spectra for  $10 \text{ GeV} < E_{e^+} < 100 \text{ GeV}$ , as seen in Figure 1.6. The excess was also extended to 200 GeV and confirmed independently by measurements from the FERMI satellite [34], and the prototype Alpha Magnetic Spectrometer (AMS-01) experiment [35]. Although the signals seem quite striking since it implies a source of  $e^+$  exists other than ordinary astrophysical ones, it is precisely the uncertainties in these backgrounds and their potentially exotic contributions to the spectra that limit the interpretation of ID signals as DM. In this respect, not only are other ID experiments necessary to confirm a signal as a potential DM discovery, but another means of detection altogether is required to corroborate a signal from indirect detection methods, since improving the simulation and understanding of astrophysical backgrounds is non-trivial.

### 1.4.2. Direct detection

The non-relativistic nature of the WIMP would allow for its detection via elastic scattering off a SM particle, which imparts a transfer of momentum to the nucleus, known as the nuclear recoil. Direct detection (DD) experiments are sensitive to the secondary effect of the nuclear recoil and thus detect a potential WIMP signature through the light, heat, or ionization of the SM material with which it interacted. DD experiments are typically conducted in deep, underground terrestrial laboratories in order to suppress the highly energized neutron fluxes produced from cosmic rays that penetrate the atmosphere, since such backgrounds are the most serious and challenging to disentangle from a potential signal. A sufficient amount of Earth material or water/ice is necessary to shield the highly sensitive detectors and reduce the high cosmic muon intensity fluxes. Furthermore, as a result of the small interaction rate of DM-SM particles, DD experiments observe single interactions as opposed to

multiple interactions, and it thus follows that any interactions would be uniformly distributed within the detector volume, contrasting the background from radioactivity expected at the detector surface.

The formalism of WIMP DD is summarized in the following steps, where more details are given in [36]:

- The kinetic energy of a recoiled nucleus, after elastic scattering is approximately,

$$E_r \approx \left(\frac{1}{2}m_\chi v^2\right) \left(\frac{4m_\chi m_N}{(m_\chi + m_N)^2}\right) \cos^2 \theta_R, \quad (1.32)$$

where  $\theta_R$  is the angle of nuclear recoil,  $m_N$  is the mass of the nucleus, and  $v$  is the velocity of  $\chi$  relative to the detector in question. With an expected WIMP local density in the Milky Way galactic halo of  $\rho_{\chi 0} = 0.4 \text{ GeV}/c^2/cm^3$ ,  $v^2$  is approximately  $\mathcal{O}(10^{-6})$  at the average detector depth, and equation (1.32) is maximized to a value of  $10^{-6}m_\chi$  when the DM and nucleus mass are equal. Thus a WIMP mass on the order of 100 GeV would lead to  $E_r \approx 0 - 100 \text{ keV}$ .

- The detection rate depends on the reaction cross section of the DM and the SM nucleus collision, which can be parametrized as a function of the nuclear momentum transfer  $q_r = 2m_r v \cos \theta_r$ , where  $m_r$  is the reduced mass of the  $\chi - N$  system. The parametrization leads to a differential cross section of a recoiled nucleus,

$$\frac{d\sigma(q_r)}{dq_r^2} = \frac{\sigma_0}{(2m_r v)^2} F^2(q_r), \quad (1.33)$$

where the denominator on the right-hand side of equation (1.33) is the square of the maximal momentum transfer that occurs for forward scattering. The form factor,  $F(q_r)$ , accounts for the finite size of the nucleus and can depend on whether the DM-SM interaction is spin-independent (SI) or spin-dependent (SD). In addition, the total recoil cross section,  $\sigma_0$ , has SI and SD contributions, where the  $\sigma_{SI}$  depends on the couplings of the WIMP to protons and neutrons in the given model, though generically they are expected to be equal.

- The interaction rate per unit detector mass in a given velocity range  $[v, v + dv]$  goes as,

$$dR = \left( \frac{\rho_{\chi^0}}{m_\chi m_N} \right) v \frac{d\sigma(q_r)}{dq_r^2} f_1(v) dv dq_r^2 \quad (1.34)$$

where the  $f_1(v)$  is a Maxwellian distribution that models the galactic WIMP velocity.

- The velocity integration in equation (1.34) gives the rate as a function of the recoil energy from equation (1.32) and yields,

$$\frac{dR}{dE_r} \propto \exp \left( \frac{-m_N E_r}{2m_r^2 v_0^2} \right). \quad (1.35)$$

Thus, in contrast to the expected peak structure that would be observed by ID experiments, the recoil spectrum that DD experiments look for is approximately described by an exponential. For this reason, there is no precise spectral signature, and most of the signal is expected to lie at the low recoil energy range requiring a

firm understanding of the experimental energy thresholds of dedicated WIMP direct detectors.

Unlike ID experiments, DD experiments may make some assumption on the particle physics model which dictates the values of  $\sigma_0$  and  $F(q_r)$  ultimately changing the interaction rate expected in a given type of detector material. Taking the example of a neutralino ( $\tilde{\chi}^0$ ) from SUSY models as the WIMP candidate, the  $\tilde{\chi}^0$ -nucleon cross section depends on the coupling between the  $\tilde{\chi}^0$  and quarks in the low-energy regime. These interactions are mediated through scalar, pseudoscalar, axial, and axial-vector currents, in the same manner that electroweak interactions are mediated via gauge *vector* bosons. In particular, the  $\tilde{\chi}^0$  is a Majorana fermion [37], and thus can only couple to the particles in the SM sector via scalar or axial-vector currents. Axial-vector and pseudoscalar couplings give rise to SD WIMP-nucleon cross sections, while vector and scalar couplings generate SI cross sections.

The most sensitive SI DD searches make use of low-temperature heat and ionization detectors, or consist of dual-phase noble liquids. Since the SI cross section is directly proportional to the target nucleus mass, such detectors employ heavy nuclei such as xenon (Xe) and germanium (Ge). An example of one such experiment is the XENON1T experiment [38], which makes use of liquid Xe (LXe) time projection chambers (TPCs). Located at a depth of 3600 m at the INFN Laboratori Nazionali del Gran Sasso (LNGS), 2 t of ultra-pure LXe serves as the active target material in the detector which produces prompt scintillation (S1) once a particle is incident upon the target LXe nucleus. Secondary electron ionization is also produced from the energy deposit and once the electrons pass through the drift field, they are extracted into gaseous Xe (GXe) where they produce proportional scintillation light (S2). The XENON1T experiment utilizes the ratio S2/S1 to discriminate between nuclear recoils produced by WIMP or neutron interactions and electronic recoil from  $\beta$  or  $\gamma$  interactions. The results

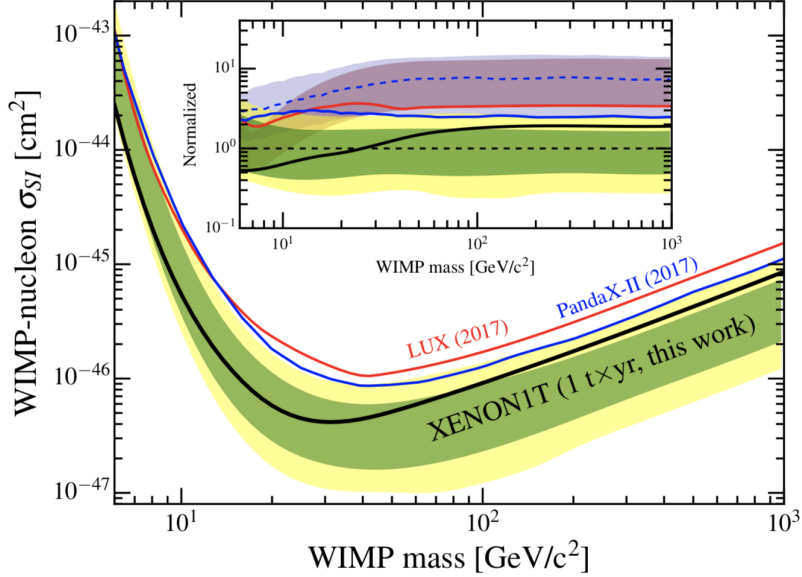


**Figure 1.7.:** Cross section limits as a function of the DM mass for spin-independent interactions for PandaX-II, LUX, and XENON1T.

from the XENON1T experiment improve upon those from PandaX-II [39] and LUX [40], both technologically similar experiments. As shown in Figure 1.7, the recent XENON1T results exclude WIMP-nucleon  $\sigma_{SI}$  of  $\mathcal{O}(10^{-46}) \text{ cm}^2$  for  $m_\chi \approx 20 - 30 \text{ GeV}$ , and demonstrate a seven-fold improvement in sensitivity over PandaX-II and LUX for  $m_\chi > 50 \text{ GeV}$  as seen in the inset by the limits normalized to the median of the XENON1T sensitivity. Over the past several decades, the detector volume of DD experiments has expanded with the aim of increasing the sensitivity by maximal exposure. The XENON1T experiment is projected to be superceded by XENONnT, an 8 t detector predicted to reach a  $\sigma_{SI}$  limit of  $1.6 \times 10^{-48} \text{ cm}^2$  for  $m_\chi \approx 50 \text{ GeV}$  [41].

The SD DD experiments are instead strongly reliant on the spin content of the target nucleus, and essentially translate to a constraint on the WIMP coupling coefficients to protons,  $a_p$ , or neutrons,  $a_n$  which affect the form factor in equation (1.33). These experiments can also employ dual-phase noble gas TPCs, or solid scintillators and superheated bubble chambers to achieve high sensitivities at high and low  $m_\chi$ ,

respectively. At present, the strongest constraints to SD WIMP-proton interactions are given by thermodynamically operated superheated detectors containing fluorine-rich liquids. Filled with approximately 52 kg of  $C_3F_8$  target and operated at SNOLAB in Sudbury, Canada, the PICO-60 bubble chamber sets the most stringent constraints on the WIMP-proton  $\sigma_{SD}$  at  $3.4 \times 10^{-41} \text{ cm}^2$  for  $m_\chi = 30 \text{ GeV}$  [42].

### 1.4.3. Collider searches

As is the case with direct DM detection, searches for DM production at colliders also take into account the possible particle nature of DM, allowing in many cases for a comparison between these two vastly differing search strategies. In order to emulate the high temperature environment of the early Universe during which WIMPs are postulated to have been produced, the energy of the colliding SM particles at accelerators is necessarily very high. The accelerated particles are typically extremely light, such as protons, anti-protons, electrons or positrons, allowing for their collision energy to be maximized. As a result, collider searches are particularly sensitive to very low WIMP masses on  $\mathcal{O}(\text{GeV})$ . However, if DM is much heavier than the  $\mathcal{O}(\text{TeV})$  scale, it may be the case that the center-of-mass energy available at present collider experiments is insufficient to kinematically allow for the production of DM. Even if DM is produced promptly within the detecting volume at a collider, the further complication for these searches is the lack of experimental signature. DM particles would not interact with the detector material and only reveal their presence through an imbalance of total transverse momentum, also known as missing transverse energy ( $p_T^{\text{miss}}$ ). This quantity, described in detail in Section 3.4, can be understood as the application of the laws of conservation of energy and conservation of momentum to a collision to infer the presence of a weakly interacting particles. SM neutrinos manifest as  $p_T^{\text{miss}}$  in a detector because of their extremely weak interactions with the

material. The saving grace of collider searches is that SM particles are predicted to be produced in conjunction with the DM particles by a plethora of relevant particle physics models. The experimental feasibility is therefore increased for such searches, since the differential distributions of SM background processes are sufficiently well-understood, that even minute deviations from the expected  $p_T^{\text{miss}}$  spectrum would allow for the constraint of DM models predicting such signals. The following section will explore the physics model context in which WIMPs are produced and collider searches are interpreted by this work.

## 1.5. Simplified models of DM: beyond the Standard Model

As mentioned earlier, the production of DM within different types of BSM particle physics models probed by collider searches allows for the detection of a potential signal indirectly via the SM particles that are expected to be produced in association with the WIMPs. Such searches performed by the ATLAS and CMS collaborations are termed Mono-X searches, where the X is the SM particle(s) produced together with the DM particles. The models which the searches in question target, are numerous and span a range of completeness. Supersymmetric (SUSY) extensions to the SM are amongst the most complete BSM theories, and correspondingly incur the largest number of model parameters. SUSY models also do not necessarily directly tie together the annihilation of SM particles to the production of DM particles, since the DM particles are often secondarily produced together with a significant number of SM particles. The constraints that exist for SUSY models are also, in large part, not related to the DM particle itself, but apply to a greater degree to the other parameters. In favor of a simpler description of the DM-SM interactions, a class of models characterized by

fewer tuneable parameters, albeit less theoretically complete, are investigated in this work.

DM production at colliders can be described, in large part, by the interaction between the SM and DM particles. Prior to Run II of the LHC, DM searches such as the one detailed in [43], had been traditionally interpreted using Effective Field Theory (EFT) models [44], wherein the interaction between the SM particles and the Dirac fermion WIMPs is mediated through higher dimensional operators. The models are solely characterized by  $m_\chi$ , and  $M_*$  which represents the strength of the interaction and is a function of the masses and coupling strengths of the mediating particles between the DM and SM fields. The benefit of the EFT formulation is the lesser degree of model dependence, and the relative ease encountered in translating experimental collider constraints to the direct detection DM-nucleon cross section- $m_\chi$  plane. The shortcoming of such field theories, however, are that they are non-renormalizable, thus they become invalid at arbitrarily high energy scales. This is represented by the masses of the mediating particles that have been integrated out. In general, for an EFT to make sense, it is required that  $M_*$  be much larger than the energy transfer through quarks at the LHC,  $M_*^2 \gg Q_{\text{tr}}^2$ . Put another way, the EFT formalism is valid only if the energy scale of the interaction involving the DM and the SM particles is small with respect to the energy scale associated to the heavy mediator,  $M_*$ . In general, ID and DD experiments adhere to this requirement since the expected energy transfers are of the order of  $m_\chi$  or  $\mathcal{O}(\text{keV})$ , respectively. In the high energy environment of collider searches, however, the processes that might be described by the EFT operators would occur in a region beyond the validity of the theory [45]. Thus, since this class of models does not truly account for the mediator, effects from resonant enhancement are not included and EFTs have no description of off-shell mediator production.

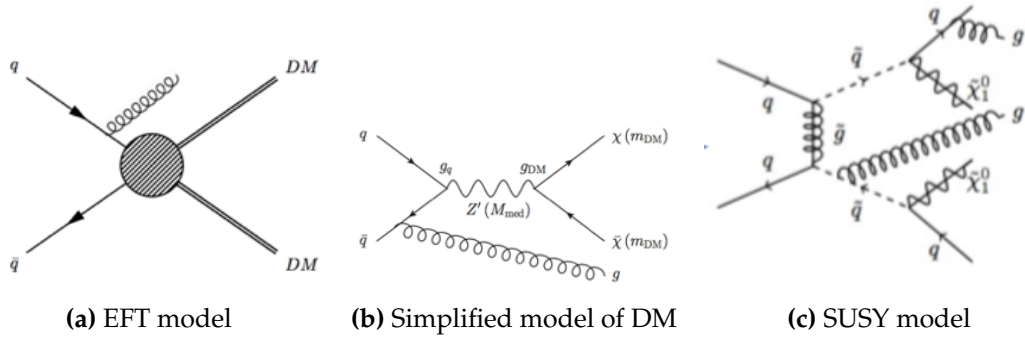


**Figure 1.8.**

In order to circumvent the deficiencies of the EFT formalism, a class of *simplified models* have been employed for the interpretation of DM searches during Run II of the LHC. In part, the increase in the center-of-mass collision energy from  $\sqrt{s} = 8$  TeV to  $\sqrt{s} = 13$  TeV further limits the region of validity for the EFT models. Hence, the contact interaction of the EFT models, as depicted in Figure 1.8a, is subsequently resolved into a mediator interaction which couples to the SM and DM particles, as shown in Figure 1.8b, thus increasing the free parameters to include the coupling of the mediator to the SM sector,  $g_q$ , the coupling of the mediator to the DM sector,  $g_\chi$ , the mass of the mediator,  $m_\phi$ , and  $m_\chi$ . For comparison, Figure 1.8c shows a SUSY model of sgluon-mediated ( $\tilde{g}$ ), di-squark ( $\tilde{q}$ ) decay to SM particles and  $\tilde{\chi}^0$ s. Figure 1.8b is called a simplified model of DM and in particular, the Feynman diagram represents a spin-1 s-channel mediated process where at least one SM particle from initial state radiation and a  $\chi\bar{\chi}$  pair is expected.

Simplified DM models are built upon three major criteria:

- The DM particle must be absolutely stable or else have a lifetime long enough to escape the LHC detectors
  - The Lagrangian should contain renormalizable terms which are also Lorentz invariant, obey the SM gauge symmetries and give stable DM

- Additional interactions between the DM and SM sector must conserve baryon and lepton number and only break custodial and flavor symmetries softly [46]

The third criterion is met by the assumption of Minimal Flavor Violation (MFV) [47] which curbs flavor and  $\mathcal{CP}$ -violation in models of new physics. The essential idea behind MFV is that new physics must preserve the general structure of flavor-changing neutral current (FCNC) processes present in the SM. Thus, any flavor and  $\mathcal{CP}$ -violating transitions are entirely dictated by the CKM matrix. In particular, this work is focused on the minimally flavor violating spin-0 models, where it is shown in [46] that through MFV the  $s$ -channel couplings of the SM fermions to the DM sector are required to be of Yukawa type. The interaction Lagrangians of the spin-0 scalar ( $\phi$ ) and pseudoscalar ( $a$ ) mediators are as follows [48],

$$\mathcal{L}_\phi = g_\chi \phi \chi \bar{\chi} + \frac{\phi}{\sqrt{2}} \sum_i (g_u y_i^u \bar{u}_i u_i + g_d y_i^d \bar{d}_i d_i + g_\ell y_i^\ell \bar{\ell}_i \ell_i), \quad (1.36)$$

$$\mathcal{L}_a = i g_\chi a \chi \gamma_5 \bar{\chi} + \frac{i a}{\sqrt{2}} \sum_i (g_u y_i^u \bar{u}_i \gamma_5 u_i + g_d y_i^d \bar{d}_i \gamma_5 d_i + g_\ell y_i^\ell \bar{\ell}_i \gamma_5 \ell_i) \quad (1.37)$$

where the Yukawa couplings are  $y_i^f = \sqrt{2} m_i^f / v$ , where  $m_i^f$  is the fermion mass, and  $v = 246 \text{ GeV}$  is the Higgs boson field vacuum expectation value.  $g_u$ ,  $g_d$  and  $g_\ell$  represent the coupling strength between the mediator and up-type quarks, down-type quarks, and leptons respectively. In the report issued by the Dark Matter Forum (DMF) [48], a collaboration between members of CMS, ATLAS and the theory community, a benchmark set of parameters for the relevant simplified models of DM were chosen after scans of the parameter space were performed. In the following work, the DMF recommendation of  $g_\chi = g_u = g_d = g_\ell = 1$  has been adopted. This reduces the free parameters to  $\{m_\chi, m_\phi\}$  which contribute to the minimal mediator width at leading order (LO) via,

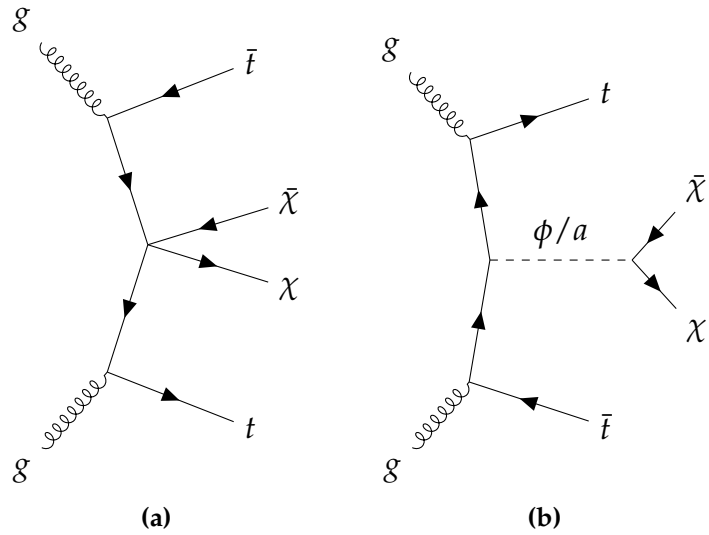


**Figure 1.9.:** The representative diagram of a top quark pair produced in association with a pair of DM particles ( $\chi\bar{\chi}$ ) using (a) the EFT formalism and (b) the simplified model formalism.

$$\Gamma_\phi = \frac{m_\chi}{8\pi} \left(1 - \frac{4m_\chi^2}{m_\phi^2}\right)^{x/2} + \sum_{f=fermions} \frac{y_f^2 m_\phi}{16\pi} \left(1 - \frac{4m_f^2}{m_\phi^2}\right)^{x/2}, \quad (1.38)$$

with  $x = 3$  for scalar mediators, and  $x = 1$  for pseudoscalar mediators. Owing to the choice of SM Higgs-like Yukawa couplings for the SM fermions, the top quark contribution to the mediator width is enhanced at mediator masses above twice the top quark mass, but conversely for lighter mediator masses, the DM contribution dominates since couplings to the lighter quarks are Yukawa-suppressed. In addition, since the Yukawa-type coupling of the spin-0 mediator to the SM favors the more massive of the fermion generations, this strongly motivates searching for DM produced in association with heavy flavor quarks, such as top quarks. The standard EFT diagram characterizing  $t\bar{t} + \chi\bar{\chi}$  production is shown in Figure 1.9a, while the simplified model investigated in this work can be seen in Figure 1.9b.



# Chapter 2.

## The experimental apparatus

### 2.1. The LHC

The Large Hadron Collider (LHC) [49] at CERN is the most powerful particle accelerator in the world, located in the same tunnel as the Large Electron-Positron collider (LEP) [50]. At 27 km in circumference, the LHC is a two-ring, superconducting accelerator and proton-proton (or proton-ion or ion-ion) collider with a two-fold experimental mandate: to probe the electroweak symmetry breaking mechanism via which particles in the Standard Model (SM) attain mass, and to extend the exploration of the energy frontier in search for new physics beyond the SM (BSM). Pictured in Figure 2.1 is the approximate LHC ring size superimposed on top of a map of the Swiss-French border near Geneva, Switzerland. The LHC is comprised of octants, and the locations at which beam collisions occur are the interaction points (IP). The general purpose high luminosity ( $L$ ) experiments on the LHC ring are the CMS (Compact Muon Solenoid) [51] and ATLAS (A Toroidal LHC ApparatuS) [52] detectors located at IP5 and IP1, respectively. The low luminosity experiment dedicated to B-physics, LHCb [53] is located at IP8,



**Figure 2.1.:** The approximate location of the LHC ring traced over the Swiss-French border near Geneva, Switzerland. Also indicated are the relative locations of the two high luminosity experiments (CMS and ATLAS), the low luminosity B-physics dedicated experiment (LHCb), and the dedicated ion experiment (ALICE).

and the dedicated ion collision detector ALICE (A Large Ion Collider Experiment) [54] is located at IP2, as depicted in Figure 2.1.

The total center-of-mass energy of a beam collision is the sum of the energy of the two incoming beam [55], and the LHC is designed to reach a center-of-mass collision energy of up to  $\sqrt{s} = 14 \text{ TeV}$ , with each beam able to reach energies of  $7 \text{ TeV}$ . The total number of events that are generated in an LHC collision are given by  $N_{\text{event}} = L\sigma_{\text{event}}$ , with  $\sigma_{\text{event}}$  being the cross section for the relevant measured event and  $L$  being the machine luminosity.  $L$  depends only on the beam parameters and goes as,

$$L = \frac{N_b^2 n_b f_{\text{rev}} \gamma_r}{4\pi \epsilon_n \beta^*} F, \quad (2.1)$$

where  $N_b$  is the number of particles per bunch,  $n_b$  is the number of bunches per beam,  $f_{\text{rev}}$  is the revolution frequency,  $\gamma_r$  is the relativistic gamma factor,  $\epsilon_n$  is the normalized transverse beam emittance,  $\beta^*$  is the beta function at the interaction point (IP), and  $F$  is the geometric luminosity reduction factor due to the crossing angle at the IP. The peak LHC design luminosity  $L = 10^{34} \text{ cm}^{-2} \text{ s}^{-1}$  dictates the necessity of high beam intensities, thus proton rather than anti-proton beams are used. The two beams of equally charged particles are circulated in opposite directions within separate beam pipes, and accelerated using separate and opposite magnet dipole fields and vacuum chambers in the main arcs.

The point of commencement for the protons circulated in the main LHC ring is a bottle of hydrogen gas at one end of the Linear accelerator 2 (Linac 2). Passing through an electric field that strips the hydrogen of its electrons, the remaining protons enter the Linac 2 and pass through alternating positive and negative cylindrical conductors charged by radiofrequency cavities, which push and pull the protons causing them to accelerate to approximately 50 MeV. The protons then enter the Proton Synchrotron (PS) Booster, which accelerate the beams to 1.4 GeV by means of four superimposed synchrotron rings. The protons then enter the PS, which is 628 m in circumference and accelerates the beams to 25 GeV through the use of conventional (i.e. not superconducting) magnets, of which 100 are dipoles that bend the beams around the ring. At this stage, a package of roughly one hundred billion protons, known as a “bunch”, is separated from another bunch by a spacing of 25 ns, meaning that a proton bunch now rotates at 40 MHz. The following stage is the Super Proton Synchrotron (SPS), which has the same function as the PS, however with a circumference of nearly 7 km

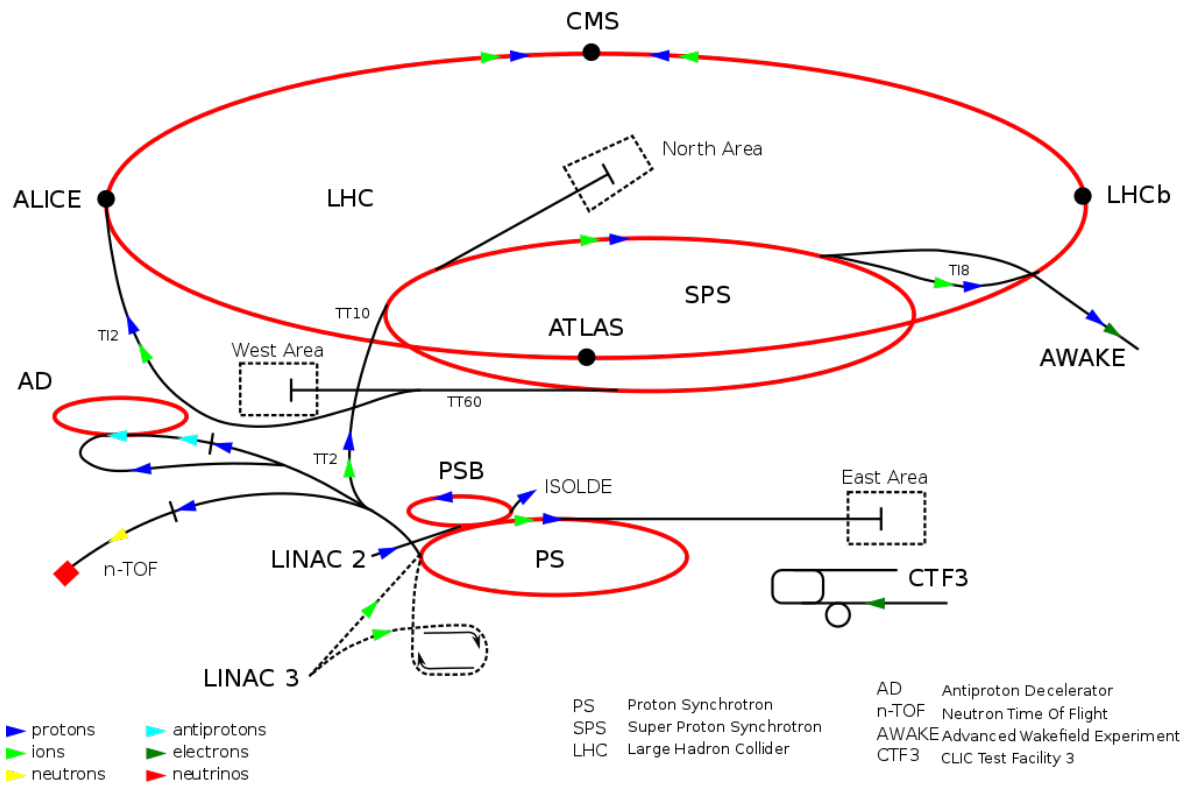


**Figure 2.2.:** A schematic of the CERN accelerator complex, where protons (blue arrows) and ions (lime green arrows) begin their journey to the main LHC ring at the Linac 2 and Linac 3, respectively.

and 744 dipole magnets, the SPS is able to accelerate the proton beams up to an energy of 450 GeV. At this stage the proton beam undergoes a bifurcation into bunch trains with two beams which enter the LHC moving in opposite directions. The chain is illustrated in Figure 2.2 showing an overview of the CERN accelerator complex and the aforementioned experiment IPs.

Once injected into the LHC, the proton beams undergo a ramp up in energy in order to reach the maximum design energy of 7 TeV per beam, typically making  $10^5$  traversals of the ring. In order to achieve these energies, the beam traverses a number of radiofrequency cavities, which are cooled with liquid helium to an operating temperature of 4.5 K. In addition, 1232 superconducting dipole magnets measuring 15 m in length are used to constrain the beam in a near circular path with a generated magnetic field of approximately 8.33 T, whilst 392 quadrupole magnets

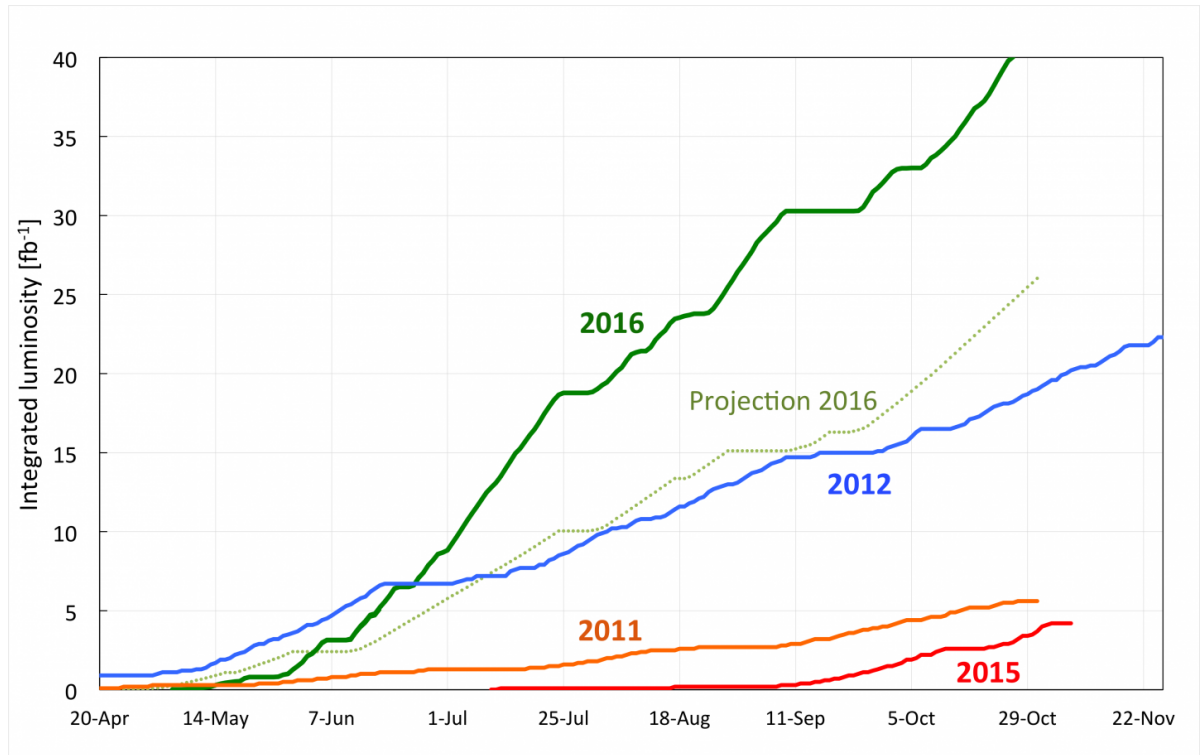


**Figure 2.3.:** The integrated luminosity as a function of time that the LHC delivered at  $\sqrt{s} = 7 \text{ TeV}$  and  $\sqrt{s} = 8 \text{ TeV}$  during 2011 and 2012, and at  $\sqrt{s} = 13 \text{ TeV}$  during 2015 and 2016.

supercooled to 1.9 K and measuring 5-7 m, focus the beams and facilitate the collisions at the designated IPs. Between 2010-2011 and during 2012, the LHC collided proton beams at  $\sqrt{s} = 7 \text{ TeV}$  and  $\sqrt{s} = 8 \text{ TeV}$  respectively, while the energy increased to  $\sqrt{s} = 13 \text{ TeV}$  in 2015 and 2016. The peak instantaneous stable luminosity reached by the LHC during 2016 was  $1.527 \times 10^{34} \text{ cm}^{-2} \text{ s}^{-1}$  and the total integrated luminosity delivered by the machine as a function of time can be seen in Figure 2.3, where the performance of the LHC was better than projected for 2016.

## 2.2. The CMS experiment

Quantities described in this and following sections and chapters will rely heavily on the cylindrical coordinate system defined by the detector structure. The z-axis

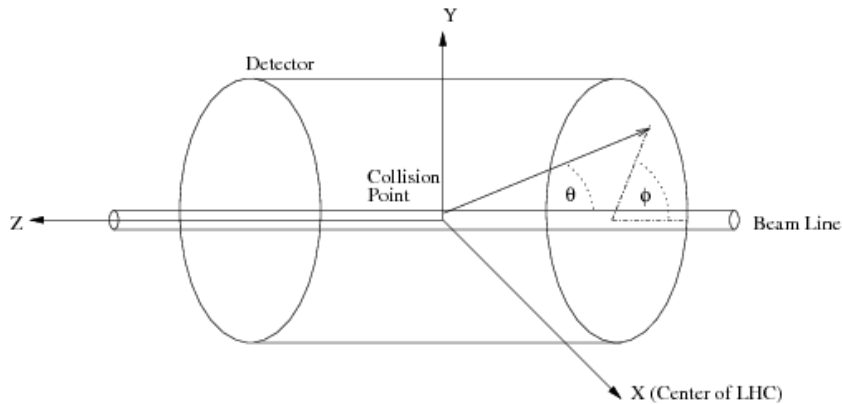


**Figure 2.4.:** A diagram of the cylindrical coordinate system for the CMS detector.

is defined to be parallel to the beam pipe pointing in the direction towards the Jura mountains from IP5, the azimuthal angle  $\phi$  is defined in the transverse  $x$ - $y$  plane perpendicular to the beam line, and  $\theta$  is the polar angle measured from the  $z$ -axis, as shown in Figure 2.4. Consequently, quantities such as  $p_T$ , the transverse momentum, and  $E_T$ , the transverse energy are defined in terms of the respective momentum and energy in the  $x$ - $y$  plane. Rather than using  $\theta$  to describe the direction of a particle trajectory within the detector, it is common practice in the case of highly relativistic particles to use *pseudorapidity* defined as,

$$\eta = -\ln \left[ \tan \left( \frac{\theta}{2} \right) \right] = \frac{1}{2} \ln \left( \frac{|\mathbf{p}| + p_z}{|\mathbf{p}| - p_z} \right) \quad (2.2)$$

in terms of both the polar angle, and  $\mathbf{p}$ , the three momentum and  $p_z$ , the momentum along the  $z$ -axis.  $\eta = 0$  for  $\theta = 90^\circ$  and approaches infinity as the polar angle goes to 0.  $\eta$  regions in detector are often referred to as “barrel” denoting the central  $|\eta|$  region from 0 to  $\approx 1.2 - 1.6$ , “endcap” denoting the region up to  $|\eta| \approx 3$ , and “forward” denoting the region beyond the endcap. The definitions are subject to slight differences depending on the reconstruction of the object in question.

The CMS detector, described in detail in [51], is a multi-purpose apparatus designed to study high- $p_T$  physics processes in proton-proton and heavy-ion collisions. In 2016, CMS collected approximately  $37.8 \text{ fb}^{-1}$  of integrated luminosity as seen in Figure 2.5, of which  $35.9 \text{ fb}^{-1}$  were certified as usable for physics analysis. The CMS detector relies on a superconducting solenoid magnet located in its central region to provide a magnetic field of 3.8 T parallel to the beam direction. Charged particle trajectories are measured by silicon pixel and strip trackers, which cover a pseudorapidity region of  $|\eta| < 2.5$ . Surrounding the tracker volume are a lead-tungstate crystal electromagnetic calorimeter (ECAL) and a brass-and-scintillator hadron calorimeter (HCAL) surround the tracking volume, covering the region of  $|\eta| < 3$ . A steel and quartz-fiber Cherenkov forward hadron calorimeter extends the coverage to  $|\eta| < 5$ . The muon system consists of gas-ionization detectors embedded in the steel flux return yoke outside the solenoid, and covers the region with  $|\eta| < 2.4$ . The detector is designed to cover a  $4\pi$  solid angle as illustrated in Figure 2.6, demonstrating the overall scale of the experiment and the surrounding cavern structure.

### 2.2.1. The magnet

The benefit of the strong magnetic field provided by the superconducting solenoid is the improvement in the momentum resolution for muons, and the increase efficiency of the inner tracking [57]. The main components comprising the magnet are the superconducting solenoid coil, the 1.5 m thick saturated iron yoke in the barrel and endcap regions which return a 2 T magnetic flux, vacuum chambers, and the cryogenic system. Stabilised, reinforced NbTi conductor is used for the 4-layer winding of the coil cold mass, which measures 12.5 m in length. Since the CMS magnet can achieve a stored energy and an energy-to-mass ( $E/M$ ) ratio significantly larger than any other previous detector magnet technologies, the shear stress level inside the coil winding is

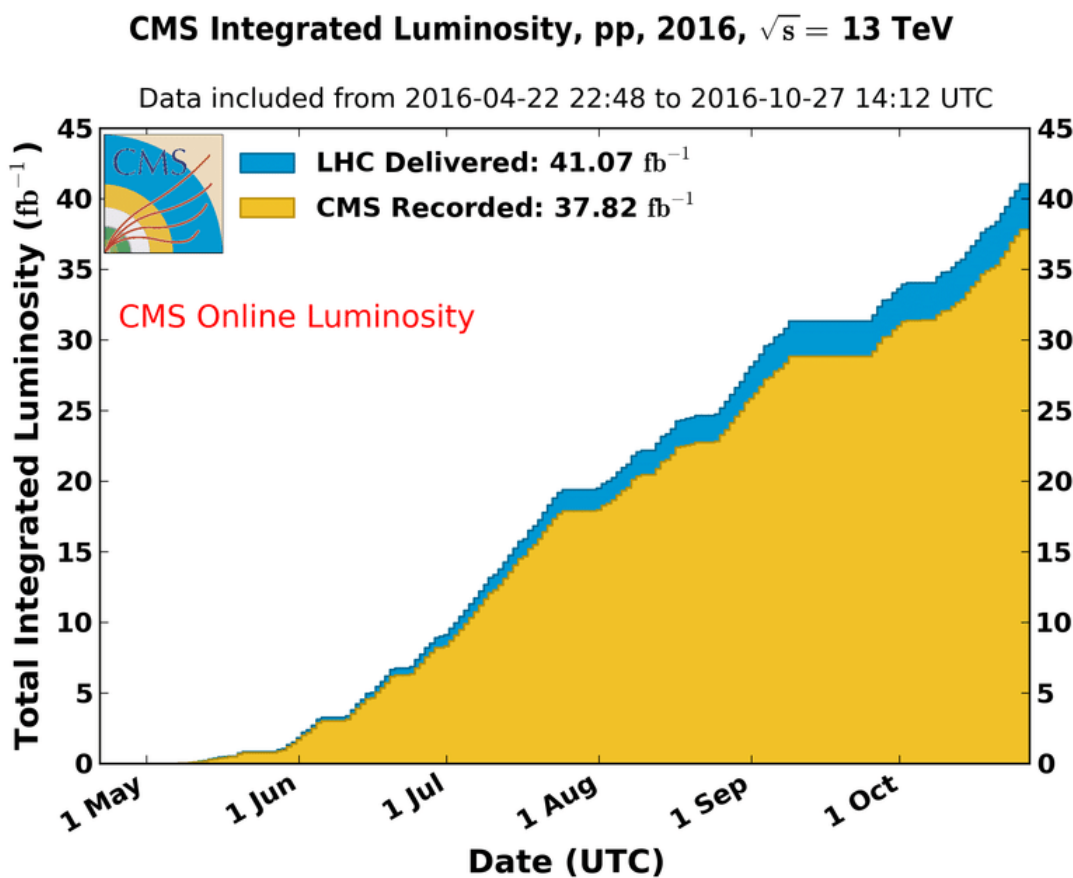


**Figure 2.5.:** The total integrated luminosity that the LHC machine delivered to CMS, and the total integrated luminosity that the detector collected during the 2016 data-taking period [56].

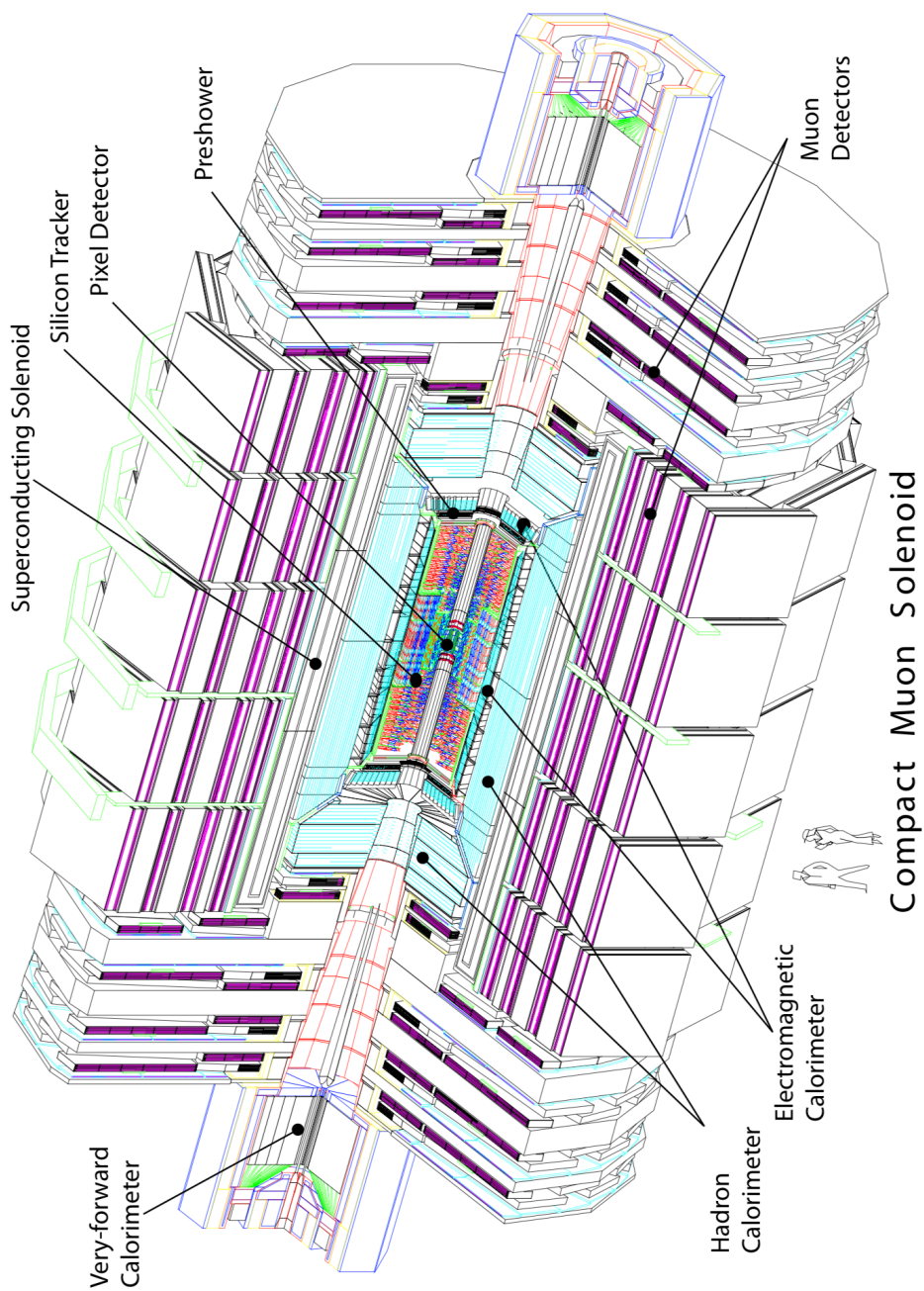


Figure 2.6: Cross-section view of CMS [51].

non-negligible, thus an innovative self-supporting aluminum conductor is included in the magnet structural material to mitigate these effects.

The 3.8 T field that is generated inside the solenoid bends charged particle trajectories in the enclosed silicon tracking detector, enabling the measurement of the  $p_T$  of a particle track via the azimuthal angle  $\phi$ , which is related to the bending radius  $\rho$  and the magnet length  $L'$  by  $\phi = L'/\rho$ . Thus measuring the  $\rho$  of a charged particle track,

$$p_T \propto z\rho B, \quad (2.3)$$

where  $B$  is the magnetic field in the  $z$  direction, parallel to the beam axis, and a particle charge of  $ze$  is assumed. The muon system stations, described in greater detail in Section 2.2.4 interleaved in the iron yoke are also subjected to a 2 T return flux, causing charged particles to bend in the opposite direction from their trajectory within the inner tracker volume. Multiple measurements  $N$  made along the trajectory of a uniform medium provide the curvature ( $k = 1/\rho$ ) error  $\delta k_{\text{res}}$  due to finite measurement resolution which goes as,

$$\delta k_{\text{res}} = \frac{\epsilon}{L'} \sqrt{\frac{720}{N+4}} \quad (2.4)$$

### 2.2.2. The inner tracker

One of the main mandates of the CMS detector is to provide good resolution and reconstruction efficiency for charged particles emitted from LHC collisions in the inner tracker, of which a cross-sectional view is shown in Figure 2.7. Furthermore, the

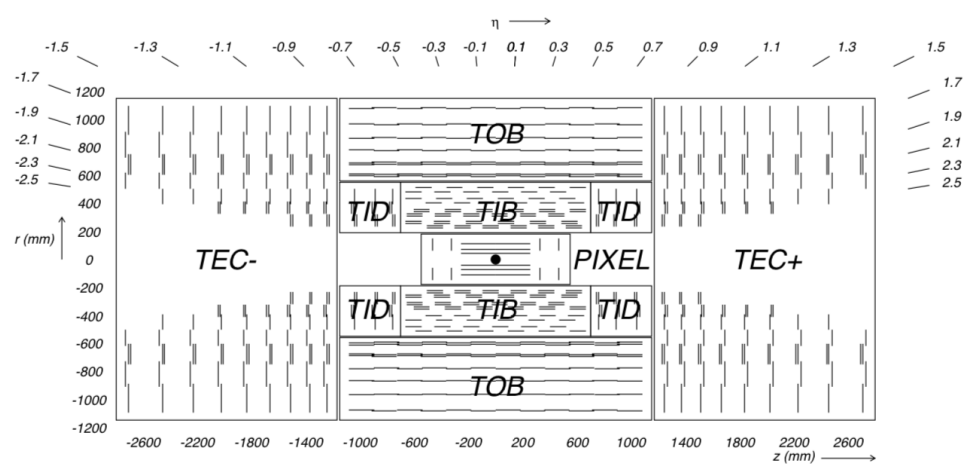


**Figure 2.7.:** Schematic cross-section through the CMS tracker, where a single detector module is represented by a line, and double lines signify back-to-back modules [58].

precise reconstruction of secondary vertices is imperative for the efficient identification of b-jets; b-jets are heavily employed in the as a effective handles in the identification of a  $t\bar{t}(2\ell)$  final state topology. To achieve this, it is imperative for the positioning of tracker layers to be close to the interaction point of a collision, hence the three pixel barrel (BPix) layers are stationed at radii 4.4 cm, 7.3 cm, and 10.4 cm from the interaction point. Designed to keep the occupancy of these inner layers below 1%, the silicon pixel cells measure  $100 \times 150 \mu\text{m}^2$  in  $r - \phi$  and  $z$  respectively, of which  $52 \times 80$  cells populate one read-out chip (ROC) and 16 ROCs comprise one BPix module sensor. In order to cover out to  $|\eta| < 2.5$ , the pixel detector also has two endcap disks (FPix) stationed on either side of the BPix at  $z = \pm 34.5$  and  $z = \pm 46.5$  cm and extending from 6 to 15 cm in  $r$ . The FPix consists of varying trapezoidal (pie-shaped) panels which contain different numbers of *plaquettes* consisting of single pixel sensors bump-bonded to a varying number of ROCs. The sensors are offset on the panels so as to ensure there are no cracks in the endcap  $\eta$  coverage. The BPix and FPix deliver up to three high precision spatial point positions (hits) for which the resolution in  $r - \phi$  is up to  $10 \mu\text{m}$  and that in  $z$  is up to  $20 \mu\text{m}$ . The operating temperature of the pixel detector during 2016 was  $-10^\circ\text{C}$ .

Surrounding the pixel layers are the four and six silicon strip layers comprising the Tracker Inner Barrel (TIB) and Tracker Outer Barrel (TOB), respectively. The TIB extends radially from 20 to 55 cm, with a relative occupancy of  $2 - 3\%$  per strip module in this intermediate region. The distance between the p+ type strip implants in the n type  $\text{SiO}_2$  bulk of the strip sensors is called the pitch [59] and is approximately  $80 \mu\text{m}$  for the first two layers and  $120 \mu\text{m}$  for the third and fourth TIB layers, providing a hit resolution of  $23 \mu\text{m}$  and  $35 \mu\text{m}$  respectively. The TOB covers a region out to  $|z| < 118$  cm along the beampipe and makes use of thicker ( $500 \mu\text{m}$ ) strip sensors as compared to those used for the TID ( $320 \mu\text{m}$ ) in order to maintain a signal-to-noise ratio greater than 10. The first four layers of the TOB make use of strips with a pitch of  $183 \mu\text{m}$ ,

while the strip pitch in layers 5 and 6 is  $122 \mu\text{m}$ , providing hit resolutions ranging from  $53 \mu\text{m}$  to  $35 \mu\text{m}$ . The strip hit resolutions in the TIB and TOB for 2016 are summarized in Figure 2.8. The last TOB layer reaches an outward radius of 110 cm from the beampipe. The TIB and TOB are complimented by disk layers on both  $\pm z$  sides, with the Tracker Inner Disks (TID) consisting of three small disks flanking the TIB and the Tracker EndCaps (TEC) consisting nine larger disks flanking the TOB. The pitch for the  $320 \mu\text{m}$  thick micro-strip detectors employed in the TID varies from  $100 \mu\text{m}$  to  $141 \mu\text{m}$ . The TEC has a positive (TEC+) and negative (TEC-)  $z$  side, where the nine disks on either side extend from  $124 < |z| < 282 \text{ cm}$  and radially from  $22.5 < |r| < 113.5 \text{ cm}$ . The disks can have up to seven rings, of which the four innermost are comprised of  $320 \mu\text{m}$  thick micro strip sensors while the fifth through seventh are  $500 \mu\text{m}$  in thickness. A maximum of nine  $\phi$  hit measurements can be obtained from each TEC disk. In addition, the innermost two layers of the TIB and TOB, and the innermost two disks TID consist of double-sided strip modules. The same is true for the first, second and fifth wheel of the TEC+/- disks. For such modules, the second module is mounted back-to-back at a stereo angle of 100 mrad in order to make it possible to compute a 2D position measurement, by also providing the  $z$  coordinate in the barrel and  $r$  coordinate on the disks, along with the  $\phi$ .

The layout of the inner tracker guarantees approximately nine hit measurements up to  $|\eta| < 2.4$ , at least 4 of which are 2D measurements. The performance of the tracker is gauged by the resolutions for the  $p_T$ , the transverse impact parameter ( $d_0$ ), and the longitudinal impact parameter ( $z_0$ ) expected for single muons of varying  $p_T$ . In the case of single muons with a  $p_T$  equal to 10 and 100 GeV, (i.e. the range considered in the following work), the  $p_T$  resolution is 0.65% and 1.5% respectively at  $\eta = 0$ , and reaches 1% and 2% for  $|\eta| = 1.6$ .

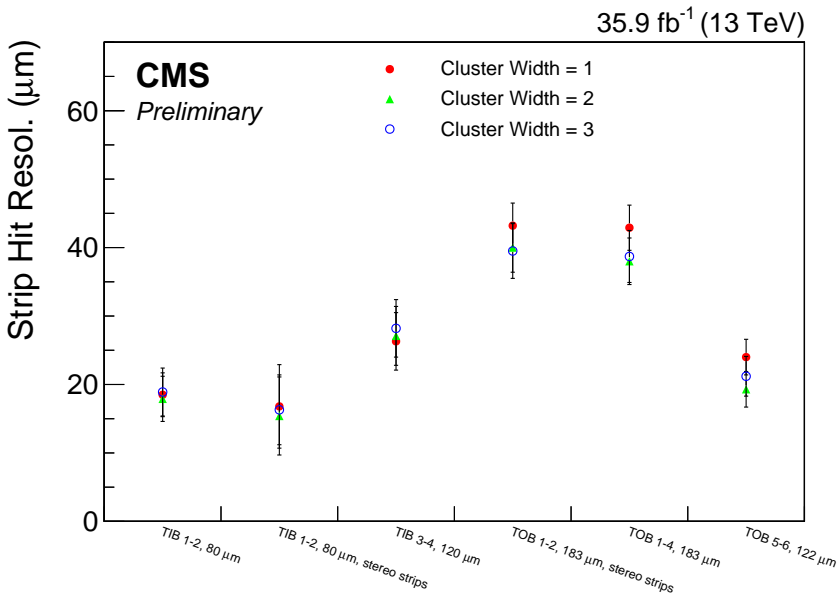


**Figure 2.8.:** The strip hit resolution for the TIB and TOB layers which are comprised of Si sensors with varying strip pitch. The tracks selected have  $p_T > 3 \text{ GeV}$ , at least six hits in the inner tracker, and  $\chi^2$  probability greater than nine [60].

### 2.2.3. The calorimeters

Along with tracking information, in order to measure electron  $p_T$  and energy, a calorimeter system is of utmost importance. Other mandates of the calorimetry system include the measurement of hadronic jet energies and the inference of the existence of neutral particles within the detector volume such as  $\pi^0$ s or photons ( $\gamma$ ). The CMS calorimeter system is comprised of an electromagnetic calorimeter and a brass and scintillating hadronic calorimeter.

#### The ECAL

The ECAL is a hermetic and homogeneous calorimeter which consists of a barrel (EB) region, from  $0 < |\eta| < 1.48$ , and two endcap regions (EE), from  $1.48 < |\eta| < 3.0$ . Chosen for its short radiation length ( $X_0$ ) and correspondingly small Molière radius

( $R_M$ ), the ECAL is comprised entirely of lead tungstate crystals ( $\text{PbWO}_4$ ). The two quantities are related by,

$$R_M = 0.0265X_0(Z + 1.2), \quad (2.5)$$

where  $Z$  is the atomic number. With the ability to emit 80% of the scintillating light within 25 ns, the crystals are fast light emitters with an emission peak located at 425 nm allowing for a suitable combination with photo-detectors [61]. With  $X_0 = 0.89$  cm and  $R_M = 2.2$  cm, a better electromagnetic (EM) shower position and shower separation is achievable because of the compact nature and fine granularity of the detector. The EB crystals are approximately  $25.8X_0$  (23 cm) in length and cover an area of  $2.6 \times 2.6 \text{ cm}^2$  at the rear, while the EE crystals are  $24.7X_0$  (22 cm) in length and cover an area of  $3 \times 3 \text{ cm}^2$  at the rear. In dimensions of  $\Delta\eta \times \Delta\phi$ , the area that is subtended by a crystal in the EB is  $0.0175 \times 0.0175$ , while the area varies from  $0.0175 \times 0.0175$  to  $0.05 \times 0.05$  for the EE crystals. The scintillation light is detected by the use of avalanche photodiodes (APDs) in the EB, with a total of two APDs glued to each crystal. Both the APDs, which operate at a gain of 50, and the crystal scintillation have a temperature dependence of approximately  $-2.4\%/\text{ }^\circ\text{C}$ , which dictates the operation of the ECAL to within  $\pm 0.05\text{ }^\circ\text{C}$ . Vacuum photo-triodes (VPTs) are employed in the EE because of their increased radiation resistance compared to the silicon diodes.

In front of each EE, flanking the inner tracker TEC+/- disks sits a preshower detector covering  $1.65 < |\eta| < 2.6$  which consists of  $2X_0$  and  $1X_0$  depth of lead absorber strips, behind which are two orthogonal planes of silicon strip detector. The preshower aids in the discrimination between  $\pi^0 \rightarrow \gamma\gamma$  process and Higgs decays of  $h \rightarrow \gamma\gamma$ , since the relatively short lifetime of the  $\pi^0$  results in its decay to a diphoton

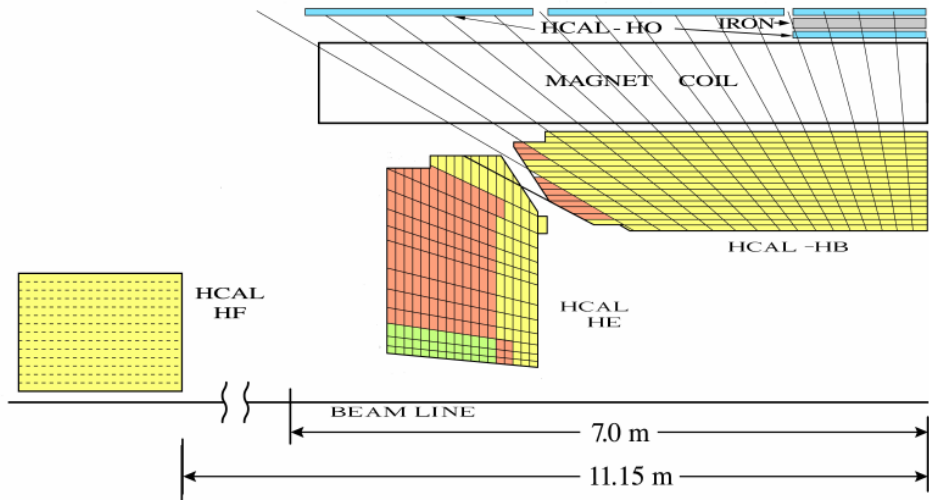


**Figure 2.9.:** A quarter-view of the CMS hadron calorimeter. The shading indicates the grouping of scintillating layers optically added together to form trigger tower signal readouts. [63]

pair upstream of the ECAL where photon conversion in the lead absorber may result. The  $\gamma \rightarrow e^+ e^-$  conversions will leave hits in the silicon strips beyond the absorber along with an energy deposit in the ECAL crystals.

The energy resolution of the ECAL contains three contributions: a stochastic term, a noise term, and a constant term listed in order in the following [62],

$$\frac{\sigma_E}{E} = \frac{2.8\%}{\sqrt{E}} \oplus \frac{12\%}{E} \oplus 0.3\%, \quad (2.6)$$

where the EB energy resolution is obtained using electrons incident on 5x5 arrays of crystals, and the EM showers are reconstructed in a 3x3 matrix of crystals inside the array around the electron impact point.

## The HCAL

The hadron calorimeter (HCAL), of which a quarter-view is shown in Figure 2.9, is essential to the measurement of the energy and direction of particle jets. In conjunction with the ECAL and the muon system, the HCAL also aids in the identification of electrons, photons and muons. Hadronic calorimetry is in general considered to be more challenging than the EM calorimetry discussed in the above section, in part due to the much larger depth of detector material required to contain a hadronic cascade in comparison to the EM fraction emitted in the ECAL. Furthermore, the energy resolution of the HCAL is worsened compared to that of the ECAL by so-called intrinsic fluctuations, which are a result of the significant incoming energy fraction being invisible, since it is employed in processes like nuclear break-up [64].

Located inside the solenoid magnet cryostat, the CMS HCAL consists of four distinctive regions, where the barrel (HB) covers the  $|\eta|$  range from 0 to 1.4, while the endcap (HE) covers the  $|\eta|$  range from 1.3 to 3.0, thus the HB and HE share the  $|\eta|$  range from 1.3 to 1.4. The calorimeter is based on sampling detector technology, and both the HB and HE consist of brass (copper) absorber plates interleaved with plastic scintillator where the sampling fraction is approximately 7%. The HB consists of 18 wedges, where each covers  $20^\circ$  in  $\phi$  and this area is further divided into  $5^\circ$  sectors. The composition and segmentation of the HE is similar, and extends from  $388 \text{ cm} < |z| < 5.68 \text{ cm}$  on either  $\pm z$  side. The space constraint from the magnet cryostat at  $\eta = 0$  requires the HB thickness be limited to approximately 5.8 nuclear interaction lengths ( $\lambda_I$ ) and increases to  $10\lambda_I$  at  $|\eta| = 1.2$ . The nuclear interaction length is the mean free path that an incident hadron can travel in a medium before the nuclear interaction resulting in the absorption of the hadron occurs, and is a material constant that goes as,

$$\frac{1}{\lambda_I} = \sigma_{\text{inel}} \cdot \frac{N_A \cdot \rho}{A} \quad (2.7)$$

where  $\sigma_{\text{inel}}$  is the inelastic cross-section,  $\rho$  is the density, and  $A$  is the atomic mass of the absorber. At  $10\lambda_I$ , more than 99% of the hadronic cascade is contained within the detector material. In the HB and HE, the scintillation light that is captured is then wavelength shifted, and guided to hybrid photodiodes (HPDs).

In addition to the HB and HE, the main objectives of the forward part of the HCAL (HF) involve the improved measurement of the missing transverse energy and to ensure the identification and reconstruction of very forward jets. The HF covers the  $|\eta|$  region from 3.0 to 5.0, and the front face is located at  $|z|=11.1$  m from the IP. Due to the high operational luminosity of the LHC and subsequently high average particle multiplicity at the IP per bunch crossing, the inner part of the HF ( $4.5 < |\eta| < 5$ ) is subjected to the largest particle flux, which when absorbed by the detector can reach radiation doses close to 100 Mrad/year. As a result, the HF is constructed with the capability to survive in a high radiation field, hence the absorber is iron and embedded with dual-length quartz fibres parallel to the beam pipe. The HF is segmented into  $20^\circ$  wedges in  $\phi$  where each wedge contains two  $10^\circ$   $\phi$  sectors. The particles that enter the absorber subsequently produce a shower of particles and those traversing the quartz fibres produce Cherenkov light in the fibres which is guided to the photomultipliers (PMTs). In order to distinguish between showers emitted from  $e/\gamma$  and hadrons, short and long fibres of approximately 165 cm and 22 cm, respectively, are used where the typical electromagnetic shower is known to be shorter and more collimated than charged hadron showering.

The final part of the HCAL, located outside the solenoid cryostat, is the outer HCAL (HO) which consists of layers of scintillators and serves to catch any energy leakage from the HB. Approximately 5% of particles with  $p_T > 100 \text{ GeV}$  deposit some energy fraction in the HO, since complete containment of the hadronic shower in the  $0 < |\eta| < 1.4$  is not feasible.

#### 2.2.4. The muon detectors

The CMS muon system is used as an exceptionally powerful tool for recognizing interesting physics processes over high background rates, and has a three-fold objective: triggering, identification, and precise momentum measurement. In particular, the latter objective is achieved as a result of the high spatial resolution of the detector and the high magnetic field of the solenoid coil and the flux-return yoke. The CMS muon spectrometer is designed to measure the momentum and charge of muons over a large kinematic range, and operate in high flux regions with non-uniform magnetic field strengths.

Comprised of both a barrel and endcaps, the muon system is situated outside of the magnet solenoid and is interleaved with layers of the steel flux-return yoke. The technologies used in both the barrel and endcaps are three types of gas ionization particle detectors and in all cases throughout the following section, the physical modules are referred to as “chambers”. Since the magnetic field is diminished to approximately 2 T outside of the solenoid magnet and subsequently reverses the muon trajectory, recording several muon track measurements along the trajectory is necessary for the momentum calculation. For this reason, the drift tube (DTs) chambers used in the barrel are positioned along several values of  $r$  in the radial direction and the cathode strip chambers (CSCs) used in the endcaps are positioned along several values of  $z$  parallel to the beampipe, as shown in Figure 2.10. There are four stations in the

barrel labeled MB1-MB4, and four stations in each of the endcaps labeled ME1-ME4, where a station is an assembly of chambers.

Owing to the low muon rate, along with low neutron background rate expected in the barrel region, and the relatively uniform and weak magnetic field inside the chambers (0.4 T), DTs are employed in this region. Each DT chamber consists of many drift cells, each filled with 85%/15% Ar/CO<sub>2</sub> and having two cathode strips on either side, and electrodes on the top and bottom walls of the cell. A singular 50  $\mu\text{m}$  gold-plated anode wire operating at +3.6 kV is centrally located within the cell volume. Meanwhile the cathodes are operated at -1.8 and +1.8 kV respectively, thus if a muon is incident on the DT, the electrons released in the gas volume drift to the anode and produce avalanches in the increasing field inside the cell. A DT chamber is comprised of three superlayers, where one is placed orthogonally to the remaining two so as to obtain both an  $r - \phi$  and  $r - z$  position measurement. A superlayer consists of four staggered layers of cells.

Conversely to the barrel case, both the muon rate and the neutron background rate are much higher in the endcaps, thus CSCs are used for their fast response time, owing to the short drift path. The endcaps are also subjected to a higher and non-uniform magnetic field and the CSCs, unlike the DTs, can tolerate this environment. Another benefit to the use of CSCs is their ability to be finely segmented providing an increased momentum resolution. Covering an  $|\eta|$  region of 0.9 to 2.4, there are four stations of chambers mounted onto the faces of steel disks perpendicular to the beam line, and each chamber consists of 6 layers of CSCs with cathode strips running radially out, while the 50  $\mu\text{m}$  diameter anode wires run perpendicularly to the strip orientation and are spaced out by 3.16 - 3.12 mm distances. Each station provides the muon position in  $r - \phi$ . The CSCs are multi-wire proportional counters with cathode strips which allow for the precise measurement of the position at which a muon or charged

particle crosses the gas gap. The CSC stations are further divided into rings where  $n$  denotes the ring number and increases radially outward in the naming convention ME1/n-ME4/n. The innermost ring of the first station (ME1/1) is subdivided into two regions in order to allow for triggering and independent readout from the region closest to the beam line.

In addition to the tracking detector technologies, the CMS muon detector also makes use of resistive plate chambers (RPCs) which are interspersed in the endcaps and barrel between the CSCs and DTs, respectively. Primarily used in fast and independent triggering over a range in  $|\eta|$  up to 1.6, the RPCs consist of two gas gaps with readout strips aligned in  $\eta$  between the gas gaps. Charged particles traversing an RPC will ionize the gas in both volumes causing avalanches to generate as a result of the high electric field. The avalanches, in turn, induce an image charged which is caught by the readout strips.

### 2.2.5. The readout system

The 2016 run of the LHC delivered more than  $6.5 \times 10^{15}$  collisions to each of the general purpose detectors. The time spacing of 25 ns between each collision corresponds to a beam crossing frequency rate of 40 MHz. In addition to this exceptionally high rate, on average 27 particle interactions per bunch crossing occurred during the 2016 proton-proton run at  $\sqrt{s} = 13$  TeV during which the LHC operated at unprecedented luminosities. In addition, the fine segmentation of the CMS subdetectors results in nearly 100 million readout channels and a correspondingly immense volume of data at the sub-detector front-end level. Hence, in order to maintain a high acceptance for events of interest, while simultaneously rejecting QCD multi-jet events which drive the readout rate to high values, CMS employs a two-level robust triggering and detector readout system: a hardware-based Level-1 (L1) trigger which reduces the readout

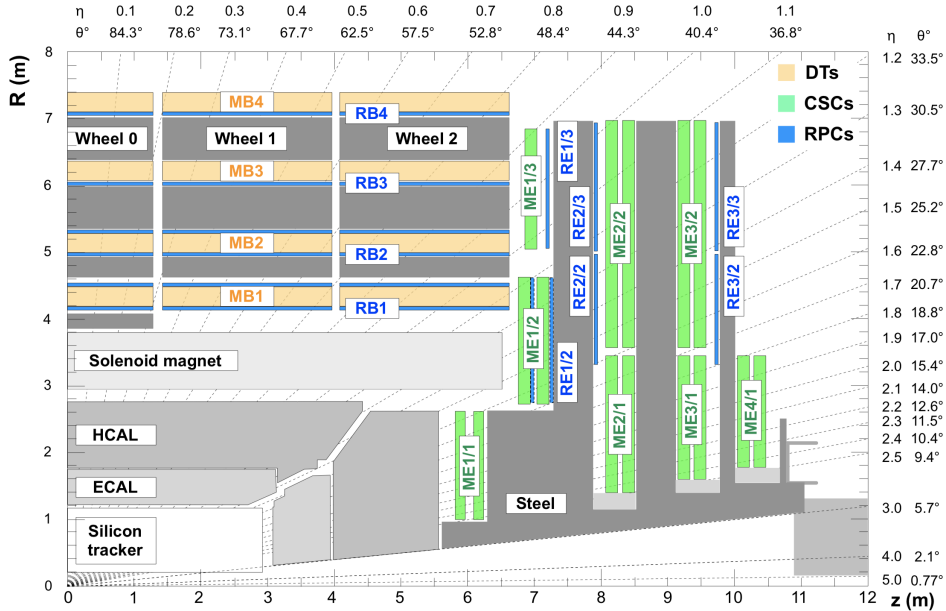


**Figure 2.10.:** A quadrant view of CMS where the IP is at the lower left corner. The dark grey areas denote the locations of the various muon stations and the steel disks. The 4 drift tube (DT, in light orange) stations are labeled MB (muon barrel) and the cathode strip chambers (CSC, in green) are labeled ME (muon endcap). The resistive plate chambers (RPC, in blue) located in the barrel and the endcaps of CMS, are labeled RB and RE, respectively. [65]

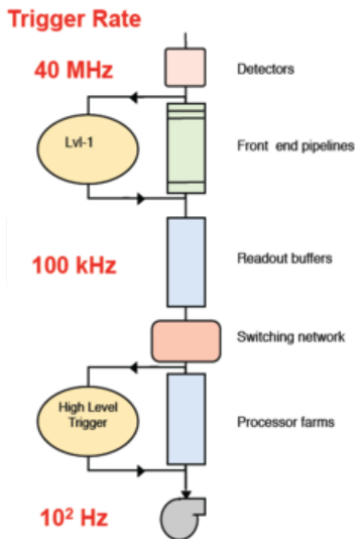


**Figure 2.11.:** A schematic of the two stage CMS trigger architecture and the corresponding rate reduction at each stage [66].

rate from 40 MHz to 100 kHz, and a software-based High-Level trigger (HLT) which further reduces the rate to approximately 200-300 Hz, before storing the data. The architecture of the triggering system can be seen in Figure 2.11.

The L1 CMS trigger system uses information from the previously described calorimeters and muon system to select the most interesting events in a fixed time interval of less than  $4 \mu\text{s}$ , which allows for  $1 \mu\text{s}$  of processing time.

The L1 triggering system relies heavily on the muon detector, where two independent and complementary technologies are employed. The DTs and CSCs in the barrel and endcaps respectively are tracking detectors which provide excellent position and time resolution, whereas the RPCs are used to correspondingly provide a very good timing resolution, but a cruder spatial resolution. For muons with  $p_T$  up to approximately 200 GeV, the momentum resolution is largely dominated by multiple scattering in the steel flux-return yoke, especially in the endcaps, thus the multi-layer CSCs are exploited by the L1 trigger, in order to be able to achieve a high precision in constructing the track segments in the chambers. With the large number of layers

and consequently track segments, sharp  $p_T$  trigger thresholds at L1 are achieved for muons with  $p_T$  up to approximately 100 GeV. The hits in the DTs and CSCs are used to construct track stubs at the chamber/sector level before they are forwarded to the designated sub-detector track-finders (DTTF and CSCTF). In order to guarantee the full coverage over the barrel-endcap transition region, these stubs are shared between the TFs. Correspondingly, the RPC uses hits in pattern comparator logic (RPC PAC) to identify potential muon candidates. The trigger primitives from these regional muon triggers are then forwarded to the Global Muon Trigger (GMT) where they are combined and the four best muon candidates in the barrel and endcap are forwarded to the Global Trigger (GT).

In addition to the muon trigger, the ECAL and HCAL contribute to the calorimeter trigger. The ECAL detector is read out from groupings of 5x5 crystals, where the APDs or VPTs are connected to multi gain pre-amplifiers and these gain ranges are fed to an analog-to-digital converter (ADC) which digitizes the signal at 40 MHz. Energy deposits are calculated in barrel trigger towers, which are  $0.0875 \times 0.0875$  regions in  $\eta - \phi$  space, and subsequently sent to the Regional Calorimeter Trigger (RCT). At this stage  $e/\gamma$  candidates are identified and the energy is further summed into  $0.35\eta \times 0.35\phi$  regions. This information is then passed to the Global Calorimeter Trigger (GCT) which performs the sorting of  $e/\gamma$  candidates, identifies jets, and energy sums. The GCT then sends the GT four isolated and four non-isolated  $e/\gamma$  candidates, and four jets of each category: forward, central, and tau. In addition, the GCT passes along total and missing energy sums ( $E_T$  and  $p_T^{\text{miss}}$ ), and scalar and magnitude of vector sums of transverse jet momenta ( $H_T$  and  $MH_T$ ) [67]. A trigger menu is programmed at the GT level, which consists of approximately 128 trigger algorithms used to make specific requirements on the candidates that have been received from the GCT and GMT. Along with requirements on energy and  $p_T$  thresholds of these candidates, the GT is able to require combinations of objects and specify criteria having

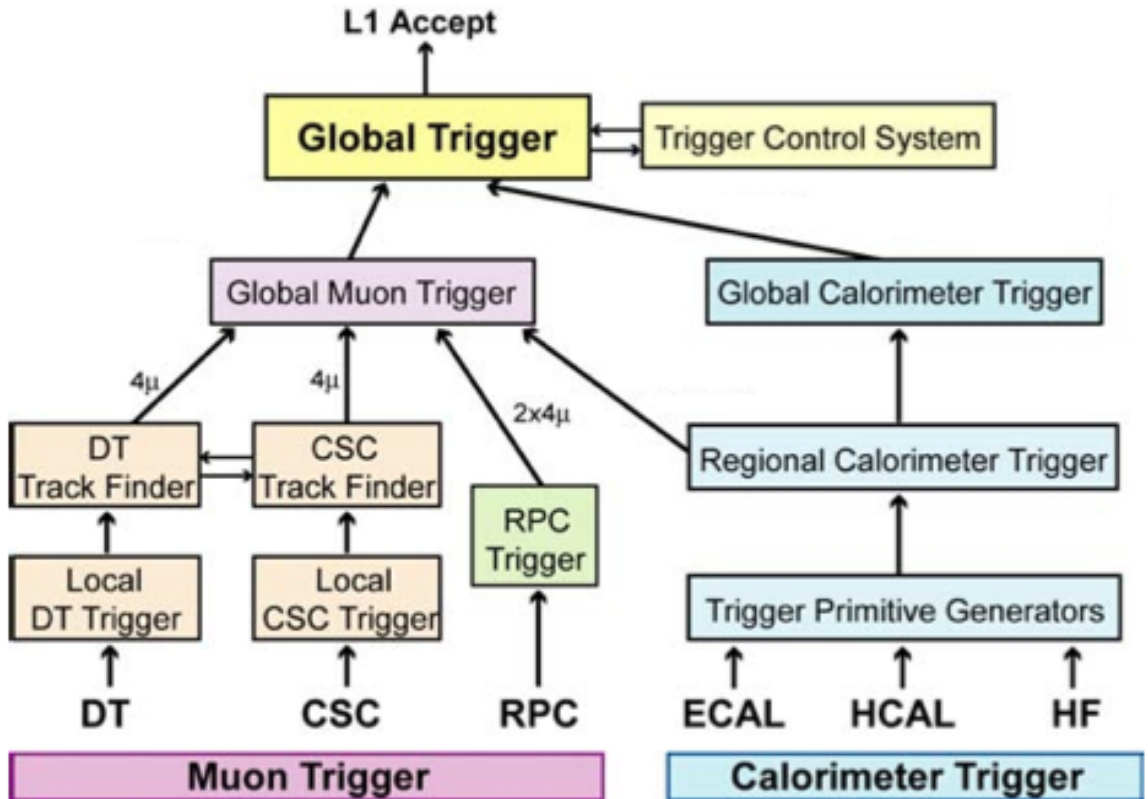


**Figure 2.12.**: An overview of the CMS L1 trigger where the detector inputs are at the bottom and the subsequent steps in rate reduction proceed vertically upwards. [66]

to do with their relative positions. The decision of whether to keep or discard data from a particular bunch crossing, known as a “L1 accept” is based on whether the trigger primitives, such as the electrons, muons, photons, and jets, pass the set  $E_T$  or  $p_T$  thresholds, and the total allocated time for the decision is  $3.2 \mu s$ .

Following the receipt of an L1 accept, a readout of the front-end electronics signals is performed and events are then processed by the HLT, the second tier of the CMS trigger. The entire CMS HLT system is implemented in a single processor cluster farm comprised of commercial computers running Linux. This so-called “Event Filter Farm” consists of three main components including the Readout Unit (RU), which is connected to the detector front-end readout and executes the primary step of data concentration by assembling fragments of an event from given detector partitions.

Following this, the Builder Unit (BU) performs a full event assembly using the event fragments from the RUs, which are subsequently buffered while they proceed through the final event selection in the Filter Unit (FU) [68]. In order to satisfy the requirements of a high and inclusive selection efficiency for various physics objects, as well as maintain a rate of accepted events within  $\mathcal{O}(100)$  Hz, the HLT algorithms employed in the FU are as close as possible to those used in standard offline reconstruction.

In order to strike a balance between the fast rejection of uninteresting events and minimization of overall CPU usage, reconstruction and selection at the HLT level makes use of two steps which nearly resemble distinct trigger systems. Denoted as “Level-2” and “Level-3”, the major distinction between the each step is the reconstruction of full tracks in the tracker used at Level-3, where Level-2 solely makes use of information from the calorimeter and muon systems. Track reconstruction requires significantly larger amounts of CPU time than the correlation of calorimeter and muon detector data owing to the high number of readout channels from the inner tracker, the complex pattern recognition algorithms, and the higher rate of combinatorics.

In electron and photon selection, the Level-2 algorithms involve the clustering of energy deposits in the ECAL and the measurement of the cluster energy and position solely from the calorimetric information. Since electrons radiate in the material between the interaction point and the ECAL, and the 4T magnetic field causes bending, the spray of radiated energy reaches the ECAL. The Level-2 algorithm reconstructs the electron energy by clustering cells along a  $\phi$  road, since the radiated spray of energy from the electron is contained in the  $\phi$  direction, to a good approximation. The following step is termed as “Level-2.5” since only partial as opposed to full tracking information is employed, such that superclusters (groups of energy clusters along the  $\phi$  direction) are matched to hits within the pixel detector. Precise electron position and momentum can be determined solely by using the pixel hits, since most of the tracker

material proceeds the pixel layers hence any photon conversions usually take place after these layers. This matching step further divides the electromagnetic triggers into two streams: one for electron candidates and one for photon candidates, which pass much higher energy threshold requirements. At the final stage, the “Level-3” step involves a full track reconstruction which is seeded by the hits in the pixel layers from the previous step. At this stage, consistency of the energy and momentum measurements ( $E/p$ ) and consistency of the track position with the ECAL hit position is required. In the endcaps, requirements on the fraction of energy found behind the ECAL supercluster (in the HCAL) over the supercluster energy ( $H/E$ ) is made in order to discriminate hadronic activity (i.e.  $\pi^0$ ) from  $e/\gamma$  candidates.

For muon selection requirements at the HLT level, the Level-2 algorithm is seeded by the maximum of four muon candidates found by the L1 GMT and employs the digitized hits in the muon detectors to reconstruct and verify the trajectories that lead to the L1 accept. Tracks are reconstructed according to the Kalman filter technique, described in greater detail in [69], which ameliorates the  $p_T$  measurement from L1. Isolation criteria on the basis of the calorimetric energy sum contained within a cone around the muon candidate can be applied at Level-2. The defining feature of the Level-3 muon selection, is the addition of silicon tracker hits to the trajectory which further refines the  $p_T$  measurement and provides a sharper trigger threshold. At this final stage, the number of pixel tracks in a region around the muon trajectory projected towards the inner detector can be used to suppress contributions from non-prompt muon decays of b, c,  $\pi$  and K particles.

The HLT algorithm for jet selection is a simplified version of the more involved offline algorithms described in the following chapter dedicated to object reconstruction. The algorithm requires the organization of calorimeter data into towers for which the HCAL segmentation in  $\eta \times \phi$  is  $0.0875 \times 0.0875$  in the barrel and approaches an

$\eta$  segmentation of 0.0175 near the edges of the endcaps. Correspondingly, for each HCAL barrel tower, there are approximately 25 ECAL crystals, whereas in the endcap regions the crystal number varies with  $\eta$ . The basic iterative algorithm for jet finding at HLT consists of designating a “seed tower” which has the highest tower  $E_T$ , and using this to calculate the direction of the “protojet”. By determining the transverse-energy-weighted angles of the towers in a cone around the protojet in  $\eta - \phi$  space, the direction measurement of the seed protojet is updated and the energy in the cone is summed to obtain the protojet  $E_T$ . The procedure is repeated until the protojet energy changes by less than 1% between iterations and the direction in  $\Delta\eta^2 + \Delta\phi^2$  space changes by less than 0.01, or on the other hand, 100 iterations have been completed. Towers that are associated with a stable protojet found after this procedure are removed from the listed sorted by descending tower  $E_T$ , and the entire jet finding procedure is repeated until no objects remain in the list or conversely, the tower with the highest  $E_T$  is below a preset “seed” threshold dictated by the algorithm. More details on the respective parameters such as cone-size, seed energy threshold, and minimum jet energy threshold can be found in [70].

The ability to use simple trigger requirements to attain high efficiencies for most physics objects is a key feature of the HLT system, along with the flexibility it allows for the modification of existing trigger thresholds or the addition of new triggers should the available computing bandwidth allow for such options. Using a single processor farm, the HLT selection of 1:1000 is achieved and subsequently the data are transmitted to the online and offline computing services.

## 2.2.6. Computing and data storage

The events selected by the HLT for physics analysis, along with events that are selected for calibration purposes, and a fraction of events rejected by the HLT are then processed

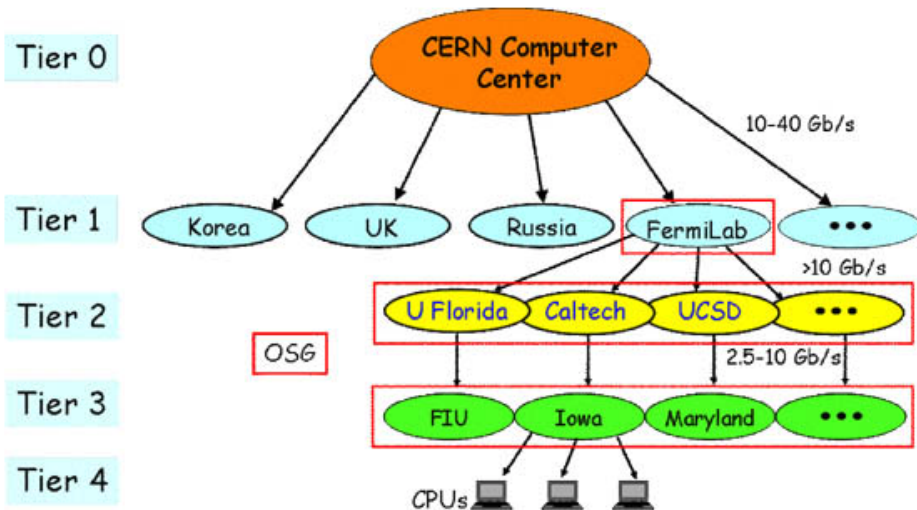


**Figure 2.13.:** A flow chart of the multi-tier worldwide LHC computing grid, where the components circled in red are examples of the U.S. resources that are part of Open Science Grid (OSG) as defined in detail in [71]. The computing resources at Northwestern University fall under the Tier 3 computing category.

either online or transmitted to the offline systems for event reconstruction, selection, and any other offline processing. The HLT farm writes “raw” data events of  $\mathcal{O}(1.5)$  MB size at an approximate rate of 100 Hz which are grouped into primary datasets based on HLT trigger object requirements and organized into  $\mathcal{O}(10)$  online streams to be processed offline. The raw data is processed at CERN’s Tier-0 farm where events are reconstructed with timescales ranging from a few to 24 hours depending on the level of priority. The Tier-0 farm writes out “reco” data events of  $\mathcal{O}(0.25)$  MB size to one of approximately 6 Tier-1 sites, which produce Analysis Object Data (AOD) events of  $\mathcal{O}(0.5)$  MB [72]. The AOD events are derived from reco events and contain a copy of the high-level physics objects along with a summary of reco information which enable additional analysis handles such as track refitting. In 2014, in an effort to reduce the event size while simultaneously retaining all the necessary data from the AOD data formats, a MiniAOD format [73] was introduced as a derivation from the AOD. MiniAOD event sizes are of  $\mathcal{O}(0.05)$  MB and contain high-level physics objects, along with Particle Flow candidates which are described in the following chapter, and

information from the simulated particles. At this stage, the MiniAOD data format can be skimmed according to the objects and selection necessary for data analysis. The multi-tier worldwide LHC computing grid shown in Figure 2.13 displays the full computing chain down to the individual CPUs employed by the end-user, the analyzer.

# Chapter 3.

## Object and event reconstruction

In order to target  $t\bar{t} + \chi\bar{\chi}$  production in the dilepton final state, where both top quarks have leptonically decaying W bosons, the selection criteria is compatible with that of SM  $t\bar{t}(2\ell)$  decays, but with a requirement targetting the harder  $p_T^{\text{miss}}$  spectra as expected from signals compared to the SM background.

Owing to the design elements of the CMS detector as described in Chapter 2, it has been found that it is well-suited to particle-flow (PF) reconstruction of physics objects, expanded upon in Section 3.1, from the signals collected by each subdetector. Section 3.2-3.4 detail the means by which the PF quantities are employed in the reconstruction of particular objects, and the criteria each object in an event must adhere to in order to be considered a potential signal event. Section 4.2 explains how the reconstructed event objects are used collectively, to target a region where a  $t\bar{t}(2\ell) + \chi\bar{\chi}$  signal is expected.

### 3.1. The Particle Flow algorithm

A key feature of the CMS detector which allows for the correlation of signals from different sources is the fine spatial granularity and segmentation of the individual constituent subdetectors. As a result of the fine-grain tracker and strong magnetic field, very efficient charged-particle track reconstruction is possible, which accounts for  $\sim 65\%$  of jet energy measurement. Additionally, the high ECAL segmentation provides the ability to separate energy deposits from particles in jets from one another, allowing for the efficient identification of photons and the measurement of  $\sim 25\%$  of the jet energy. The remaining  $\sim 10\%$  of the jet energy measurement comes from the HCAL, which has a sufficient segmentation to allow for the separation of charged and neutral hadron energy deposits from particles in jets. Lastly, as per its namesake, the CMS detector has an excellent muon system enabling pure and efficient muon identification regardless of the surrounding particles.

The goal of the PF algorithm is thus to optimally combine the information from the aforementioned subdetectors, which is done via the following simplified description, where more details can be found in [74]:

- Tracks from the pixel and strip tracker are extrapolated through the calorimeters (“inside-out”).
- If the tracks land within certain spatial boundary requirements of one or several clusters, they are linked to the track in question resulting in a charged hadron candidate. This PF candidate is subsequently not considered in the remainder of the algorithm.
- By this point, muons have been independently identified by a correlation of hits between the tracker and the muon system detectors, thus removing any potential ambiguity of track association to muons or charged hadrons.

- The treatment of electrons is complicated by the fact that frequent Bremsstrahlung gives rise to multiple possible energy clusters that can be associated to a track, thus dedicated track reconstruction is required to properly match ECAL clusters from the emitted photons to the electron track.
- Finally, the remaining ECAL and HCAL clusters are designated as photon and neutral hadron candidates, respectively.

The preceding steps yield a list of particles, consisting of neutral and charged hadrons, photons, electrons, and muons, all of which are then employed in the reconstruction of jets,  $p_T^{\text{miss}}$ , and  $\tau$  leptons from their decay products. In addition, the list of PF candidates is used to measure the isolation of the particles.

## 3.2. Leptons

A top and anti-top quark are expected in the signal event, and each decays via a  $W^+$  and  $W^-$  respectively. The  $W^\pm$  boson in turn decays to a lepton and its corresponding lepton neutrino, as shown in Figure 3.1. Although the  $W^\pm$  boson decays democratically to each lepton generation, only the first and second generation are considered in this work. Namely, since the top and anti-top produce a positively and negatively charged  $W$  boson, the final state topology is expected to contain two oppositely charged leptons which are the same lepton flavor or different lepton flavors. In the context of this work, the term flavor is used to distinguish between the first and second lepton generations. Thus, dielectron ( $ee$ ) and dimuon ( $\mu\mu$ ) events are referred to as same flavor (SF) and events containing an electron and muon pair ( $e\mu$ ) are referred to as opposite flavor (OF). The  $\tau$  lepton final state is not considered in this work, as very little sensitivity is expected to be gained as a result of the challenges in detector reconstruction. The  $\tau$  lepton is the only lepton that can decay into hadrons, doing so

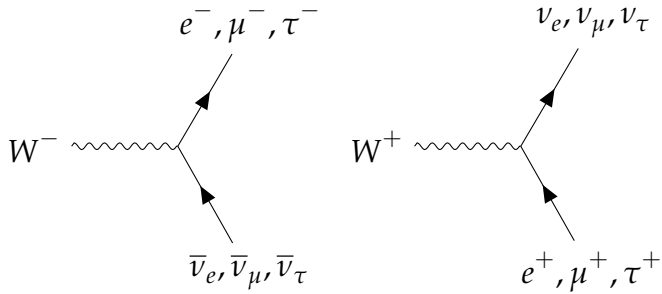


**Figure 3.1.:**  $W^+$  and  $W^-$  decay to leptons and corresponding lepton neutrinos for all lepton generations.

approximately 65% of the time, and its remaining branching ratio consists of purely leptonic decays to the first and second generation. As such, the hadronic decay mode in this channel is overwhelmed by background from multijet QCD processes, and would also necessitate higher lepton trigger  $p_T$  thresholds along with more stringent lepton identification and isolation criteria. The higher thresholds and identification criteria would subsequently result in lower trigger and selection efficiencies, amounting to minimal gains in sensitivity from the addition of the  $\tau$  lepton decay mode.

### 3.2.1. Muons

In order to be selected, muons must pass a stringent set of criteria which guarantee a high muon identification efficiency. In general, the muon object reconstruction process consists of associating independently reconstructed tracks in the muon system (i.e. standalone muon) to tracks in the inner tracker (i.e. tracker muon), where a final fit is performed over the combined set of hits. The matching procedure can be performed from an “outside-in” or “inside-out” detector approach. The quantities derived from the track fit quality and number of hits or track segments enables the selection of well-measured muons and those less likely to be fakes. The following list of criteria describe the “Tight” working point employed to select a well-identified muon:

- *Global Muon* (outside-in) reconstruction: A standalone muon constructed from track segments in the outer muon detectors is matched to a tracker track constructed from hits in the pixel and strip tracker and a *global muon track* is fitted.
- *Tracker Muon* (inside-out) reconstruction: Tracker tracks with  $p_T > 0.5 \text{ GeV}$  and  $p > 2.5 \text{ GeV}$  are taken to be muon candidates and are extrapolated to the muon system, factoring in energy loss expected and the uncertainty from multiple Coulomb scattering. An extrapolated track qualifies as a tracker-muon track if it is matched with at least one short stub from DT or CSC hits.
- *Particle Flow Muon*: A muon is required to pass *Global Muon* and *Tracker Muon* criteria. In the case that a muon is not well-isolated as a result of final state radiation or Bremsstrahlung, energy deposits in the calorimeter may be used to assign the momentum of a the muon.
- $\chi^2/\text{ndof} < 10$  for *Global Muon* track fit: This requirement is intended to suppress particles that come from hadronic punchthroughs wherein the muon originates from  $\pi$  and K meson decays in a hadronic cascade. In such cases, the standalone muon will have a lower  $p_T$  as a result of the energy loss of the  $\pi$  in the calorimetry, while the tracker muon will exhibit a higher  $p_T$ .
- At least one muon-chamber hit included in *Global Muon* track fit: This requirement is intended to suppress particles originating from hadronic punchthrough and muons coming from in-flight decays of  $\pi^\pm$
- Muon segments in at least two muon stations: A tracker track must be matched to these segments, using more than 10 inner-tracker hits, with at least 5 tracker layers containing hits, and at least one pixel hit. This suppresses the punchthrough rate, any accidental track-to-segment matching, and guarantees a good  $p_T$  measurement.

- $|d_{xy}| < 2$  mm: The tracker track must have a transverse impact parameter,  $d_{xy}$ , less than 2 mm with respect to the location of the primary vertex interaction point. This requirement is intended to suppress backgrounds from cosmic muons and further suppress muons originating from in-flight decays.
- $|d_z| < 5$  mm: The tracker track must have a longitudinal distance,  $d_z$ , less than 5 mm with respect to the location of the primary interaction vertex in order to further suppress cosmic muons, muons originating from in-flight decays, and tracks from pile-up.

In addition to the aforementioned selection criteria, to further reduce contamination from jets, muon candidates are required to be isolated from all other reconstructed particles within a radius of 0.4 according to the isolation variable defined as,

$$I = I_{h^+} + \max\left(I_{h^0} + I_\gamma - 0.5 \cdot I_{\text{pu}}, 0\right). \quad (3.1)$$

where  $h^+$ ,  $\gamma$ , and  $h^0$  correspond to charged hadrons, photons, and neutral hadrons, respectively, and each  $I$  quantity is the sum  $p_T$  (sum  $E_T$  for  $\gamma$ , and  $h^0$ ) of these particle types in the  $R = 0.4$  cone.  $I_{\text{pu}}$  is the contribution from neutral hadrons from pileup meant to account for effects of additional neutral particles not associated with the primary vertex. The value computed in equation (3.1) is divided by the muon  $p_T$  which is not included in the calculation, hence the value is turned into a relative isolation,  $I_{\text{rel}}$ . Muons in the event are required to have a relative isolation of less than 0.15.

A looser set of muon identification and isolation requirements are also used in this work. In one case the “Fake-able Object” (FO) working point is employed in a background estimation method described in Chapter 5. In addition, a “Loose” muon identification and isolation working point is also used to veto any additional muons in an event. The three muon working points are summarized in Tab. 3.1.

Variable	FO WP	Loose WP	Tight WP
PF-muon	true	true	true
global muon	-	-	true
global OR tracker muon	true	true	-
$\chi^2/\text{ndof}$ of global muon fit <	-	-	10
No. of muon chamber hit in global muon fit $\geq$	-	-	1
No. of muon stations with muon segments $\geq$	-	-	2
$ d_{xy}  \text{ (cm)} <$	-	-	0.2
$ d_z  \text{ (cm)} <$	-	-	0.5
No. of pixel hits $>$	-	-	0
No. of tracker layers with hits $>$	-	-	5
relative isolation <	0.4	0.25	0.15
track isolation <	0.4	-	-

**Table 3.1.:** Variables and thresholds that define “FO”, “Loose”, and “Tight”. “-” indicates the variable is not considered for that working point.

### 3.2.2. Electrons

Similarly to muons, electron reconstruction involves the association of tracker tracks to superclusters (i.e.  $5 \times 5$  arrays of crystals in  $\eta \times \phi$  surrounding a seed crystal of minimum  $E_T > E_{T,\text{seed}}^{\min}$ ) of energy in the ECAL. Electron-track building involves the Gaussian-sum filter (GSF) algorithm that accounts for the non-Gaussian distributed Bremsstrahlung electron energy loss. Electron candidates must also pass a stringent set of selection requirements in order to be considered a candidate component of the signal event. The criteria are outlined in the following list:

- $\sigma_{i\eta i\eta}$ : This variable describes the lateral extension of the hadronic shower along the  $\eta$  direction. It is defined as,

$$(\sigma_{i\eta i\eta})^2 = [\sum (\eta_i - \bar{\eta}) w_i] / \sum w_i \quad (3.2)$$

and the sum runs over the 5x5 matrix of crystals around the highest  $E_T$  crystal of the supercluster (SC), and  $w_i$  denotes a weight that is logarithmically dependent on the contained energy.

- $|\Delta\phi_{in}| = |\phi_{SC} - \phi_{in}^{\text{extrap}}|$ : This denotes the azimuthal separation between the SC energy-weighted  $\phi$  position and the track  $\phi$  extrapolated from the innermost track position and direction to the point of closest approach (PCA) to the SC.
- $|\Delta\eta_{in}| = |\eta_{SC} - \eta_{in}^{\text{extrap}}|$ : This denotes the lateral separation between the SC energy-weighted  $\eta$  position and the track  $\eta$  position extrapolated from the innermost track position and direction to the PCA to the SC.
- $H/E$ : The ratio between the energy deposits in the HCAL and ECAL supercluster. A well-identified electron would be expected to have a low  $H/E$  owing to the high  $X_0$  of the CMS detector, thereby containing the EM showering before it reaches the HCAL.
- $|1/E - 1/p|$ : This quantity expresses an energy-momentum matching requirement using the SC energy,  $E$ , and the track momentum,  $p$ , at the PCA to the track vertex. The requirement helps to reject backgrounds from hadronic activity where the spread of the  $E$  is not localized resulting in a low  $E/p$ , but also backgrounds where a  $\pi^0 \rightarrow \gamma\gamma$  decay occurs in the close vicinity of a charged hadron, resulting in a very high  $E/p$  ratio.
- $|d_{xy}|$ : The transverse impact parameter of the tracker track with respect to the primary interaction vertex.
- $|d_z|$ : The longitudinal impact parameter of the tracker track with respect to the primary interaction vertex.
- Missing hits: After track-fitting is performed to electron-tracks seeded by an ECAL crystal with maximum energy in a considered region, if several tracker hits

are found to be compatible with those expected in a layer from the track trajectory, at most one missing hit is allowed for an accepted candidate. The idea is that trajectories of prompt electrons commence at the beamline, and thus they are not expected to have missing hits in the inner layers of the tracker, while photon conversions taking place within the tracker volume often do not commence at the innermost layers indicating missing hits in this area. Furthermore, in order to avoid the inclusion of hits originating from Bremsstrahlung photons converted to  $e^+ e^-$  pairs, in the reconstruction of primary electron tracks, an increased  $\chi^2$  penalty is applied to trajectory candidates which have one missing hit.

- Pass conversion veto: In order to reject secondary electrons produced in the conversion of photons in the tracker material, a vertexing algorithm is used. The hits in the tracker from the converted photon are fit to a common vertex using the well-defined topological constraint that tracks from conversions have virtually the same tangent at the conversion vertex in both the  $(r, \phi)$  and  $(r, z)$  planes. The converted photon candidates are rejected according to the  $\chi^2$  probability of the fit.

In addition to the aforementioned selection criteria, electrons are required to be isolated from nearby activity, namely significant energy flow that may be a result of misidentified jets or that may be due to genuine electrons within a jet resulting from a semileptonic b or c quark decay. Similarly to the isolation definition for muons in equation (3.1), the electron isolation definition is a sum of PF-candidates within  $R = 0.3$  of the electron. Explicitly, the isolation is computed as,

$$I = I_{h^+} + \max \left( I_{h^0} + I_\gamma - A_{eff} \cdot \rho, 0 \right), \quad (3.3)$$

where  $I_{h^+}$ ,  $I_{h^0}$ , and  $I_\gamma$  are the contributions from charged hadrons, neutral hadrons, photons, respectively.  $\rho$  denotes the event energy density. Effects due to pileup

are mitigated using corrections based on the “effective area”, denoted as  $A_{eff}$  in equation (3.3). In order to obtain the  $A_{eff}$ , the isolation is plotted as a function of  $\rho$  in bins of  $\eta$ , and the value at which the isolation is 90% efficient is determined in slices of  $\rho$ , known as the cutoff. A first order polynomial is fit to the cutoff and the slope is taken as the value of the correction, as listed in Tab. 3.2 for the various  $|\eta|$  ranges.

$ \eta $ range	$A_{eff}$
0.0 – 1.0	0.1703
1.0 – 1.479	0.1715
1.479 – 2.0	0.1213
2.0 – 2.2	0.1230
2.2 – 2.3	0.1635
2.3 – 2.4	0.1937
2.4 – 2.5	0.2393

**Table 3.2.:** Effective areas for electron isolation PU subtraction.

A looser set of electron identification and isolation requirements are also used in this work. In one case the “Fake-able Object” (FO) working point is employed in a background estimation method described later. In addition, a “Veto” electron identification and isolation working point is also used to veto events with any additional electrons. The three electron working points are summarized in Tab. 3.3, for both the barrel and endcap regions, where an electron is defined as being in the barrel if it has a supercluster  $|\eta| < 1.479$ .

### 3.3. Jets

Jets are reconstructed from particle candidates obtained by the PF algorithm, using the anti- $k_T$  clustering algorithm [75] with size parameter,  $R = 0.4$ .

Variable	FO WP		Veto WP		Tight WP	
	Barrel	Endcap	Barrel	Endcap	Barrel	Endcap
$\sigma_{i\eta i\eta} <$	0.011	0.031	0.0115	0.037	0.00998	0.0292
$\Delta\eta_{\text{in}} <$	0.04	-	0.00749	0.00895	0.00308	0.00605
$\Delta\phi_{\text{in}} <$	0.02	-	0.228	0.213	0.0816	0.0394
$H/E$	0.06	0.06	0.356	0.211	0.0414	0.0641
$ 1/E - 1/p  <$	0.013	0.013	0.299	0.15	0.0129	0.0129
$ d_{xy}  \text{ (cm)} <$	0.1	0.2	0.05	0.10	0.05	0.10
$ d_z  \text{ (cm)} <$	0.373	0.602	0.10	0.20	0.10	0.20
No. of missing expected hits $\leq$	1	1	2	3	1	1
relative isolation $<$	-	-	0.175	0.159	0.0588	0.0571
relative ECAL PFCluster iso $<$	0.16	0.12	-	-	-	-
relative HCAL PFCluster iso $<$	0.12	0.12	-	-	-	-
relative track iso $<$	0.08	0.08	-	-	-	-
pass conversion veto	true	true	true	true	true	true

**Table 3.3.:** Variables and thresholds that define “FO”, “Veto”, and “Tight” electrons. An electron is in the barrel if it has supercluster  $|\eta| < 1.479$ , otherwise it is in the endcap.

The anti- $k_T$  algorithm is part of a group of sequential jet clustering algorithms that make use of the distance between candidate particles and their respective energies when forming a jet. Such algorithms make the assumption that the particles contained in a jet have minimal differences in  $p_T$ , hence the grouping is performed based on momentum-space. These algorithms share a similar underlying method where a distance is computed between two candidate particles according to:

$$d_{ij} = \min \left( p_{Ti}^a, p_{Tj}^a \right) \times \frac{R_{ij}^2}{R} \quad (3.4)$$

where  $R_{ij} = (\eta_i - \eta_j)^2 + (\phi_i - \phi_j)^2$  is the  $(\eta - \phi)$  distance between the two particles and  $R$  is the radius parameter of the jet cone. These methods also require the computation of a second distance variable,  $d_{iB} = p_{Ti}^a$ , the momentum-space distance

between the beam axis and the candidate particle. Subsequently, the minimum of the entire set  $\{d_{ij}, d_{iB}\}$  is determined and if  $d_{ij}$  is the minimum, then particles  $i$  and  $j$  are combined by the summation of their respective four-vectors, and removed from the list of particles. If  $d_{iB}$  is determined as the minimum, the candidate  $i$  is taken as the final jet and removed from the list of particles. The process is repeated until either a desired number of jets have been found (exclusive), or the separation between particles in a jet,  $R_{ij}$ , is greater than the jet size parameter  $R$  (inclusive).

In the anti- $k_T$  algorithm, the value of  $a$  corresponds to -2, such that equation (3.4) results in,

$$d_{ij} = \min \left( \frac{1}{p_{Ti}^2}, \frac{1}{p_{Tj}^2} \right) \times \frac{R_{ij}^2}{R} \quad (3.5)$$

and  $d_{iB} = \frac{1}{p_{Ti}^2}$ . The anti- $k_T$  algorithm is minimally affected by activity from the underlying event and pile-up, since equation (3.5) is dominated by high  $p_T$  particles, so the algorithm preferentially begins clustering hard particles, causing the jet area to fluctuate a small amount.

In order to reduce the effects of “in-time” pile-up, that is additional pp collisions occurring in the same bunch-crossing as the collision of interests, a charge hadron subtraction (CHS) treatment is performed during the anti- $k_T$  clustering of PF jets. The CHS technique removes any charged hadrons well-matched to PU vertices, allowing for the clustering of remaining PF candidates to form jets. In the PF algorithm, a charged hadron is defined as a track possibly associated with hits in the ECAL and HCAL. In order to determine a primary vertex, the proto-vertex with the largest magnitude of the sum of squares of the track transverse momenta  $(\sum |p_T^{TRK}|^2)$  is chosen. Subleading vertices are deemed as originating from PU and their minimum

degrees of freedom,  $N_{\text{dof}}$ , in the vertex fit is required to be larger than four. Based on the chi-square per degree of freedom ( $\chi^2/\text{d.o.f}$ ), a charged hadron can be assigned to the chosen PV if this value is less than 20, otherwise it is associated to a PU vertex. The final step of the CHS procedure entails the removal of PU tracks which are determined by the association of the charged hadron track to a good PU PV. The tracks associated to the PV, and any other tracks not associated to the PU vertices, are kept. The primary effect of the application of CHS is the removal of jets from pileup, although the procedure also improves the angular and  $p_T$  resolution of jets, along with reducing the rate of low  $p_T$  jets created solely from PU in the tracker acceptance region ( $|\eta| < 2.5$ ).

Furthermore, a set of loose identification criteria on the relative fractions of reconstructed PF jet constituents are imposed in order to suppress noise contributions from the HCAL and ECAL. Requirements on the relative energy fractions carried by the various types of PF candidates with respect to the total PF jet energy are made. Tracker acceptance limits the validity region of the charged PF candidate to  $|\eta| < 2.4$ , however the neutral PF candidates extend up to  $|\eta| < 5$ . The “loose” PF jet identification working point defined in Tab. 3.4 targets the removal of jets emerging from calorimetric noise.

Variable	$ \eta  < 2.7$	$2.7 <  \eta  < 3$	$ \eta  > 3$
Neutral Hadron Fraction	< 0.99	< 0.98	-
Neutral EM Fraction	< 0.99	> 0.01	< 0.9
Number of Constituents	> 1	-	-
Number of Neutrals	-	> 2	> 10
<i>Additional cuts for <math> \eta  &lt; 2.4</math></i>			
Charged Hadron Fraction	> 0		
Charged Multiplicity	> 0		
Charged EM Fraction	< 0.99		

**Table 3.4.:** Variables and thresholds that define the “Loose” PF jet ID.

Clustering algorithms have no means by which to distinguish which PF constituents correspond to well-identified leptons, thus jets can include such leptons. In this work, the ambiguity is treated after the “good” leptons are selected a jet is not considered if it is within  $\Delta R < 0.4$  of a such an electron or muon. In this sense, the precedent is given to the well-identified muons and electrons.

All jets with  $p_T > 15 \text{ GeV}$  and less than 0.9 of their energy deposited in the ECAL are corrected. In addition, the muon four-momentum is subtracted from the jet four-momentum when the correction is performed, if a muon is found within a jet. Jet energy corrections consist of several stages and are derived and applied in a factorized manner, although the underlying procedure of scaling the jet four-momentum with a scale factor (SF) which depends on jet quantities such as  $p_T$ ,  $\eta$ , and flavor is universal. The corrections are listed and described briefly below in the order they are applied.

- L1 Pile up: Aimed at removing energy contributions from pile-up events, this correction is determined from a simulation sample of QCD dijet events which are processed with and without pileup overlay. The corrections are parametrized as a function of the jet area ( $A$ ), jet  $\eta$  and  $p_T$ , and  $\rho$  (i.e. the same quantity used in electron isolation calculations). The correction applied to data is parametrized in  $\eta$  and determined using zero bias events.
- L2L3 MC-truth corrections: The reconstructed jet  $p_T$  is compared to the particle level jet  $p_T$  in order to derive jet response corrections from a QCD dijet simulation sample. The jet response is made uniform over  $p_T$  and  $\eta$ , the jet variables in which it is derived.
- L2L3 Residuals: These corrections are applied to jets in data only and include both an  $\eta$  and  $p_T$  component. For the  $\eta$  dependence (relative corrections), dijet events are compared to a jet of similar  $p_T$  in the barrel region ( $|\eta| < 1.3$ ). For the  $p_T$  dependence (absolute corrections), the JES relative to the reference JES of

the barrel jet is taken into account. The jet absolute scale corrections are derived using  $Z(\mu\mu/ee)$ +jets, photon+jet, and multijet events.

### 3.3.1. b-jet tagging

In addition to the preceding jet requirements, an algorithm developed to distinguish jets originating from the hadronization of b quarks is employed in the analysis. This identification relies heavily on the precise reconstruction of secondary vertices associated to weakly decaying b hadrons present in jets origination from the hadronization of b quarks.

The algorithm, known as the Combined Secondary Vertex (v2) (CSV) makes use of the Inclusive Vertex Finder (IVF), which is exploited in the reconstruction of secondary vertices. The IVF is seeded by a collection of reconstructed tracks in the event which satisfy a loose set of requirements, such that tracks with at least 8 hits in the silicon pixel tracker are selected. The selected tracks must have a  $p_T$  greater than 0.8 GeV and the longitudinal impact parameter, the distance between the primary vertex and the track at their point of closest approach, should be smaller than 0.3 cm. In order to create the secondary vertices, the tracks must be displaced, having an IP no larger than  $50 \mu m$  and IP significance (IP divided by its uncertainty) of at least 1.2. Clusters are then formed from the displaced seed tracks using requirements on minimum distances and the opening angles between them. An adaptive vertex fitter is used to fit the clusters. The vertex reconstruction algorithm then proceeds with multiple iterations of track arbitration in order to appropriately associate the cluster tracks with the primary or secondary vertex. Each step makes requirements on the fraction of tracks from the secondary vertex shared with the primary and the angular distances between the two vertices.

The CSV algorithm subsequently makes use of the tracks and vertices passing the requirements of the IVF. In the CSV algorithm, at least two displaced tracks identified with the IVF procedure are required within a jet, and furthermore must have an angular distance,  $\Delta R$ , less than 0.3 with respect to the jet axis. The CSV algorithm categorizes the input vertices into three independent categories. The categories are listed and briefly defined below.

- Jets are associated with at least one reconstructed SV: Vertices are sorted according to increasing uncertainty on the flight distance if more than one reconstructed SV is found. Most discriminating variables relying on a SV are such that the leading SV is required, such as the vertex mass or the flight distance significance.
- Jets are associated with a “pseudo-vertex”: No vertex fit is applied to candidates satisfying this category since the jet contains at least two tracks incompatible with a window of 50 MeV around the  $K_s^0$  meson mass and a signed IP larger than 2. Since the calculation of a flight distance is not feasible, the discriminating variables are reduced in this category as compared to the previous.
- Jets are not associated with any reconstructed SV or “pseudo-vertex”: This category complements the above two, meaning only variables related to the displaced track vertex are exploited.

The variables defined in each category are combined in each respective category via a multilayer perceptron (MLP) with one hidden layer. An MLP is a type of artificial neural network where the information in each layer is fed uni-directionally to the next. It has the advantage of distinguishing non-linearly separable data. A likelihood ratio taking into account the expected fraction of jet flavors in  $t\bar{t}$  events is combined with the information from the three categories, to yield the final CSV discriminant, as shown in Figure 3.2, for multi-jet events where at least one jet satisfies an online  $p_T$  requirement of greater than 40 GeV.

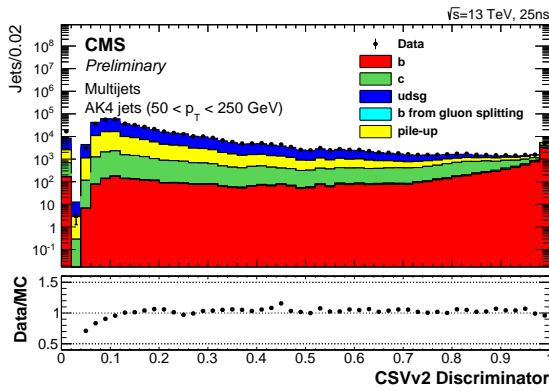


**Figure 3.2:** Discriminator values for the CSVv2 algorithm for an inclusive multi-jet topology, where the total number of entries in the simulation is normalized to the observed number of entries in the data.

### 3.4. Missing transverse energy

A crucial aspect of this search requires the precise modeling of the missing transverse energy, and denoted by  $p_T^{\text{miss}}$ . Owing to momentum and energy conservation,  $p_T^{\text{miss}}$  corresponds to the magnitude of the transverse momentum that is carried by weakly interacting particles, such as neutrinos. This observable is of particular importance in the search for  $t\bar{t} + \chi\bar{\chi}$ , since the neutral DM particles are also predicted to interact weakly, hence they will escape the detector volume without being detected. The measurement of  $p_T^{\text{miss}}$  relies heavily on the detectable and reconstructed physics objects mentioned in the preceding sections. Thus,  $p_T^{\text{miss}}$  is defined as the imbalance in the transverse momentum of all particles that interact with the detectors. As described in Section 3.1, the CMS PF algorithm provides a list of PF candidates reconstructed from correlation of subdetector signals. It then follows that the  $\vec{p}_T^{\text{miss}}$  is defined as the negative vectorial sum of the transverse momenta of all PF candidates in the event, such that,

$$\vec{p}_T^{\text{miss}} = - \sum_{i=\text{PF particles}} \vec{p}_{T,i} \quad (3.6)$$

The measurement of the  $p_T^{\text{miss}}$  can be mismeasured as a cause of a variety of reasons. The nonlinear response of the calorimeter for neutral and charged hadrons due to its noncompensating nature, minimum energy thresholds in the calorimeters, inefficiencies in the tracker, or neutrinos from semileptonic particle decays are sources from which bias can be introduced in the  $p_T^{\text{miss}}$  measurement. In order to mitigate these biases, the  $p_T^{\text{miss}}$  derived is corrected for using jet energy scale corrections, so equation (3.6) then becomes,

$$\vec{p}_T^{\text{miss}} = - \sum_{i=\text{PF particles}} \vec{p}_{T,i} - \sum_{\text{jets}} \left( \vec{p}_{T,\text{jet}}^{\text{corr}} - \vec{p}_{T,\text{jet}} \right). \quad (3.7)$$

The quantity in equation (3.7) is the  $p_T^{\text{miss}}$  quantity used throughout this work and shown in all experimental plots in the following chapters.

# Chapter 4.

## Signal simulation and event selection

### 4.1. $t\bar{t} + \chi\bar{\chi}$ simplified models

The DM collider signal under investigation in this work is characterized by the production of a top quark pair recoiling against a spin-0 mediator that decays to a pair of DM particles, as shown in Figure 4.1. As described in greater detail in Section 1.5, the model predicts the production of DM via a scalar (S) or pseudoscalar (PS) mediator, which couples to SM fermions and the Dirac fermion DM particles. The coupling of the mediator to the top quarks is Yukawa-type hence  $g_q$ , which is effectively the multiplier to the Yukawa coupling, is taken to be unitary. Meanwhile, the direct coupling of the mediator to the DM particles,  $g_\chi$ , is also equal to one.

The most important characteristic of  $t\bar{t} + \chi\bar{\chi}$  models is the  $p_T$  of the  $\chi\bar{\chi}$  system. This quantity is equivalent to the  $p_T$  of the mediator and is translated to the  $p_T^{\text{miss}}$  detector observable in an event. The  $p_T^{\text{miss}}$  spectra for the  $t\bar{t} + \chi\bar{\chi}$  models, although dependent on the mediator mass, are expected to have longer “tails” at high  $p_T^{\text{miss}}$ , than that of the SM  $t\bar{t}$  process, owing to the additional contribution from the  $\chi\bar{\chi}$

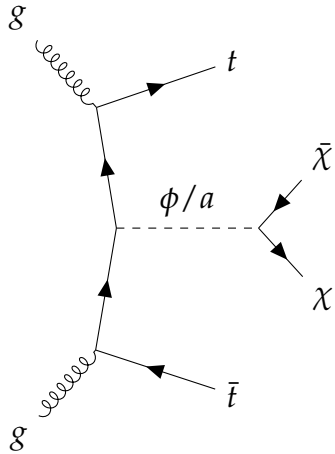


**Figure 4.1.:** The representative diagram of a top quark pair produced in association with a pair of DM particles ( $\chi\bar{\chi}$ ) which are produced via a S or PS mediator coupled to the tops.

system. In general, the mediator  $p_T$  spectrum broadens with increasing mediator mass, as demonstrated in Figure 4.2, where the  $p_T$  is shown for various S and PS mediator masses with  $m_\chi = 1$  GeV. It is also the case that at low masses, the PS  $p_T$  is harder than the S  $p_T$  of equivalent mediator mass, however the distributions converge to at higher mediator mass. The trend of broadening mediator  $p_T$  spectra with increasing mediator mass does not hold in the off-shell regime where the mediator mass is less than twice the DM fermion mass ( $2m_\chi > m_\phi$ ). In the off-shell regime, the  $p_T$  of the mediator is not dependent on the mass, and in addition, if the  $m_\chi$  is varied for a fixed mediator mass, the  $p_T$  distribution is harder for the off-shell production rather than the on-shell. Due to the finite mediator width, in the area near the on/off-shell threshold, the kinematics will contain contributions from both types of production, as seen in Figure 4.3.

The  $t\bar{t} + \chi\bar{\chi}$  signals are generated in the dilepton final state at LO accuracy in perturbative QCD using MADGRAPH5\_AMC@NLO v2.2.2 [76] with up to one additional jet, however as described in [77], the cross section is computed at NLO with no additional partons in the Born process, and the samples are normalized to the NLO values listed in Table 4.1. The MLM parton-jet matching prescription [78] is used to match jets

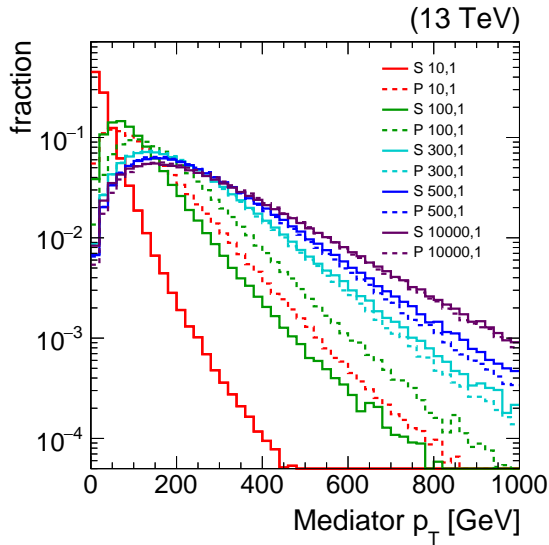


**Figure 4.2.:** Generator level  $p_T$  distributions for S (solid lines) and PS (dashed lines) mediators, with  $m_\chi = 1$  GeV. The label “S 10, 1” can be understood as a model with S mediator mass  $m_\phi = 10$  GeV, and DM mass  $m_\chi = 1$  GeV.  $p_T$  distributions with the same color have the same mediator mass.

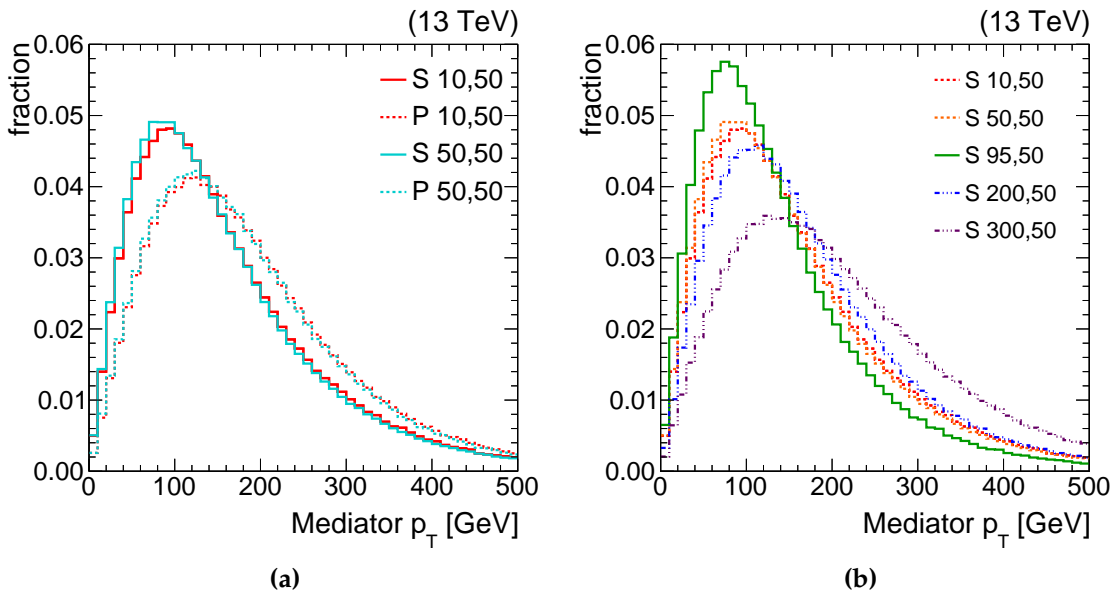


**Figure 4.3.:** (a) Generator level  $p_T$  distributions for off-shell production, with solid (dashed) lines for S (PS) mediated models, and  $m_\chi = 50$  GeV. The label “S 10, 50” can be understood as a model with S  $m_\phi = 10$  GeV and  $m_\chi = 50$  GeV. (b) Near the on-shell/off-shell threshold (green solid line), the kinematics have contributions from on-shell and off-shell production.

$m_\phi$ [GeV]	$m_\chi$ [GeV]	Scalar (pb)	Pseudoscalar (pb)
10	1	26.09	0.6218
20	1	13.96	0.5653
50	1	3.923	0.4314
100	1	0.8891	0.2716
200	1	0.1229	0.1189
300	1	0.04079	0.05946
500	1	0.007796	0.008171

**Table 4.1.:** A summary of the signal model samples and the corresponding NLO cross sections used in this work for S and PS mediator masses with  $m_\chi = 1$  GeV.

from the matrix element to the parton shower. The spin correlations in the decays of top quarks are preserved through the use of MADSPIN. The partial width formulae given in [79] are used to calculate the minimum decay widths for the mediators. The calculation assumes that the mediator couples only to SM quarks and the fermion DM particle ( $\chi$ ), and decays exclusively to a DM pair.

A striking feature in Table 4.1, is that the  $t\bar{t} + \chi\bar{\chi}$  production cross section for mediator mass of  $\mathcal{O}(10)$  GeV via a S mediator is approximately an order of magnitude larger with respect to the rate obtained via a PS mediator of equivalent mass. This disparity is a result of the fact that for  $m_\chi < m_\phi \ll m_{\text{top}}$  (where  $m_{\text{top}}$  is the top quark mass), the fragmentation process  $t \rightarrow t\phi$  dominates the cross section. In the case of the S mediator, this fragmentation function contains soft singularities with the form  $(1 - x)/x$ , where  $x$  is the momentum fraction carried by the mediator [77]. This causes an enhancement in the production cross section for the S mediated processes, while the absence of this term in the PS mediated cases explains the order of magnitude difference in the total rates between the two. As  $m_\phi \rightarrow 2m_{\text{top}}$ , the gap in production cross section between S and PS mediator processes closes, where the PS cross section becomes more dominant. At the on/off-shell threshold, the S cross section is suppressed since the production

can only proceed via a  $P$ -wave meaning it is suppressed by two additional powers of  $\beta = \sqrt{1 - 4m_{\text{top}}^2/s}$  [80], while the PS mediated production of DM proceeds via an  $S$ -wave and is not kinematically suppressed as a result.

## 4.2. Signal region event selection

The objects defined in Section 3.2-3.4 are all employed to target the events consistent with  $t\bar{t} + p_T^{\text{miss}}$  where both tops have leptonically decaying W bosons. The selection is as follows,

- Two “Tight” leptons with opposite charge ( $ee$  or  $e\mu$  or  $\mu\mu$ ) with  $p_T > 25 \text{ GeV}$  for the leading lepton and  $p_T > 15 \text{ GeV}$  for the trailing lepton,
- No additional leptons with  $p_T > 10 \text{ GeV}$  and that pass the criteria of the “Loose” muon working point or “Veto” electron working point,
- Two or more jets where at least one jet is a b-tagged jet,
- $M_{\ell\ell} > 20 \text{ GeV}$ ,
- $|M_{\ell\ell} - M_Z| > 15 \text{ GeV}$  for  $ee$  and  $\mu\mu$  events,
- $p_T^{\text{miss}} > 50 \text{ GeV}$ ,

Dilepton candidate events with an invariant mass  $M_{\ell\ell} < 20 \text{ GeV}$  are removed in order to suppress any backgrounds from low-mass Drell-Yan (DY) processes such as  $J/\psi$  and  $Y$  meson resonances in the  $1 \text{ GeV} < M_{\ell\ell} < 10 \text{ GeV}$  range and  $\rho$ ,  $\omega$ , and  $\phi$  meson resonances at  $M_{\ell\ell} \approx 1 \text{ GeV}$  where the modeling of the production rates of these particles is quite poor. The requirement for events in the same flavor (SF) channel, which consists of  $ee$  and  $\mu\mu$  events, to have an invariant mass  $\pm 15 \text{ GeV}$  away from the Z boson pole mass is also used to reject resonant  $Z(\ell\ell)$  background events. The

moderate requirement of  $p_T^{\text{miss}} > 50 \text{ GeV}$  aims to further suppress contamination from DY events in the same flavor channel. The jet and lepton multiplicity requirements are compatible with the expected visible particles in the final state.

#### 4.2.1. The $M_{\ell 2}^{\ell\ell}$ variable

The selection requirements are compatible with criteria which might be employed to target SM dileptonic  $t\bar{t}$ , denoted throughout by  $t\bar{t}(2\ell)$ . The moderate  $p_T^{\text{miss}}$  requirement is efficient in reducing this dominant background to a small extent, but by examining the global  $t\bar{t}$  event topology, observables with strong discrimination can be constructed.

The production of SM  $t\bar{t}$  at the LHC, and its subsequent decay route to the dilepton decay channel proceeds as,

$$pp \rightarrow t\bar{t} \rightarrow W^+ b + W^- \bar{b} \rightarrow \ell^+ \nu b + \ell^- \bar{\nu} \bar{b}, \quad (4.1)$$

In principle, decay products from the right-most side of the reaction can be used to reconstruct their mother particles from the previous step in the chain. Namely, given the  $p_T$  of the lepton and neutrino, it is possible to use energy-momentum conservation in the transverse plane to reconstruct the transverse mass ( $M_T$ ) of the W boson, such that,

$$M_T = \sqrt{M_\ell^2 + M_\nu^2 + 2(E_T^\ell E_T^\nu - \vec{p}_T^\ell \cdot \vec{p}_T^\nu)}, \quad (4.2)$$

where  $M_\ell$  and  $M_\nu$  are the masses of the lepton and neutrino, respectively, and  $\vec{p}_T^\ell$  and  $\vec{p}_T^\nu$  are their transverse momenta.  $E_T^\ell$  and  $E_T^\nu$  denote their energies in the transverse plane. In this case, the maximum value of  $M_T$  is bounded from above by the W boson pole mass,  $M_W$ .

In the case of  $t\bar{t}(2\ell)$ , since two leptonically decaying W bosons are expected, the upper bounding by  $M_W$  can be expanded to,

$$M_W^2 \geq \max \left\{ M_T^2 \left( \vec{p}_T^{\ell^+}, \vec{p}_T^\nu \right), M_T^2 \left( \vec{p}_T^{\ell^-}, \vec{p}_T^{\bar{\nu}} \right) \right\}, \quad (4.3)$$

assuming that the assignments of the neutrinos to their corresponding lepton partners is correct. This latter point however, is non-trivial to achieve in the experimental sense since, the neutrinos leave their signature in the detector collectively as  $p_T^{\text{miss}}$ , a singular observable. Thus, without the a priori knowledge of the correct lepton-neutrino pairings, a scan over all possible partitions of the  $p_T^{\text{miss}}$  into two sources can be performed leading to,

$$M_W \geq \min_{\vec{p}_{T1}^{\text{miss}} + \vec{p}_{T2}^{\text{miss}} = \vec{p}_T^{\text{miss}}} \left( \max \left\{ M_T \left( \vec{p}_T^{\ell_1}, \vec{p}_{T1}^{\text{miss}} \right), M_T \left( \vec{p}_T^{\ell_2}, \vec{p}_{T2}^{\text{miss}} \right) \right\} \right). \quad (4.4)$$

The quantity on the right-hand side of equation (4.4) is defined as the stransverse mass [81],

$$M_{T2}^{\ell\ell} = \min_{\vec{p}_{T1}^{\text{miss}} + \vec{p}_{T2}^{\text{miss}} = \vec{p}_T^{\text{miss}}} \left( \max \left[ M_T \left( \vec{p}_T^{\ell_1}, \vec{p}_{T1}^{\text{miss}} \right), M_T \left( \vec{p}_T^{\ell_2}, \vec{p}_{T2}^{\text{miss}} \right) \right] \right). \quad (4.5)$$

Clearly for the case of SM  $t\bar{t}(2\ell)$ , the  $M_{T2}^{\ell\ell}$  quantity is expected to be bounded from above by  $M_W$ . However if the decay path of the  $t\bar{t}+\chi\bar{\chi}$  signal in the dilepton decay channel is considered, where

$$pp \rightarrow t\bar{t} + \phi \rightarrow W^+ b + W^- \bar{b} + \chi\bar{\chi} \rightarrow \ell^+ \nu b + \ell^- \bar{\nu} \bar{b} + \chi\bar{\chi}, \quad (4.6)$$

it can be noted that a signal event is expected to contain *four* as opposed to two particles that leave their signature in the detector collectively as  $p_T^{\text{miss}}$ . Thus, the additional  $p_T^{\text{miss}}$  contribution from the  $\chi\bar{\chi}$  particles allows the  $M_W$  upper bound on  $M_{T2}^{\ell\ell}$  to be broken, resulting in higher  $M_{T2}^{\ell\ell}$  values for the case of the signal with respect to SM  $t\bar{t}(2\ell)$ .

A so-called kinematic endpoint at the  $W$  boson pole mass in the  $M_{T2}^{\ell\ell}$  distribution for the SM  $t\bar{t}(2\ell)$  as can be seen in Figure 4.4, while two signal models with S and PS mediators of mass  $m_\phi = 100$  GeV and  $m_\chi = 1$  GeV contribute well beyond  $M_W$ . With this in mind, two signal regions are formed using the  $M_{T2}^{\ell\ell}$  variable, where events with  $M_{T2}^{\ell\ell} > 110$  GeV comprise the high signal purity region, since the SM  $t\bar{t}(2\ell)$  background is not expected to be dominant in the region above  $M_W$ . Conversely, the low signal purity category is formed by the remaining events, for which  $M_{T2}^{\ell\ell} < 110$  GeV, where the SM  $t\bar{t}(2\ell)$  background prevails over the expected signal contribution.

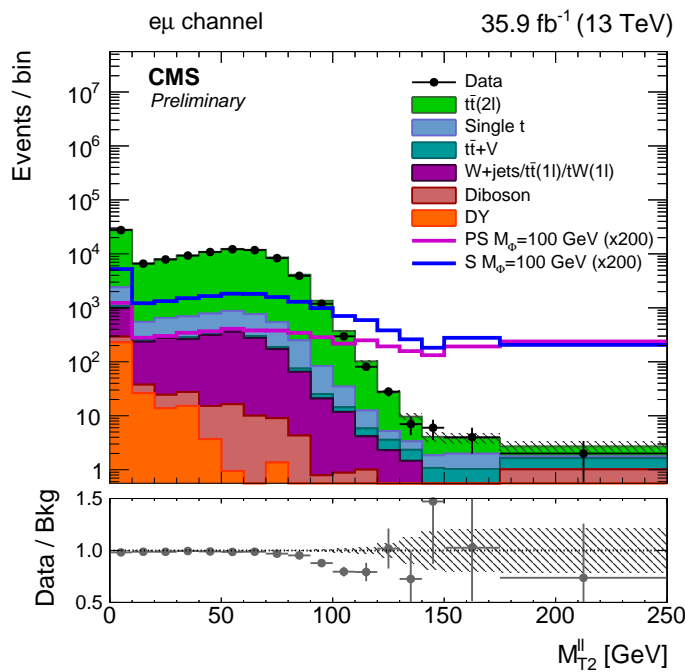


**Figure 4.4:** The  $M_{T2}^{ll}$  distribution in data and simulation for events passing selection requirements for the  $e\mu$  channel. The distributions of two example signal models with S and PS mediators of  $m_\phi = 100$  GeV, and with  $m_\chi = 1$  GeV are also presented and scaled up by a factor of 200. The last bin in the distribution includes overflow, and the uncertainties are statistical only.



# Chapter 5.

## Background processes

Two classes of background processes are present in this search: reducible and irreducible. For the former category, a particle in the background process may “fake” the signature of a particle that is expected in the signal process. On the contrary, in the case of the latter category, the final state topology of the background process yields the same visible particles as a potential signal process. A key feature of reducible backgrounds is the ability to suppress such processes by employing the selection cuts as described in Section 4.2. Furthermore, some of the reducible background contributions are estimated using data-driven techniques. In large part, however, the dominant backgrounds in the search are estimated from simulations.

Section 5.1–Section 5.4 describe the relevant SM backgrounds in the search for  $t\bar{t}(2\ell) + \chi\bar{\chi}$ . The production cross sections at  $\sqrt{s} = 13$  TeV for these backgrounds are shown in Figure 5.1, giving a sense of the relative importance of the processes. The phase space targeted by the selection requirements as described in Section 4.2 also affects the relative hierarchy of the backgrounds. However, it remains true that processes with larger cross sections, such as  $t\bar{t}$  with a cross section of 831.76 pb and Drell-Yan with cross sections of 18610 pb and 5765.4 pb for  $10 < M_{DY} < 50$  GeV and

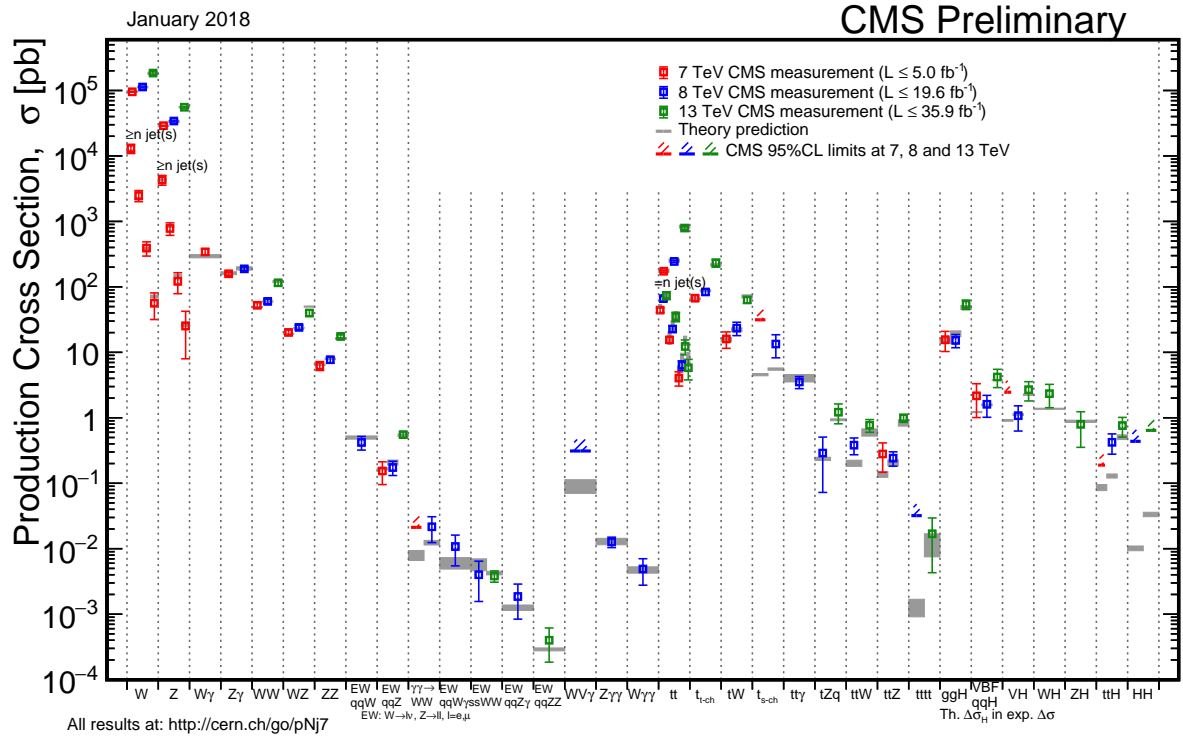


**Figure 5.1.:** Summary of the cross section measurements of SM processes as of January 2018 with data collected by the CMS experiment at  $\sqrt{s} = 7, 8$ , and  $13 \text{ TeV}$ .

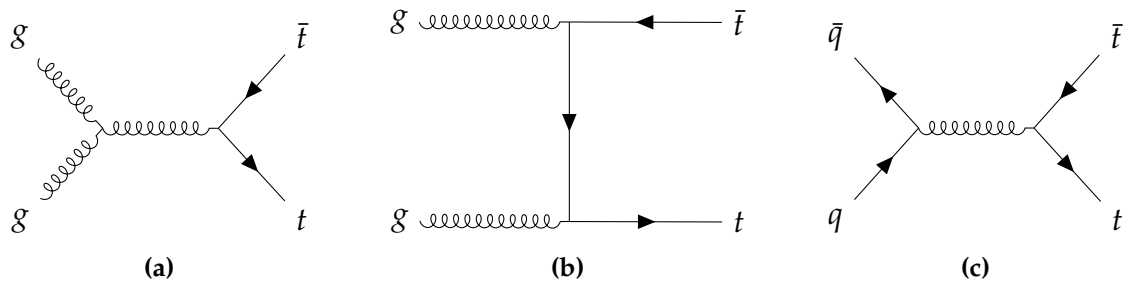


**Figure 5.2.:** Leading order  $t\bar{t}$  production diagrams probed at the LHC via (a), (b) gluon fusion, and (c) quark-antiquark annihilation.

$M_{DY} > 50 \text{ GeV}$  respectively, are dominant in the highest sensitivity regions of this search.

## 5.1. $t\bar{t}(2\ell)$

SM  $t\bar{t}(2\ell)$  is the dominant background contribution and is irreducible, owing to the similarity of the final state topology with the signal processes topology. At the LHC, approximately 90% of  $t\bar{t}$  events are produced via gluon fusion as shown in Figure 5.2a and Figure 5.2b, in contrast to the Tevatron at Fermilab, where quark-antiquark annihilation shown in Figure 5.2c constituted roughly 85-90% of the relative  $t\bar{t}$  production.

The theoretical uncertainties incurred at leading order (LO) in perturbative QCD are quite large for  $t\bar{t}$  production. In addition to the LO simulation, the  $t\bar{t}$  process decaying to the dilepton final state is simulated at next-to-leading order (NLO) using the POWHEG v2 [82, 83] generator, with the top quark mass assumed to be  $m_{top} = 172.5$  GeV. These events are then interfaced to Pythia v8.2 [84] for parton fragmentation, hadronization, and to simulate the underlying event. As pertains to all simulated samples subsequently described, once the  $t\bar{t}(2\ell)$  events are showered, the detector response is simulated using the GEANT4 program [85]. Finally, the  $t\bar{t}(2\ell)$  events are normalized to the theoretical cross section calculated at next-to-next-to-leading order (NNLO) in perturbative QCD, which also includes soft-gluon resummation calculations at next-to-next-to-leading-log-order (NNLL) [86–90]. The cross section folds in the branching fraction of  $t\bar{t}$  to the dilepton final state, which is 10.5%. The cross section value employed in this work is  $\sigma_{t\bar{t}(2\ell)} = 87.31$  pb.

As mentioned in Section 4.2.1, the  $t\bar{t}(2\ell)$  background should be suppressed below the kinematic endpoint,  $M_W$ , in the  $M_{T2}^{\ell\ell}$  distribution. This would only be possible in ideal measurement conditions, however as a cause of detector and energy resolution effects, the mismeasurement of the objects in  $t\bar{t}(2\ell)$  background events can contribute to values of  $M_{T2}^{\ell\ell} > M_W$ .

### 5.1.1. Top $p_T$ re-weighting

The generated top quark  $p_T$  in  $t\bar{t}$  simulation appears to disagree with the distribution observed in data. The discrepancy arises due to the harder  $p_T$  in the simulation as compared to data, thus a correction based on a comparison of the top  $p_T$  spectrum between data and the predicted distribution at NLO accuracy from POWHEG v2 interfaced with Pythia v8.2 is used as, developed in [91]. For each top in a  $t\bar{t}$  MC simulation event, a scale factor is computed according to,

$$\text{SF}(p_T) = e^{0.0615 - 0.0005 \cdot p_T}, \quad (5.1)$$

where the exponential function describes the fit to the ratio of data to POWHEG +Pythia simulation for dileptonic and semileptonic  $t\bar{t}$  decays. The  $p_T$  in equation (5.1) is taken at the matrix element level. Subsequently, a weight is applied on an event-by-event basis where the weight is given by the geometric mean of the scale factors,

$$w = \sqrt{\text{SF}(p_{Tt}) \cdot \text{SF}(p_{T\bar{t}})}. \quad (5.2)$$

The effect of the re-weighting is seen in Figure 5.3 for SM  $t\bar{t}(2\ell)$  simulation events passing the selection requirements in Section 4.2 with (a)  $M_{T2}^{\ell\ell} < 110$  GeV and (b)  $M_{T2}^{\ell\ell} > 110$  GeV. It can be seen that the correction tends to grow with increasing  $p_T^{\text{miss}}$ , which is expected since this observable is correlated with the top  $p_T$ , and the higher the  $p_T$  value, the farther from unitary (in the decreasing direction) the SF in equation (5.1) becomes.

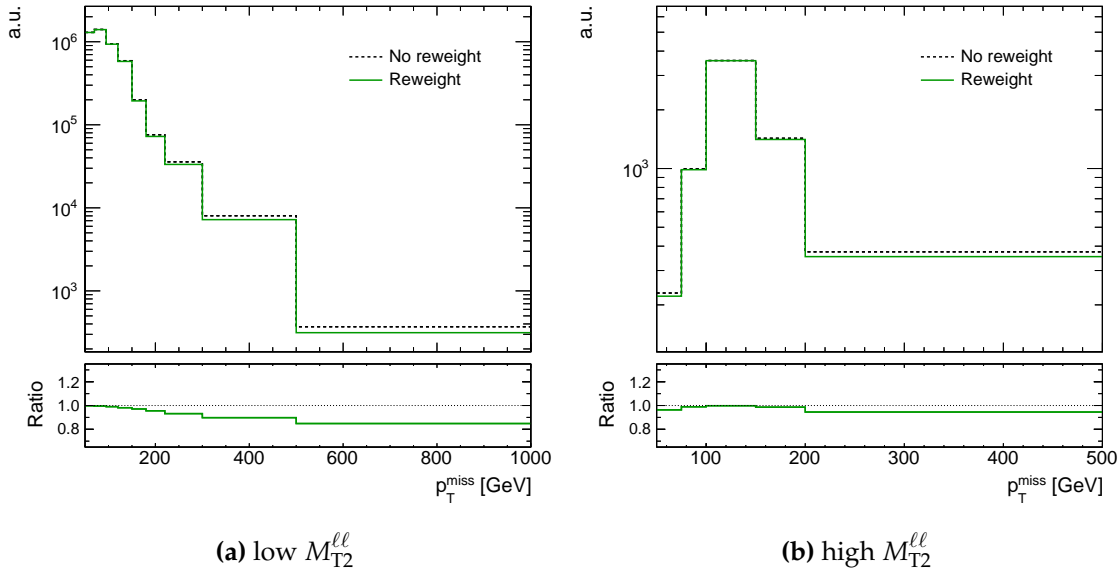


**Figure 5.3.:** Effect of the top  $p_T$  re-weighting on the expected  $t\bar{t}(2\ell)$  background  $p_T^{\text{miss}}$  shape for events passing selection defined in Section 4.2 and having (a)  $M_{T2}^{\ell\ell} < 110 \text{ GeV}$  and (b)  $M_{T2}^{\ell\ell} > 110 \text{ GeV}$ .

## 5.2. $t\bar{t} + V$ , diboson, and single top processes

Among the more rare processes considered as backgrounds to this search are processes wherein a top quark pair is produced in association with a boson, denoted as  $t\bar{t} + V$  (where  $V = \gamma, Z, W$ ). In particular, the  $t\bar{t}+Z$  process, as shown in Figure 5.4a, exhibits the same final state as the signal, so this process falls under the class of irreducible backgrounds. Although the production cross sections for  $t\bar{t} + V$  processes are orders of magnitude smaller than the  $t\bar{t}$  production cross section, this background is significant in the high  $M_{T2}^{\ell\ell}$  category. The moderate  $p_T^{\text{miss}}$  requirement is inefficient in  $t\bar{t} + V$  background reduction, since large values of  $p_T^{\text{miss}}$  are expected from the additional energetic neutrinos from the  $Z$  boson. In addition, the  $M_{T2}^{\ell\ell}$  calculation can be biased to high values for the  $t\bar{t} + Z$  process, since the minimization over all the two-way partitions of the  $p_T^{\text{miss}}$  accounts for the additional neutrinos from the  $Z$  boson decay, as well as from the top quarks.

The diboson background processes encompass WW, ZZ, and WZ production where all possible final states (i.e. decays to  $q\bar{q}$ ,  $\ell\nu$ ,  $\ell\ell$ , and  $\nu_\ell\bar{\nu}_\ell$ ) are considered for the relevant boson. Owing in part to the largest relative production cross section, the WW process is the dominant diboson process. In particular, the signal region requirements target the final state where both W bosons decay to lepton-neutrino pairs.

The single top background is also expected to contribute sub-dominantly in the signal region. The lepton multiplicity requirement serves to suppress the contributions from s- and t-channel production (i.e. processes whose amplitudes go as  $\mathcal{M} \sim 1/s$  and  $\mathcal{M} \sim 1/t$ , where  $s$  and  $t$  correspond to the Mandelstam variables), as seen in Figure 5.5a and Figure 5.5b, since only one prompt lepton is expected. Thus, the dilepton final state tW associated production diagram, shown in Figure 5.5c, contributes the most significantly to the single top background, where more than one lepton may be expected depending on the W boson decay mode.

Similarly to the  $t\bar{t}(2\ell)$  process, the  $t\bar{t} + V$ , diboson, and single top processes are simulated at NLO. The  $t\bar{t} + V$  processes are generated using MADGRAPH5\_AMC@NLO v2.2.2. For single top, the s- and t-channel processes are simulated using POWHEG v2 and interfaced with MADSPIN which decays the top and preserves the spin correlation and any finite width effects in narrow resonance decays. The tW channel, on the other hand, is generated using POWHEG v1 at NLO accuracy and normalized to the approximate NNLO cross section. The diboson samples are generated at NLO using either MADGRAPH5\_AMC@NLO v2.2.2 or POWHEG v2.

### 5.3. Drell-Yan

From the diagrams in Figure 5.6, it can be noted that the DY pair-production process falls under the class of reducible backgrounds, since many of the selection criteria

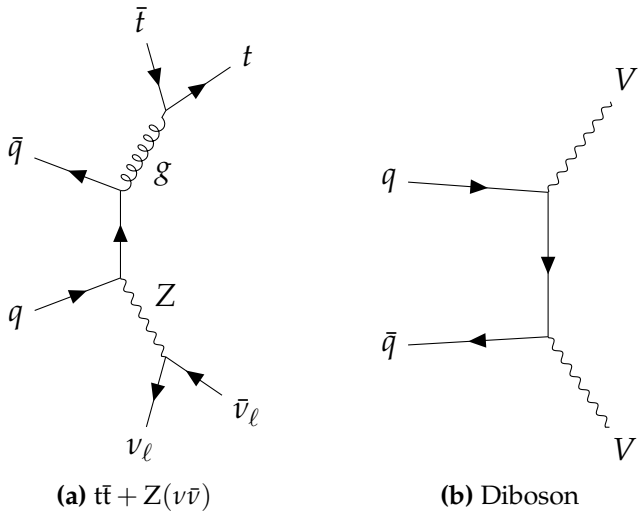


**Figure 5.4.:** Examples of the (a)  $t\bar{t} + Z(\nu\bar{\nu})$  process, and (b) diboson production at LO.

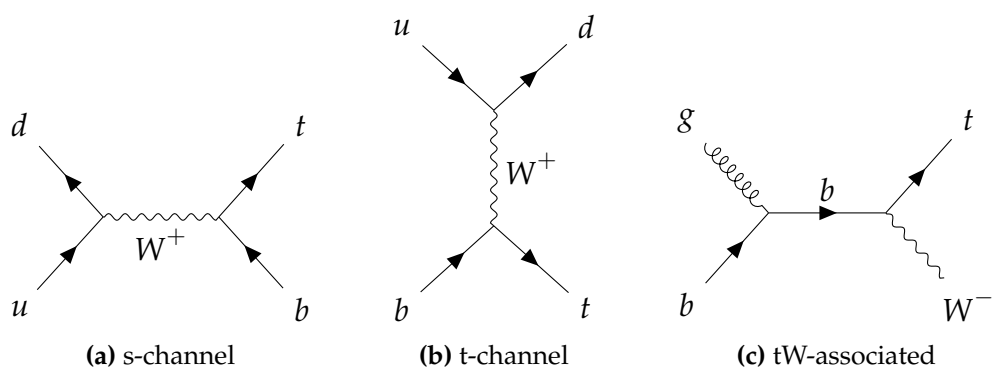


**Figure 5.5.:** Single top quark production via (a) s-channel, (b) t-channel, and (c) in association with a  $W$  boson.

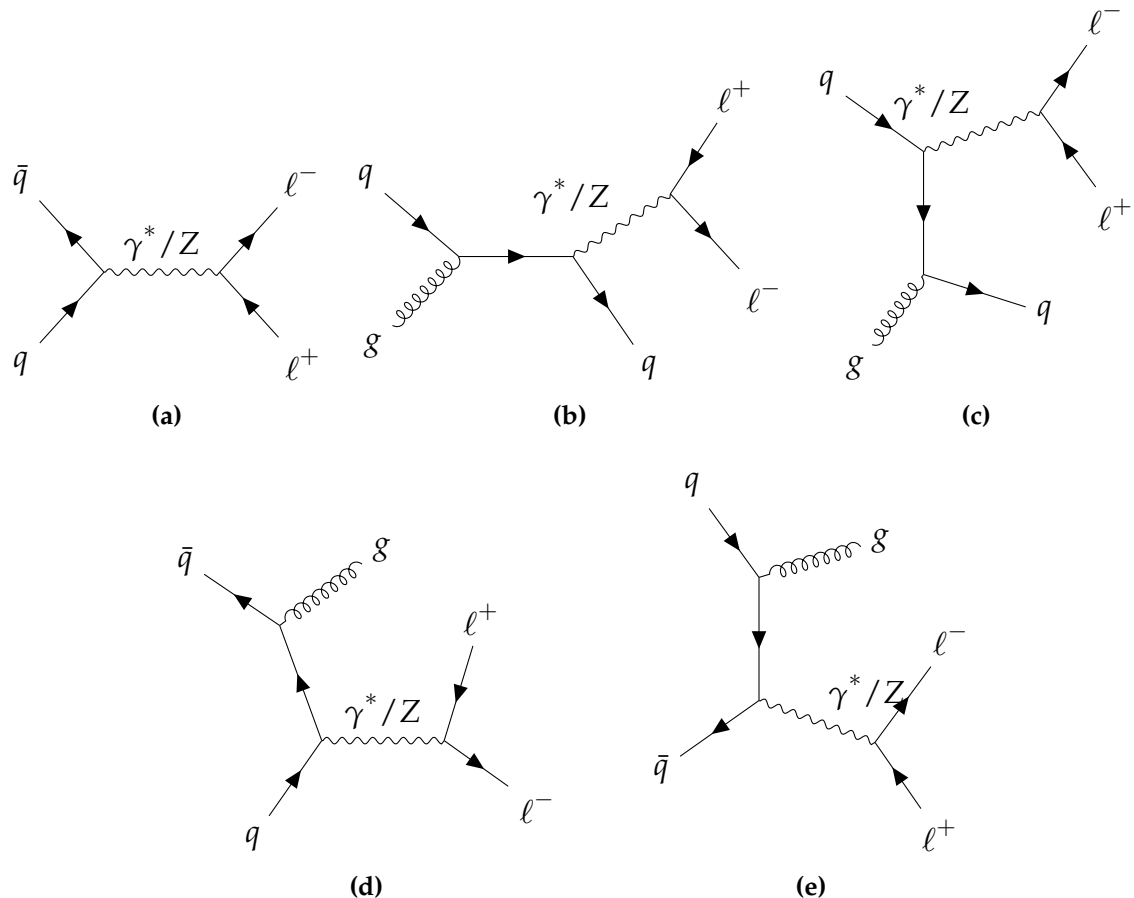


**Figure 5.6.:** The DY lepton pair-production process mediated by a virtual photon ( $\gamma^*$ ) or Z boson at (a)  $\mathcal{O}(\alpha)$  and (b),(c),(d),(e)  $\mathcal{O}(\alpha\alpha_s)$ .

act to suppress processes where the selected SF leptons are produced at the same vertex, such as from the exchange of a real Z boson or a virtual photon ( $\gamma^*$ ). For instance, near the Z boson pole mass, the resonant dilepton production is greatly enhanced relative to  $\gamma^*$  exchange and consequently, the requirement for the mass of the selected SF lepton pair to be outside a  $\pm 15$  GeV window relative to the Z boson mass, removes a large contribution of dilepton decays stemming from real Z bosons. In addition, the requirement for the event to contain at least two jets, with at least one b-tagged jet acts to eliminate contributions from Figure 5.6a, where the  $q\bar{q}$  annihilation to a SF lepton pair proceeds at LO in  $\alpha$ . The DY process is simulated at NLO using MADGRAPH5\_AMC@NLO v2.3.3, and thus includes contributions from higher order processes as shown in Figure 5.6b-Figure 5.6e, where at least one jet is expected from the fragmentation and hadronization of particles emitted in initial state radiation.

After the contribution from SM  $t\bar{t}(2\ell)$ , the DY process is the next most dominant background to the signal search presented in this work, therefore the precise estimation of its relative normalization and expected  $p_T^{\text{miss}}$  spectra is imperative. In view of this requirement, a data-driven process is used to estimate the normalization of this background, while the simulation is used to derive the DY  $p_T^{\text{miss}}$  templates. Furthermore, DY is not a process from which genuine sources of  $p_T^{\text{miss}}$  such as neutrinos are expected, thus it is referred to as having “fake”  $p_T^{\text{miss}}$  which arises from the mismeasurement of jet/lepton energies. The instrumental detector effects that influence this final state topology are non-trivial to simulate, as is apparent from the discrepancy between data and simulation at high  $p_T^{\text{miss}}$  values in Figure 5.7, where  $Z \rightarrow \ell\ell$  events are selected. Therefore, it is more appropriate to use calibrated samples from data to arrive at these estimates.

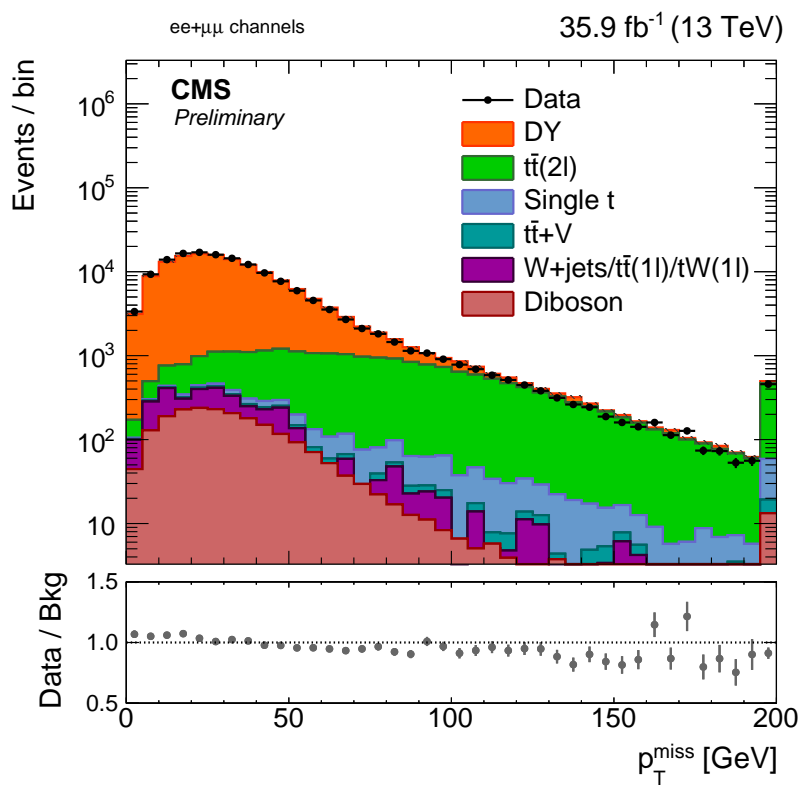


**Figure 5.7.:** The  $p_T^{\text{miss}}$  distribution in data and simulation for SF events, where the dilepton mass is required to be *inside* the  $\pm 15$  GeV window relative to the Z boson mass. In addition the events must contain at least two jets, and no b-tagged jets.

### 5.3.1. The $R_{\text{in/out}}$ method

The data-driven method used to predict the DY normalization,  $N_{DY}$ , is referred to throughout as the  $R_{\text{in/out}}$  method. Essentially, the method aims to estimate the contribution of DY in the signal region, by extrapolating from the observed data yield inside the Z mass window,  $N_{in}$ , according to:

$$N_{DY} = N_{in} \frac{R_{\text{MC}}^{0b}}{R_{\text{MC}}^{1b} \cdot R_{\text{data}}^{0b}}, \quad (5.3)$$

where each quantity  $R$  in equation (5.3) is defined as the ratio of DY yields **inside** to **outside** the Z mass window,

$$R_{\text{in/out}} = \frac{N(|M_{\ell\ell} - M_Z| < 15 \text{ GeV})}{N(|M_{\ell\ell} - M_Z| > 15 \text{ GeV and } M_{\ell\ell} > 20 \text{ GeV})}. \quad (5.4)$$

Hence, the events rejected by the Z boson mass veto are used to estimate the residual contributions from  $\text{DY} \rightarrow e^+e^-$  and  $\mu^+\mu^-$  in the remaining selected sample. The yields are computed with all other selection requirements applied. Ideally, the  $R_{\text{in/out}}$  in a region where the number of b-tagged jets is required to be zero would be equal to the  $R_{\text{in/out}}$  in a region where at least one b-tagged jet is required, such that  $R_{\text{in/out}}^{0b} = R_{\text{in/out}}^{1b}$ . This assumption, however, is invalid since the numerator and denominator in equation (5.4) differ significantly when measured in DY simulation with a looser set of selection cuts, such as the removal of the  $p_T^{\text{miss}}$  requirement or a looser jet multiplicity requirement. A weaker assumption is made instead, which is as follows:

$$\frac{\left(R_{\text{in/out}}^{1b}\right)_{\text{data}}}{\left(R_{\text{in/out}}^{1b}\right)_{\text{MC}}} = \frac{\left(R_{\text{in/out}}^{0b}\right)_{\text{data}}}{\left(R_{\text{in/out}}^{0b}\right)_{\text{MC}}}. \quad (5.5)$$

equation (??) posits that the ratio of the measured  $R_{\text{in/out}}^{0b}$  between data and MC should be equivalent to the ratio of the measured  $R_{\text{in/out}}^{1b}$  between data and MC. Then the estimate for the DY normalization in the signal region as defined in equation (5.3) is expanded into,

$$\left(N_{\text{out}}^{1b}\right)_{\text{data}} = \frac{\left(N_{\text{in}}^{1b}\right)_{\text{data}}}{\left(R_{\text{in/out}}^{1b}\right)_{\text{data}}} = \frac{\left(N_{\text{in}}^{1b}\right)_{\text{data}}}{\left(R_{\text{in/out}}^{1b}\right)_{\text{MC}}} \cdot \frac{\left(R_{\text{in/out}}^{0b}\right)_{\text{MC}}}{\left(R_{\text{in/out}}^{0b}\right)_{\text{data}}} \quad (5.6)$$

Consequently, every quantity on the right-hand side of equation (5.6) can be determined in the data or simulation as applicable. It should be noted however, that non-DY contributions are present in the measurements made in the data, and hence must be subtracted off from the yields both inside and outside the Z mass window in the zero b-tag and the one-or-more b-tag regions (i.e. all the quantities  $N_{\text{in}}^{0b}$ ,  $N_{\text{out}}^{0b}$ ,  $N_{\text{in}}^{1b}$ , and  $N_{\text{out}}^{1b}$ ). The non-DY contributions in the  $\{0b, 1b\} \otimes \{\text{in, out}\}$  regions, such as  $t\bar{t}(2\ell)$ , are estimated from data using opposite flavor ( $e^\pm, \mu^\mp$ ) events, that are denoted by  $N_{\text{in}}^{e\mu}$  and  $N_{\text{out}}^{e\mu}$ . Thus, the number of events in data in each of the aforementioned regions, after the subtraction of non-DY backgrounds is,

$$N = N^{\ell\ell} - 0.5 \cdot k_{\ell\ell} \cdot N^{e\mu}, \quad (5.7)$$

where the 0.5 factor accounts for combinatorics, and  $k_{\ell\ell}$  is a correction factor applied to account for the differences in reconstruction efficiencies between electrons and muons. The correction factor is derived from an inclusive selection targeting  $Z \rightarrow \ell\ell$ , and is defined as,

$$k_{ee} = \sqrt{\frac{N^{ee}}{N^{\mu\mu}}}, \quad k_{\mu\mu} = \sqrt{\frac{N^{\mu\mu}}{N^{ee}}} \quad (5.8)$$

The value for  $k_{ee}(k_{\mu\mu})$  measured in data is 0.64 (1.55).

In order to capture any  $p_T^{\text{miss}}$  dependence of the DY normalization, the various  $R_{\text{in}/\text{out}}$  quantities are computed in four bins of  $p_T^{\text{miss}}$ , shown in the fifth column of Table 5.1-Table 5.4, since the relative contribution of DY is expected to drop off at higher  $p_T^{\text{miss}}$  values and incur larger statistical uncertainties in the simulation. The “on” Z peak (i.e.  $|M_{\ell\ell} - M_Z| < 15 \text{ GeV}$ ) yields for a 0 b-tag selection listed in the second column of Table 5.1 and Table 5.2 can be seen in Figure 5.8 and Figure 5.9 for the  $ee$  and  $\mu\mu$  channels, respectively. The predicted DY normalization in the signal region in each  $p_T^{\text{miss}}$  bin is listed in Table 5.5 and Table ?? under the column heading  $(N_{\text{out}}^{1b})_{\text{data}}$ . The simulation yields, under the column heading  $(N_{\text{out}}^{1b})_{\text{MC}}$ , are scaled by the factors in the last column of Table 5.5 and Table ??, and shown in Figure 5.10 in red and blue markers, respectively for the  $ee$  and  $\mu\mu$  channel. The dashed line in Figure 5.10 represents the inclusively calculated scale factors, which are not used in the analysis but are simply used as a cross-check to ensure the  $p_T^{\text{miss}}$  binned scale factors do not drastically differ from the inclusive. The larger scale factors for the  $ee$  channel are attributed to a broader DY line shape in data compared to simulation, while in the  $\mu\mu$  channel the line shapes in data and simulation are more similar.

**Table 5.1.:** DY yields and  $R_{\text{in/out}}$  values in the  $ee$  channel, for 0 b-tag selection

		$ M_{\ell\ell} - M_Z  < 15 \text{ GeV}$	$ M_{\ell\ell} - M_Z  > 15 \text{ GeV}$	$R_{\text{in/out}}^{0b}$
$50 \text{ GeV} < p_T^{\text{miss}} < 75 \text{ GeV}$	data	$35602.72 \pm 191.00$	$4912.88 \pm 92.65$	$7.25 \pm 0.14$
	MC	$38417.99 \pm 233.36$	$4932.28 \pm 155.12$	$7.79 \pm 0.25$
$75 \text{ GeV} < p_T^{\text{miss}} < 100 \text{ GeV}$	data	$4503.12 \pm 72.21$	$875.04 \pm 61.05$	$5.15 \pm 0.37$
	MC	$5651.58 \pm 86.47$	$865.83 \pm 58.83$	$6.53 \pm 0.45$
$100 \text{ GeV} < p_T^{\text{miss}} < 150 \text{ GeV}$	data	$714.20 \pm 37.79$	$415.24 \pm 56.38$	$1.72 \pm 0.25$
	MC	$746.41 \pm 31.32$	$225.78 \pm 21.53$	$3.31 \pm 0.34$
$150 \text{ GeV} < p_T^{\text{miss}} < 1000 \text{ GeV}$	data	$221.68 \pm 22.05$	$415.24 \pm 56.38$	$0.53 \pm 0.090$
	MC	$55.27 \pm 7.33$	$105.28 \pm 11.92$	$0.24 \pm 0.040$

**Table 5.2.:** DY yields and  $R_{\text{in/out}}$  values in the  $\mu\mu$  channel, for 0 b-tag selection

		$ M_{\ell\ell} - M_Z  < 15 \text{ GeV}$	$ M_{\ell\ell} - M_Z  > 15 \text{ GeV}$	$R_{\text{in/out}}^{0b}$
$50 \text{ GeV} < p_T^{\text{miss}} < 75 \text{ GeV}$	data	$76878.78 \pm 282.38$	$11061.48 \pm 151.71$	$6.95 +/- 0.099$
	MC	$84516.00 \pm 353.40$	$12266.77 \pm 277.25$	$6.89 +/- 0.16$
$75 \text{ GeV} < p_T^{\text{miss}} < 100 \text{ GeV}$	data	$9757.90 \pm 109.88$	$1551.43 \pm 104.12$	$6.29 +/- 0.43$
	MC	$11972.59 \pm 130.57$	$2267.89 \pm 104.23$	$5.28 +/- 0.25$
$100 \text{ GeV} < p_T^{\text{miss}} < 150 \text{ GeV}$	data	$1468.25 \pm 61.59$	$401.18 \pm 96.96$	$3.66 +/- 0.90$
	MC	$1639.18 \pm 45.61$	$646.05 \pm 43.72$	$2.54 +/- 0.19$
$150 \text{ GeV} < p_T^{\text{miss}} < 1000 \text{ GeV}$	data	$305.85 \pm 34.16$	$396.34 \pm 97.66$	$0.77 +/- 0.20$
	MC	$86.42 \pm 10.45$	$290.42 \pm 21.26$	$0.33 +/- 0.018$

**Table 5.3.:** DY yields and  $R_{\text{in/out}}$  values in the  $ee$  channel, for  $\geq 1$  b-tag selection

		$ M_{\ell\ell} - M_Z  < 15 \text{ GeV}$	$ M_{\ell\ell} - M_Z  > 15 \text{ GeV}$	$R_{\text{in/out}}^{1b}$
$50 \text{ GeV} < p_T^{\text{miss}} < 75 \text{ GeV}$	data	$5236.16 \pm 90.60$	—	—
	MC	$5132.28 \pm 84.32$	$623.60 \pm 58.67$	$8.23 +/- 0.79$
$75 \text{ GeV} < p_T^{\text{miss}} < 100 \text{ GeV}$	data	$1038.20 \pm 58.76$	—	—
	MC	$915.35 \pm 34.19$	$137.98 \pm 22.97$	$6.63 +/- 1.13$
$100 \text{ GeV} < p_T^{\text{miss}} < 150 \text{ GeV}$	data	$289.88 \pm 51.08$	—	—
	MC	$193.95 \pm 14.94$	$27.61 \pm 8.35$	$7.02 +/- 2.19$
$150 \text{ GeV} < p_T^{\text{miss}} < 1000 \text{ GeV}$	data	$154.72 \pm 29.57$	—	—
	MC	$22.96 \pm 5.00$	$17.32 \pm 4.47$	$1.33 +/- 0.45$

**Table 5.4.:** DY yields and  $R_{\text{in/out}}$  values in the  $\mu\mu$  channel, for  $\geq 1$  b-tag selection

		$ M_{\ell\ell} - M_Z  < 15 \text{ GeV}$	$ M_{\ell\ell} - M_Z  > 15 \text{ GeV}$	$R_{\text{in/out}}^{1b}$
$50 \text{ GeV} < p_T^{\text{miss}} < 75 \text{ GeV}$	data	$10398.33 \pm 141.70$	—	—
	MC	$11001.22 \pm 126.39$	$1444.20 \pm 92.95$	$7.62 +/- 0.50$
$75 \text{ GeV} < p_T^{\text{miss}} < 100 \text{ GeV}$	data	$1689.88 \pm 97.73$	—	—
	MC	$1867.68 \pm 50.40$	$293.68 \pm 38.12$	$6.36 +/- 0.84$
$100 \text{ GeV} < p_T^{\text{miss}} < 150 \text{ GeV}$	data	$372.47 \pm 89.03$	—	—
	MC	$342.57 \pm 21.09$	$113.32 \pm 16.96$	$3.02 +/- 0.49$
$150 \text{ GeV} < p_T^{\text{miss}} < 1000 \text{ GeV}$	data	$100.40 \pm 49.44$	—	—
	MC	$30.05 \pm 6.52$	$41.85 \pm 9.82$	$0.72 +/- 0.23$

**Table 5.5.:** Signal region DY yields in MC and data (from  $R_{\text{in/out}}$  prediction) in the  $ee$  channel

	$(N_{\text{out}}^{1b})_{\text{MC}}$	$(N_{\text{out}}^{1b})_{\text{data}}$	scale factor
$50 \text{ GeV} < p_T^{\text{miss}} < 75 \text{ GeV}$	$623.60 \pm 58.67$	$683.83 \pm 13.85$	$1.10 \pm 0.11$
$75 \text{ GeV} < p_T^{\text{miss}} < 100 \text{ GeV}$	$137.98 \pm 22.97$	$198.51 \pm 13.65$	$1.44 \pm 0.26$
$100 \text{ GeV} < p_T^{\text{miss}} < 150 \text{ GeV}$	$27.61 \pm 8.35$	$79.32 \pm 17.34$	$2.87 \pm 1.07$
$150 \text{ GeV} < p_T^{\text{miss}} < 1000 \text{ GeV}$	$17.32 \pm 4.47$	$53.58 \pm 13.66$	$3.09 \pm 1.12$

**Table 5.6.:** Signal region DY yields in MC and data (from  $R_{\text{in/out}}$  prediction) in the  $\mu\mu$  channel

	$(N_{\text{out}}^{1b})_{\text{MC}}$	$(N_{\text{out}}^{1b})_{\text{data}}$	scale factor
$50 \text{ GeV} < p_T^{\text{miss}} < 75 \text{ GeV}$	$1444.20 \pm 92.95$	$1353.21 \pm 97.49$	$0.94 \pm 0.091$
$75 \text{ GeV} < p_T^{\text{miss}} < 100 \text{ GeV}$	$293.68 \pm 38.12$	$223.03 \pm 37.18$	$0.76 \pm 0.16$
$100 \text{ GeV} < p_T^{\text{miss}} < 150 \text{ GeV}$	$113.32 \pm 16.96$	$85.42 \pm 32.96$	$0.75 \pm 0.31$
$150 \text{ GeV} < p_T^{\text{miss}} < 1000 \text{ GeV}$	$41.85 \pm 9.82$	$24.53 \pm 16.18$	$0.59 \pm 0.41$

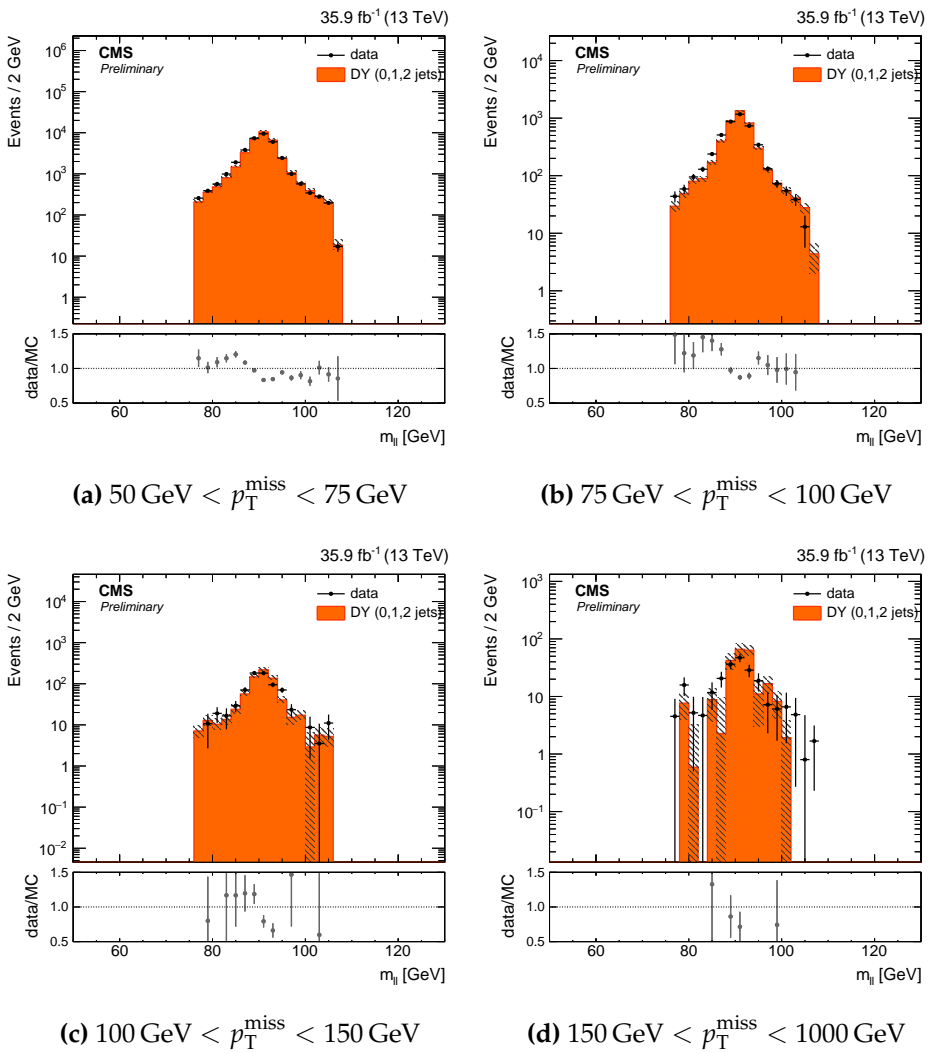


**Figure 5.8:** Z peak in data and MC after subtraction of non-DY contribution estimate from opposite-flavor data events in the  $ee$  channel for various  $p_T^{\text{miss}}$  bins.

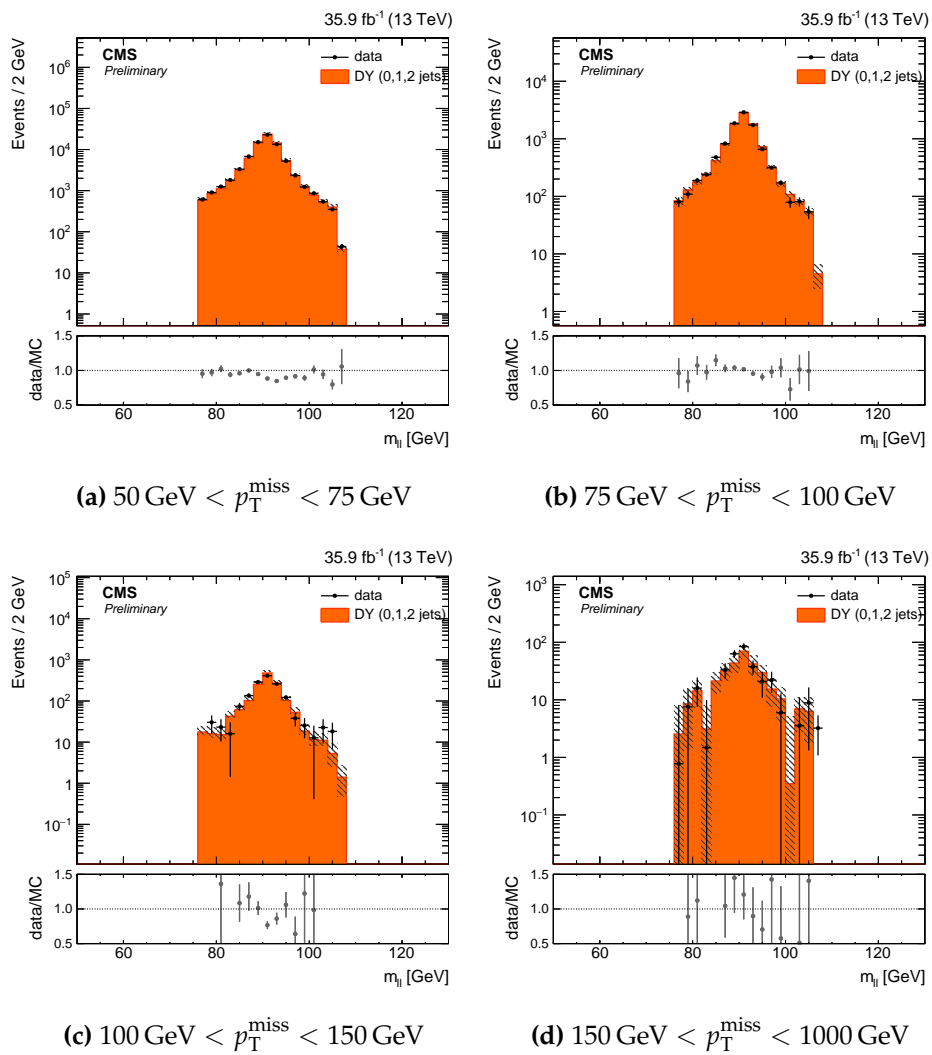


**Figure 5.9.:** Z peak in data and MC after subtraction of non-DY contribution estimate from opposite-flavor data events in the  $\mu\mu$  channel for various  $p_T^{\text{miss}}$  bins.

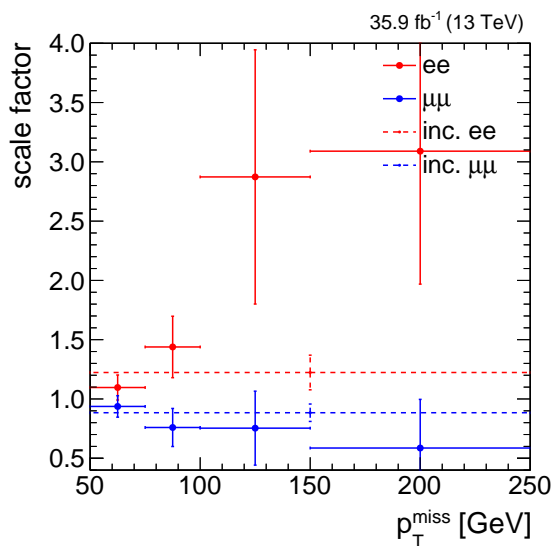


**Figure 5.10.:** Data/MC scale factors binned in  $p_T^{\text{miss}}$  applied to MC events used for the estimate of the DY normalization in the dilepton channel signal regions.

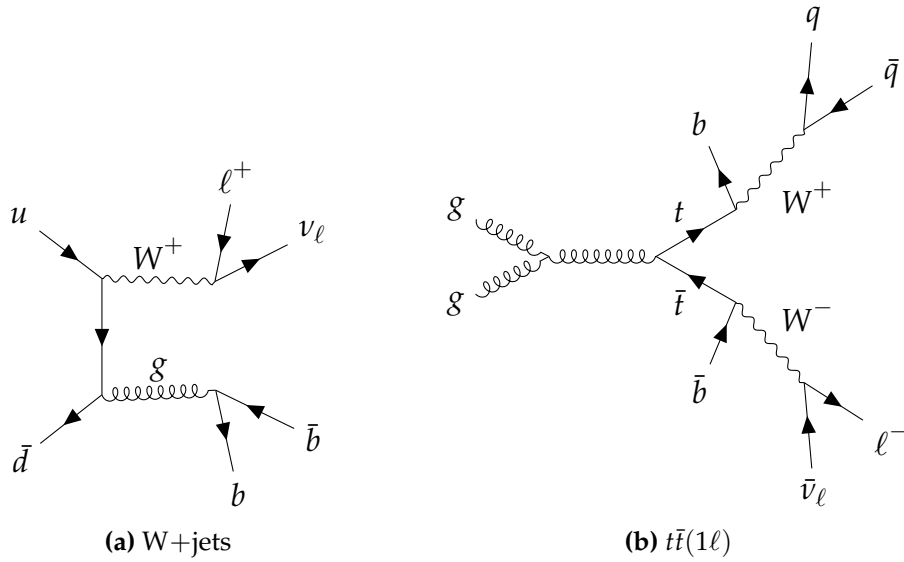


**Figure 5.11.:** Examples of (a)  $W + \text{jets}$ , and (b) semileptonic  $t\bar{t}$  that contribute to the fake lepton background.

## 5.4. Fake lepton background

Another type of reducible background, the fake (or non-prompt) lepton background, is also estimated using observed events, rather than simulation. Processes which are expected to contain only one prompt electron or muon in the final state may pass the signal region selection as described in Section 4.2 by a jet-induced faking of a second lepton. Namely, processes such as  $W + \text{jets}$ , semileptonic decays of  $t\bar{t}$  and  $tW$  associated production, and leptonic single top decays, a few of which are shown in Figure 5.11, comprise the fake lepton background processes.

The data-driven technique used to estimate the relative contribution of fake lepton backgrounds in the signal regions is based on the measurement of the fake rate. This rate is obtained from a sample in data which is enriched in QCD multijet events. Very loose working points for an electron object and muon object are defined; these are called “fake-able objects” (“FO”) and their definitions are found under the heading “FO WP” in Table 3.1 and 3.3 for muons and electrons, respectively.

The method consists of two main steps,

1. **Measurement:** The probability of a “FO” to pass “Tight” lepton selection is measured in a data sample enriched in QCD and is referred to as the fake rate (FR).
2. **Application:** The FR determined in step 1 is applied to a sample consisting of one “Tight” lepton and one “FO” that fails “Tight” selection, so as to estimate the fake lepton background in the signal region.

#### 5.4.1. Fake rate measurement

The FR does not give a direct measure for an absolute lepton fake rate; rather it is the probability for a potential fake lepton which passes loose identification criteria, to additionally pass tight identification and isolation criteria. Thus to determine the denominator of the FR, a sample enriched in jet-induced fake leptons is required and the following selection criteria must be met,

- The event must pass one of the following triggers:
  - HLT\_Ele[12,23]\_CaloIdM\_TrackIdM\_PFJet30
  - HLT\_Ele[12,23]\_CaloIdL\_TrackIdL\_IsoVL\_PFJet30
  - HLT\_Mu[8,17]\_TrkIsoVVL
- There is exactly one “FO” in the event, which matches to the trigger that was fired
- $p_T^{\text{miss}} < 40 \text{ GeV}$
- $M_T < 35 \text{ GeV}$
- The event must contain at least one jet with  $p_T > 30 \text{ GeV}$  and  $|\eta| < 4$

- The opening angle between the leading jet in the event and the “FO” must be greater than 2 ( $\Delta\phi(\text{jet}, \text{FO}) > 2$ )

The criteria above are chosen such that the W+jets contribution is suppressed by the low  $M_T$  requirement, and the QCD multi-jet contribution is enhanced in the low  $p_T^{\text{miss}}$  region. Even then, however, the level of contamination from electroweak processes (W+jets, Z+jets, t $\bar{t}$ ) in this phase space ranges from 10% at low FO  $p_T$  to 70% at high FO  $p_T$ . The contamination is significant, particularly in the muon FO sample, thus a subtraction of prompt, real leptons is performed based on expectations from simulation. The fake rate (FR) is then defined as the efficiency of a FO to pass “Tight” requirements,

$$\text{FR}_{ij} = \left[ \frac{(N_{\text{Tight}}^{\text{data}} - N_{\text{Tight}}^{\text{EWK}})}{(N_{\text{FO}}^{\text{data}} - N_{\text{FO}}^{\text{EWK}})} \right]_{i=\eta j=p_T} \quad (5.9)$$

The measured fake rates for electrons and muons are listed in Table 5.7 and Table 5.8, respectively. From their visualization in Figure 5.12 and Figure 5.13, it can be noted that the electron FR is in general lower than what is observed for muons. The difference can be understood as arising from the definition of the FO between electrons and muons, on which the FR depends strongly. A comparison of the WPs that define a FO muon compared to a “Tight” muon as listed in Table 3.1, demonstrates that the only major change in the extrapolation from FO to “Tight” are the isolation requirements, where the FO isolation cut is slightly relaxed with respect to the “Tight”. Although requirements such as pixel and outer tracker hits are not made explicit in the FO WP, as they are for the “Tight” WP, these criteria are often met regardless as a result of the PF-muon definition. On the other hand, the extrapolation from the FO WP to the “Tight” WP for electrons, shown in Table 3.3 is significant, as many of the spatial and supercluster energy-related requirements are far more stringent in going from a FO to a “Tight” electron. In general, the efficiency of the “Tight” WP for electrons

compared to muons is measured to be 40% lower, while the “FO” WPs are much closer in efficiency between electrons and muons. Hence, owing to the larger extrapolation distance between definitions of FO and “Tight” for electrons compared to muons, the muon FR is observed to be higher than that for electrons. In addition, Figure 5.12b and Figure 5.13b demonstrate that the fake rates depend more strongly on  $\eta$  than on  $p_T$ .

	$0.0 <  \eta  < 0.5$	$0.5 <  \eta  < 1.0$	$1.0 <  \eta  < 1.5$	$1.5 <  \eta  < 2.0$	$2.0 <  \eta  < 2.5$
$10 < p_T < 15$	$0.063 \pm 0.008$	$0.088 \pm 0.009$	$0.121 \pm 0.008$	$0.181 \pm 0.009$	$0.176 \pm 0.012$
$15 < p_T < 20$	$0.085 \pm 0.003$	$0.085 \pm 0.003$	$0.106 \pm 0.003$	$0.164 \pm 0.004$	$0.153 \pm 0.005$
$20 < p_T < 25$	$0.062 \pm 0.008$	$0.059 \pm 0.007$	$0.080 \pm 0.009$	$0.131 \pm 0.010$	$0.148 \pm 0.012$
$25 < p_T < 30$	$0.073 \pm 0.011$	$0.078 \pm 0.078$	$0.090 \pm 0.011$	$0.140 \pm 0.012$	$0.162 \pm 0.012$
$p_T > 30$	$0.065 \pm 0.007$	$0.091 \pm 0.008$	$0.089 \pm 0.007$	$0.169 \pm 0.008$	$0.190 \pm 0.008$

**Table 5.7.:** Electron fake rates

	$0.0 <  \eta  < 0.5$	$0.5 <  \eta  < 1.0$	$1.0 <  \eta  < 1.5$	$1.5 <  \eta  < 2.0$	$2.0 <  \eta  < 2.4$
$10 < p_T < 15$	$0.192 \pm 0.004$	$0.210 \pm 0.004$	$0.235 \pm 0.004$	$0.283 \pm 0.004$	$0.294 \pm 0.005$
$15 < p_T < 20$	$0.202 \pm 0.001$	$0.214 \pm 0.001$	$0.253 \pm 0.001$	$0.293 \pm 0.001$	$0.307 \pm 0.002$
$20 < p_T < 25$	$0.187 \pm 0.001$	$0.200 \pm 0.001$	$0.240 \pm 0.001$	$0.286 \pm 0.001$	$0.307 \pm 0.002$
$25 < p_T < 30$	$0.177 \pm 0.002$	$0.196 \pm 0.002$	$0.239 \pm 0.002$	$0.279 \pm 0.002$	$0.310 \pm 0.003$
$p_T > 30$	$0.172 \pm 0.002$	$0.200 \pm 0.002$	$0.233 \pm 0.002$	$0.279 \pm 0.002$	$0.311 \pm 0.003$

**Table 5.8.:** Muon fake rates

#### 5.4.2. Fake rate application

To estimate the fake lepton background yield in the signal region requires an application sample which is closely related to the SR. Thus, the sample selection is entirely compatible with the SR selection as detailed in Section 4.2, however instead of requiring two “Tight” oppositely charged leptons, one “Tight” lepton and one “FO” that

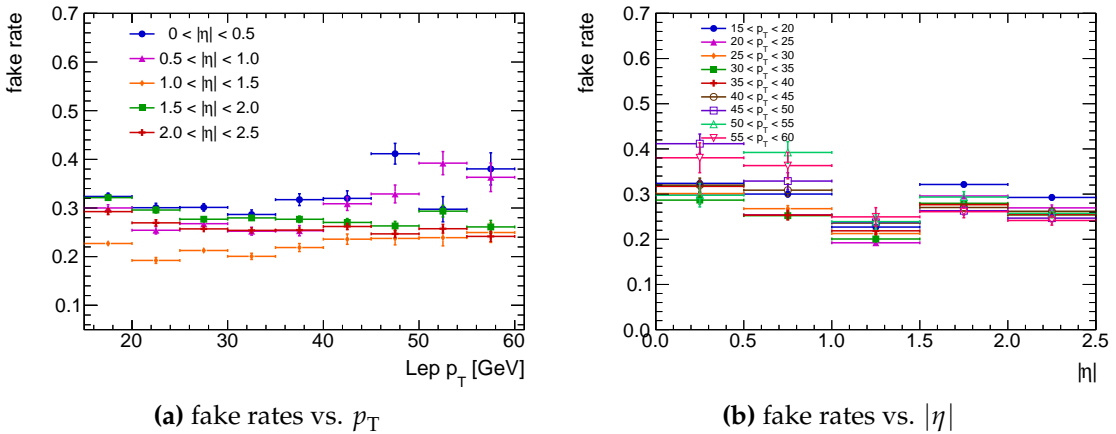


Figure 5.12.: Measured electron fake rates as a function of lepton (a)  $p_T$  and (b)  $|\eta|$ .

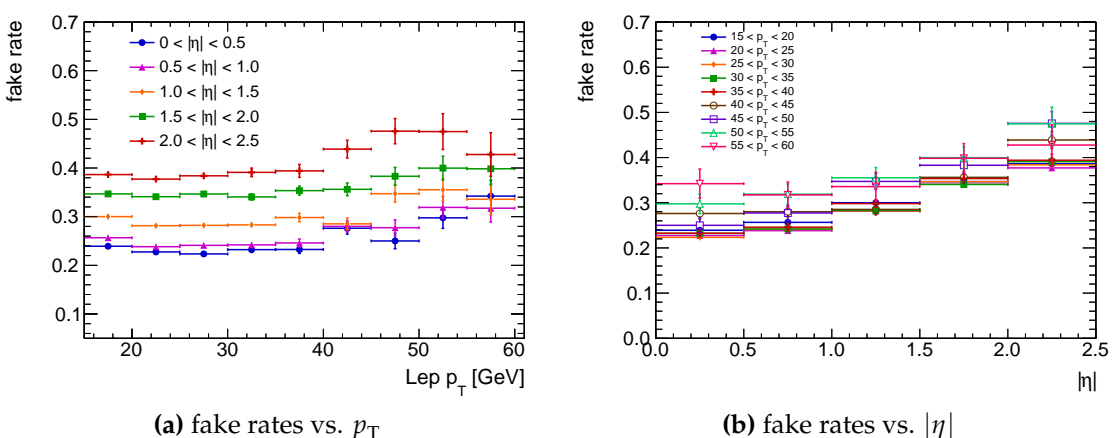


Figure 5.13.: Measured muon fake rates as a function of lepton (a)  $p_T$  and (b)  $|\eta|$ .

explicitly fails “Tight” selection is required. Each “Tight”+“FO” pair is then assigned a weight based on the FR,

$$w_i = \frac{\text{FR}_i}{1 - \text{FR}_i}, \quad (5.10)$$

corresponding to a likelihood that the “FO” in the pair will be promoted to a “Tight” lepton. The sum of these weighted pairs give a prediction for the fake lepton background yield and distributions. In principle, a single event can contribute multiple “Tight”+“FO” pairs to the application sample, but in practice rarely more than one pair is contained in a given event.

Genuine dileptonic processes can contaminate the application sample and need to be subtracted off, thus expectations from simulation are used to perform the subtraction; approximately 95% of this contamination comes from  $t\bar{t}(2\ell)$  events.

### 5.4.3. Fake rate method validation

As a means of validating the estimation procedure, a closure test is performed in a region which is orthogonal to the signal region, and is also enriched in fake leptons. The events in this region are required to pass the same selection as for the signal region thus ensuring a similar phase space, with the only modification being that the selected leptons must be equally charged (same-sign or SS). The SS validation region, although dominated by the fake lepton contribution can contain processes with prompt opposite-sign (OS) dielectrons where the charge of one electron in the pair is misidentified due to severe bremsstrahlung in the tracker material. The charge misidentification rate,  $f$ , can be determined using the SS and OS yields,  $N_{SS}$  and  $N_{OS}$ , from a  $Z \rightarrow ee$  selection, such that

$$N_{OS} = N \left[ (1-f)^2 + f^2 \right] \quad (5.11)$$

$$N_{SS} = 2N \left[ (1-f)f \right], \quad (5.12)$$

where  $N = N_{OS} + N_{SS}$ , is the total number of OS and SS events.  $f$  can be quadratically solved for in terms of the known quantities yielding,

$$f = \frac{1}{2} - \frac{1}{2} \sqrt{1 - \frac{2N_{SS}}{N}}. \quad (5.13)$$

The charge misidentification rate is measured to be approximately 0.56% in the data, which differs from the 0.76% measured in the simulation, thus a ratio of the rates is applied as a scale factor to correct the dielectron events from simulation in the SS validation region. A categorization based on  $M_{T2}^{\ell\ell} > 110$  GeV is not performed because too few events pass the high  $M_{T2}^{\ell\ell}$  requirement, to make a statistically meaningful test. Good agreement between the data and the combination of simulation and data-driven fake lepton estimation is observed in the  $p_T^{\text{miss}}$  distribution, as shown in Figure 5.14 for the three dilepton channels. The degree to which the observed and predicted yields in Figure 5.14 disagree is included in the normalization uncertainty on the fake lepton background prediction in the signal regions, which amounts to 30% in the  $ee$  channel, 5% in the  $e\mu$  channel, and 5% in the  $\mu\mu$  channel.

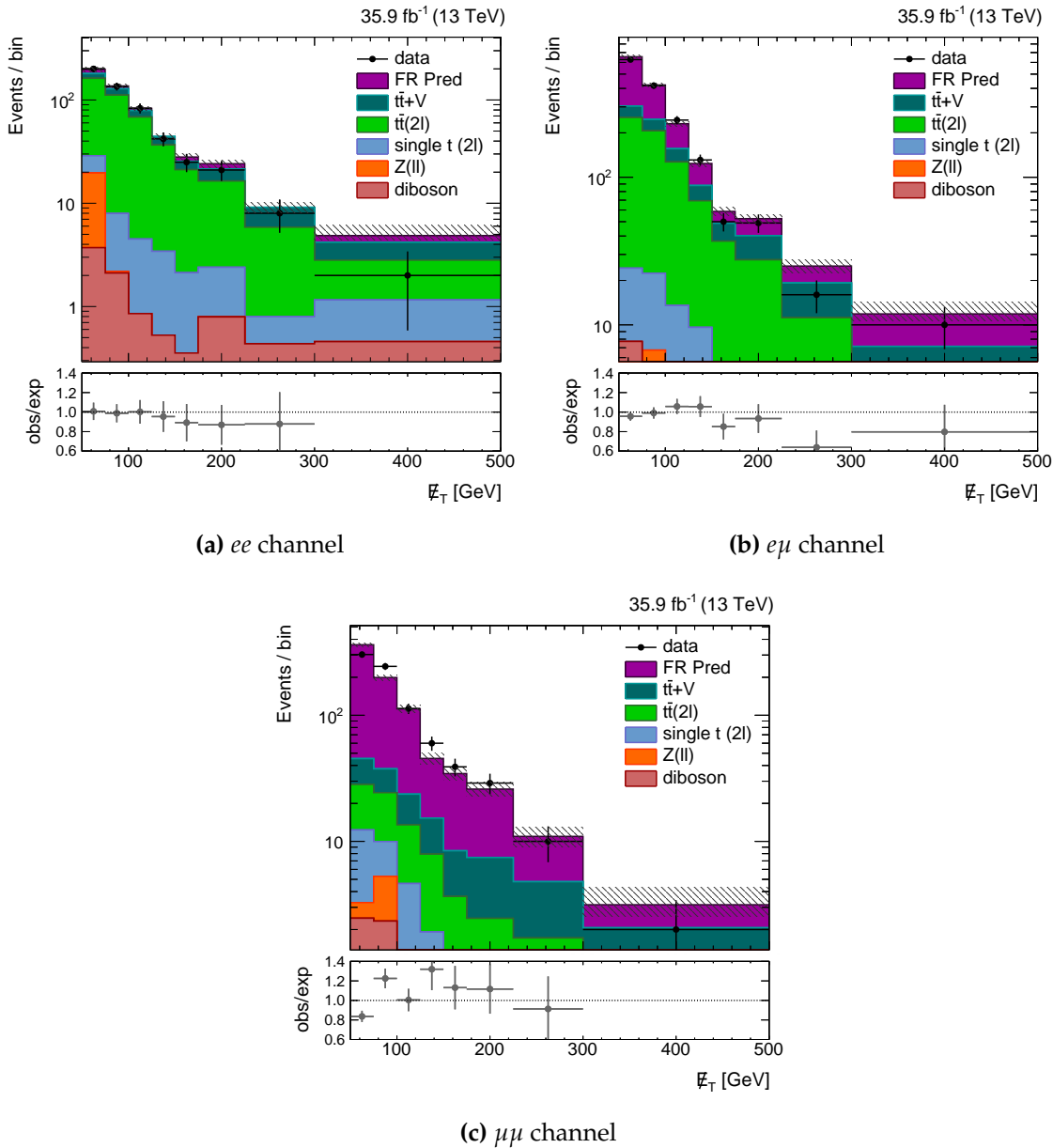


**Figure 5.14:** The  $p_T^{\text{miss}}$  distributions in the fake rate method validation region. All expected backgrounds are estimated using simulation, except for the fake lepton contribution, denoted “FR Pred” which is estimated via the fake rate method.

# Chapter 6.

## Analysis

### 6.1. Search strategy

The strategy employed in this search is to define regions targeting both a high signal acceptance and purity, called signal regions (SRs). As indicated in Section 1.5 and shown in Figure 4.2, the expected shape of the signal varies according to the mediator mass and type ( $\phi/a$ ), thus the strategy also aims to be as inclusive as possible in order to accommodate a wide range of potential signal  $p_T^{\text{miss}}$  spectra. To this end, a categorization of the events passing the outlined selection criteria in Section 4.2 is performed based on the  $M_{\text{T}2}^{\ell\ell}$  quantity defined in Section 4.2.1. As alluded to earlier, the SM  $t\bar{t}(2\ell)$  process is the most significant background for this search and by categorizing selected events according to whether the  $M_{\text{T}2}^{\ell\ell}$  quantity is greater or less than 110 GeV, the discrimination power of the variable can be used to isolate a region highly enriched in the potential signal, as well as a less pure SR. Retaining events which comprise the low signal purity ( $M_{\text{T}2}^{\ell\ell} < 110$  GeV) category is meant to increase the sensitivity to potential signals with softer  $p_T^{\text{miss}}$  spectra and correspondingly lower values of  $M_{\text{T}2}^{\ell\ell}$ , despite the overwhelming dominance of SM  $t\bar{t}(2\ell)$  in this category. The categorization

is taken a step further and the events in each  $M_{\text{T}2}^{\ell\ell}$  category are further split according to whether the leptons in the selected dilepton pair are the same or opposite flavor. Classifying the events based on SF vs OF changes the background composition of the categories, since almost no DY is expected in the case of the OF categories, while a far larger contribution is expected in the SF. The differing background composition as a result of the split into flavor regions also protects approximately half of the total search region from systematic uncertainties incurred only in the other half of the search region. Thus, events are separated into the following four SRs: high  $M_{\text{T}2}^{\ell\ell}$ -SF, high  $M_{\text{T}2}^{\ell\ell}$ -OF, low  $M_{\text{T}2}^{\ell\ell}$ -SF, and low  $M_{\text{T}2}^{\ell\ell}$ -OF. A potential signal observation would manifest as an excess over the expected  $p_{\text{T}}^{\text{miss}}$  from SM background processes, thus the signal extraction strategy is to perform a fit to the  $p_{\text{T}}^{\text{miss}}$  distribution. The  $p_{\text{T}}^{\text{miss}}$  distributions in each of the four SRs are fit simultaneously. This approach exploits the kinematic differences between the  $p_{\text{T}}^{\text{miss}}$  shapes of the  $t\bar{t} + \chi\bar{\chi}$  signals described in Chapter 4 and the  $p_{\text{T}}^{\text{miss}}$  shapes of SM backgrounds detailed in Chapter 5. The fitting procedure and statistical method is described later on in this chapter, in Section 6.5.

## 6.2. Data to simulation corrections

Various corrections, in addition to the top  $p_{\text{T}}$  correction applied to the  $t\bar{t}(2\ell)$  background only, are applied to the all processes estimated using simulation. The corrections account for mismodeling of distributions in the MC simulation, or to attempt to cover the difference between efficiencies measured in the data compared to those measured in the simulation. The corrections applied in this work are listed and described in the following section.

### 6.2.1. Trigger efficiency

The HLT triggers employed online to select potential dilepton events are a combination of dielectron, electron-muon, and dimuon triggers. In addition, single lepton triggers are used, but only approximately 4 – 6% of the events passing the offline selection criteria as defined in Section 4.2 are picked up by these. The suite of dilepton triggers make requirements on the lepton object reconstruction at the HLT level. As an example, the HLT trigger with the path name `HLT_Ele23_Ele12_CaloIdL_TrackIdL_IsoVL_DZ` is fired if an event contains two electrons with  $p_T$  thresholds above 23 GeV and 12 GeV, and both electrons pass the loose working points for online electron identification from the calorimeters (CaloIdL), and the tracker (TrackIdL). The isolation requirement is very relaxed or “very loose” (IsoVL), and a quality requirement on the  $|d_z|$  of the associated tracks to the PV is made (DZ). The following is a list of the dilepton triggers used:

- `HLT_Ele23_Ele12_CaloIdL_TrackIdL_IsoVL_DZ`
- `HLT_Mu8_TrkIsoVVL_Ele23_CaloIdL_TrackIdL_IsoVL`
- `HLT_Mu23_TrkIsoVVL_Ele12_CaloIdL_TrackIdL_IsoVL`
- `HLT_Mu23_TrkIsoVVL_Ele12_CaloIdL_TrackIdL_IsoVL_DZ`
- `HLT_Mu17_TrkIsoVVL_Mu8_TrkIsoVVL`
- `HLT_Mu17_TrkIsoVVL_Mu8_TrkIsoVVL_DZ`
- `HLT_Mu17_TrkIsoVVL_TrkMu8_TrkIsoVVL_DZ`

The efficiencies of each lepton “leg” of the triggers listed is measured in the data and simulation using a method standard to experimental particle physics, generically called the “Tag and Probe” method. In this work, the method exploits dilepton

resonances, such as  $Z \rightarrow \ell\ell$  events for the  $ee$  and  $\mu\mu$  measurements, and dileptonic  $t\bar{t}(2\ell)$  decays for the  $e\mu$  measurements. In this case, a “tag” electron is required to fire a single electron trigger and pass the “Tight” working point as outlined in Table 3.3, and have a  $p_T > 40$  GeV and  $|\eta| < 2.1$ , for the efficiency measurements of the  $ee$  trigger and  $\mu$ -leg of the  $e\mu$  trigger. A “tag” muon is required to fire a single muon trigger and pass the “Tight” working point criteria as outlined in Table 3.1 and have a  $p_T > 30$  GeV, for the efficiency measurements of the  $\mu\mu$  trigger and  $e$ -leg of the  $e\mu$  trigger. Subsequently, the “probe” is the other lepton in the event and is termed as “passing”/“failing” if the trigger leg in question for which the efficiency is being measured has/not been fired by the lepton. Orthogonal samples of “tag + passing probe” and “tag + failing probe” are then obtained and the efficiency is computed as a ratio of the former category to the sum of the two categories. The efficiencies are measured in data and simulation and are parametrized in both lepton  $p_T$  and  $|\eta|$ , where the scale factor applied to the simulation is the ratio of the data to simulation efficiencies. Figure 6.1 shows the scale factors derived for the electron and muon legs of the muon-electron trigger, where the scale factors are nearly unitary though a lower efficiency is observed for the electron leg for low  $p_T$  electrons with  $2.1 < \eta < 2.4$  in data than in the simulation. The correction is then applied to the simulation as,

$$\frac{\left[ \epsilon_{\ell 1} \cdot \epsilon_{\ell 2} \cdot f + (1 - f) \right]_{\text{data}}}{\left[ \epsilon_{\ell 1} \cdot \epsilon_{\ell 2} \cdot f + (1 - f) \right]_{\text{MC}}}, \quad (6.1)$$

where  $\epsilon_{\ell 1/\ell 2}$  denotes the double lepton trigger efficiency of either lepton leg as measured, and  $f$  denotes the approximate fraction of events triggered on using the double lepton triggers as measured in data and simulation.

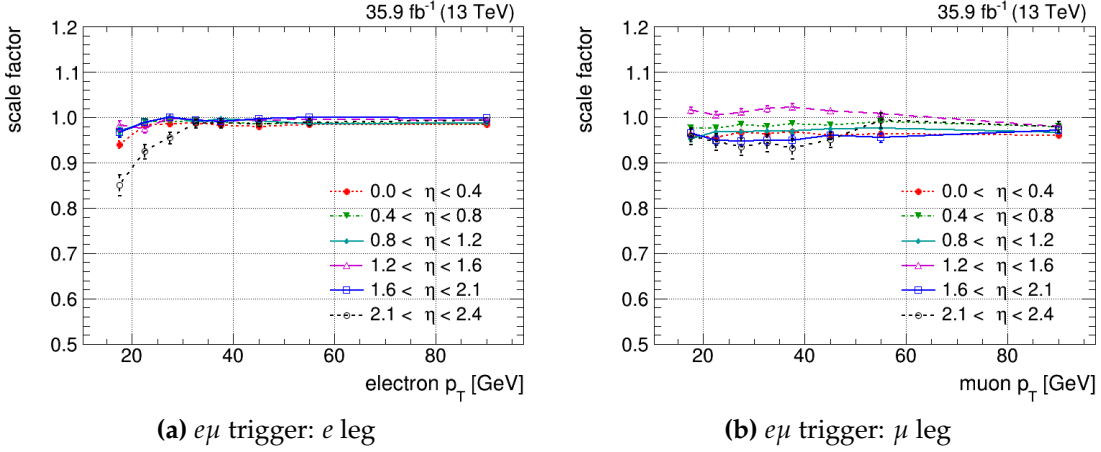


**Figure 6.1.:** Scale factors for the electron and muon leg of the muon-electron trigger parametrized in lepton  $p_T$  and  $\eta$ .

### 6.2.2. PU reweighting

The simulation does not reproduce the PU distribution as observed in the data, so in order to alleviate this discrepancy, the simulation is re-weighted to the estimated PU distribution in data. The re-weighting is derived from the measured instantaneous luminosity of the bunch crossings during the 2016 pp collision data-taking period and the estimated total inelastic cross section. The cross section is estimated using minimum bias (MB) events. In the experimental sense, a MB event is one which has been triggered on as a result of minimum detector activity and in the theoretical sense, MB triggers target non-single diffractive inelastic interactions. The total pp cross section,  $\sigma_{\text{tot}}$  is comprised of,

$$\sigma_{\text{tot}} = \sigma_{\text{elas}} + \sigma_{\text{SD}} + \sigma_{\text{DD}} + \sigma_{\text{ND}} + \sigma_{\text{CD}} \quad (6.2)$$

where from left to right, the terms on the right-hand side of Eq. 6.2 correspond to contributions to the cross section from elastic scattering, single diffractive dissociation,

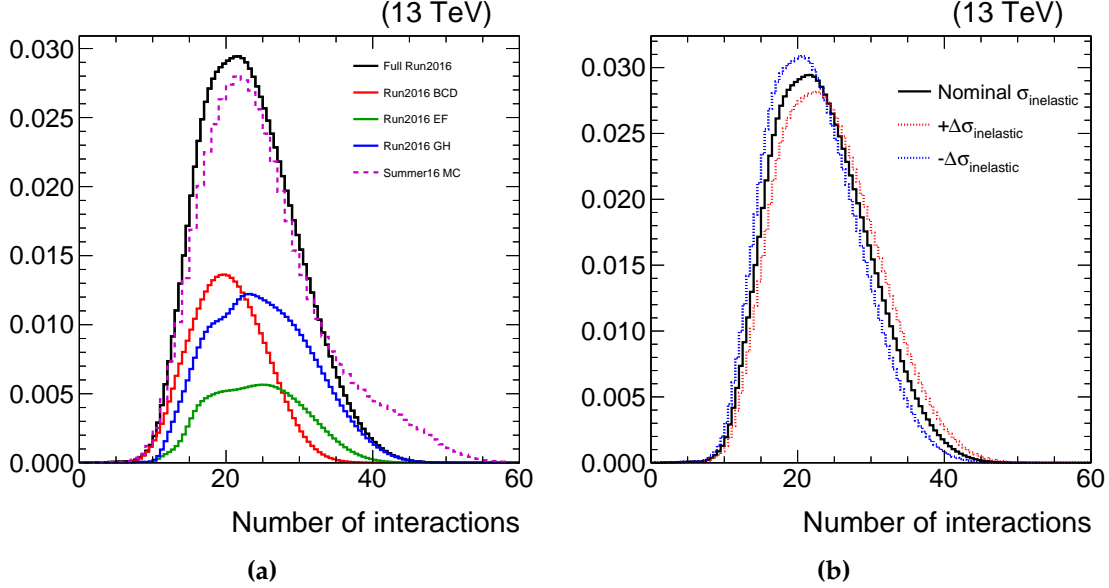


**Figure 6.2:** (a) Pileup distributions in data and MC. Also shown are the pileup profiles in a few run ranges scaled to the relative contribution to the total integrated luminosity.(b) The pileup distributions from varying the total inelastic cross section by  $\pm 4.6\%$ .

double diffractive dissociation, non-diffractive inelastic scattering, and central diffractive dissociation. In a more accurate sense, MB events are covered by the  $\sigma_{DD}$  and  $\sigma_{ND}$  terms. The cross section estimate for 2016 data-taking is 69.2 mb for MB events, with an uncertainty of 4.6%. The ratio of normalized distributions of the number of PU interactions in data and  $t\bar{t}(2\ell)$  simulation is used to extract the scale factors that are applied to the simulation on an event-by-event basis. The PU profiles in data and simulation are shown in Figure 6.2, where the simulation is also shown with the MB cross section varied by  $\pm 4.6\%$  in Figure 6.2b. The effect of the PU re-weighting can be seen in Figure 6.3, where the distribution of the number of reconstructed primary vertices (PV) is shown before and after the re-weighting. Discrepancies between the data and the simulation still exist in the  $N_{PV}$  distribution, however this search is not strongly reliant on the modeling of the number of PV or PU interactions. In addition, the effects of such discrepancies are taken into account and treated as a systematic uncertainty in the final fit, to be described later.

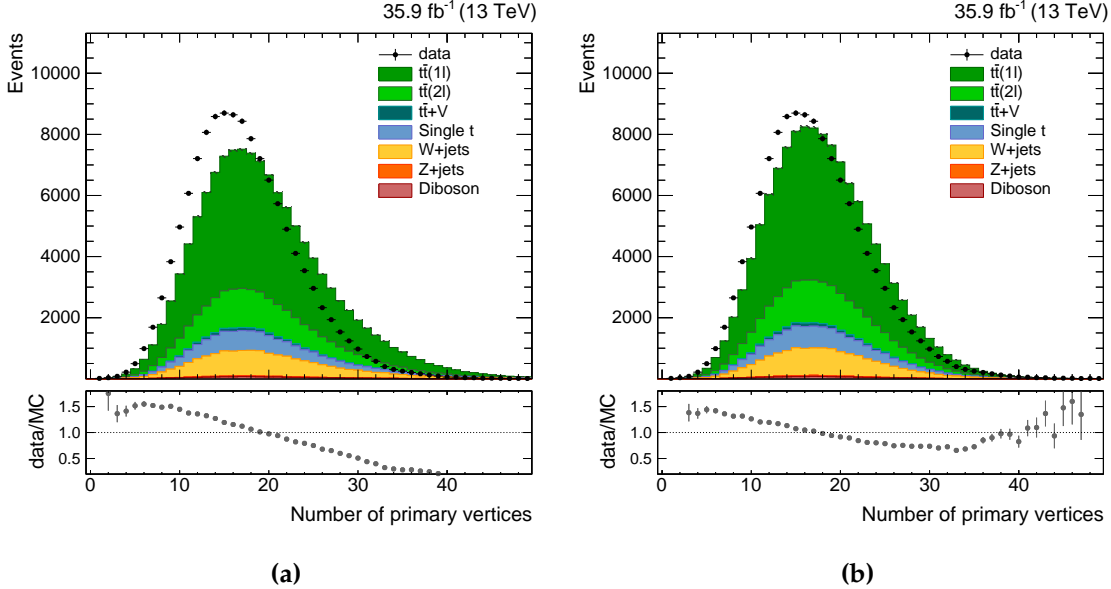


**Figure 6.3.:**  $N_{PV}$  distributions in data and MC pre and post PU re-weighting in a region dominated by semileptonic  $t\bar{t}$  events. The MC is normalized to the observed yield.

### 6.2.3. b-tagging efficiency

The efficiency to tag jets originating from b-quark hadronization is dependent on the working point of the b-tagging algorithm used (in this case the CSV algorithm as defined in Section 3.3.1), and the jet kinematics in the signal region of interest. Hence, the performance is characterized based on the probabilities to correctly tag a b jet ( $\epsilon_b$ ), to misidentify the hadronization of a c-quark as a b jet ( $\epsilon_c$ ), and to misidentify light flavor or gluon initiated jets as b jets ( $\epsilon_{uds g}$ ). Each efficiency is defined by,

$$\epsilon_f(p_T, \eta) = \frac{N_f^{\text{b-tagged}}(p_T, \eta)}{N_f^{\text{Total}}(p_T, \eta)}, f = b, c, uds g \quad (6.3)$$

where the efficiency is determined in bins of jet  $p_T$  and  $\eta$ , and  $N_f^{\text{Total}}$  and  $N_f^{\text{b-tagged}}$  are the total number of jets and the number of b-tagged jets of flavor  $f$ .

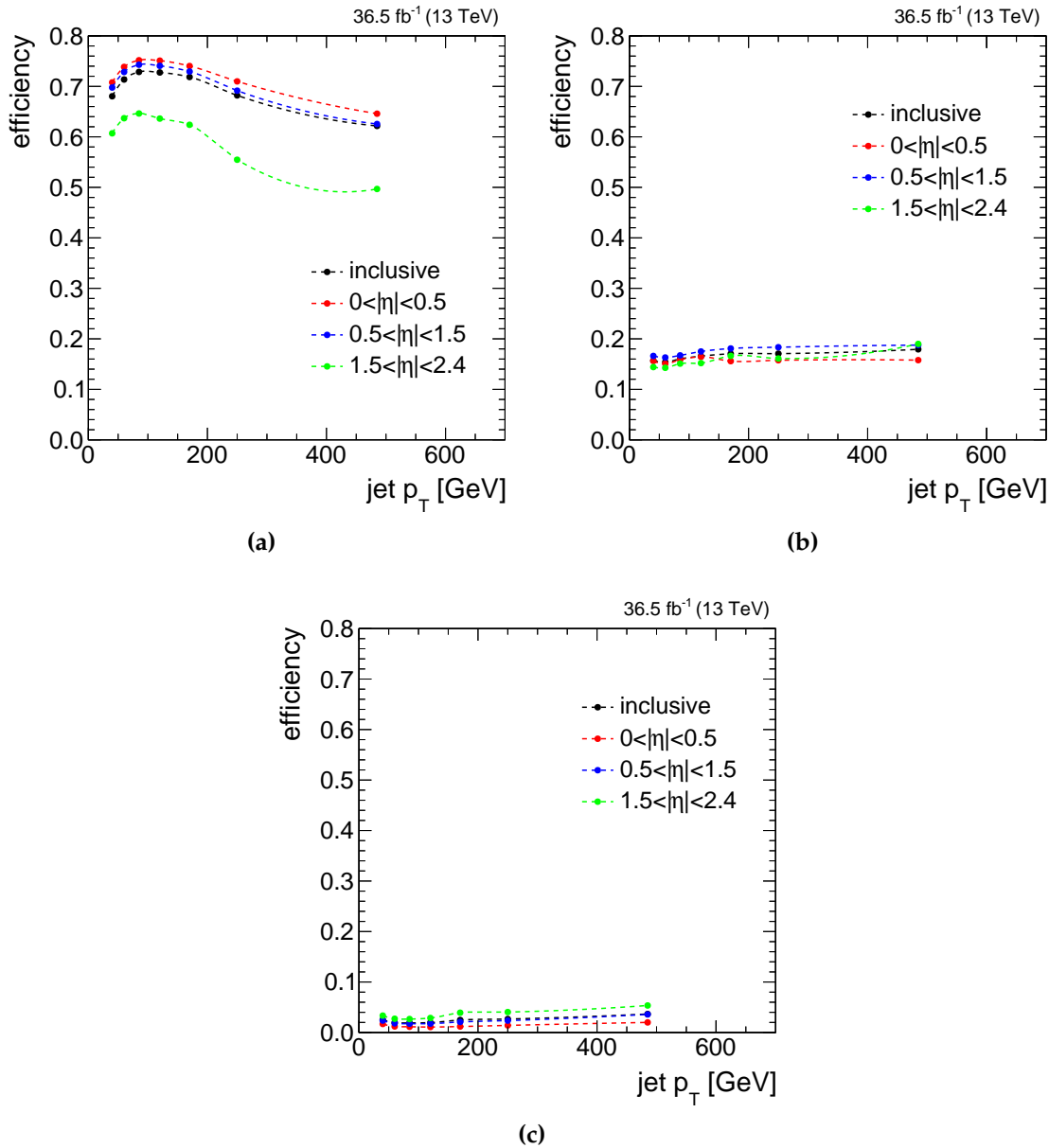


**Figure 6.4:** The efficiency in  $t\bar{t}(2\ell)$  simulation is measured as a function of jet  $p_T$  and various  $\eta$  bins for (a) correctly tagging b jets, (b) misidentifying c jets, (c) and misidentifying light flavor or gluon jets.

The CSV algorithm has three working points which correspond to different values of  $\epsilon_{uds g}$  as measured in data. They are defined as loose ( $\epsilon_{uds g} = 10\%$ ), medium ( $\epsilon_{uds g} = 1\%$ ), and tight ( $\epsilon_{uds g} = 0.1\%$ ). In the following analysis, the medium working point is used and corresponds to a b-tagging efficiency of  $\epsilon_b = 69\%$ , and an c-jet mistag efficiency of  $\epsilon_c = 35\%$  in data. The efficiency of the medium working point is measured in a simulation sample of dilepton  $t\bar{t}$  and shown in Figure 6.4 for each jet flavor as a function of  $p_T$  and  $\eta$ . In general, the more central a jet is within the detector volume (corresponding to smaller  $|\eta|$ ), the higher the b-tagging efficiency and lower the mistag rate is expected to be. As can be understood from Figure 6.4a, although the efficiency in the highest  $\eta$  bin ranges from 0.62 to 0.5 for low to high jet  $p_T$  values, the inclusive efficiency lies at approximately 0.7 demonstrating that most of the selected b-jets are central.

The corrections are applied in an event-by-event method, where the b-tagging combinatorics are also accounted for. For every selected jet in the event, the probability that it is correctly tagged or mis-tagged depending on flavor is  $\epsilon^{\text{tag}}$  and  $(1 - \epsilon^{\text{tag}})$ , respectively. If no b-tagged jets are expected, the corresponding event efficiency is then,

$$\epsilon_{\text{event}} = \prod_{i=\# \text{jets}} (1 - \epsilon_i^{\text{tag}}). \quad (6.4)$$

The signal region selection stipulates that events must contain at least one b-tagged jet, so it follows that the event efficiency is defined as the “inverse” of Eq. 6.4, such that,

$$\epsilon_{\text{event}} = 1 - \prod_{i=\#\text{jets}} (1 - \epsilon_i^{\text{tag}}). \quad (6.5)$$

The corrections are applied to the simulation based on the ratio of the event efficiencies measured in the data and simulation,  $\text{SF}_{\text{b-tag}} = \frac{\epsilon_{\text{event}}^{\text{data}}}{\epsilon_{\text{event}}^{\text{MC}}}$ , in order to cover any differences in efficiency with respect to the performance in data.

### 6.3. Discriminating observables

$p_T^{\text{miss}}$  is the detector observable which provides the strongest discrimination between the  $t\bar{t} + \chi\bar{\chi}$  signal and the dominant SM dileptonic  $t\bar{t}$  background. In addition to the main observable used for the signal extraction, multiple other observables are scrutinized as a means to ascertain that significant discrepancies between the data and the simulation are not present in the signal region. These can be seen in the same flavor and opposite flavor channels, respectively, in Figure 6.6 and Figure 6.8. The observables include the multiplicity of jets ( $N_{\text{jets}}$ ), and that of b-tagged jets ( $N_{\text{b-jets}}$ ), as well as kinematic distributions for the highest  $p_T$  (leading) lepton and jet in the event. Variables which combine the kinematic information from the two leptons in the event such as the  $p_T$  and mass of the dilepton system,  $p_T^{\ell\ell}$  and  $m_{\ell\ell}$  are presented.

The  $M_{\text{T2}}^{\ell\ell}$  distribution used to categorize events into a low ( $M_{\text{T2}}^{\ell\ell} < 110 \text{ GeV}$ ) and high ( $M_{\text{T2}}^{\ell\ell} > 110 \text{ GeV}$ ) signal purity category is shown in Figure 6.9. The subsequent  $p_T^{\text{miss}}$  spectra in the low and high purity signal regions are shown in Figure 6.10 and Figure 6.11, respectively.

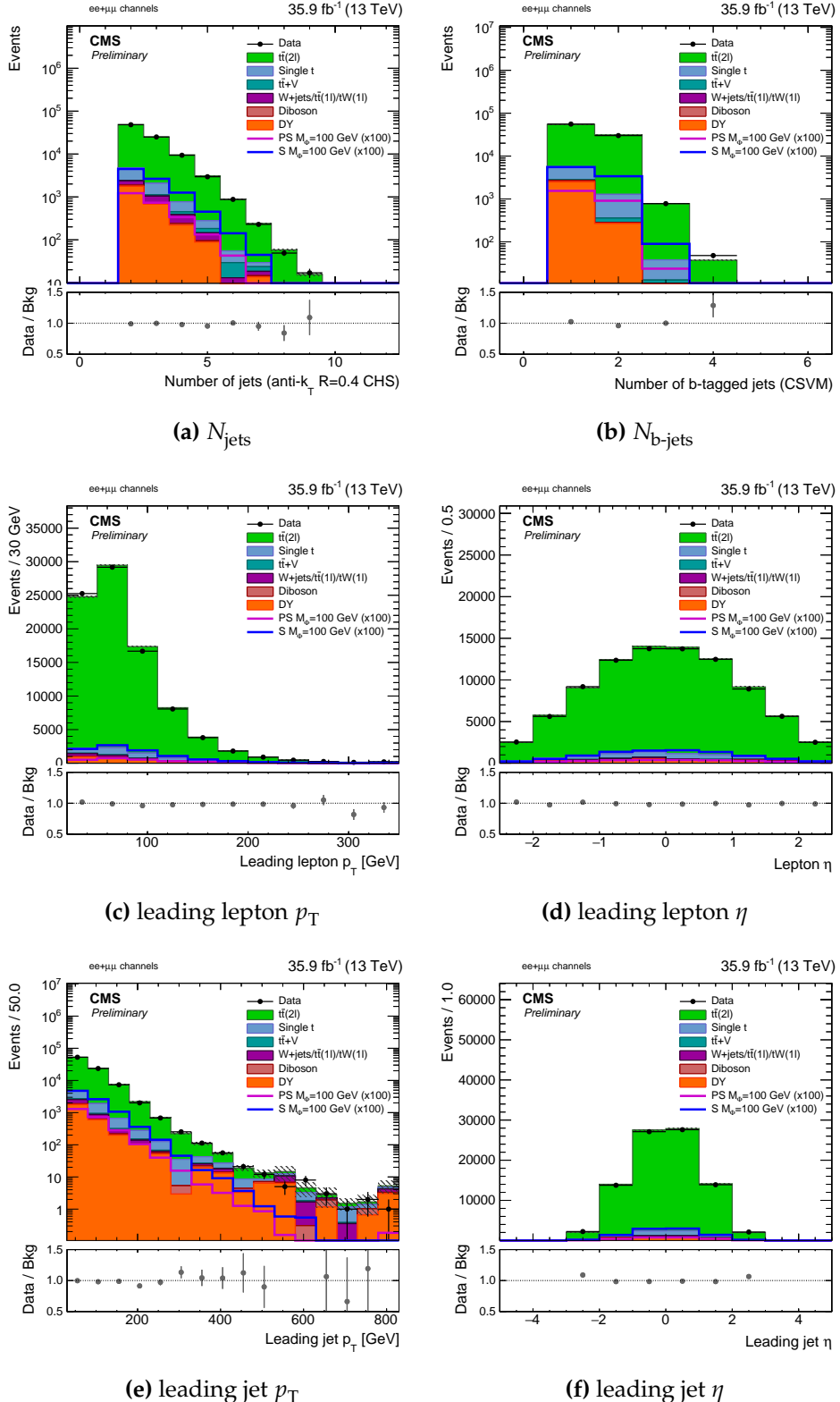


**Figure 6.5.:** Kinematic distributions in the same flavor ( $ee + \mu\mu$ ) channel. Signals with a pseudoscalar (magenta) and scalar (blue) mediator with  $m_\phi = 100$  GeV and  $m_\chi = 1$  GeV are overlayed and scaled by a factor of 200 to illustrate the potential shape differences between the signal and background in the various distributions. The uncertainties shown in these plots on the data and background are purely statistical.

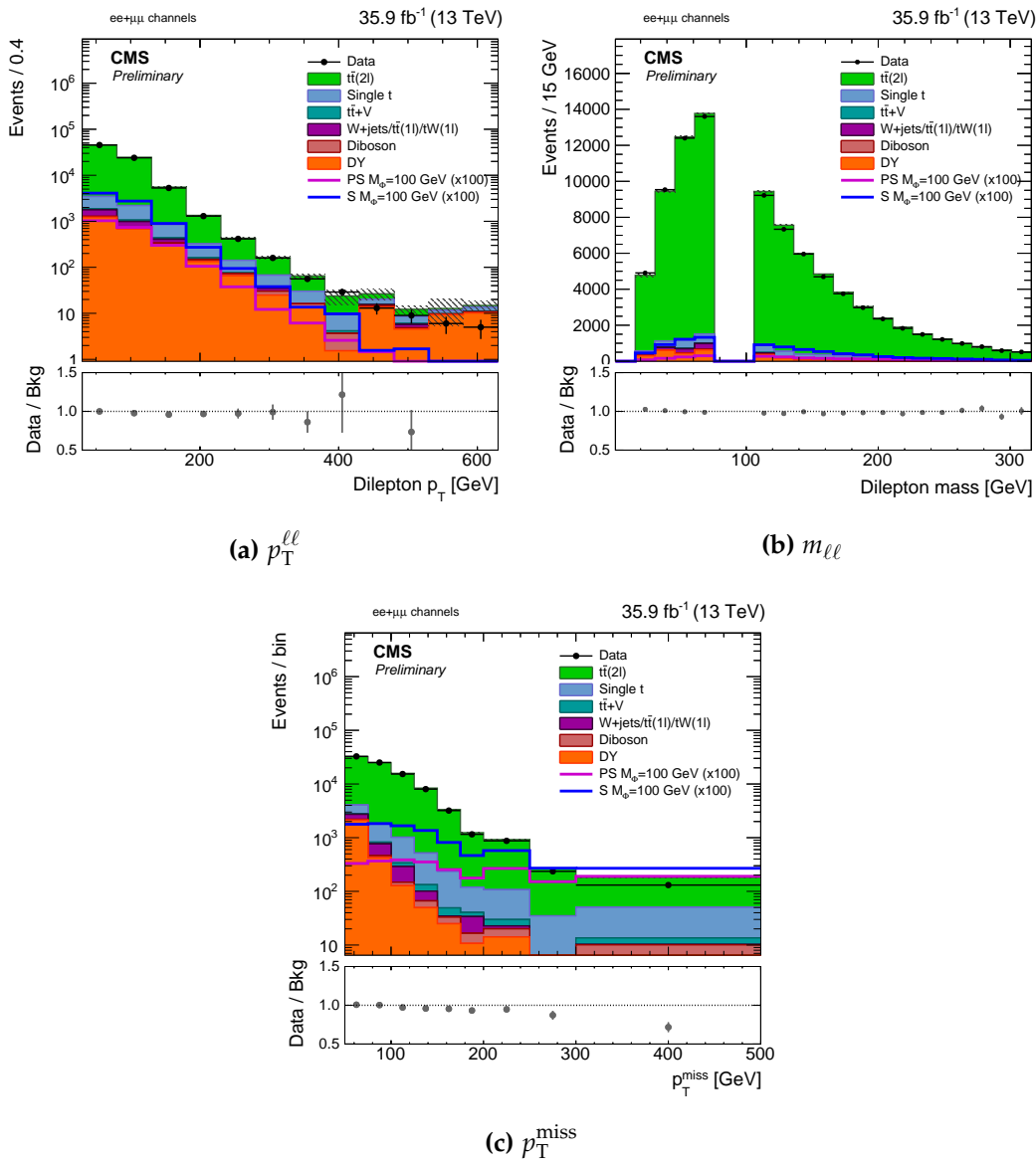


**Figure 6.6.:** Kinematic distributions in the same flavor ( $ee + \mu\mu$ ) channel. Signals with a pseudoscalar (magenta) and scalar (blue) mediator with  $m_\phi = 100$  GeV and  $m_\chi = 1$  GeV are overlayed and scaled by a factor of 200 to illustrate the potential shape differences between the signal and background in the various distributions. The uncertainties shown in these plots on the data and background are purely statistical.

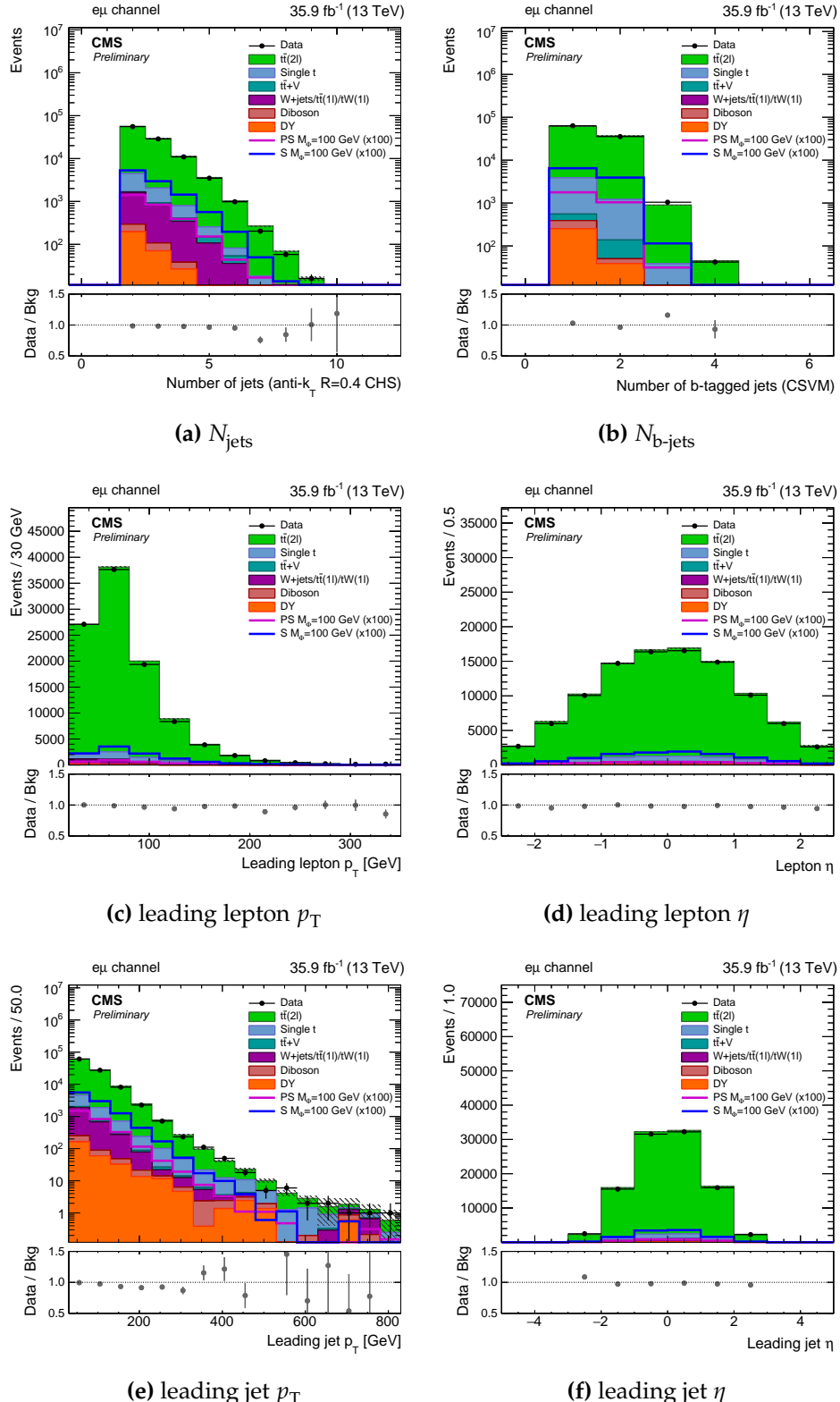


**Figure 6.7.:** Kinematic distributions in the same flavor ( $e\mu$ ) channel. Signals with a pseudoscalar (magenta) and scalar (blue) mediator with  $m_\phi = 100 \text{ GeV}$  and  $m_\chi = 1 \text{ GeV}$  are overlayed and scaled by a factor of 200 to illustrate the potential shape differences between the signal and background in the various distributions. The uncertainties shown in these plots on the data and background are purely statistical.

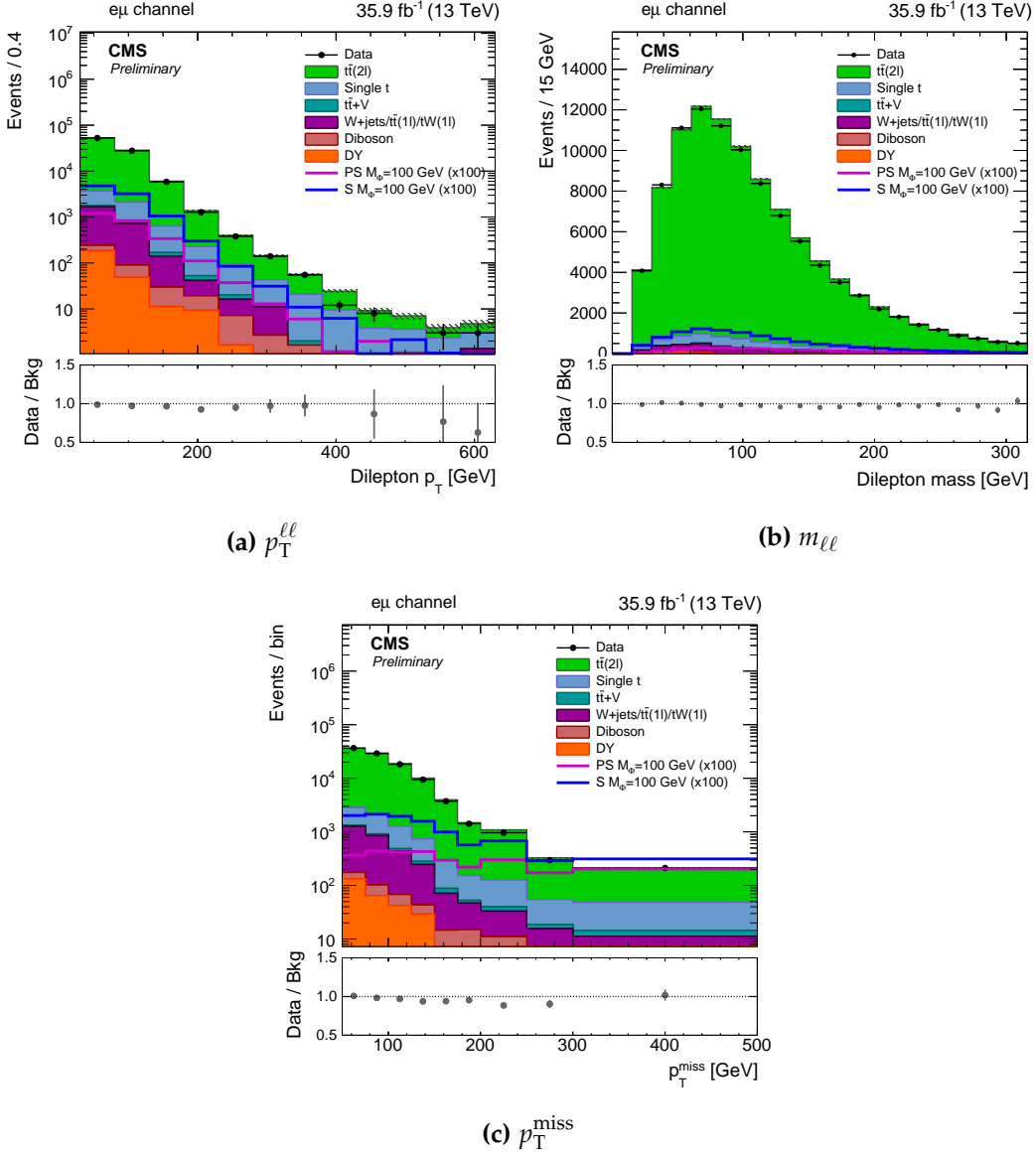


**Figure 6.8:** Kinematic distributions in the same flavor ( $e\mu$ ) channel. Signals with a pseudoscalar (magenta) and scalar (blue) mediator with  $m_\phi = 100$  GeV and  $m_\chi = 1$  GeV are overlaid and scaled by a factor of 200 to illustrate the potential shape differences between the signal and background in the various distributions. The uncertainties shown in these plots on the data and background are purely statistical.

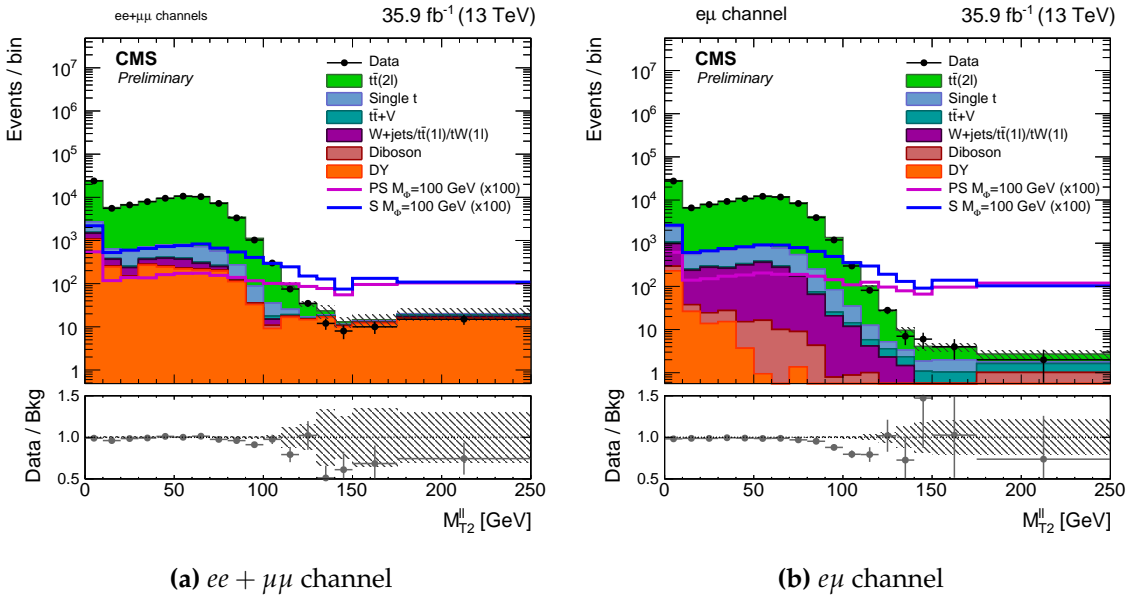


**Figure 6.9.:** The  $M_{T2}^{\ell\ell}$  distribution in the (a) same flavor and (b) opposite flavor channels. Events with  $M_{T2}^{\ell\ell}$  below (above) 110 GeV form the low (high) signal purity categories. The uncertainties in the above plots are statistical only. The  $M_{T2}^{\ell\ell}$  templates for signals with a pseudoscalar (magenta) and scalar (blue) mediator with  $m_\phi = 100$  GeV and  $m_\chi = 1$  GeV are overlayed and scaled by a factor of 200.

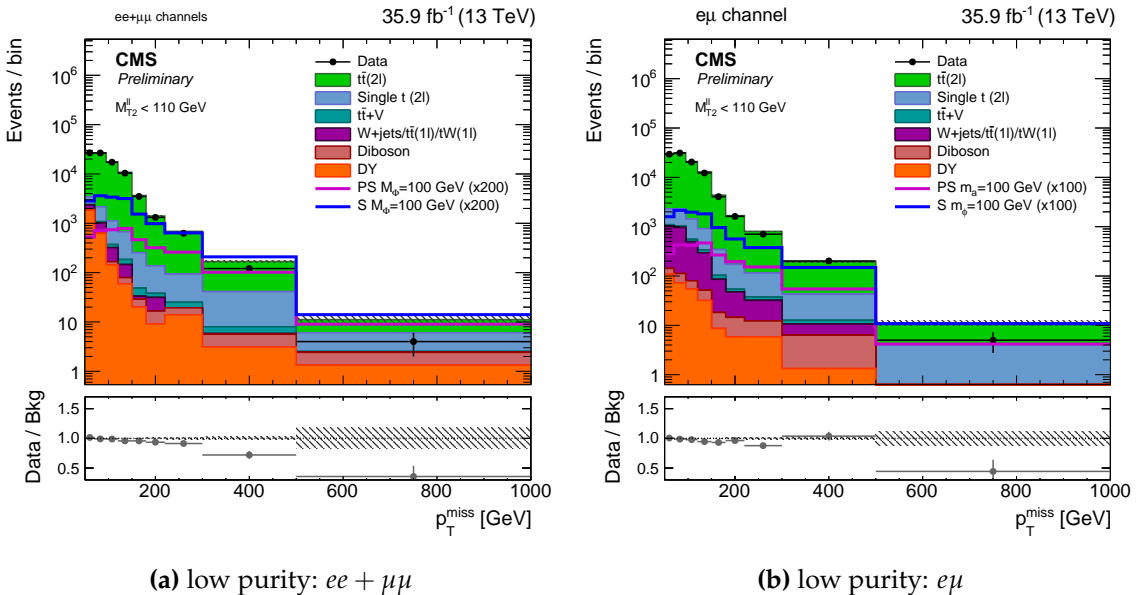


**Figure 6.10.**: The  $p_T^{\text{miss}}$  distributions in the low purity signal region for (a) same flavor and (b) opposite flavor events. The uncertainties in the above plots are statistical only. The  $p_T^{\text{miss}}$  templates in the low purity signal region for signals with a pseudoscalar (magenta) and scalar (blue) mediator with  $m_\phi = 100 \text{ GeV}$  and  $m_\chi = 1 \text{ GeV}$  are overlaid and scaled by a factor of 200.

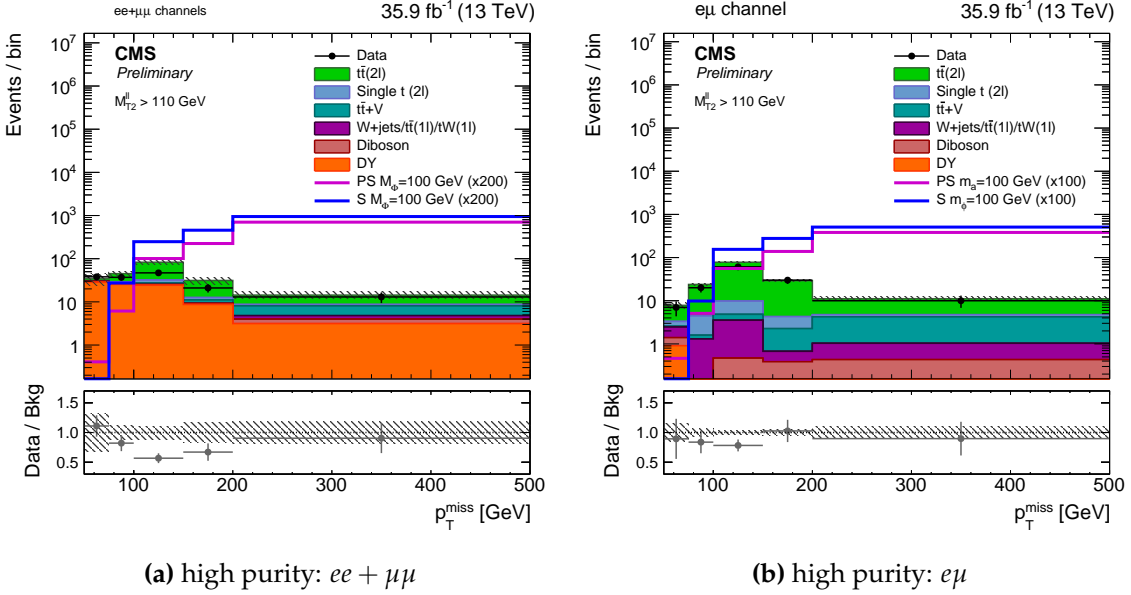


**Figure 6.11.:** The  $p_T^{\text{miss}}$  distributions in the high purity signal region for (a) same flavor and (b) opposite flavor events. The uncertainties in the above plots are statistical only. The  $p_T^{\text{miss}}$  templates in the high purity signal region for signals with a pseudoscalar (magenta) and scalar (blue) mediator with  $m_\phi = 100 \text{ GeV}$  and  $m_\chi = 1 \text{ GeV}$  are overlaid and scaled by a factor of 200.

## 6.4. Systematic uncertainties

The signal and background  $p_T^{\text{miss}}$  templates derived from simulation are subject to effects incurred from experimental and theoretical sources of uncertainty. The  $p_T^{\text{miss}}$  distributions are parametrized in order to allow for constrained shape and normalization variations as a cause of the systematic uncertainties, referred to throughout as “systematics”. Each systematic is represented by a nuisance parameter,  $\theta$ , with a probability density function,  $pdf$ , denoted as  $\rho(\theta)$ , that contains the central value of the nuisance,  $\tilde{\theta}$ , and other parameters that describe the overall shape of the  $pdf$ , such as its width.

Uncertainties which affect the normalization of the signal and background processes are modeled using nuisance parameters with log-normal probability densities. The log-normal  $pdf$  follows the form [92],

$$\rho(\theta) = \frac{1}{\sqrt{2\pi} \ln \kappa} \exp \left( -\frac{(\ln(\theta/\tilde{\theta}))^2}{2(\ln \kappa)^2} \right) \frac{1}{\theta}. \quad (6.6)$$

where the width of the log-normal distribution is characterized by  $\kappa$ , and  $\tilde{\theta}$  represents the best estimate of the nuisance  $\theta$ . In the limit of small uncertainty ( $\epsilon$ ), the width of a Gaussian *pdf* is given by  $\sigma = \epsilon$ , which equates directly to the log-normal width via a Taylor expansion for  $\kappa = e^\epsilon$ , such that  $\kappa = 1 + \epsilon$ . The log-normal *pdf* is useful in the case of large uncertainties as the distribution has a longer tail in comparison with a Gaussian *pdf*, and avoids the problem of negative parameter values obtained from a Gaussian probability density, since  $\rho(\theta) \rightarrow 0$  as  $\theta \rightarrow 0$ .

A number of uncertainties influence the overall shape of the signal and background  $p_T^{\text{miss}}$  templates along with the normalization. Systematics of this type are implemented using a general technique known as “vertical morphing” [93]. A change in a particular type of uncertainty (such as an energy scale) can cause a distortion in both the shape and overall normalization of the efficiency as a function of the observable ( $p_T^{\text{miss}}$ ) bin. Raising and lowering a particular parameter to its corresponding values at one standard deviation will cause the bin efficiencies, denoted as  $\epsilon_{ij}$  for source  $i$  in observable bin  $j$ , to also shift, thus resulting in three measures of the bin efficiency shape, referred to as  $\epsilon_{ij}^+$ ,  $\epsilon_{ij}^0$ , and  $\epsilon_{ij}^-$ . In order to transform the three shape measures into a continuous estimate as a function of the parameter value, a morphing parameter, represented by  $f$  and nominally equal to 0 with a unitary uncertainty, is used. A quadratic interpolation is used for values where  $|f| < 1$ , to express the efficiency in a bin as a function of the morphing parameter such that,

$$\epsilon_{ij} = \frac{f(f-1)}{2}\epsilon_{ij}^- - (f-1)(f+1)\epsilon_{ij}^0 + \frac{f(f+1)}{2}\epsilon_{ij}^+. \quad (6.7)$$

The form of Eq. 6.7 guarantees that the value of the expression is  $\epsilon_{ij}^\pm$  for  $f = \pm 1$ . In the case that a nuisance parameter is shifted by more than one standard deviation from its nominal value and thereby resulting in efficiency values in the range  $|f| > 1$ , a linear extrapolation is performed.

#### 6.4.1. Sources of systematic uncertainty

The following sources of uncertainty affect the normalization of the signal and background processes:

- **Pileup modeling:** As described in Section 6.2.2, the total inelastic cross section used to calculate the data pileup distributions is varied by  $\pm 4.6\%$ , in order to account for systematic uncertainties due to pileup modeling. Normalization differences in the range of  $0.3 - 11\%$  across the different physics processes result from reweighting the simulation accordingly.
- **Integrated luminosity:** The overall uncertainty of the measurement of the integrated luminosity delivered to the CMS Experiment during the 2016 LHC pp run at  $\sqrt{s} = 13$  TeV is estimated to be 2.5% [94].
- **Lepton reconstruction and selection:** The uncertainty on lepton reconstruction and selection efficiency is associated with the efficiency measurement with samples of Z bosons decaying to dielectrons or dimuons [95]. The  $p_T$ - and  $\eta$ -dependent scale factors are varied within their uncertainties which amounts to  $\approx 2\%$  per lepton.

- **Lepton trigger:** The uncertainty on lepton triggering efficiency is associated with the efficiency measurement with samples of Z bosons decaying to dielectrons or dimuons. For muon triggers, the uncertainties across physics processes for both low and high  $M_{T2}^{\ell\ell}$  SRs are approximately 2% in the SF and 1.5% in the OF categories. Analogously, the uncertainties for electron triggers are approximately 1.8% in the SF and 2.2% in the OF categories.
- **b-tagging efficiency:** The b-tagging efficiency and mis-tag rate and the respective uncertainties are measured on independent control samples. Uncertainties from gluon splitting, the b quark fragmentation function, and the selections used to define the control samples are propagated to the efficiency scale factors [96]. The uncertainties on the mis-tag rate range from 0.1 – 4%, while the b-tagging efficiency uncertainties range from 0.1 – 2%, across physics processes across all categories where the largest uncertainty is incurred in the low  $M_{T2}^{\ell\ell}$  category for the diboson background.
- **Single top and diboson normalization:** In practice, the expected yields for background processes are either scaled to data or to theory predictions with the best available accuracy. The PDF and the renormalization and factorization scale variations take into account the uncertainties on the background acceptances. However, in the single top and diboson simulation samples used, the aforementioned variations are not available, so a conservative uncertainty of 20% and 10% is assigned respectively to the normalizations, and these uncertainties are treated independently of each other.
- **Drell-Yan background uncertainty:** The uncertainties incurred from the data-driven estimate of the Drell-Yan background normalization are dominated by the statistical uncertainties on  $N_{in}$  and  $R_{MC}^{1b}$ , quantities used to extrapolate yields from a region near the Z boson mass to regions away from it, as described in

Section 5.3. The uncertainties are 11% and 6% for the  $ee$  and  $\mu\mu$  channels and only applies to the DY background in the SF regions.

- **Fake lepton background uncertainty:** The sources of uncertainty in the fake lepton background stem from the uncertainty in the measured fake rate, and from the statistical uncertainty of the single-lepton application sample to which the rate is applied, as described in Section 5.4. The uncertainties are 78% ( $ee$ ), 70% ( $e\mu$ ), 74% ( $\mu\mu$ ) in the high signal purity category and 47% ( $ee$ ), 12% ( $e\mu$ ), and 20% ( $\mu\mu$ ) in the low signal purity category, and are dominated by the statistical uncertainty associated with the single-lepton application sample. Since the fake lepton background is small, these relatively large uncertainties do not significantly degrade the sensitivity of the search.

The systematics affecting the overall  $p_T^{\text{miss}}$  shape and normalization are listed below in order of decreasing dominance on the final result. For some systematics, the changes in the  $p_T^{\text{miss}}$  spectra as a result of the  $\pm 1\sigma$  uncertainty variation has been shown for pertinent processes. A full suite of such experimental plots for all systematics affecting the  $p_T^{\text{miss}}$  templates derived for various signal and background processes can be found in Appendix ??.

- **Jet energy scale (JES):** The reconstructed energy of every jet in an event taken from simulation is varied simultaneously by one standard deviation of the JES uncertainty of the corresponding jet above and below the nominal energy. These JES uncertainties are coherently propagated to all observables impacted, including the jet  $p_T$ , jet multiplicity,  $p_T^{\text{miss}}$ , and  $M_{T2}^{\ell\ell}$ . Figure A.6 shows an example of the effect on the SM  $t\bar{t}(2\ell)$   $p_T^{\text{miss}}$  templates in the high and low  $M_{T2}^{\ell\ell}$ -SF region after variation by  $\pm 1\sigma$  of the JES uncertainty, as represented by the dashed red ( $+1\sigma$ ) and blue ( $-1\sigma$ ) shapes. Uncertainty effects due to the jet energy resolution (JER) were found to be negligible.

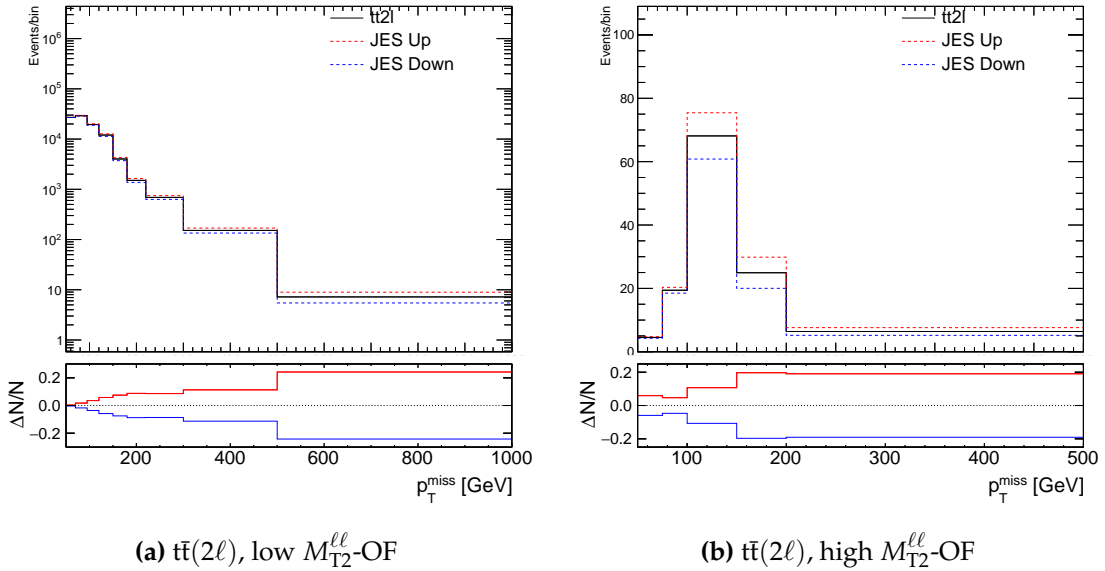


**Figure 6.12.:** The variation in the  $p_T^{\text{miss}}$  spectra for  $t\bar{t}(2\ell)$  in the low and high  $M_{T2}^{\ell\ell}$ -OF SRs due to the variation of the JES uncertainty by  $+1\sigma$  (red) and  $-1\sigma$  (blue). The normalized residuals of the “up” and “down” shapes are shown in the lower panel.

- **Fake  $p_T^{\text{miss}}$  uncertainty:** As discussed in Section 4.2.1, in perfect conditions, the SM  $t\bar{t}(2\ell)$  contribution should be suppressed below  $M_W$ , however in practice, the mismeasurement of  $p_T^{\text{miss}}$  is possible as a result of jet and lepton detector misreconstruction effects. Hence, SM  $t\bar{t}(2\ell)$  events with large values of “fake”  $p_T^{\text{miss}}$  leak into the high  $M_{T2}^{\ell\ell}$  SRs. Similarly, although genuine sources of  $p_T^{\text{miss}}$  are not expected in DY events, lepton mismeasurements lead to an observed “fake”  $p_T^{\text{miss}}$  in such events. Thus, in the high  $M_{T2}^{\ell\ell}$ -SF and  $M_{T2}^{\ell\ell}$ -OF categories, an uncertainty is assigned to the background  $p_T^{\text{miss}}$  shapes derived from simulation to account for potential mismodeling of the rate of events with large fake  $p_T^{\text{miss}}$  in simulation. This uncertainty is derived using Z bosons decaying to dielectrons and dimuons, as a function of hadronic recoil (i.e.  $p_T^{\text{miss}}$  with the two leptons removed), and also passing  $M_{T2}^{\ell\ell} > 110 \text{ GeV}$ . The difference between the simulation and data after the subtraction of non-DY events as expected from simulation, is taken as the uncertainty and added/subtracted to the nominal recoil distribution to

obtain the one standard deviation variations. A second-order polynomial is fit to the fake  $p_T^{\text{miss}}$  uncertainty scale factor distributions in an effort to smoothen the uncertainty as a function of the recoil, as shown in Figure 6.13. The effect on the DY and  $t\bar{t}(2\ell)$  templates in the high  $M_{T2}^{\ell\ell}$ -SF region after the variation of the  $\pm 1\sigma$  fake  $p_T^{\text{miss}}$  uncertainty is applied is shown in Figure A.7.

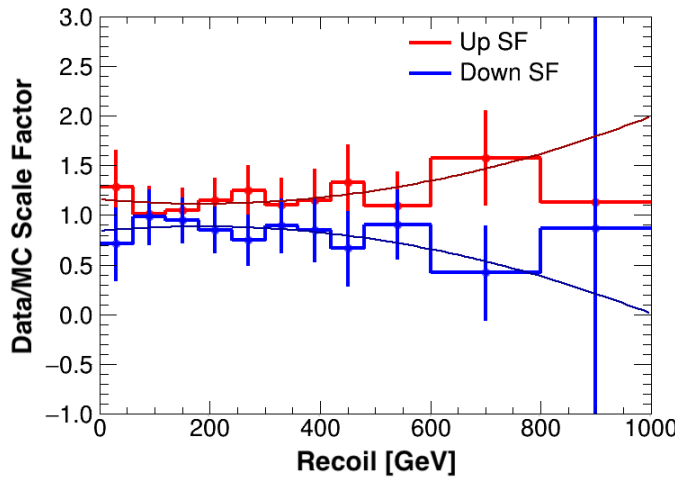


**Figure 6.13.:** The fake  $p_T^{\text{miss}}$  uncertainty at one standard deviation from the nominal recoil distribution as derived in simulation using Z bosons decaying to dielectrons and dimuons with  $M_{T2}^{\ell\ell} > 110$  GeV. In order to smoothen out the binned uncertainty, it is fit with a second-order polynomial.

- **Factorization and renormalization scales:** In order to estimate the effects incurred from missing corrections from higher order perturbative QCD calculations for background processes, the renormalization scale,  $\mu_R$ , and the factorization scale,  $\mu_F$ , employed in the simulation matrix-element generator are halved or doubled independently [97], and the changes are propagated to the  $p_T^{\text{miss}}$  templates. The variation also covers the uncertainty in the finite order QCD calculations which are reliant on the scale choice as well. This is accommodated via weights obtained directly from the generator information in the MC simulation where available. The uncertainty is considered to be uncorrelated among the different background processes.

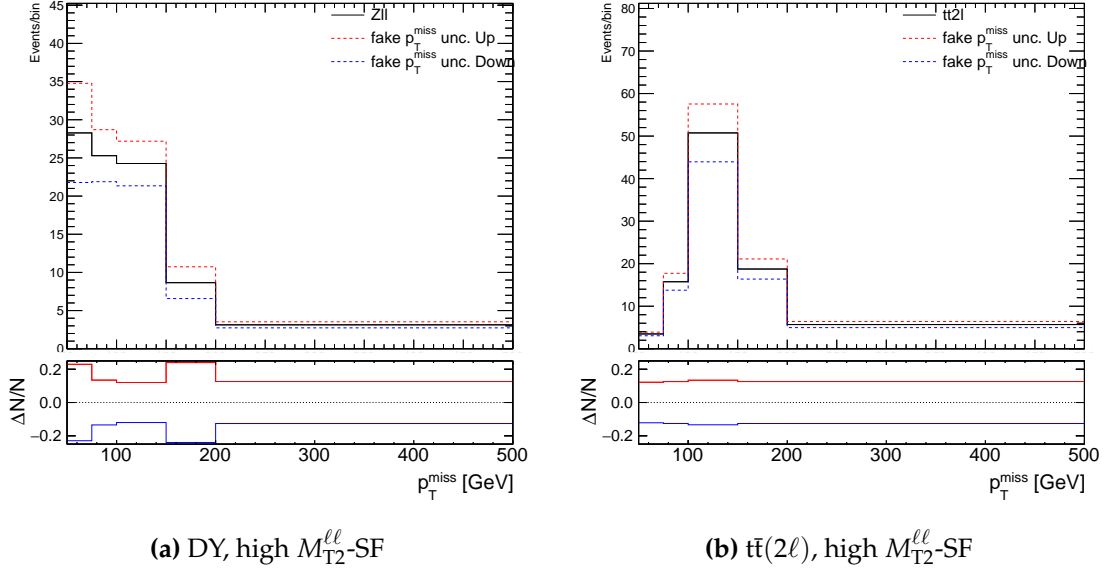


**Figure 6.14.:** The variation in the  $p_T^{\text{miss}}$  spectra for (a) DY and (b)  $t\bar{t}(2\ell)$  in the high  $M_{T2}^{\ell\ell}$ -SF SRs due to the variation of the fake  $p_T^{\text{miss}}$  uncertainty by  $+1\sigma$  (red) and  $-1\sigma$  (blue). The normalized residuals of the “up” and “down” shapes are shown in the lower panel.

- **Top quark  $p_T$  reweighting:** The top quark  $p_T$  spectrum as measured in differential top quark pair production is observed to be softer than that of simulation, as discussed in Section 5.1.1. In order to cover this effect, the scale factors derived in previous CMS measurements [91] are applied to the  $t\bar{t}$  simulation by default. The uncertainty is estimated from a comparison of the top  $p_T$  spectrum obtained without the reweighting applied.
- **Parton distribution function (PDF):** Uncertainties due to the choice of PDF used to simulate the hard scatter process are estimated by reweighting the simulation samples with the ensemble of 100 PDF replicas [98] provided by NNPDF3.0 [99].

## 6.5. Statistical analysis

The methods by which the statistical analysis is performed are outlined in the following section. A brief description of the model parameter estimation and statistical model inference methods are outlined. Finally, the means by which the signal is extracted is described. An in-depth discussion of statistical methods can be found in Ref. [100].

### 6.5.1. Maximum likelihood

The maximum likelihood estimates the best value of the parameters (i.e. signal strength and background shape and normalizations), for which the observed data has the highest probability of estimating the true parameter value according to the hypothesis model. Following the discussion in [100], supposing in a set of  $N$  events, we observe a set of measured quantities,  $\bar{x}$ . In the space of these observables we can define a set of bins,  $n_{bin}$ , and it is assumed that the number of events  $n_i$  in each bin  $i$  are Poisson-distributed such that,

$$\mathcal{P}(n_i | \lambda_i) = \frac{\lambda_i^{n_i} e^{-\lambda_i}}{n_i!}, \quad (6.8)$$

where  $\lambda_i$  is the number of expected events in the bin containing contributions from both signal and background processes such that  $\lambda = \mu s + b$ . The number of signal (background) events is denoted by  $s$  ( $b$ ), and subsequently the parameter  $\mu$  represents the signal strength scaling, where  $\mu = 0$  corresponds to the background-only hypothesis, and  $\mu = 1$  is the nominal signal hypothesis. The likelihood function is then simply the product of Poisson probabilities for all bins,

$$\mathcal{L} = \prod_{j=1}^N \frac{(\mu s_j + b_j)^{n_j}}{n_j!} e^{-(\mu s_j + b_j)}, \quad (6.9)$$

where the mean number of entries in the  $j$ th bin from signal and background are

$$s_j = s_{\text{tot}} \int_{\text{bin } j} f_s(x; \boldsymbol{\theta}_s) dx, \quad (6.10)$$

$$b_j = b_{\text{tot}} \int_{\text{bin } j} f_b(x; \boldsymbol{\theta}_b) dx. \quad (6.11)$$

The functions  $f_s(x; \boldsymbol{\theta}_s)$  and  $f_b(x; \boldsymbol{\theta}_b)$  are the *pdfs* of the variable  $x$  for signal and background events and  $\boldsymbol{\theta}_s$  and  $\boldsymbol{\theta}_b$  are the nuisance parameters described in Section 6.4, which characterize the shape of the *pdfs*. The integrals in Eq. 6.10 and Eq. 6.11 represent the probabilities for an event to be found in bin  $j$ , and  $s_{\text{tot}}$  and  $b_{\text{tot}}$  denote the total mean numbers of signal and background events, respectively. It is then clear that the likelihood in Eq. 6.9 is a function of the nuisance parameters,  $\mathcal{L}(\boldsymbol{\theta})$ , and the values of  $\boldsymbol{\theta}$  which maximize this quantity are said to fit the observation best.

### 6.5.2. Hypothesis testing

In order to determine whether to accept or reject a model depending on the outcome of a measurement, a frequentist test of a hypothesis is performed. In this case, we test the hypothesized value of the signal strength,  $\mu$ , which is interpreted as the ratio of the measured cross section,  $\sigma$ , to the predicted value from the theory model,  $\sigma_{\text{TH}}$ , such

that  $\mu = \frac{\sigma}{\sigma_{\text{TH}}}$ . Hence, a null value of  $\mu$  corresponds to an observation compatible with the SM background-only hypothesis, whereas if the observation is compatible with signal events as predicted by the model cross section, then  $\mu = 1$ .

Quantifying the level of agreement between the observation and a tested hypothesis is done via a test statistic  $q(\mu)$ , which is defined as the ratio of maximum likelihoods,

$$q(\mu) = \frac{\mathcal{L}(\mathcal{D} | \mu, \hat{\theta}(\mu))}{\mathcal{L}(\mathcal{D} | \hat{\mu}, \hat{\theta})} \quad (6.12)$$

where the  $\hat{\theta}(\mu)$  indicates the values of the profiled nuisance parameters  $\theta$ , which maximize  $\mathcal{L}$  for a fixed value of  $\mu$ , the dataset  $\mathcal{D}$ , and global observables. The denominator of the so-called *profile likelihood ratio* defined by Eq. 6.12 is the value of  $\mathcal{L}$  when evaluated with the maximum likelihood estimators (MLEs)  $\hat{\mu}$  and  $\hat{\theta}$ . The MLEs and profiled nuisance parameters can analogously minimize the quantity  $-2 \ln \mathcal{L}$ , so it is common to write the definition of the test statistic as,

$$q(\mu) = -2 \ln \frac{\mathcal{L}(\mu, \hat{\theta}(\mu))}{\mathcal{L}(\hat{\mu}, \hat{\theta})}, \mu' \leq \mu. \quad (6.13)$$

For the purposes of setting limits on theoretical parameters (i.e. determining the values of the parameters that are allowed or excluded given the available data) the test statistic  $q(\mu)$  is used to discriminate between the hypothesis of the signal being produced at a rate  $\mu$  from an alternative hypothesis of signal events being produced at a lesser rate  $\mu' < \mu$ . Thus, it is a test statistic for a one-sided alternative or moreover provides a one-sided upper limit. If the experiment were to be repeated multiple times,  $q(\mu)$  would take on different values, thus the test statistic itself has a particular

probability density function,  $f(q(\mu) | H)$ , dependent on the particular hypothesis,  $H$ , being tested. Then the probability that a given  $q(\mu)_{\text{obs}}$  is an equal or more “extreme” outcome than observed, assuming  $H$  is,

$$p = \int_{q(\mu)_{\text{obs}}}^{\infty} f(q(\mu) | H) dq(\mu). \quad (6.14)$$

The quantity in Eq. 6.14 and visualized in Figure 6.15, known as the *p-value*, indicates a worse agreement with the corresponding  $H$  for small *p*-values. In the language of discovery in high energy physics, it is customary to relate the *p*-value into a quantile of a unit Gaussian to express the significance  $Z$ , as shown in Figure 6.15. The area of the tail starting at an upward fluctuation of  $Z$  standard deviations from the mean of the Gaussian random variable, should be equal to the *p*-value. The transformation is defined formally as,

$$Z = \Phi^{-1}(1 - p) \quad (6.15)$$

where  $\Phi^{-1}$  is the inverse of the cumulative distribution of the single sided standard Gaussian. A  $5\sigma$  significance is the standard requirement in experimental particle physics to claim a discovery, which is analogous to a *p*-value of  $2.87 \times 10^{-7}$ .

In the absence of a discovery, such that the *p*-value determined from the observed data cannot exclude the background-only hypothesis, the upper limit on the signal strength parameter,  $\mu$ , is established. The one-sided modified frequentist confidence level ( $\text{CL}_s$ ) upper limit on  $\mu$  is defined as,

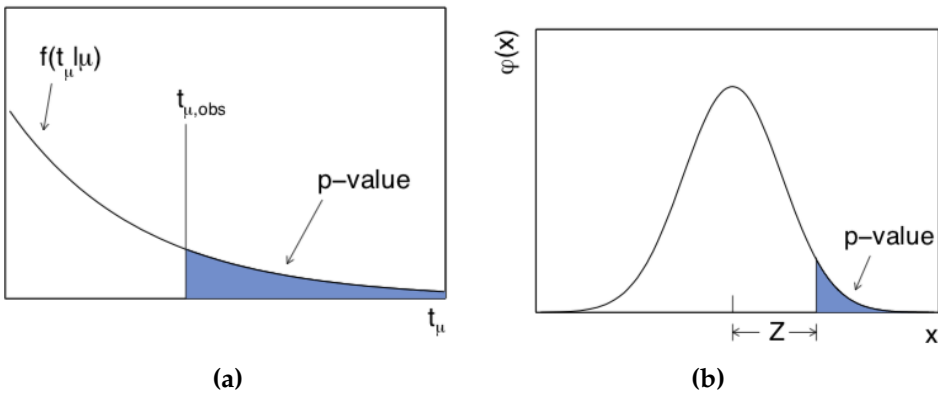


**Figure 6.15.:** A visualization of the relation (a) between the observed value of the test statistic  $q(\mu)_{\text{obs}}$ , the probability density function  $f(q(\mu) \mid H)$  and the  $p$ -value, and (b) between the  $p$ -value and the significance  $Z$ .

$$\text{CL}_s = \frac{p_\mu}{1 - p_0} \quad (6.16)$$

where  $p_0$  is the  $p$ -value determined given that the hypothesis under test is that of the SM background-only. In practice, results are calculated at 95%  $\text{CL}_s$  which is defined as the  $\mu$  that produces  $\text{CL}_s = 0.05$ .

### 6.5.3. Signal extraction

In order to extract the results, a binned maximum likelihood fit is performed simultaneously on the  $p_T^{\text{miss}}$  distributions in the SRs as defined in more detail in Section 6.3. A single strength parameter is used to scale the signal across all the SRs. The sources of systematic uncertainties are represented by nuisance parameters in the fit, as described in greater detail in Section 6.4.

The likelihood ratio defined by Eq. 6.13 is used to assess the fit for the saturated model, and provides a generalization of the  $\chi^2$  goodness-of-fit test as per [101]. The

fitted background-only  $p_T^{\text{miss}}$  distributions are shown in Figure 6.16 and Figure 6.17. The corresponding observed data yield and post-fit SM background expected yields are presented for the high and low purity categories in Table 6.1 and 6.2, respectively. The  $p$ -value of 0.06, as defined by Eq. 6.14, is determined from the distribution of the likelihood ratio obtained from pseudodata generated from the fitted simulation yields. No significant excess in the SRs is observed.

**Table 6.1.:** Background-only post-fit event yields passing selection in the  $M_{\text{T2}}^{\ell\ell} > 110 \text{ GeV}$  (high signal purity) category. The expected (pre-fit) yield is also shown for a pseudoscalar  $m_a = 100 \text{ GeV}$ ,  $m_\chi = 1 \text{ GeV}$  signal. The uncertainties include contributions from both systematic and statistical sources.

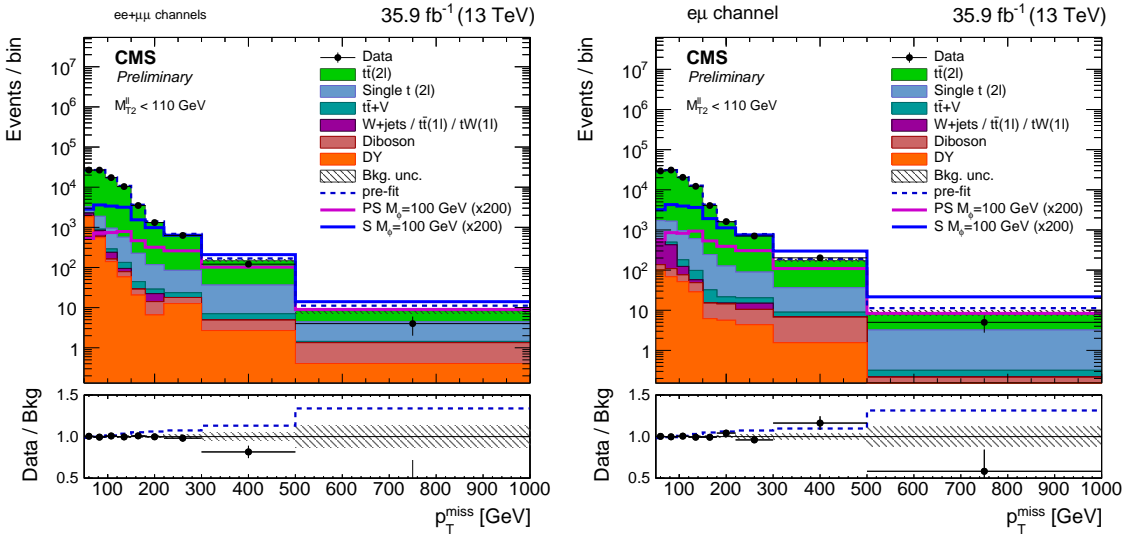
$M_{\text{T2}}^{\ell\ell} > 110 \text{ GeV}$		
	$ee + \mu\mu$	$e\mu$
Diboson	$3.83 \pm 0.51$	$1.42 \pm 0.58$
Drell-Yan	$68.51 \pm 9.88$	$0.85 \pm 0.51$
Single t ( $2\ell$ )	$7.34 \pm 1.51$	$8.59 \pm 1.88$
$t\bar{t} + V$	$7.83 \pm 1.12$	$5.87 \pm 0.95$
$t\bar{t}(2\ell)$	$77.67 \pm 5.60$	$104.91 \pm 7.49$
Fakes	$0.72 \pm 0.92$	$4.14 \pm 2.82$
SM Expected	$165.90 \pm 10.26$	$125.77 \pm 8.96$
Observed		$156$
$m_a = 100, m_\chi = 1$	$5.18 \pm 0.089$	$5.82 \pm 0.094$

#### 6.5.4. Post-fit diagnostics

The observed *pull* statistic in Eq. 6.17 as defined in [102], is used to assess whether the fit gives unbiased central values of the nuisance parameters and errors of correct coverage. The metric quantifies how far from the expected value, a nuisance parameter had to be “pulled” in order to find the maximum likelihood estimate. The pull is expected to follow a unit Gaussian, with a mean of 0 and unitary width.

**Table 6.2.:** Background-only post-fit event yields passing selection in the  $M_{T2}^{\ell\ell} < 110$  GeV (low signal purity) category. The expected (pre-fit) yield is also shown for a pseudoscalar  $m_a = 100$  GeV,  $m_\chi = 1$  GeV signal. The uncertainties include contributions from both systematic and statistical sources.

	$M_{T2}^{\ell\ell} < 110$ GeV	
	$ee + \mu\mu$	$e\mu$
Diboson	$178.05 \pm 10.85$	$148.68 \pm 9.19$
Drell-Yan	$2633.18 \pm 279.35$	$267.71 \pm 29.52$
Single t (2 $\ell$ )	$3356.63 \pm 553.19$	$3946.44 \pm 648.20$
t $\bar{t}$ + V	$232.94 \pm 31.56$	$256.39 \pm 33.33$
t $\bar{t}$ (2 $\ell$ )	$79534.15 \pm 702.17$	$94338.27 \pm 805.11$
Fakes	$689.18 \pm 322.88$	$792.42 \pm 80.64$
SM Expected	$86624.13 \pm 401.67$	$99749.92 \pm 469.50$
Observed	86619	99793
$m_a = 100, m_\chi = 1$	$19.63 \pm 0.17$	$22.70 \pm 0.19$



(a) low purity,  $ee + \mu\mu$  channel

(b) low purity,  $e\mu$  channel

**Figure 6.16.:** The background-only post-fit  $p_T^{\text{miss}}$  distributions in the low signal purity SRs. The expected (pre-fit)  $p_T^{\text{miss}}$  distributions for two example signals (scalar and pseudoscalar mediator,  $m_{\phi/a} = 100$  GeV) with  $m_\chi = 1$  GeV are scaled up by a factor of 200. The dashed blue line represents the total expected (pre-fit) MC background  $p_T^{\text{miss}}$  shape, and the subsequent ratio between the pre-fit and post-fit shape in the lower ratio panel. The last bin of the distributions includes overflow. Statistical and systematic uncertainties are shown.

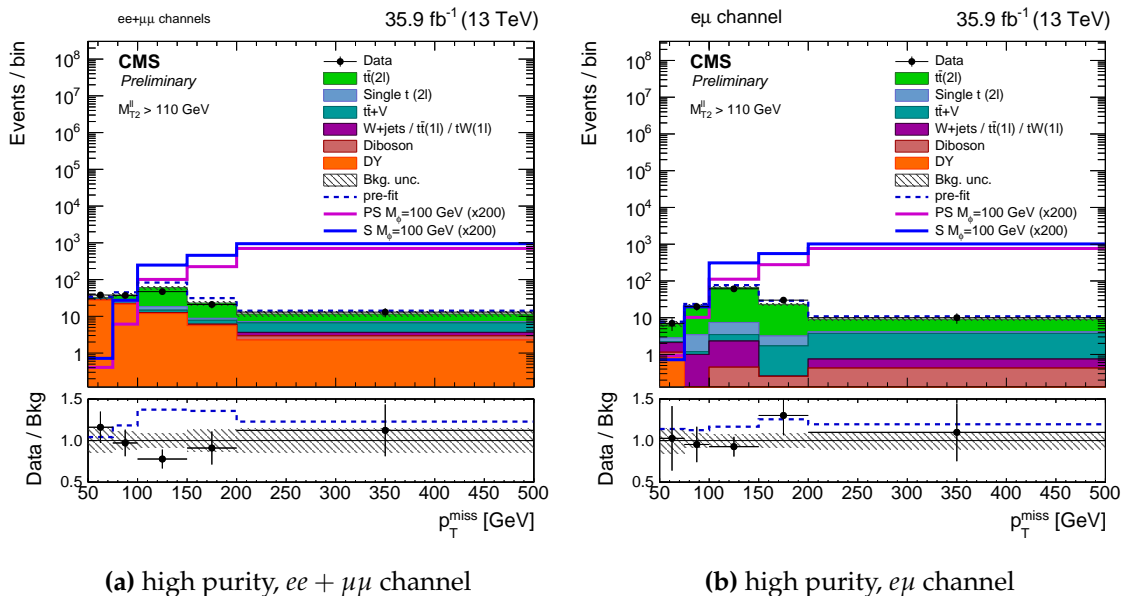


**Figure 6.17.**: The background-only post-fit  $p_T^{\text{miss}}$  distributions in the high signal purity SRs. The pre-fit  $p_T^{\text{miss}}$  distributions for two example signals (scalar and pseudoscalar mediator,  $m_{\phi/a} = 100 \text{ GeV}$ ) with  $m_\chi = 1 \text{ GeV}$  are scaled up by a factor of 200. The dashed blue line represents the total expected (pre-fit) MC background  $p_T^{\text{miss}}$  shape, and the subsequent ratio between the pre-fit and post-fit shape in the lower ratio panel. The last bin of the distributions includes overflow. Statistical and systematic uncertainties are shown.

$$\text{pull}(\theta) = \frac{\theta^{\text{fit}} - \theta^{\text{true}}}{\sigma_{\theta^{\text{fit}}}} \quad (6.17)$$

The *impact* quantity [103] is measured as a means to gauge how much the parameter of interest (POI), that being the signal strength parameter  $\mu$ , depends on changes in the nuisance parameters. The impact of a nuisance parameter is defined as,

$$\text{Impact}(\theta) = \Delta\mu^{\pm} = \hat{\mu}_{\theta^{\text{true}} \pm \sigma_{\theta}} - \hat{\mu}, \quad (6.18)$$

where  $\hat{\mu}_{\theta^{\text{true}} \pm \sigma_{\theta}}$  is defined as the maximum likelihood estimator of  $\mu$  when every nuisance parameter except  $\theta$  is profiled, and  $\theta$  is set to its expectation value ( $\theta^{\text{true}}$ ) plus or minus one standard deviation according to the post-fit uncertainty. The relative importance of the various systematic uncertainties are determined according to their impact on  $\mu$ , since not all nuisance parameters are of equal importance in the fitting procedure.

The pulls are computed for the nuisance parameters representing the systematic uncertainties defined in Section 6.4. Table 6.3 relates the nuisance name as seen in the pulls plot in Figure 6.18 to the corresponding systematic uncertainty. The table also summarizes which process is affected, and if the uncertainty affects the shape or normalization of a process. Unless indicated under the description heading, a nuisance is treated as correlated across both same and opposite flavor, high and low  $M_{T2}^{\ell\ell}$  signal regions, and across the signal and all background processes. The pulls in Figure 6.18 are computed considering the background-only hypothesis (red markers) and signal-plus-background hypothesis (blue markers), where the signal under consideration is a

psuedoscalar mediator with  $m_a = 100 \text{ GeV}$  and  $m_\chi = 1 \text{ GeV}$ . None of the nuisances are pulled significantly relative to the a priori uncertainties (grey hatching). The most constrained nuisances are the JES (`CMS_scale_j`), constrained to 0.14 of the a priori value, and the renormalization/factorization scale uncertainty on the  $t\bar{t}(2\ell)$  (`tt_qcdScale`), constrained to the 0.27 of the a priori value. The level of constraint on the JES uncertainty is quite strong, but is not necessarily unwarranted or alarming for that matter. As given in Section 6.4.1, the procedure used to assess the effects of the JES uncertainty are such that the energy of the two or more required jets in an event is raised and lowered by the  $1\sigma$  uncertainty coherently. The change in energy is propagated to the  $p_T^{\text{miss}}$  to obtain the “up” and “down”  $p_T^{\text{miss}}$  templates. Varying the energy in a correlated way where events can have a high jet multiplicity can yield large variations in the  $p_T^{\text{miss}}$ . To this end, the uncertainty applied is not necessarily incorrect but is instead very conservative since it is unlikely that all the jet energies in an event are mismeasured in the same direction. In addition, the statistical power of the low  $M_{T2}^{\ell\ell}$  region is quite significant, thus a conservative per-event uncertainty combined with a large sample size will unsurprisingly yield the level of constraint observed.

Name	Description	Type	Signal	$t\bar{t}(2\ell)$	Single t ( $2\ell$ )	$t\bar{t}+V$	Diboson	Drell-Yan	Fakes
CMS_eff_b	b-tagging efficiency	InN	✓	✓	✓	✓	✓	✓	✓
CMS_eff_e	electron reconstruction / selection efficiency	InN	✓	✓	✓	✓	✓	✓	✓
CMS_eff_m	muon reconstruction / selection efficiency	InN	✓	✓	✓	✓	✓	✓	✓
CMS_eff_mistag	b mistag rate	InN	✓	✓	✓	✓	✓	✓	✓
CMS_norm_ST	single top normalization	InN	✓	✓	✓	✓	✓	✓	✓
CMS_scale_j	jet energy scale	InN	✓	✓	✓	✓	✓	✓	✓
CMS_scale_pu	pile up shape	InN	✓	✓	✓	✓	✓	✓	✓
RecoilCorr	fake $p_T^{\text{miss}}$ uncertainty (high $M_{T2}^{\ell\ell}$ )	InN	✓	✓	✓	✓	✓	✓	✓
Zjets_qcdScale	factorization/renormalization uncertainty on DY	InN	✓	✓	✓	✓	✓	✓	✓
hi_ee_Rinout	$R_{\text{in}/\text{out}}$ uncertainty: high $M_{T2}^{\ell\ell}$ , $ee$ events	InN	✓	✓	✓	✓	✓	✓	✓
hi_mm_Rinout	$R_{\text{in}/\text{out}}$ uncertainty: high $M_{T2}^{\ell\ell}$ , $\mu\mu$ events	InN	✓	✓	✓	✓	✓	✓	✓
lo_ee_Rinout	$R_{\text{in}/\text{out}}$ uncertainty: low $M_{T2}^{\ell\ell}$ , $ee$ events	InN	✓	✓	✓	✓	✓	✓	✓
lo_mm_Rinout	$R_{\text{in}/\text{out}}$ uncertainty: low $M_{T2}^{\ell\ell}$ , $\mu\mu$ events	InN	✓	✓	✓	✓	✓	✓	✓
hi_ee_fakes	fakes uncertainty: high $M_{T2}^{\ell\ell}$ , $ee$ events	InN	✓	✓	✓	✓	✓	✓	✓
hi_em_fakes	fakes uncertainty: high $M_{T2}^{\ell\ell}$ , $e\mu$ events	InN	✓	✓	✓	✓	✓	✓	✓
hi_mm_fakes	fakes uncertainty: high $M_{T2}^{\ell\ell}$ , $\mu\mu$ events	InN	✓	✓	✓	✓	✓	✓	✓
lo_ee_fakes	fakes uncertainty: low $M_{T2}^{\ell\ell}$ , $ee$ events	InN	✓	✓	✓	✓	✓	✓	✓
lo_em_fakes	fakes uncertainty: low $M_{T2}^{\ell\ell}$ , $e\mu$ events	InN	✓	✓	✓	✓	✓	✓	✓
lo_mm_fakes	fakes uncertainty: low $M_{T2}^{\ell\ell}$ , $\mu\mu$ events	InN	✓	✓	✓	✓	✓	✓	✓
lumi_13TeV	luminosity	InN	✓	✓	✓	✓	✓	✓	✓
pdf	parton distribution function	InN	✓	✓	✓	✓	✓	✓	✓
topPt	top $p_T$ modeling	InN	✓	✓	✓	✓	✓	✓	✓
trigeff_ll	dilepton trigger efficiency	InN	✓	✓	✓	✓	✓	✓	✓
ttV_qcdScale	dilepton trigger efficiency uncertainty on $t\bar{t}+V$	InN	✓	✓	✓	✓	✓	✓	✓
tt_qcdScale	factorization/renormalization uncertainty on $t\bar{t}(2\ell)$	InN	✓	✓	✓	✓	✓	✓	✓

**Table 6.3:** A summary of the naming convention for the nuisance parameters used in the fit, whether each is implemented as “InN” (normalization uncertainty) or “shape” (shape uncertainty), and which processes each affects. Unless indicated under the description heading, a nuisance is treated as correlated across both same and opposite flavor, high and low  $M_{T2}^{\ell\ell}$  signal regions, and across the signal and all background processes.

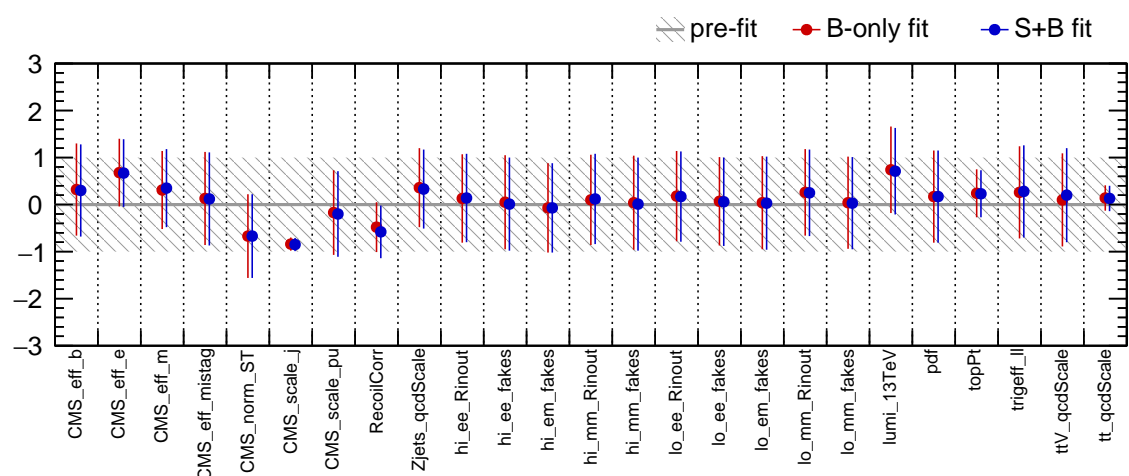


**Figure 6.18.**: Background-only (red) and signal-plus-background (blue) post-fit nuisance pulls.



# Chapter 7.

## Dark matter interpretation

This chapter covers the results and interpretation of the fitting procedure described in the previous chapter, including the upper limits on signal cross sections for the  $t\bar{t}+\chi\bar{\chi}$  process in the dilepton channel presented in Section 7.1. The results presented in this work have been combined with the  $t\bar{t}+\chi\bar{\chi}$  searches performed using the all-hadronic and lepton+jets  $t\bar{t}$  decay modes as presented in [104]. The sensitivity in the combined search is driven by the all-hadronic channel, however this work contributes significantly to the sensitivity for scalar mediated signal models with  $m_\phi < 50 \text{ GeV}$ , where the softer signal  $p_T^{\text{miss}}$  spectra are exploited. The CMS  $t\bar{t}+\chi\bar{\chi}$  search performed in 2016 provides the best sensitivity for low mediator mass models when compared with other spin-0 Mono-X LHC searches, including monojet [105]. Section 7.2 presents the results in the same planes as results from dedicated direct DM detection experiments.

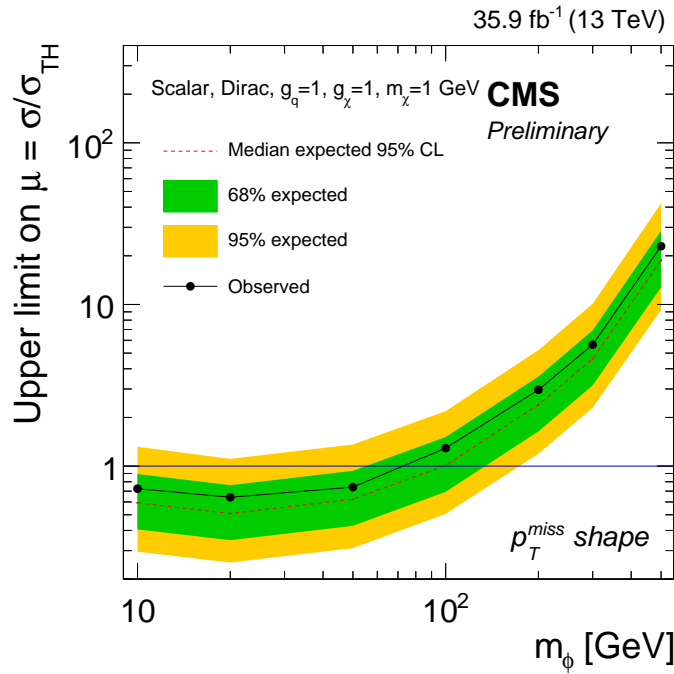
## 7.1. Upper limits on $t\bar{t}(2\ell) + \chi\bar{\chi}$ production at the LHC

The background-only post-fit yields presented in Table 6.1 and Table 6.2 reveal an observed yield compatible with the events expected from SM backgrounds, within statistical and systematic uncertainties. Thus, without a significant excess of events expected over the SM processes, 95% CL<sub>s</sub> upper limits on the signal strength parameter  $\mu$ , defined in Section 6.5.3 as the ratio of the observed cross section to the theoretical model cross section, are set. The expected and observed upper limits on  $\mu$  for signal models with varying S and PS mediator masses and  $m_\chi = 1$  GeV are listed in Table 7.1, along with the  $\pm 1\sigma$  and  $\pm 2\sigma$  uncertainties on the expected limit. Recalling the discussion in Section 4.1, the more stringent limit at low mediator mass for S compared to PS models can be understood as a manifestation of the order of magnitude difference in cross section between the S and PS mediated DM production at low mass. A similar reasoning is followed at high mediator mass, when the cross section for PS models becomes equivalent or marginally larger than the S mediated production rate, where it is observed that the upper limit is more comparable between S and PS models than at low mass. The results shown in the tables are visualized in Figure 7.1a and Figure 7.1b as a function of  $m_\phi$ , where the couplings are assumed to be  $g_q = g_\chi = 1$  and  $m_\chi = 1$  GeV. The logarithmic scaling of the x and y axes in Figure 7.1a and Figure 7.1b somewhat conceal the sharp rise in the expected and observed upper limits beginning at  $m_\phi \approx 300$  GeV. However, following the discussion in Section 1.5 regarding the enhancement of  $t\bar{t}$  production to the minimal mediator width in the region  $m_\phi > 2m_{\text{top}}$ , this rising trend is unsurprising, as the  $\chi\bar{\chi}$  production mode is no longer dominant and therefore the cross section for DM production drops off drastically. The rise in upper limit is also noticeably sharper for the S compared to the PS mediated signal models owing to the kinematic suppression of S compared to PS production as discussed in Section 4.1. In the high  $M_{T2}^{\ell\ell}$  category post-fit  $p_T^{\text{miss}}$

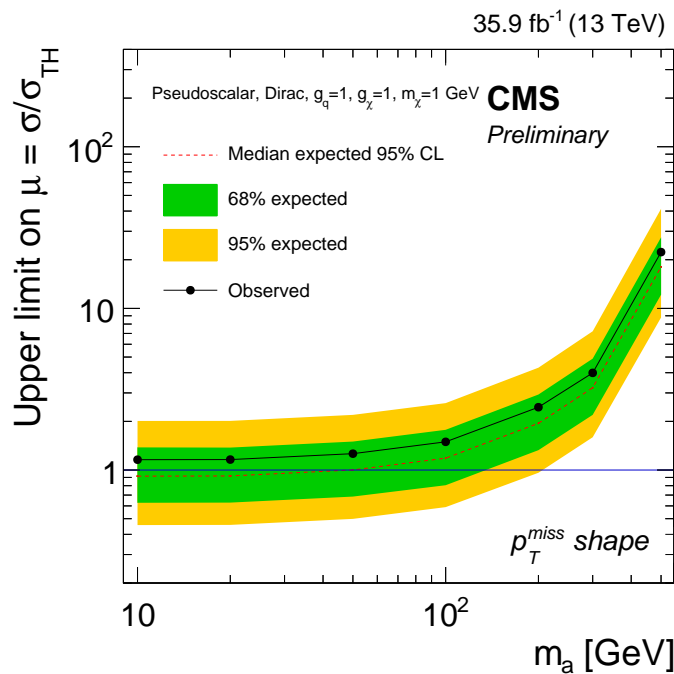
Model ( $m_\phi, m_\chi$ ) [GeV]	Obs.	Exp.	$[-1\sigma, +1\sigma]$	$[-2\sigma, +2\sigma]$
S 10, 1	0.72	0.59	[0.41, 0.89]	[0.30, 1.32]
S 20, 1	0.64	0.51	[0.35, 0.76]	[0.25, 1.11]
S 50, 1	0.74	0.62	[0.43, 0.94]	[0.31, 1.36]
S 100, 1	1.29	1.01	[0.69, 1.51]	[0.51, 2.19]
S 200, 1	2.97	2.40	[1.64, 3.58]	[1.19, 5.22]
S 300, 1	5.64	4.61	[3.16, 6.91]	[2.30, 10.11]
S 500, 1	22.93	18.74	[12.78, 28.52]	[9.26, 42.20]
PS 10, 1	1.16	0.92	[0.63, 1.38]	[0.46, 2.01]
PS 20, 1	1.16	0.92	[0.63, 1.38]	[0.46, 2.01]
PS 50, 1	1.26	1.00	[0.69, 1.50]	[0.50, 2.19]
PS 100, 1	1.49	1.18	[0.81, 1.77]	[0.59, 2.59]
PS 200, 1	2.45	1.95	[1.33, 2.93]	[0.96, 4.30]
PS 300, 1	3.99	3.23	[2.19, 4.89]	[1.60, 7.22]
PS 500, 1	22.29	18.06	[12.15, 27.49]	[8.78, 41.31]

**Table 7.1.:** Observed and expected upper limits at 95% CL<sub>s</sub> on  $\mu$  as a function of scalar (S) and pseudoscalar (PS) mediator masses for  $m_\chi = 1$  GeV with  $\pm 1\sigma$  and  $\pm 2\sigma$  uncertainties on the expected limits.

distributions shown in Figure 6.17, a modest excess of observed events over the expected SM backgrounds can be seen at high  $p_T^{\text{miss}}$  for both flavor categories. As a result, this causes the observed upper limits for both S and PS mediators to be consistently 15 – 25% weaker than the corresponding expected limits across the  $m_\phi$  range in the absence of a signal. Contrary to mass peak searches where the postulated signal may be localized in a window of the mass distribution being fit, this search would anticipate an excess over a non-localized range of the  $p_T^{\text{miss}}$  distribution, thus also explaining the uniformity of the weaker observed compared to expected limits. The range of  $m_\phi$  are referred to as excluded by the search, when the upper limit on  $\mu$  is less than 1. As can be seen in Figure 7.1a and Figure 7.1b, the observed (expected) 95% CL<sub>s</sub> exclusions for a S mediator are  $m_\phi < 74(99)$  GeV, while for a PS mediator, the expected exclusion is  $m_a < 50$  GeV, and no exclusion is observed.



(a) Upper limits for scalar mediators



(b) Upper limits for pseudoscalar mediators

**Figure 7.1.:** The expected (red dashed) and observed (solid black) 95% CL<sub>s</sub> upper limits on the  $t\bar{t} + \chi\bar{\chi}$  signal strength in the dilepton channel for various (a) scalar and (b) pseudoscalar mediator masses where  $m_\chi = 1$  GeV and  $g_q = g_\chi = 1$  is assumed. The green (yellow) band represents the 68% (95%) interval of probability around the expected limit. The results are obtained using 35.9 fb<sup>-1</sup> collected by the CMS detector in 2016.

The 1D mediator exclusion range observed and expected for the scalar mediated  $t\bar{t} + \chi\bar{\chi}$  signal in Figure 7.1a is expanded into a 2D contour as a function of  $m_\phi$  and  $m_\chi$  as shown in Figure 7.2. The 1D upper limit curves can be thought of as slices across the x axis ( $m_\phi$ ) for a given y value ( $m_\chi$ ) in the 2D plane. The solid (finely dashed) contour encloses the region where the observed (expected) upper limit on  $\mu$  is less than 1. The triangular nature of the exclusion contour is based on the grounding assumption that the kinematics for a given  $m_\phi$  do not change dramatically as a function of  $m_\chi$ , provided the DM particles are produced sufficiently on-shell. In addition, as the on/off-shell threshold (dashed diagonal) line is approached, both the width as given by equation (1.38) and the cross section fall monotonically and plateau at very small, but non-zero values, thus the exclusion contour runs close to the diagonal but does not cross. The narrow mediator width would nominally enhance the cross section in such a limiting case as the threshold regime, however the allowable phase space for the decay products is greatly reduced at  $m_\phi \approx 2m_\chi$ , ultimately suppressing the total cross section.

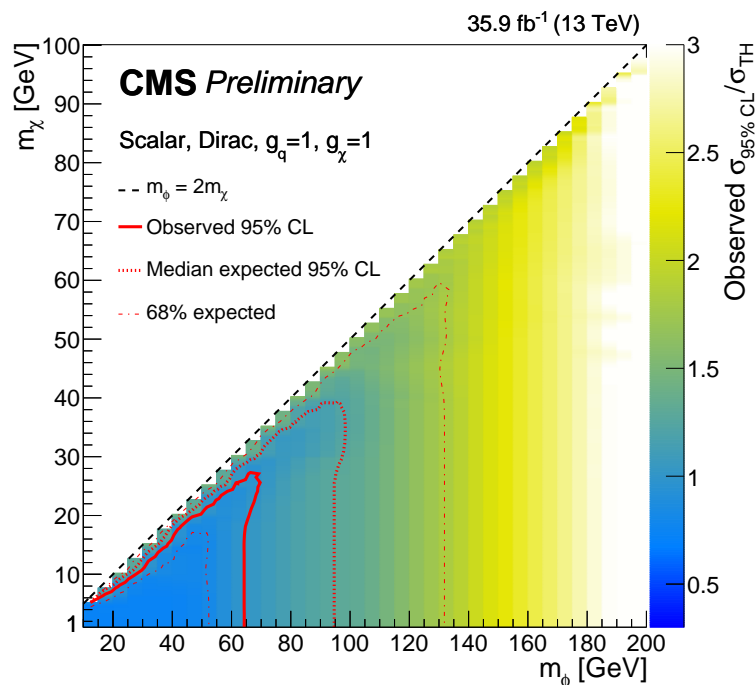


**Figure 7.2.:** The exclusion limits at 95%  $\text{CL}_s$  on the signal strength parameter  $\mu$  for the  $t\bar{t} + \chi\bar{\chi}$  process in the dilepton channel, computed as a function of the mediator mass and DM mass, assuming a scalar mediator. The mediator couplings are assumed to be  $g_q = g_\chi = 1$ .

## 7.2. Comparison with direct detection

The problem of DM is one of many dimensions, thus many independent and complementary approaches are required in attempts to solve it. Although this work does not provide evidence for a potential WIMP discovery, the role that collider detection plays in the search for DM is important in relation to ID and DD methods. The latter are necessary for determining the existence of DM particles whether through nuclear scattering, or annihilation to ordinary particles. From one perspective, these approaches can establish DM particle existence and provide information on the SM particles it may interact with. Particle accelerator production of DM then allows for the detailed study of DM particle properties under a controlled environment. Characterization of DM particle properties would subsequently allow particle physicists to make an appropriate decision on the theoretical framework that contains the new particle. Conversely, supposing a WIMP discovery is made via a collider search, such as a weakly interacting neutralino, and its properties such as decay modes, spin-parity, and mass can be characterized at the LHC; it then remains for the ID and DD experiments to ascertain that the new particle is indeed a DM particle. As a result of the complementarity of the approaches, the interpretation of results from different detection methods is instrumental in mapping out the search phase space.

To facilitate the comparison with constraints from DD experiments of the type mentioned in Section 1.4.2, the exclusion contours obtained from the scalar  $t\bar{t} + \chi\bar{\chi}$  model as shown in Figure 7.2 are calculated at 90% CL<sub>s</sub>. Subsequently, the upper limits on  $\mu$  are translated to upper limits on the SI DM-nucleon scattering cross section via the approach taken from [106] as briefly described in the proceeding section.

### 7.2.1. Spin-indepedent comparison

The general form of the SI DM-nucleon scattering cross section is,

$$\sigma_{\text{SI}} = \frac{f^2(g_q) g_\chi^2 m_r^2}{\pi m_\phi^4} \quad (7.1)$$

where  $m_r = m_N m_\chi / (m_N + m_\chi)$  is the DM-nucleon reduced mass, as in equation (1.33), with  $m_N \simeq 0.939$  GeV being the approximate nucleon mass. The mediator-nucleon coupling, denoted by  $f(g_q)$ , has a non-trivial dependence on the mediator-quark couplings and the Higgs boson vacuum expectation value, so the full definition is omitted. However, using the most state-of-the-art values for these dependencies from [107] and [108], the numerical value of  $f(g_q)$  is,

$$f(g_q) = 1.16 \times 10^{-3} g_q. \quad (7.2)$$

Thus, equation (7.1) takes the form,

$$\sigma_{\text{SI}} \simeq 6.9 \times 10^{-43} \left( \frac{g_q g_\chi}{1} \right)^2 \left( \frac{125 \text{ GeV}}{m_\phi} \right)^4 \left( \frac{m_r}{1 \text{ GeV}} \right)^2. \quad (7.3)$$

As a result, the upper limit on  $\mu$  for the scalar-mediated  $t\bar{t}(2\ell) + \chi\bar{\chi}$  process is presented as an exclusion bound in the  $m_\chi$ - $\sigma_{\text{SI}}$  plane in Figure 7.3. The assumptions made in the translation include that the DM particle is a Dirac fermion, the coupling values are  $g_q = g_\chi = 1$ , and the CMS expected and observed exclusions are calculated

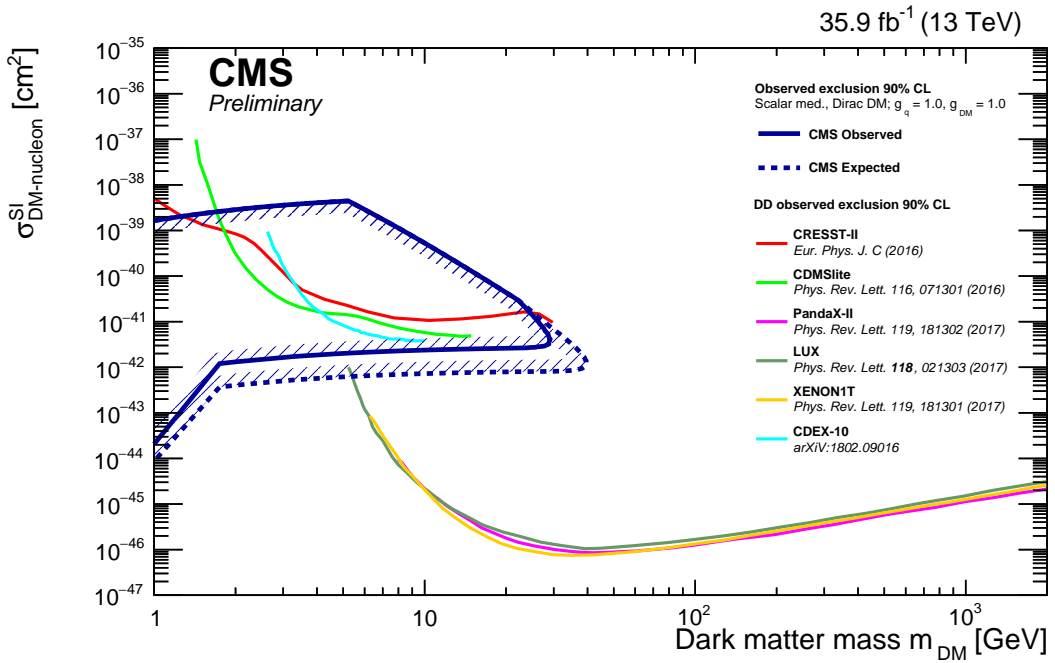


**Figure 7.3.:** A comparison of the  $t\bar{t}(2\ell)+\chi\bar{\chi}$  scalar-mediated results (CMS expected and observed lines) to the exclusion contours of the LUX, PandaX-II, XENON1T, CDEX-10, CDMSlite, and CRESST-II limits in the  $m_\chi$ - $\sigma_{\text{SI}}$  plane. The DM particle is assumed to be a Dirac fermion and  $g_q = g_\chi = 1$ .

at 90% CL<sub>s</sub>, as is standard in the DD community. In the translation performed using equation (7.3), for a given  $m_\chi$ , the  $m_\phi$  value used is the one for which the upper limit on  $\mu$  is equal to one. At  $m_\chi \gtrsim 5$  GeV, the larger dual-phase noble gas detectors discussed in Section 1.4.2 greatly constrain the search phase space. In contrast, the collider limits presented in this work are the most constraining at low DM mass, a fact well-supported by the strong constraints at low  $m_\phi$  as seen in the upper limit curve in Figure 7.1a where  $m_\chi = 1$  GeV.



# Chapter 8.

## Conclusions

A search for an excess of events with large  $p_T^{\text{miss}}$  produced in association with a top quark pair decaying to the dilepton final state has been presented, using proton-proton collisions. The integrated luminosity of the data sample used corresponds to  $35.9 \text{ fb}^{-1}$ , and was collected by the CMS detector at  $\sqrt{s} = 13 \text{ TeV}$  at the LHC during 2016. Observations are consistent with no significant deviation from the SM background expectation in the  $p_T^{\text{miss}}$  spectrum, in same and opposite lepton flavor channels. Results are interpreted in terms of simplified dark matter (DM) models with scalar and pseudoscalar mediators. Assuming coupling values of  $g_q = g_\chi = 1$  and DM mass  $m_\chi = 1 \text{ GeV}$ , the observed (expected) 95% CL<sub>s</sub> exclusions for a scalar mediator are  $m_\phi < 74$  (99) GeV, and the expected exclusion for a pseudoscalar mediator is  $m_a < 50 \text{ GeV}$ , while no pseudoscalar mediator exclusion is observed. This result improves upon the previous search for DM production in association with a top quark pair [109] performed using a data sample with integrated luminosity of  $2.2 \text{ fb}^{-1}$  collected by the CMS detector at  $\sqrt{s} = 13 \text{ TeV}$  at the LHC during 2015. The previous search fell short of observing and expecting to observe an exclusion at 95% CL<sub>s</sub> for simplified DM models with scalar and pseudoscalar mediators.



# Appendix A.

## Shape systematics

In the binned likelihood fit, systematics are taken into account in the form of nuisance parameters. In cases where the nuisance parameter can affect the  $p_T^{\text{miss}}$  shape and normalization of a given signal or background process, it is necessary to construct the  $p_T^{\text{miss}}$  shape after the  $\pm 1\sigma$  uncertainty variation is propagated to this observable. The relevant shape systematics are detailed in Section 6.4.1, and are shown for the dominant background, SM  $t\bar{t}(2\ell)$  in Section A.1 and for a scalar mediated signal with  $m_\phi = 10 \text{ GeV}$  and  $m_\chi = 1 \text{ GeV}$  in Section A.2.

## A.1. $t\bar{t}(2\ell)$ shape systematics

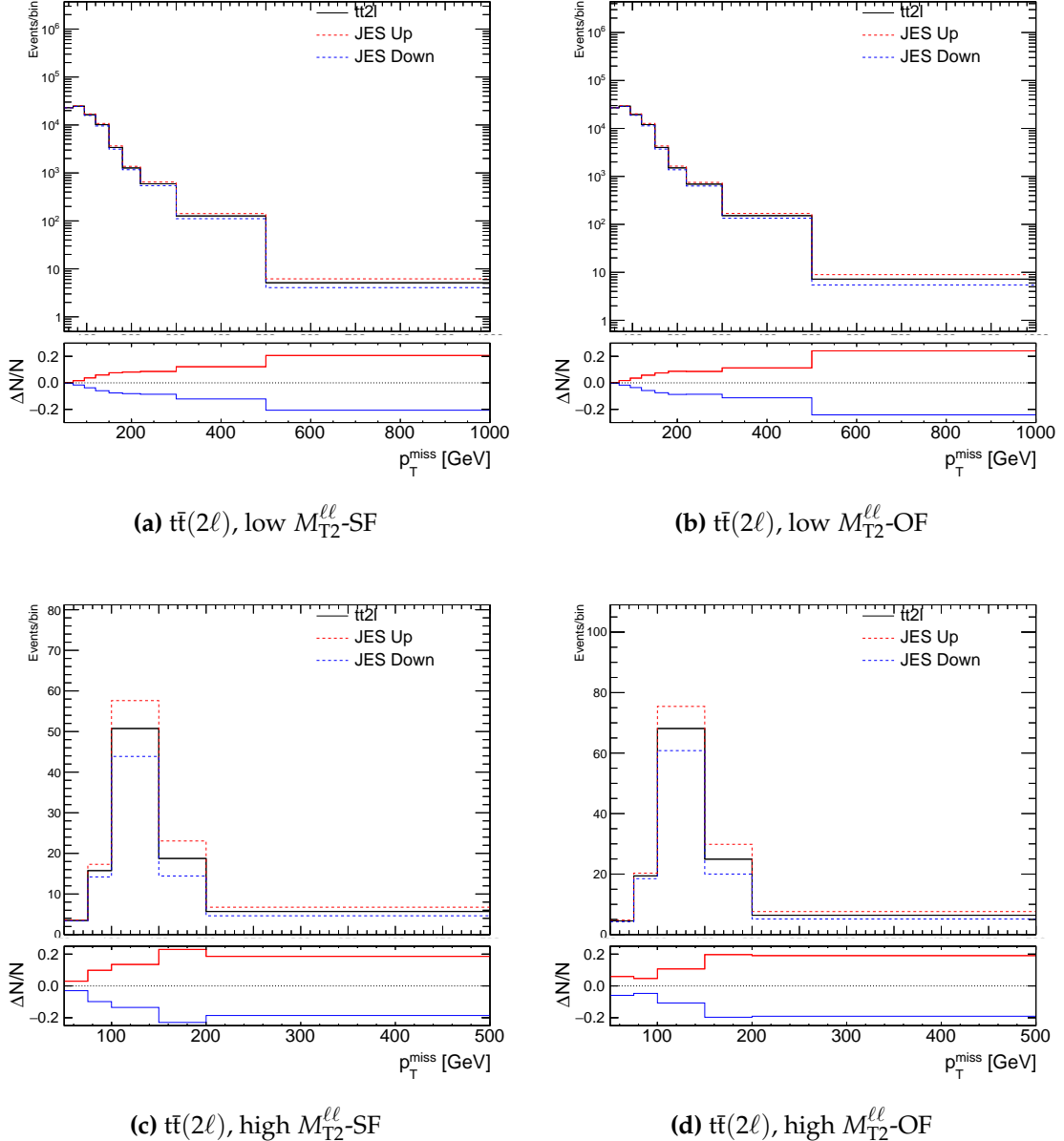


**Figure A.1.:** The variation in the  $p_T^{\text{miss}}$  spectra for  $t\bar{t}(2\ell)$  in the low and high  $M_{T2}^{\ell\ell}$  SRs due to the variation of the JES uncertainty by  $+1\sigma$  (red) and  $-1\sigma$  (blue). The normalized residuals of the “up” and “down” shapes are shown in the lower panel.

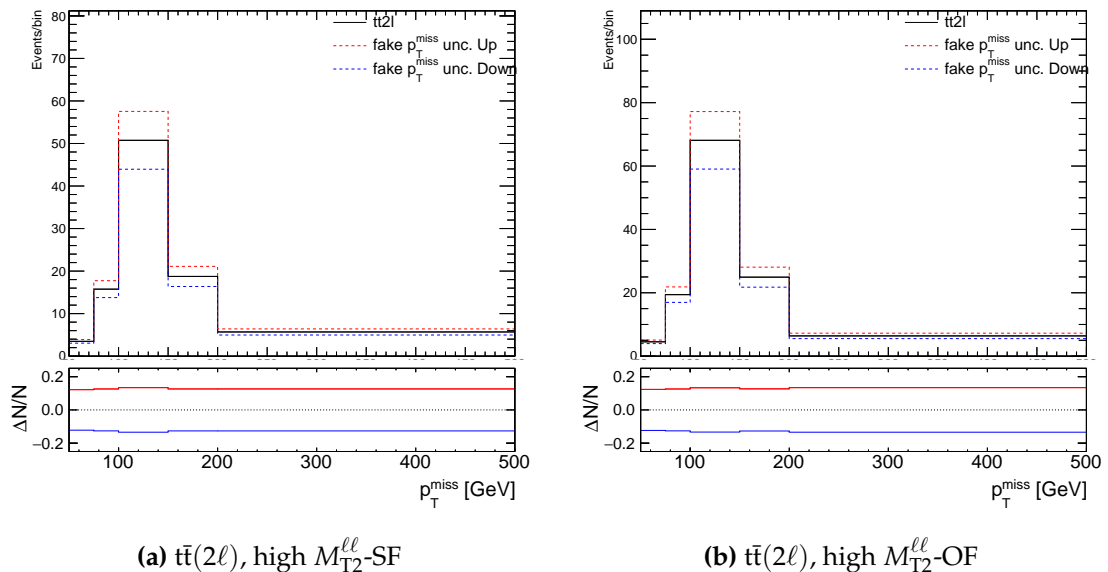


**Figure A.2:** The variation in the  $p_T^{\text{miss}}$  spectra for  $t\bar{t}(2\ell)$  in the high  $M_{T2}^{\ell\ell}$  SRs due to the variation of the fake  $p_T^{\text{miss}}$  uncertainty by  $+1\sigma$  (red) and  $-1\sigma$  (blue). The normalized residuals of the “up” and “down” shapes are shown in the lower panel.

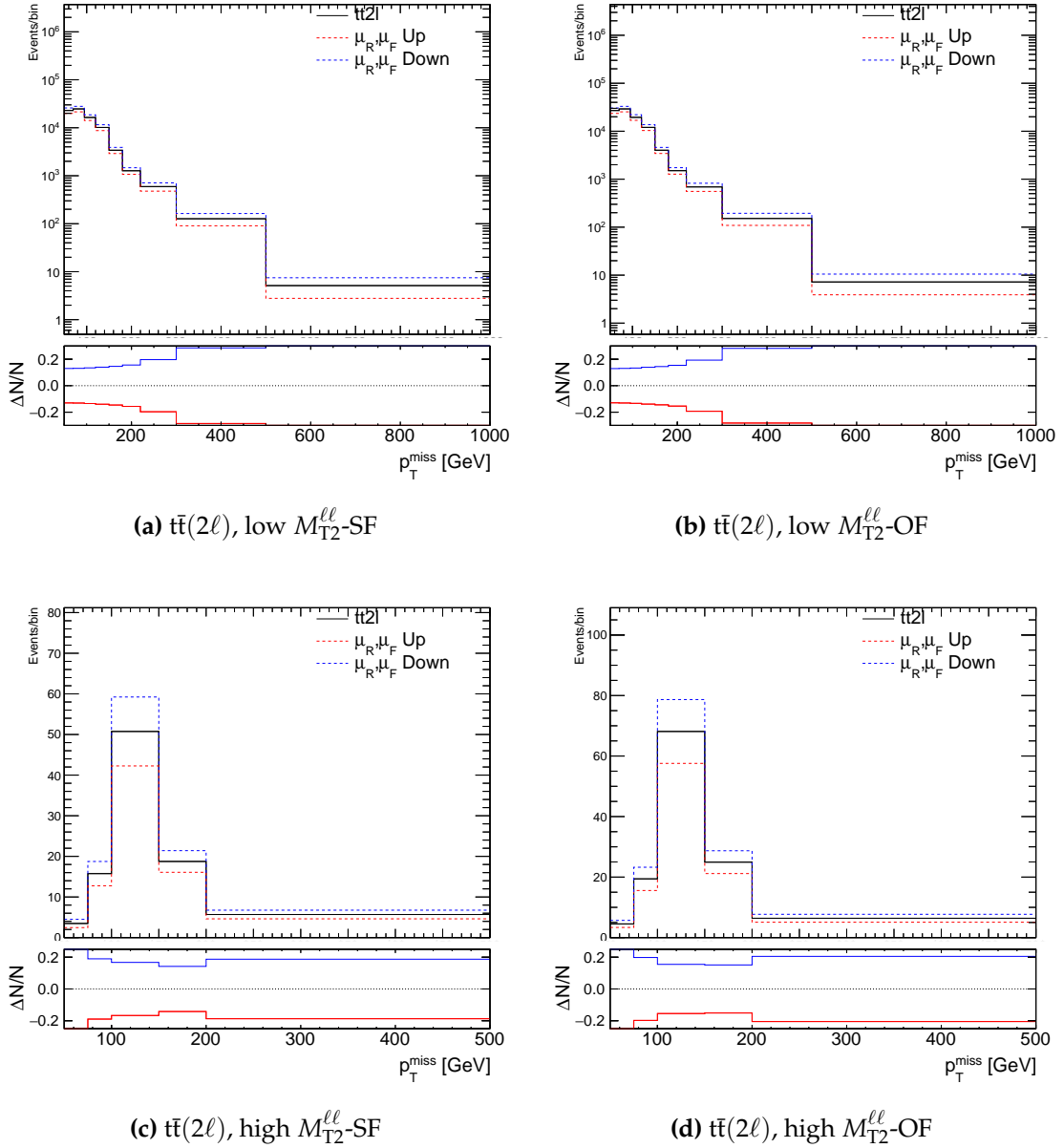


**Figure A.3.:** The variation in the  $p_T^{\text{miss}}$  spectra for  $t\bar{t}(2\ell)$  in the low and high  $M_{T2}^{\ell\ell}$  SRs due to the variation of the factorization and renormalization scales by  $+1\sigma$  (red) and  $-1\sigma$  (blue). The normalized residuals of the “up” and “down” shapes are shown in the lower panel.

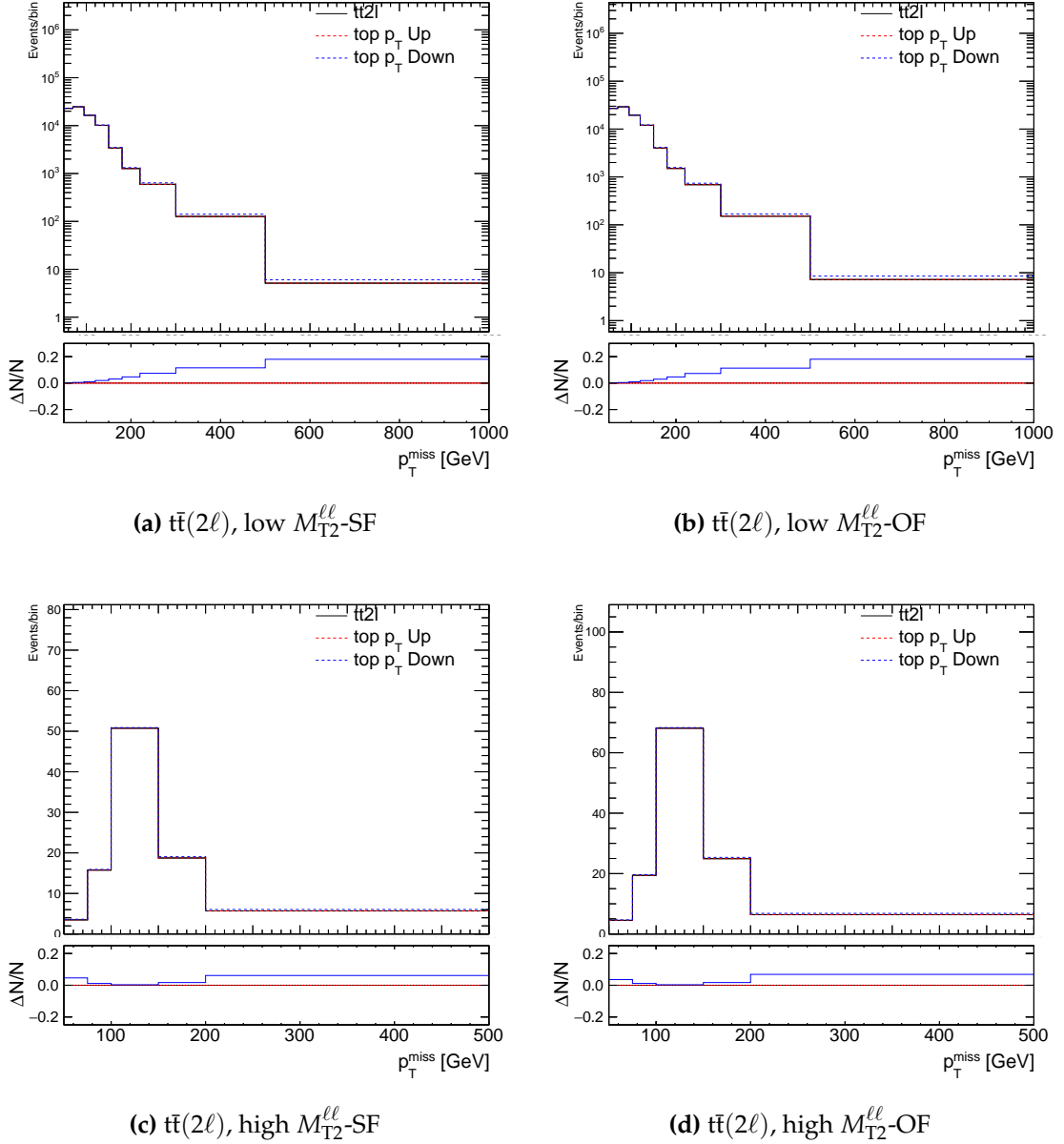


**Figure A.4:** The variation in the  $p_T^{\text{miss}}$  spectra for  $t\bar{t}(2\ell)$  in the low and high  $M_{T2}^{\ell\ell}$  SRs due to the variation of top quark  $p_T$  by  $+1\sigma$  (red) and  $-1\sigma$  (blue) of the uncertainty. The normalized residuals of the “up” and “down” shapes are shown in the lower panel.

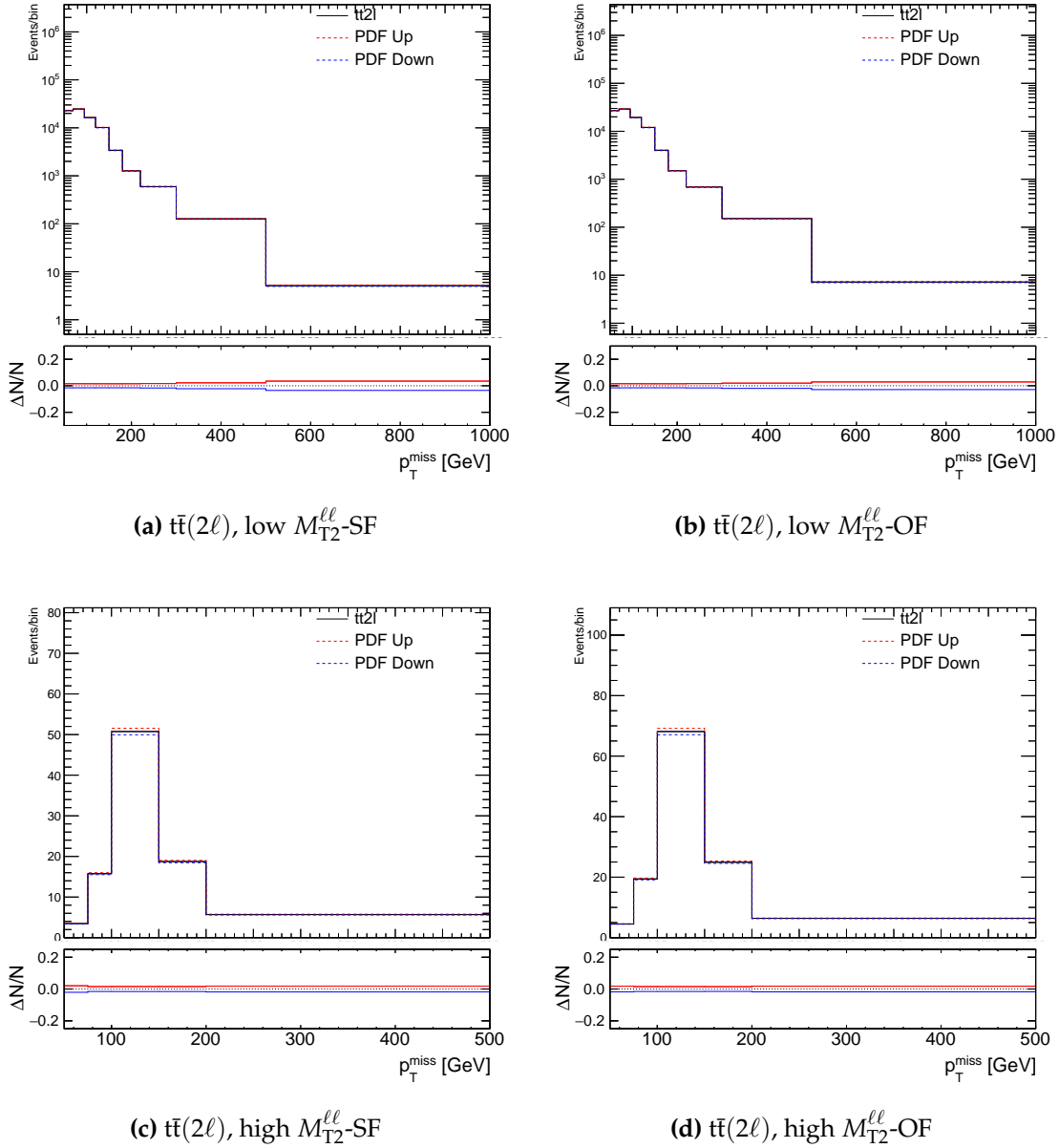


**Figure A.5.:** The variation in the  $p_T^{\text{miss}}$  spectra for  $t\bar{t}(2\ell)$  in the low and high  $M_{T2}^{\ell\ell}$  SRs due to the variation of the pdf uncertainty  $+1\sigma$  (red) and  $-1\sigma$  (blue). The normalized residuals of the “up” and “down” shapes are shown in the lower panel.

## A.2. Signal shape systematics: scalar mediated,

$$m_\phi = 10 \text{ GeV}, m_\chi = 1 \text{ GeV}$$

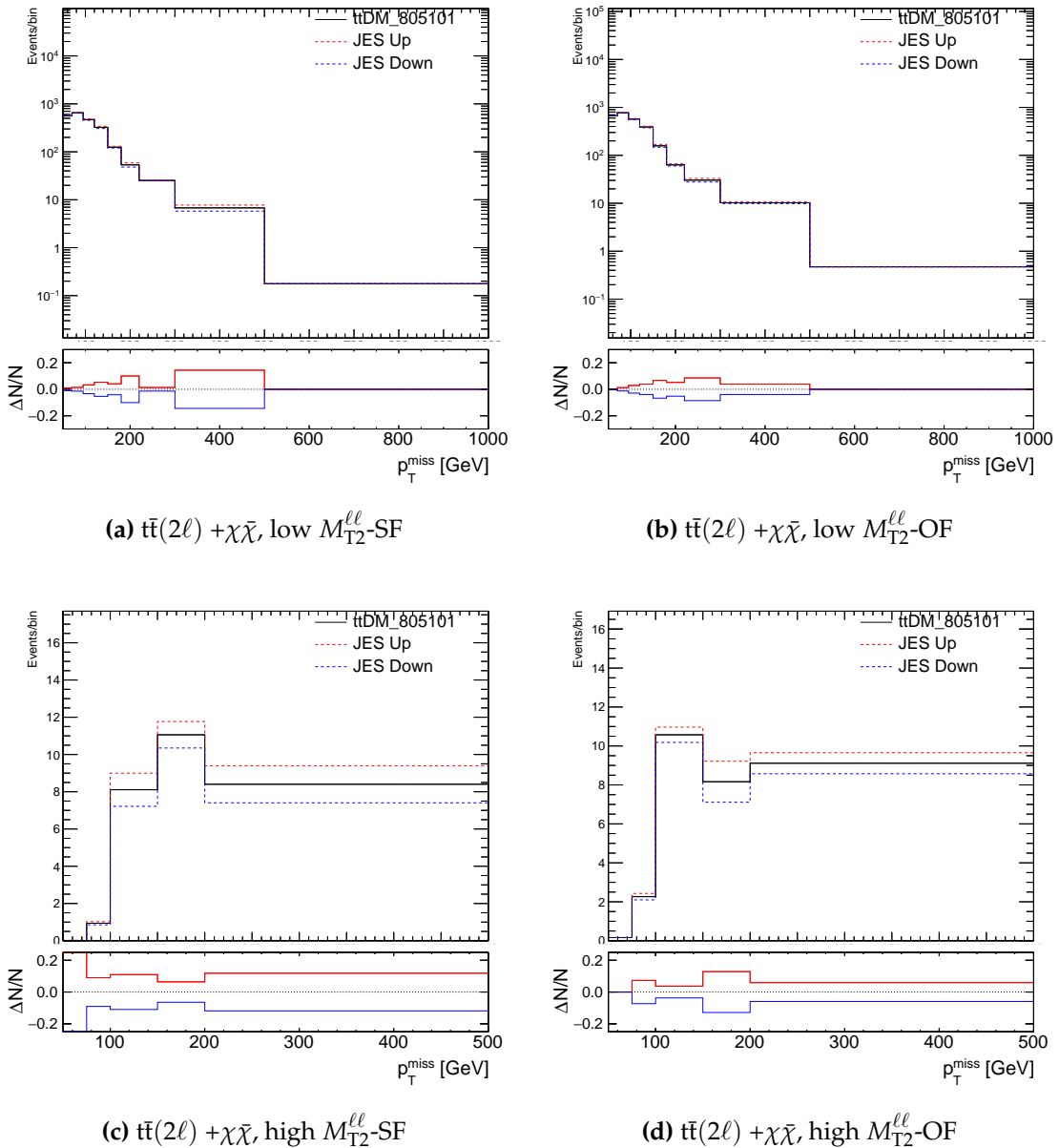


**Figure A.6.:** The variation in the  $p_T^{\text{miss}}$  spectra for a scalar mediated  $m_\phi = 10 \text{ GeV}$  signal with  $m_\chi = 1 \text{ GeV}$  in the low and high  $M_{T2}^{\ell\ell}$  SRs due to the variation of the JES uncertainty by  $+1\sigma$  (red) and  $-1\sigma$  (blue). The normalized residuals of the “up” and “down” shapes are shown in the lower panel.

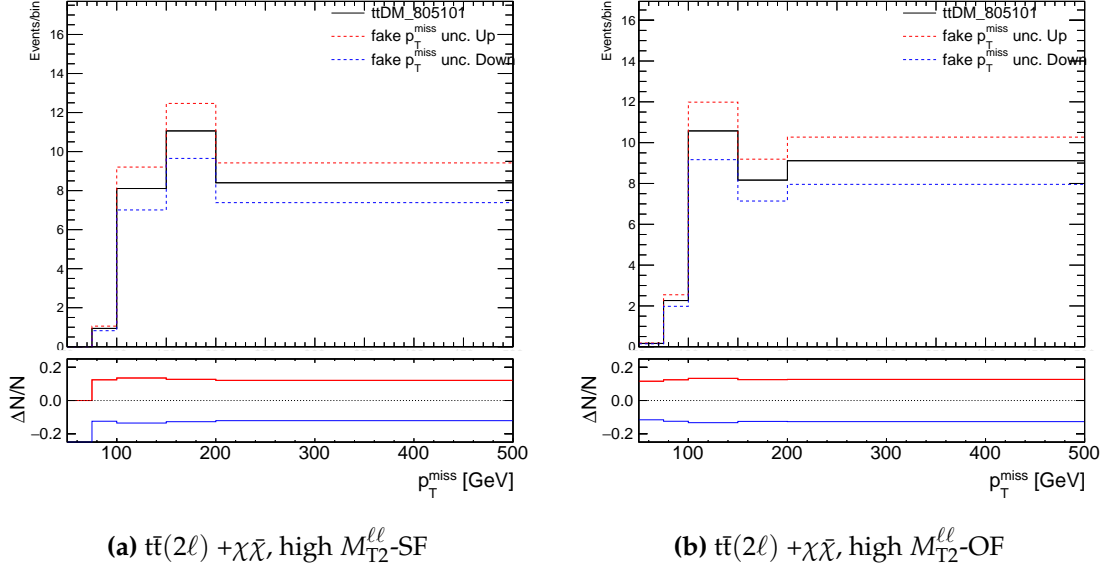


**Figure A.7.:** The variation in the  $p_T^{\text{miss}}$  spectra for scalar mediated  $m_\phi = 10 \text{ GeV}$  signal with  $m_\chi = 1 \text{ GeV}$  in the high  $M_{T2}^{\ell\ell}$  SRs due to the variation of the fake  $p_T^{\text{miss}}$  uncertainty by  $+1\sigma$  (red) and  $-1\sigma$  (blue). The normalized residuals of the “up” and “down” shapes are shown in the lower panel.

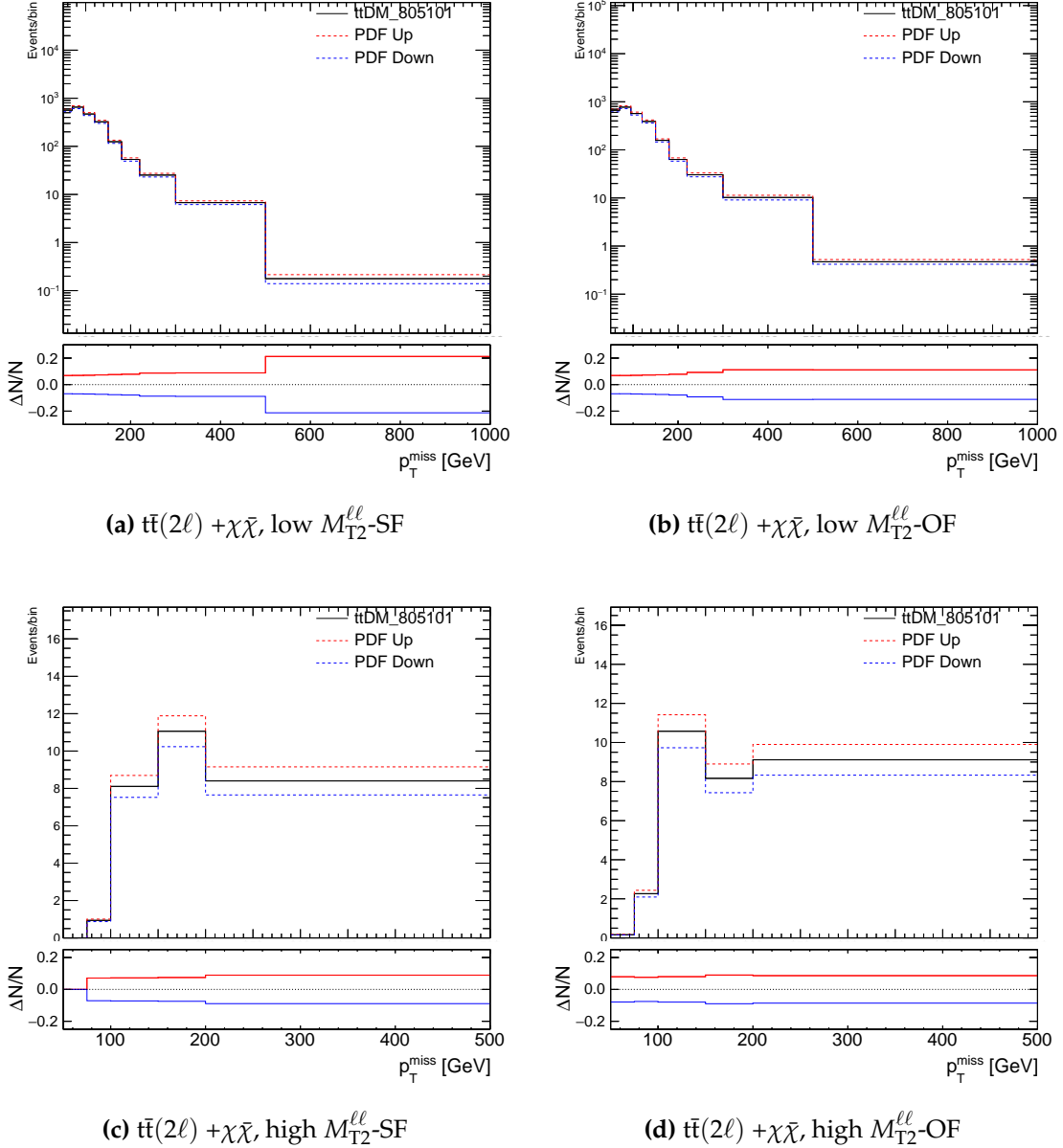


**Figure A.8:** The variation in the  $p_T^{\text{miss}}$  spectra for scalar mediated  $m_\phi = 10 \text{ GeV}$  signal with  $m_\chi = 1 \text{ GeV}$  in the low and high  $M_{T2}^{\ell\ell}$  SRs due to the variation of the pdf uncertainty  $\pm 1\sigma$  (red) and  $\pm 1\sigma$  (blue). The normalized residuals of the “up” and “down” shapes are shown in the lower panel.



# Bibliography

- [1] G. Bertone, D. Hooper, and J. Silk, Phys. Rept. **405**, 279 (2005), hep-ph/0404175.
- [2] J. L. Feng, Ann. Rev. Astron. Astrophys. **48**, 495 (2010), 1003.0904.
- [3] T. A. Porter, R. P. Johnson, and P. W. Graham, Ann. Rev. Astron. Astrophys. **49**, 155 (2011), 1104.2836.
- [4] F. Zwicky, General Relativity and Gravitation **41**, 207 (2009).
- [5] Planck, P. A. R. Ade *et al.*, Astron. Astrophys. **594**, A13 (2016), 1502.01589.
- [6] G. Bertone and D. Hooper, Submitted to: Rev. Mod. Phys. (2016), 1605.04909.
- [7] J. F. Meekins, G. Fritz, T. A. Chubb, H. Friedman, and R. C. Henry, Nature **231**, 107 EP (1971).
- [8] V. C. Rubin and W. K. Ford, Jr., Astrophys. J. **159**, 379 (1970).
- [9] S. W. Allen, A. C. Fabian, R. W. Schmidt, and H. Ebeling, Mon. Not. Roy. Astron. Soc. **342**, 287 (2003), astro-ph/0208394.
- [10] A. Refregier, Ann. Rev. Astron. Astrophys. **41**, 645 (2003), astro-ph/0307212.
- [11] J. A. Tyson, G. P. Kochanski, and I. P. Dell'Antonio, Astrophys. J. **498**, L107 (1998), astro-ph/9801193.
- [12] M. Markevitch, (2005), astro-ph/0511345, [ESA Spec. Publ.604,723(2006)].

- 
- [13] R. H. Dicke, P. J. E. Peebles, P. G. Roll, and D. T. Wilkinson, *Astrophysical Journal*, vol. 142, p.414-419 **142**, 414 (1965).
  - [14] S. Seager, D. D. Sasselov, and D. Scott, *Astrophys. J. Suppl.* **128**, 407 (2000), astro-ph/9912182.
  - [15] WMAP, D. N. Spergel *et al.*, *Astrophys. J. Suppl.* **170**, 377 (2007), astro-ph/0603449.
  - [16] Particle Data Group, K. A. Olive *et al.*, *Chin. Phys.* **C38**, 090001 (2014).
  - [17] Particle Data Group, J. Beringer *et al.*, *Phys. Rev. D* **86**, 010001 (2012).
  - [18] S. L. Glashow, *Nucl. Phys.* **10**, 107 (1959).
  - [19] A. Salam, *Conf. Proc.* **C680519**, 367 (1968).
  - [20] S. Weinberg, *Phys. Rev. Lett.* **19**, 1264 (1967).
  - [21] D. J. Griffiths, *Introduction to elementary particles; 2nd rev. version*Physics textbook (Wiley, New York, NY, 2008).
  - [22] H. D. Politzer, *Phys. Rev. Lett.* **30**, 1346 (1973).
  - [23] D. J. Gross and F. Wilczek, *Phys. Rev. Lett.* **30**, 1343 (1973).
  - [24] L. Álvarez Gaumé and J. Ellis, *Nature Physics* **7**, 2 EP (2010).
  - [25] ATLAS, G. Aad *et al.*, *Phys. Lett.* **B716**, 1 (2012), 1207.7214.
  - [26] CMS, S. Chatrchyan *et al.*, *Phys. Lett.* **B716**, 30 (2012), 1207.7235.
  - [27] G. J. Feldman, J. Hartnell, and T. Kobayashi, *Adv. High Energy Phys.* **2013**, 475749 (2013), 1210.1778.
  - [28] S. D. M. White, C. S. Frenk, and M. Davis, *Astrophys. J.* **274**, L1 (1983), [,80(1984)].

- [29] C. Park, Monthly Notices of the Royal Astronomical Society **242**, 59P (1990).
- [30] R. J. Scherrer and M. S. Turner, Phys. Rev. D **33**, 1585 (1986).
- [31] E. W. Kolb and M. S. Turner, Front. Phys. **69**, 1 (1990).
- [32] M. Cirelli, Pramana **79**, 1021 (2012), 1202.1454.
- [33] PAMELA, O. Adriani *et al.*, Nature **458**, 607 (2009), 0810.4995.
- [34] Fermi LAT Collaboration, M. Ackermann *et al.*, Phys. Rev. Lett. **108**, 011103 (2012).
- [35] AMS 01, M. Aguilar *et al.*, Phys. Lett. **B646**, 145 (2007), astro-ph/0703154.
- [36] G. Jungman, M. Kamionkowski, and K. Griest, Phys. Rept. **267**, 195 (1996), hep-ph/9506380.
- [37] E. Majorana and L. Maiani, *A symmetric theory of electrons and positrons* (Springer Berlin Heidelberg, Berlin, Heidelberg, 2006), pp. 201–233.
- [38] Aprile, E. *et al.*, Eur. Phys. J. C **77**, 881 (2017).
- [39] PandaX-II Collaboration, X. Cui *et al.*, Phys. Rev. Lett. **119**, 181302 (2017).
- [40] LUX Collaboration, D. S. Akerib *et al.*, Phys. Rev. Lett. **118**, 021303 (2017).
- [41] E. Aprile and Xenon Collaboration, The XENONnT Dark Matter Experiment, in *APS April Meeting Abstracts*, p. J9.003, 2017.
- [42] PICO, C. Amole *et al.*, Phys. Rev. Lett. **118**, 251301 (2017), 1702.07666.
- [43] CMS, V. Khachatryan *et al.*, JHEP **12**, 088 (2016), 1603.08914.
- [44] J. Goodman *et al.*, Phys. Rev. D **82**, 116010 (2010), 1008.1783.
- [45] G. Busoni, A. D. Simone, E. Morgante, and A. Riotto, Physics Letters B **728**, 412

(2014).

- [46] J. Abdallah *et al.*, Phys. Dark Univ. **9-10**, 8 (2015), 1506.03116.
- [47] L. J. Hall and L. Randall, Phys. Rev. Lett. **65**, 2939 (1990).
- [48] D. Abercrombie *et al.*, (2015), 1507.00966.
- [49] O. S. Bruning *et al.*, (2004).
- [50] G. Brianti, Phys. Rept. **403-404**, 349 (2004).
- [51] CMS, S. Chatrchyan *et al.*, JINST **3**, S08004 (2008).
- [52] ATLAS, G. Aad *et al.*, JINST **3**, S08003 (2008).
- [53] LHCb, A. A. Alves, Jr. *et al.*, JINST **3**, S08005 (2008).
- [54] ALICE, K. Aamodt *et al.*, JINST **3**, S08002 (2008).
- [55] B. Martin and G. Shaw, *Particle Physics* Manchester Physics Series (Wiley, 2008).
- [56] The CMS Collaboration, CMS Luminosity-Public Results, 2016 proton-proton 13 TeV collisions, 2016, [https://twiki.cern.ch/twiki/bin/view/CMSPublic/LumiPublicResults#2016\\_proton\\_proton\\_13\\_TeV\\_collis](https://twiki.cern.ch/twiki/bin/view/CMSPublic/LumiPublicResults#2016_proton_proton_13_TeV_collis), Last accessed on 2018-06-08.
- [57] CMS Collaboration, *The CMS magnet project: Technical Design Report* Technical Design Report CMS (CERN, Geneva, 1997).
- [58] T. C. Collaboration, *Tracker technical design report* (, 1998).
- [59] L. Borrello, A. Messineo, E. Focardi, and A. Macchiolo, (2003).
- [60] The CMS Collaboration, CMS Tracker Detector Performance Results, 13 TeV Data, 2017, [https://twiki.cern.ch/twiki/bin/view/CMSPublic/DPGResultsTRK#13\\_TeV\\_Data](https://twiki.cern.ch/twiki/bin/view/CMSPublic/DPGResultsTRK#13_TeV_Data), Last accessed on 2018-06-08.

- [61] CMS ECAL, D. J. A. Cockerill, The CMS Electromagnetic Calorimeter at the LHC, in *Proceedings, 34th International Conference on High Energy Physics (ICHEP 2008): Philadelphia, Pennsylvania, July 30-August 5, 2008*, 2008, 0810.0381.
- [62] CMS, S. Chatrchyan *et al.*, JINST **8**, P09009 (2013), 1306.2016, [JINST8,9009(2013)].
- [63] CMS, S. Chatrchyan *et al.*, JINST **5**, T03014 (2010), 0911.4881.
- [64] C. Leroy and P.-G. Rancoita, *Principles of radiation interaction in matter and detection* (World Scientific, Singapore, 2009).
- [65] CMS, S. Chatrchyan *et al.*, JINST **8**, P11002 (2013), 1306.6905.
- [66] V. Halyo, A. Hunt, P. Jindal, P. LeGresley, and P. Lujan, JINST **8**, P10005 (2013), 1305.4855.
- [67] CMS, J. Brooke, PoS **ICHEP2012**, 508 (2013), 1302.2469.
- [68] J.-M. Andre *et al.*, **664**, 082033 (2015).
- [69] R. Fruhwirth, Nucl. Instrum. Meth. **A262**, 444 (1987).
- [70] CMS Collaboration, S. Cittolin, A. Rácz, and P. Sphicas, *CMS The TriDAS Project: Technical Design Report, Volume 2: Data Acquisition and High-Level Trigger*. CMS trigger and data-acquisition project Technical Design Report CMS (CERN, Geneva, 2002).
- [71] P. Avery, First Monday **12** (2007).
- [72] C. Eck *et al.*, *LHC computing Grid: Technical Design Report. Version 1.06* (20 Jun 2005) Technical Design Report LCG (CERN, Geneva, 2005).
- [73] G. Petrucciani, A. Rizzi, and C. Vuosalo, Journal of Physics: Conference Series **664**, 072052 (2015).

- 
- [74] CMS, A. M. Sirunyan *et al.*, JINST **12**, P10003 (2017), 1706.04965.
  - [75] M. Cacciari, G. P. Salam, and G. Soyez, JHEP **04**, 063 (2008), 0802.1189.
  - [76] J. Alwall *et al.*, JHEP **07**, 079 (2014), 1405.0301.
  - [77] M. Backovi *et al.*, Eur. Phys. J. **C75**, 482 (2015), 1508.05327.
  - [78] M. L. Mangano, M. Moretti, F. Piccinini, and M. Treccani, JHEP **01**, 013 (2007), hep-ph/0611129.
  - [79] P. Harris, V. V. Khoze, M. Spannowsky, and C. Williams, Phys. Rev. D **91**, 055009 (2015).
  - [80] T. Han, J. Sayre, and S. Westhoff, JHEP **04**, 145 (2015), 1411.2588.
  - [81] C. G. Lester and D. J. Summers, Phys. Lett. **B463**, 99 (1999), hep-ph/9906349.
  - [82] S. Frixione, P. Nason, and C. Oleari, JHEP **11**, 070 (2007), 0709.2092.
  - [83] S. Alioli *et al.*, JHEP **06**, 043 (2010), 1002.2581.
  - [84] T. Sjöstrand *et al.*, Comput. Phys. Commun. **191**, 159 (2015), 1410.3012.
  - [85] S. Agostinelli *et al.*, Nuclear Instruments and Methods in Physics Research Sec. A: Accelerators, Spectrometers, Detectors and Associated Equipment **506**, 250 (2003).
  - [86] M. Beneke, P. Falgari, S. Klein, and C. Schwinn, Nucl. Phys. B **855**, 695 (2012), 1109.1536.
  - [87] M. Cacciari, M. Czakon, M. Mangano, A. Mitov, and P. Nason, Phys. Lett. B **710**, 612 (2012), 1111.5869.
  - [88] P. Bärnreuther, M. Czakon, and A. Mitov, Phys. Rev. Lett. **109**, 132001 (2012), 1204.5201.

- [89] M. Czakon and A. Mitov, JHEP **12**, 054 (2012), 1207.0236.
- [90] M. Czakon and A. Mitov, JHEP **01**, 080 (2013), 1210.6832.
- [91] CMS, V. Khachatryan *et al.*, Phys. Rev. **D95**, 092001 (2017), 1610.04191.
- [92] The ATLAS Collaboration, The CMS Collaboration, The LHC Higgs Combination Group, CERN Report No. CMS-NOTE-2011-005. ATL-PHYS-PUB-2011-11, 2011 (unpublished).
- [93] J. S. Conway, Incorporating Nuisance Parameters in Likelihoods for Multisource Spectra, in *Proceedings, PHYSTAT 2011 Workshop on Statistical Issues Related to Discovery Claims in Search Experiments and Unfolding, CERN, Geneva, Switzerland 17-20 January 2011*, pp. 115–120, 2011, 1103.0354.
- [94] CMS Collaboration, CERN Report No. CMS-PAS-LUM-17-001, 2017 (unpublished).
- [95] CMS, S. Chatrchyan *et al.*, JHEP **10**, 132 (2011), 1107.4789.
- [96] CMS, CERN Report No. CMS-PAS-BTV-15-001, 2016 (unpublished).
- [97] J. C. Collins, D. E. Soper, and G. F. Sterman, Adv. Ser. Direct. High Energy Phys. **5**, 1 (1989), hep-ph/0409313.
- [98] J. Butterworth *et al.*, Journal of Physics G: Nuclear and Particle Physics **43**, 023001 (2016).
- [99] NNPDF, R. D. Ball *et al.*, JHEP **04**, 040 (2015), 1410.8849.
- [100] L. Lista, Practical Statistics for Particle Physicists, in *Proceedings, 2016 European School of High-Energy Physics (ESHEP2016): Skeikampen, Norway, June 15-28 2016*, pp. 213–258, 2017, 1609.04150.
- [101] S. Baker and R. D. Cousins, Nuclear Instruments and Methods in Physics

- Research **221**, 437 (1984).
- [102] T. M. Karbach and M. Schlupp, (2012), 1210.7141.
- [103] E. Gross, CERN Yellow Reports: School Proceedings **4**, 165 (2017).
- [104] CMS Collaboration, CERN Report No. CMS-PAS-EXO-16-049, 2018 (unpublished).
- [105] CMS, A. M. Sirunyan *et al.*, Phys. Rev. **D97**, 092005 (2018), 1712.02345.
- [106] G. Busoni *et al.*, (2016), 1603.04156.
- [107] M. Hoferichter, J. Ruiz de Elvira, B. Kubis, and U.-G. Meißner, Phys. Rev. Lett. **115**, 092301 (2015), 1506.04142.
- [108] P. Junnarkar and A. Walker-Loud, Phys. Rev. **D87**, 114510 (2013), 1301.1114.
- [109] CMS, A. M. Sirunyan *et al.*, Eur. Phys. J. **C77**, 845 (2017), 1706.02581.

# List of figures

1.1.	The velocities of emission regions from M31 as a function of distance to the center of the galaxy measured in minutes of arc along the NE major axis as reported by Rubin and Ford in [8]. . . . .	3
1.2.	A composite image from the Hubble, Chandra, and Magellan telescopes of the 1E 0657-558 cluster of galaxies (Bullet cluster) depicting the X-rays emitted by the baryonic matter as a diffuse red gas, while the approximate location of the DM surrounding the visible matter is represented in a blue hue. . . . .	5
1.3.	The CMB radiation temperature anisotropy power spectrum as a function of the multipole order, $\ell$ , as measured by various experiments [16]. The angular scales that correspond to the multipole orders are listed across the top of the graph. The data points correspond to the experimental measurements and the error bars account for measurement uncertainties. The black curve represents the best global fit of the standard model of cosmology to the Planck data. . . . .	8
1.4.	The vacuum value, or the lowest-energy state, of the Higgs potential as shown in the 3-dimensional plot is described by a randomly chosen point at the bottom of the “sombrero” [24]. . . . .	15

1.5. The WIMP comoving number density as a function of time, also parametrized as $x_f = \frac{m_\chi}{T_f}$ , where an increase in the annihilation cross section ultimately results in a later freeze-out time, and a correspondingly lower thermal relic density [31]. . . . .	26
1.6. The positron energy spectra measured by a compilation of recent (PAMELA and FERMI) and less recent ID experiments dedicated to measurements of secondary charged particles emitted in cosmic ray fluxes. The data is superimposed on a compilation of uncertain astrophysical backgrounds from secondary production. [32] . . . . .	28
1.7. Cross section limits as a function of the DM mass for spin-independent interactions for PandaX-II, LUX, and XENON1T. . . . .	33
1.8. . . . .	37
1.9. The representative diagram of a top quark pair produced in association with a pair of DM particles ( $\chi\bar{\chi}$ ) using (a) the EFT formalism and (b) the simplified model formalism. . . . .	39
2.1. The approximate location of the LHC ring traced over the Swiss-French border near Geneva, Switzerland. Also indicated are the relative locations of the two high luminosity experiments (CMS and ATLAS), the low luminosity B-physics dedicated experiment (LHCb), and the dedicated ion experiment (ALICE). . . . .	42
2.2. A schematic of the CERN accelerator complex, where protons (blue arrows) and ions (lime green arrows) begin their journey to the main LHC ring at the Linac 2 and Linac 3, respectively. . . . .	44

2.3. The integrated luminosity as a function of time that the LHC delivered at $\sqrt{s} = 7 \text{ TeV}$ and $\sqrt{s} = 8 \text{ TeV}$ during 2011 and 2012, and at $\sqrt{s} = 13 \text{ TeV}$ during 2015 and 2016. . . . .	45
2.4. A diagram of the cylindrical coordinate system for the CMS detector. . . . .	46
2.5. The total integrated luminosity that the LHC machine delivered to CMS, and the total integrated luminosity that the detector collected during the 2016 data-taking period [56]. . . . .	48
2.6. Cross-section view of CMS [51]. . . . .	49
2.7. Schematic cross-section through the CMS tracker, where a single detector modules is represented by a line, and double lines signify back-to-back modules [58]. . . . .	51
2.8. The strip hit resolution for the TIB and TOB layers which are comprised of Si sensors with varying strip pitch. The tracks selected have $p_T > 3 \text{ GeV}$ , at least six hits in the inner tracker, and $\chi^2$ probability greater than nine [60]. . . . .	54
2.9. A quarter-view of the CMS hadron calorimeter. The shading indicates the grouping of scintillating layers optically added together to form trigger tower signal readouts. [63] . . . . .	56
2.10. A quadrant view of CMS where the IP is at the lower left corner. The dark grey areas denote the locations of the various muon stations and the steel disks. The 4 drift tube (DT, in light orange) stations are labeled MB (muon barrel) and the cathode strip chambers (CSC, in green) are labeled ME (muon endcap). The resistive plate chambers (RPC, in blue) located in the barrel and the endcaps of CMS, are labeled RB and RE, respectively. [65] . . . . .	62

2.11. A schematic of the two stage CMS trigger architecture and the corresponding rate reduction at each stage [66]. . . . .	63
2.12. An overview of the CMS L1 trigger where the detector inputs are at the bottom and the subsequent steps in rate reduction proceed vertically upwards. [66] . . . . .	65
2.13. A flow chart of the multi-tier worldwide LHC computing grid, where the components circled in red are examples of the U.S. resources that are part of Open Science Grid (OSG) as defined in detail in [71]. The computing resources at Northwestern University fall under the Tier 3 computing category. . . . .	69
3.1. $W^+$ and $W^-$ decay to leptons and corresponding lepton neutrinos for all lepton generations. . . . .	74
3.2. Discriminator values for the CSVv2 algorithm for an inclusive multi-jet topology, where the total number of entries in the simulation is normalized to the observed number of entries in the data. . . . .	87
4.1. The representative diagram of a top quark pair produced in association with a pair of DM particles ( $\chi\bar{\chi}$ ) which are produced via a S or PS mediator coupled to the tops. . . . .	90
4.2. Generator level $p_T$ distributions for S (solid lines) and PS (dashed lines) mediators, with $m_\chi = 1 \text{ GeV}$ . The label “S 10, 1” can be understood as a model with S mediator mass $m_\phi = 10 \text{ GeV}$ , and DM mass $m_\chi = 1 \text{ GeV}$ . $p_T$ distributions with the same color have the same mediator mass. . .	91

4.3. (a) Generator level $p_T$ distributions for off-shell production, with solid (dashed) lines for S (PS) mediated models, and $m_\chi = 50$ GeV. The label “S 10, 50” can be understood as a model with S $m_\phi = 10$ GeV and $m_\chi = 50$ GeV. (b) Near the on-shell/off-shell threshold (green solid line), the kinematics have contributions from on-shell and off-shell production. . . . .	91
4.4. The $M_{T2}^{\ell\ell}$ distribution in data and simulation for events passing selection requirements for the $e\mu$ channel. The distributions of two example signal models with S and PS mediators of $m_\phi = 100$ GeV, and with $m_\chi = 1$ GeV are also presented and scaled up by a factor of 200. The last bin in the distribution includes overflow, and the uncertainties are statistical only. . . . .	97
5.1. Summary of the cross section measurements of SM processes as of January 2018 with data collected by the CMS experiment at $\sqrt{s} = 7, 8,$ and $13$ TeV. . . . .	100
5.2. Leading order $t\bar{t}$ production diagrams probed at the LHC via (a), (b) gluon fusion, and (c) quark-antiquark annihilation. . . . .	100
5.3. Effect of the top $p_T$ re-weighting on the expected $t\bar{t}(2\ell)$ background $p_T^{\text{miss}}$ shape for events passing selection defined in Section 4.2 and having (a) $M_{T2}^{\ell\ell} < 110$ GeV and (b) $M_{T2}^{\ell\ell} > 110$ GeV. . . . .	103
5.4. Examples of the (a) $t\bar{t} + Z(\nu\bar{\nu})$ process, and (b) diboson production at LO.105	
5.5. Single top quark production via (a) s-channel, (b) t-channel, and (c) in association with a W boson. . . . .	105

5.6. The DY lepton pair-production process mediated by a virtual photon ( $\gamma^*$ ) or Z boson at (a) $\mathcal{O}(\alpha)$ and (b),(c),(d),(e) $\mathcal{O}(\alpha\alpha_s)$ . . . . .	106
5.7. The $p_T^{\text{miss}}$ distribution in data and simulation for SF events, where the dilepton mass is required to be <i>inside</i> the $\pm 15$ GeV window relative to the Z boson mass. In addition the events must contain at least two jets, and no b-tagged jets. . . . .	108
5.8. Z peak in data and MC after subtraction of non-DY contribution estimate from opposite-flavor data events in the $ee$ channel for various $p_T^{\text{miss}}$ bins. . . . .	114
5.9. Z peak in data and MC after subtraction of non-DY contribution estimate from opposite-flavor data events in the $\mu\mu$ channel for various $p_T^{\text{miss}}$ bins. . . . .	115
5.10. Data/MC scale factors binned in $p_T^{\text{miss}}$ applied to MC events used for the estimate of the DY normalization in the dilepton channel signal regions. . . . .	116
5.11. Examples of (a) W+jets, and (b) semileptonic t <bar>t} that contribute to the fake lepton background. . . . .</bar>	117
5.12. Measured electron fake rates as a function of lepton (a) $p_T$ and (b) $ \eta $ . .	121
5.13. Measured muon fake rates as a function of lepton (a) $p_T$ and (b) $ \eta $ . .	121
5.14. The $p_T^{\text{miss}}$ distributions in the fake rate method validation region. All expected backgrounds are estimated using simulation, except for the fake lepton contribution, denoted “FR Pred” which is estimated via the fake rate method. . . . .	124

6.1. Scale factors for the electron and muon leg of the muon-electron trigger parametrized in lepton $p_T$ and $\eta$ . . . . .	129
6.2. (a) Pileup distributions in data and MC. Also shown are the pileup profiles in a few run ranges scaled to the relative contribution to the total integrated luminosity.(b) The pileup distributions from varying the total inelastic cross section by $\pm 4.6\%$ . . . . .	130
6.3. $N_{PV}$ distributions in data and MC pre and post PU re-weighting in a region dominated by semileptonic $t\bar{t}$ events. The MC is normalized to the observed yield. . . . .	131
6.4. The efficiency in $t\bar{t}(2\ell)$ simulation is measured as a function of jet $p_T$ and various $\eta$ bins for (a) correctly tagging b jets, (b) misidentifying c jets, (c) and misidentifying light flavor or gluon jets. . . . .	132
6.5. Kinematic distributions in the same flavor ( $ee + \mu\mu$ ) channel. Signals with a pseudoscalar (magenta) and scalar (blue) mediator with $m_\phi = 100$ GeV and $m_\chi = 1$ GeV are overlayed and scaled by a factor of 200 to illustrate the potential shape differences between the signal and background in the various distributions. The uncertainties shown in these plots on the data and background are purely statistical. . . . .	135
6.6. Kinematic distributions in the same flavor ( $ee + \mu\mu$ ) channel. Signals with a pseudoscalar (magenta) and scalar (blue) mediator with $m_\phi = 100$ GeV and $m_\chi = 1$ GeV are overlayed and scaled by a factor of 200 to illustrate the potential shape differences between the signal and background in the various distributions. The uncertainties shown in these plots on the data and background are purely statistical. . . . .	136

- 
- 6.7. Kinematic distributions in the same flavor ( $e\mu$ ) channel. Signals with a pseudoscalar (magenta) and scalar (blue) mediator with  $m_\phi = 100 \text{ GeV}$  and  $m_\chi = 1 \text{ GeV}$  are overlayed and scaled by a factor of 200 to illustrate the potential shape differences between the signal and background in the various distributions. The uncertainties shown in these plots on the data and background are purely statistical. . . . . 137
- 6.8. Kinematic distributions in the same flavor ( $e\mu$ ) channel. Signals with a pseudoscalar (magenta) and scalar (blue) mediator with  $m_\phi = 100 \text{ GeV}$  and  $m_\chi = 1 \text{ GeV}$  are overlayed and scaled by a factor of 200 to illustrate the potential shape differences between the signal and background in the various distributions. The uncertainties shown in these plots on the data and background are purely statistical. . . . . 138
- 6.9. The  $M_{T2}^{\ell\ell}$  distribution in the (a) same flavor and (b) opposite flavor channels. Events with  $M_{T2}^{\ell\ell}$  below (above)  $110 \text{ GeV}$  form the low (high) signal purity categories. The uncertainties in the above plots are statistical only. The  $M_{T2}^{\ell\ell}$  templates for signals with a pseudoscalar (magenta) and scalar (blue) mediator with  $m_\phi = 100 \text{ GeV}$  and  $m_\chi = 1 \text{ GeV}$  are overlayed and scaled by a factor of 200. . . . . 139
- 6.10. The  $p_T^{\text{miss}}$  distributions in the low purity signal region for (a) same flavor and (b) opposite flavor events. The uncertainties in the above plots are statistical only. The  $p_T^{\text{miss}}$  templates in the low purity signal region for signals with a pseudoscalar (magenta) and scalar (blue) mediator with  $m_\phi = 100 \text{ GeV}$  and  $m_\chi = 1 \text{ GeV}$  are overlayed and scaled by a factor of 200. . . . . 139

---

6.11. The $p_T^{\text{miss}}$ distributions in the high purity signal region for (a) same flavor and (b) opposite flavor events. The uncertainties in the above plots are statistical only. The $p_T^{\text{miss}}$ templates in the high purity signal region for signals with a pseudoscalar (magenta) and scalar (blue) mediator with $m_\phi = 100 \text{ GeV}$ and $m_\chi = 1 \text{ GeV}$ are overlayed and scaled by a factor of 200. . . . .	140
6.12. The variation in the $p_T^{\text{miss}}$ spectra for $t\bar{t}(2\ell)$ in the low and high $M_{T2}^{\ell\ell}$ -OF SRs due to the variation of the JES uncertainty by $+1\sigma$ (red) and $-1\sigma$ (blue). The normalized residuals of the “up” and “down” shapes are shown in the lower panel. . . . .	145
6.13. The fake $p_T^{\text{miss}}$ uncertainty at one standard deviation from the nominal recoil distribution as derived in simulation using Z bosons decaying to dielectrons and dimuons with $M_{T2}^{\ell\ell} > 110 \text{ GeV}$ . In order to smoothen out the binned uncertainty, it is fit with a second-order polynomial. . . . .	146
6.14. The variation in the $p_T^{\text{miss}}$ spectra for (a) DY and (b) $t\bar{t}(2\ell)$ in the high $M_{T2}^{\ell\ell}$ -SF SRs due to the variation of the fake $p_T^{\text{miss}}$ uncertainty by $+1\sigma$ (red) and $-1\sigma$ (blue). The normalized residuals of the “up” and “down” shapes are shown in the lower panel. . . . .	147
6.15. A visualization of the relation (a) between the observed value of the test statistic $q(\mu)_{\text{obs}}$ , the probability density function $f(q(\mu)   H)$ and the $p$ -value, and (b) between the $p$ -value and the significance $Z$ . . . . .	152

- 
- 6.16. The background-only post-fit  $p_T^{\text{miss}}$  distributions in the low signal purity SRs. The expected (pre-fit)  $p_T^{\text{miss}}$  distributions for two example signals (scalar and pseudoscalar mediator,  $m_{\phi/a} = 100 \text{ GeV}$ ) with  $m_\chi = 1 \text{ GeV}$  are scaled up by a factor of 200. The dashed blue line represents the total expected (pre-fit) MC background  $p_T^{\text{miss}}$  shape, and the subsequent ratio between the pre-fit and post-fit shape in the lower ratio panel. The last bin of the distributions includes overflow. Statistical and systematic uncertainties are shown. . . . . 154
- 6.17. The background-only post-fit  $p_T^{\text{miss}}$  distributions in the high signal purity SRs. The pre-fit  $p_T^{\text{miss}}$  distributions for two example signals (scalar and pseudoscalar mediator,  $m_{\phi/a} = 100 \text{ GeV}$ ) with  $m_\chi = 1 \text{ GeV}$  are scaled up by a factor of 200. The dashed blue line represents the total expected (pre-fit) MC background  $p_T^{\text{miss}}$  shape, and the subsequent ratio between the pre-fit and post-fit shape in the lower ratio panel. The last bin of the distributions includes overflow. Statistical and systematic uncertainties are shown. . . . . 155
- 6.18. Background-only (red) and signal-plus-background (blue) post-fit nuisance pulls. . . . . 159
- 7.1. The expected (red dashed) and observed (solid black) 95% CL<sub>s</sub> upper limits on the  $t\bar{t} + \chi\bar{\chi}$  signal strength in the dilepton channel for various (a) scalar and (b) pseudoscalar mediator masses where  $m_\chi = 1 \text{ GeV}$  and  $g_q = g_\chi = 1$  is assumed. The green (yellow) band represents the 68% (95%) interval of probability around the expected limit. The results are obtained using  $35.9 \text{ fb}^{-1}$  collected by the CMS detector in 2016. . . . . 164

7.2. The exclusion limits at 95% CL <sub>s</sub> on the signal strength parameter $\mu$ for the $t\bar{t} + \chi\bar{\chi}$ process in the dilepton channel, computed as a function of the mediator mass and DM mass, assuming a scalar mediator. The mediator couplings are assumed to be $g_q = g_\chi = 1$ .	166
7.3. A comparison of the $t\bar{t}(2\ell) + \chi\bar{\chi}$ scalar-mediated results (CMS expected and observed lines) to the exclusion contours of the LUX, PandaX-II, XENON1T, CDEX-10, CDMSLite, and CRESST-II limits in the $m_\chi$ - $\sigma_{\text{SI}}$ plane. The DM particle is assumed to be a Dirac fermion and $g_q = g_\chi = 1$ .	169
A.1. The variation in the $p_T^{\text{miss}}$ spectra for $t\bar{t}(2\ell)$ in the low and high $M_{\text{T2}}^{\ell\ell}$ SRs due to the variation of the JES uncertainty by $+1\sigma$ (red) and $-1\sigma$ (blue). The normalized residuals of the “up” and “down” shapes are shown in the lower panel.	174
A.2. The variation in the $p_T^{\text{miss}}$ spectra for $t\bar{t}(2\ell)$ in the high $M_{\text{T2}}^{\ell\ell}$ SRs due to the variation of the fake $p_T^{\text{miss}}$ uncertainty by $+1\sigma$ (red) and $-1\sigma$ (blue). The normalized residuals of the “up” and “down” shapes are shown in the lower panel.	175
A.3. The variation in the $p_T^{\text{miss}}$ spectra for $t\bar{t}(2\ell)$ in the low and high $M_{\text{T2}}^{\ell\ell}$ SRs due to the variation of the factorization and renormalization scales by $+1\sigma$ (red) and $-1\sigma$ (blue). The normalized residuals of the “up” and “down” shapes are shown in the lower panel.	176
A.4. The variation in the $p_T^{\text{miss}}$ spectra for $t\bar{t}(2\ell)$ in the low and high $M_{\text{T2}}^{\ell\ell}$ SRs due to the variation of top quark $p_T$ by $+1\sigma$ (red) and $-1\sigma$ (blue) of the uncertainty. The normalized residuals of the “up” and “down” shapes are shown in the lower panel.	177

---

A.5. The variation in the $p_T^{\text{miss}}$ spectra for $t\bar{t}(2\ell)$ in the low and high $M_{T2}^{\ell\ell}$ SRs due to the variation of the pdf uncertainty $+1\sigma$ (red) and $-1\sigma$ (blue). The normalized residuals of the “up” and “down” shapes are shown in the lower panel. . . . .	178
A.6. The variation in the $p_T^{\text{miss}}$ spectra for a scalar mediated $m_\phi = 10 \text{ GeV}$ signal with $m_\chi = 1 \text{ GeV}$ in the low and high $M_{T2}^{\ell\ell}$ SRs due to the variation of the JES uncertainty by $+1\sigma$ (red) and $-1\sigma$ (blue). The normalized residuals of the “up” and “down” shapes are shown in the lower panel. . . . .	179
A.7. The variation in the $p_T^{\text{miss}}$ spectra for scalar mediated $m_\phi = 10 \text{ GeV}$ signal with $m_\chi = 1 \text{ GeV}$ in the high $M_{T2}^{\ell\ell}$ SRs due to the variation of the fake $p_T^{\text{miss}}$ uncertainty by $+1\sigma$ (red) and $-1\sigma$ (blue). The normalized residuals of the “up” and “down” shapes are shown in the lower panel. . . . .	180
A.8. The variation in the $p_T^{\text{miss}}$ spectra for scalar mediated $m_\phi = 10 \text{ GeV}$ signal with $m_\chi = 1 \text{ GeV}$ in the low and high $M_{T2}^{\ell\ell}$ SRs due to the variation of the pdf uncertainty $+1\sigma$ (red) and $-1\sigma$ (blue). The normalized residuals of the “up” and “down” shapes are shown in the lower panel. . . . .	181

# List of tables

1.1. The particles of the SM including the leptons ( $e^-$ , $\mu^-$ , $\tau^-$ , $\nu_e$ , $\nu_\mu$ , $\nu_\tau$ ), the quarks ( $u$ , $d$ , $c$ , $s$ , $t$ , $b$ ), the gauge bosons ( $W^\pm$ , $Z$ , $g$ , $\gamma$ ), and the scalar Higgs boson ( $H$ ). The spin, charge, and mass are specified where the neutrinos are taken to be massless, and indirect measurements posit the mass eigenstates are less than 0.23 eV [17]. The forces via which the particles interact are listed for each lepton and quark and the force mediated is listed for the gauge bosons. . . . .	11
3.1. Variables and thresholds that define “FO”, “Loose”, and “Tight”. “-” indicates the variable is not considered for that working point. . . . .	77
3.2. Effective areas for electron isolation PU subtraction. . . . .	80
3.3. Variables and thresholds that define “FO”, “Veto”, and “Tight” electrons. An electron is in the barrel if it has supercluster $ \eta  < 1.479$ , otherwise it is in the endcap. . . . .	81
3.4. Variables and thresholds that define the “Loose” PF jet ID. . . . .	83

4.1. A summary of the signal model samples and the correpsonding NLO cross sections used in this work for S and PS mediator masses with $m_\chi = 1 \text{ GeV}$ .	92
5.1. DY yields and $R_{\text{in}/\text{out}}$ values in the $ee$ channel, for 0 b-tag selection	112
5.2. DY yields and $R_{\text{in}/\text{out}}$ values in the $\mu\mu$ channel, for 0 b-tag selection	112
5.3. DY yields and $R_{\text{in}/\text{out}}$ values in the $ee$ channel, for $\geq 1$ b-tag selection	112
5.4. DY yields and $R_{\text{in}/\text{out}}$ values in the $\mu\mu$ channel, for $\geq 1$ b-tag selection	113
5.5. Signal region DY yields in MC and data (from $R_{\text{in}/\text{out}}$ prediction) in the $ee$ channel	113
5.6. Signal region DY yields in MC and data (from $R_{\text{in}/\text{out}}$ prediction) in the $\mu\mu$ channel	113
5.7. Electron fake rates	120
5.8. Muon fake rates	120
6.1. Background-only post-fit event yields passing selection in the $M_{\text{T2}}^{\ell\ell} > 110 \text{ GeV}$ (high signal purity) category. The expected (pre-fit) yield is also shown for a pseudoscalar $m_a = 100 \text{ GeV}$ , $m_\chi = 1 \text{ GeV}$ signal. The uncertainties include contributions from both systematic and statistical sources.	153
6.2. Background-only post-fit event yields passing selection in the $M_{\text{T2}}^{\ell\ell} < 110 \text{ GeV}$ (low signal purity) category. The expected (pre-fit) yield is also shown for a pseudoscalar $m_a = 100 \text{ GeV}$ , $m_\chi = 1 \text{ GeV}$ signal. The uncertainties include contributions from both systematic and statistical sources.	154

6.3. A summary of the naming convention for the nuisance parameters used in the fit, whether each is implemented as “lnN” (normalization uncertainty) or “shape” (shape uncertainty), and which processes each affects. Unless indicated under the description heading, a nuisance is treated as correlated across both same and opposite flavor, high and low $M_{T2}^{\ell\ell}$ signal regions, and across the signal and all background processes.	158
7.1. Observed and expected upper limits at 95% CL <sub>s</sub> on $\mu$ as a function of scalar (S) and pseudoscalar (PS) mediator masses for $m_{\chi} = 1$ GeV with $\pm 1\sigma$ and $\pm 2\sigma$ uncertainties on the expected limits.	163